Unravelling the Degradation Pathways and Charging Mechanism in the Li-O_2 Battery: The Role of Singlet Oxygen

Ceren Zor

St Edmund Hall

Department of Materials

University of Oxford

A thesis submitted for the degree of
Doctor of Philosophy
Trinity 2022

Declaration of Originality

I, Ceren Zor, hereby confirm that the work presented in this Thesis is my own. Where information has been derived from other sources, I confirm that this has been indicated in the Thesis. This work has not been submitted to another institution for any other degree or qualification.

This thesis is approximately 35,000 words in length, excluding the tables, lists, figure captions, and the supplementary information. It complies with the Departmental word limit for doctoral theses.

Acknowledgements

First and foremost, I would like to thank my supervisor Professor Peter G. Bruce for giving me the opportunity to do research as a member of his world-leading battery group. I am grateful for his advice and support. Doing research with him and his team has been immensely scientifically intriguing.

I have enjoyed working with all the PGB Group members and would like to thank the past and current members who were there when I needed a hand.
I would like to acknowledge Dr Sunyhik Ahn for the SECM measurements and Dr Sixie Yang for the help with the initial development of the singlet oxygen generation setup. I appreciate Dr John Walsby-Tickle's help with the LC-MS measurements and his valuable insights in this area. I thank Dr Gregory Rees for helping me with all the NMR studies, but more importantly, for introducing the term "bin fire" to me. It's not my data, it is just Li-air...I am grateful to Dr Xiangwen Gao for all the fruitful scientific discussions and his patience towards my Sambuca attacks. I thank Dr Rob House and Dr Boyang Liu for their support in my job search hassle and endurance against my random chemistry questions.

It was a great experience working with our former lab manager Dr Nadia Abdul-Karim. She is a true hero. Fighting fires and floods, she is the most patient and helpful researcher I have ever met. Dr Nadia Abdul-Karim, I loved troubleshooting with you. I learned a lot from you, and you have been a great friend as well. I would like to thank the estates team Les Chorley, Mike Stanley and, Francis Dunleavey for making research possible at Rex Richards and being helpful and cheerful at all times. Dr Diana P., Miki B., Dr Erez C., and Zsofia L. have been very sympathetic and friendly throughout my DPhil. I thank them and all the kind Department of Materials staff warmly.

I would like to acknowledge all the field service engineers I watched fixing equipment. I learned a lot from them! They say that with a week of training, I could do their jobs now!

I thank all the group members who proof-read my thesis so that there are (hopefully) no last-minute surprises. This thesis has been proof-read by:

Abstract – Dr Mikkel Juelsholt, Dr Tammy Nimmo, and Dr Paul Adamson
Ch1-Intro. – Dr Xiangwen Gao and Dr Tammy Nimmo
Ch2-Exp. – Dr Dominic Spencer Jolly and Dr Paul Adamson
Ch3-Results – Dr Robert House and Dominic Melvin
Ch4-Results – Dr Xiangwen Gao and Dr Gregory Rees
Ch5-Results – Dr Gregory Rees and Dr Xiangwen Gao
Ch6-Conc. – Dr Dominic Spencer Jolly, Dr Mikkel Juelsholt, Dr Tammy Nimmo, and Dr Paul Adamson

I am grateful to have such great, loyal, and fun friends. Big thanks and huge hugs to NdD members Dr Albert Xiao (99% Rex), Dr Pablo Quijano, Eoin O'Sullivan, John Ballentine, Pierre Romain, and Dillon McGurty. I wouldn't be able to keep my last little bits of sanity together wi thout you. It was great being one of the lads. We will always be the keepers of Aston's. My housemate and queen of the pole world Dr Robin de Meyere, thanks for all the glam and for encouraging me to start doing pole sports. It is the second best thing (the first thing is batteries) I got to do in Oxford. JJ Marie, Dr Alex P., Dr Hui G., Varnika A., Dr Sofia S.C., Max J., Dr William J. H., Francesco A., Jemma G., Dr Gareth H., Dr Zhanet Z., Dr Faidra F., Dr Yusuf O., Mehpare A., the OUPS family, and all the extraordinary folk that crossed my path here in Oxford, I am grateful to have met you all!

I completed my MSc (2014-2016) here, and now I am finishing my DPhil (2018-2022). I have spent most of my "adult" life in Oxford. I have been trying to figure out whether I should be one of those people who came to Oxford for a year and never left, and I have decided that it is time for me to leave the bell jar. With all its ups and downs, it has been a tremendous odyssey. This place will be my second home and witness of many exciting beginnings.

Coming towards the end of my acknowledgements, I would like to take this opportunity to (as I will not be able to do this elsewhere) dis-acknowledge all the researchers who mix ambition with rivalry and are biased about their data.
There are researches whom I look up to as well. I am thankful to have met and worked with Professor Mehmet Suat Somer and Dr Semih Afyon. They both encouraged me to stay in research and help me throughout my research career.

From midnight lab sessions to midnight cocktails to me, a city girl -according to Risto-, seeing rabbits and baby deer in the wild for the first time, lots of remarkable things happened here! Once I got on top of one of the biggest magnets in the UK and felt my earlobes wiggle… I had forgotten to remove my cheap earrings. This is my only confession here.

I am thankful to the University of Oxford and Research England for the GCRF QR Fund, the British Federation of Women Graduates/Funds for Women Graduates for the emergency grant, and St Edmund Hall for the College Hardship fund.

I would like to thank my family for all their love and support. Firstly, I would like to thank my grandfather, Kâzım, for believing in me and supporting my studies. I think I have not made a scientific breakthrough (yet) or maybe it is hidden somewhere in these pages. Nevertheless, I will always try my best for you. My lovely parents, Semra and Erkan, I am finishing school now. I will always need your support, but you can relax a bit from now on. Mefküre, Sumru, and my London mum –Cemre, thanks for being there whenever I needed a psychological hug. And Risto, I am grateful to have met you, thanks for all the silliness and love.

Ceren
October 2022

"She's a Killer Queen
Gunpowder, gelatine
Dynamite with a laser beam
Guaranteed to blow your mind
Anytime"
Freddie Mercury

Contents

Abstract

Lithium-oxygen batteries (LOBs) have attracted immense research interest as they have the highest theoretical energy density among the advanced battery systems. Achieving such high energy densities can substantially reduce the need for fossil fuels, enable greater use of renewable energy, and revolutionise the transportation sector. However, due to the complexity of oxygen reduction and evolution reaction chemistries and reactivity of reduced oxygen species, LOBs still need significant improvement in their fundamental understanding to overcome the electrolyte and cathode stability issues.

In the Thesis, firstly, the redox mediated charging process was studied to understand the mechanism to enable fast charging with low overpotentials and side reactions. It is demonstrated that the redox mediated oxidation follows Marcus theory of electron transfer and the rate limiting step is the first 1-electron oxidation, $Li_2O_2 \rightarrow LiO_2$. The kinetically dominant step is the LiO_2 disproportionation. It is also shown that the singlet oxygen ($^1O_2$) yield does not correlate with the amount of degradation. This casts doubt on whether $^1O_2$ is the main cause of degradation in LOBs.

Secondly, due to the discrepancy in $^1O_2$ and electrolyte degradation amounts, the stability of the common LOB salts and solvents towards $^1O_2$ were tested. It is shown that tetraglyme-LiTFSI, one of the most widely used electrolytes, is stable towards $^1O_2$ under chemical conditions. In the LOB literature, $^1O_2$ is mainly detected and quantified using DMA, a $^1O_2$ trap. Here, it is revealed that DMA can react with superoxide depending on the salt-solvent combination and $DMAO_2$, the reaction product of $^1O_2$ with DMA, can degrade into by-products depending on the solvent environment.

Finally, the stability of the electrolyte and the cathode towards $^1O_2$ under electrochemical conditions and the real cause of faradaic efficiency loss are investigated. It is demonstrated that $^1O_2$ is not the main source of degradation and fresh Li_2O_2 surfaces is the culprit. This finding should redirect the focus of LOB research from avoiding $^1O_2$ to developing electrolytes inert towards peroxide and peroxide-derived side products for an electro/chemically stable cell.

Abbreviations

$^1O_2$	Singlet oxygen
$^3O_2$	Triplet oxygen
CE	Counter electrode
CP-MAS	Cross-polarisation Magic-angle-spinning
CV	Cycling voltammetry
DMA	9, 10-Dimethylanthracene
DME	1,2-Dimethoxyethane
DMSO	Dimethyl sulfoxide
$DMSO_2$	Dimethyl sulfone
DMPZ	5,10-Dimethylphenazine
DN	Donor number
Fc	Ferrocene
HMBC	Heteronudear multiple bond correlation
HPLC	High-pressure liquid chromatography
HSQC	Heteronudear single quantum coherence
FTIR	Fourier transform infrared
LFP	Lithium iron phosphate
$LiClO_4$	Lithium perchlorate
LiTFSI	Lithium Bis(trifluoromethane)sulfonimide
MAZO	1-Methyl-2-azaadamantane-N-oxyl
MeO-TEMPO	4-Methoxy-2,2,6,6-tetramethyl-1-piperidinyloxy
MPT	N-Methylphenothiazine
MS	Mass spectrometry
NMR	Nuclear magnetic resonance
OCV	Open-circuit potential
OER	Oxygen evolution reaction
ORR	Oxygen reduction reaction
PPT	10-Isopropylphenothiazine
PTFE	Polytetrafluoroethylene
PXRD	Powder X-ray Diffraction
RB	Rose Bengal
REF	Reference electrode
RM	Redox mediator
RM^+	Oxidised redox mediator
SECM	Scanning electrochemical microscopy
SEM	Scanning electron microscopy
SS	Stainless steel
TBA	Tetrabutylammonium
TBATFSI	Tetrabutylammonium bis(trifluoromethane)sulfonimide
Tetraglyme	Tetraethylene glycol dimethyl ether
TEMPO	2,2,6,6-Tetramethyl-1-piperidinyloxy
TMPD	N,N,N′,N′-Tetramethyl-p-phenylenediamine
TOCSY	Total correlation spectroscopy
TPP	Tetraphenylporphyrin
TTF	Tetrathiafulvalene
UV-Vis	Ultraviolet-visible
WE	Working electrode

1 Chapter 1 – Introduction

The Li-O_2 battery (LOB) has the highest energy density among current conventional battery systems. However, Li-O_2 batteries are far from reaching practical targets. Electrode and electrolyte degradation and sluggish kinetics are some of the main reasons hindering the Coulombic efficiency and cyclability in LOBs. Hence, in this Thesis, the kinetics of the mediated charging process and the effect of singlet oxygen, a reactive O_2 species recently detected in LOBs, on degradation were studied.

Key findings in this work:

- Kinetics of the redox mediated charging process is elucidated. It is shown that the mediated charging follows Marcus theory of electron transfer.
- The yield of singlet oxygen with redox mediators shows that first 1-electron transfer is the rate limiting step.
- Singlet oxygen is not the major source of carbon electrode and electrolyte degradation and fresh Li_2O_2 surfaces are true cause of Faradaic efficiency loss.
- The singlet oxygen trap, DMA, is not as selective as it is suggested in the literature and it reacts with superoxide in some electrolytes. Reaction of DMA in LOB cells do not only yield $DMAO_2$, which is used to quantify the amount of singlet oxygen product. Hence, the detection and quantification of singlet oxygen in LOBs using DMA should be re considered.

It is essential to understand the fundamentals of the charging process and the degradation mechanism to work towards a practical LOB.

1.1 Energy Storage and Batteries

The energy demand of the world continuously increases as well as the emission of CO_2 and other greenhouses gases. It is essential to move away from using fossil fuels and develop efficient energy storage systems. Electrochemical energy sources and storage are one of the main alternatives to fossil fuels. Batteries have a vital role in electrification and utilisation of intermittent renewable energy sources, and their chemistry can be tailored to meet the specific applications. The energy density of a battery is the product of its voltage and capacity. Hence, operation voltage, capacity, and rate capability of a battery are some of the main parameters to address when developing a new battery for a specific application. Low cost, low volume, low toxicity, and safety are other important aspects which need to be considered for commercialisation of new battery

technologies. From the invention of the first battery, voltaic pile (copper and zinc discs in brine electrolyte) to the commercialisation of the first rechargeable Li-ion battery by Sony in 1991, many different battery chemistries such as rechargeable lead-acid, nickel-metal hydride and Whittingham's rechargeable TiS_2-Li metal batteries were developed.[1] Although other metal batteries such as Na, Mg, and Al are under consideration. Among them Li has the lowest reduction potential (-3.04 V vs. SHE) and the highest gravimetric capacity. Hence, Li-based battery chemistry have been extensively studied.[2]

Li-ion batteries (LIBs) are the most widely used battery technologies in portable electronics and electric vehicles. Currently, the maximum specific energy is ~250 Wh kg^{-1} and further research could push the specific energy to maximum ~300 Wh kg^{-1}.[3] However, this specific energy is not enough to meet the targeted 500-600 km range for electric vehicles.[4] A battery with 500 Wh kg^{-1} specific energy can be developed by focusing on beyond Li-ion technologies, where among them the Li-O_2 battery (LOB) has the highest theoretical specific energy (3500 Wh kg^{-1} based on mass of the discharge product Li_2O_2) and energy density (3500 Wh L^{-1}) (**Figure 1-1**). Li-air batteries, once realised, would work with air instead O_2 by utilising Li metal anode protection strategies and electrolyte additives. A practical Li-O_2 battery would either require installing an O_2 tank, incorporating O_2 in the solid state, or adding a gas separator to eliminate N_2 and moisture. Hence,

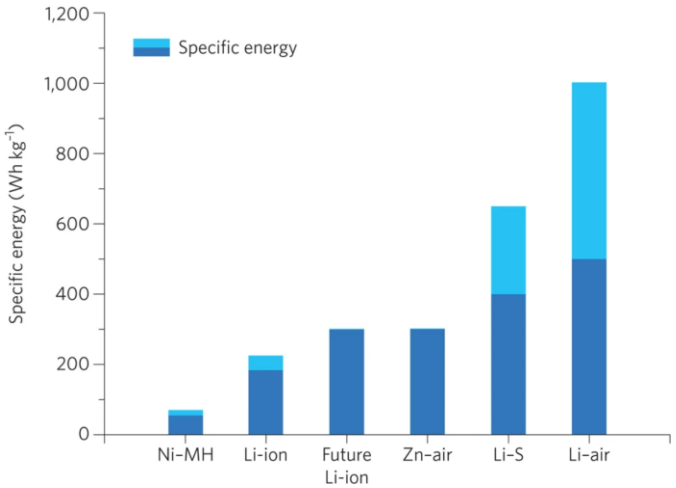

Figure 1-1 *Theoretical specific energies of different battery systems (light blue) and their practical energies which are reduced due to mass of cell packing, current collectors etc. (dark blue). Reproduced with permission from ref 4. Copyright 2016 Springer Nature.*

LOBs practical capacity would fall below Li-air but could exceed Li-S batteries.[3,4] The specific capacity of a LIB is calculated by taking into account the cathode material chemistry. The practical capacity of the battery decreases due to the mass of the other components such as separator, cell casing etc., **Figure 1-1**. Volume changes in the electrodes, such as volume change going from a Si anode to lithiated Si anode upon charging, are also usually overlooked in the capacity calculations.[3] In a practical system, LOB technology can reach a specific energy of 400-550 Wh kg^{-1}, which is much closer to the practical energy of gasoline (1700 Wh kg^{-1}) than that of a LIB.[5] Hence, LOBs gained a growing interest in the early 2010s. However, complex reactions involving reduced oxygen species and parasitic chemistry are some of the main challenges in achieving the theoretical specific energy of a LOB.

1.2 Li-ion vs Li-O_2

Most of the commercial Li-ion batteries consist of a graphite anode, an intercalation cathode, and a Li^+ salt containing liquid organic electrolyte. These batteries work by shuttling Li-ions between anode and cathode. On charge, an external current is applied and Li-ions intercalate into the anode (to form LiC_6), and on discharge Li-ions are inserted back into the cathode structure and corresponding number of electrons flow through an external circuit (**Figure 1-2a**).[2]

The Li-O_2 battery chemistry is very different from the Li-ion battery chemistry even though the working principles include redox reactions and diffusions of ions in the electrolyte. Li-O_2 batteries work with a Li anode and a porous air cathode under O_2 atmosphere. Depending on the type of the Li-O_2 battery, it either consists of an aprotic electrolyte[6], aqueous electrolyte[7,8], solid-state electrolyte,[9] or it can be hybrid[10] consisting of an aprotic, aqueous, and solid-state electrolyte in the same system.[11] In all cases, O_2 is reduced on discharge and the discharge product is oxidised on charge to form O_2 (**Figure 1-2b**). This means there is oxygen reduction reaction (ORR) and oxygen evolution reaction (OER) at the cathode while Li^+ dissolution and deposition is observed at the anode.

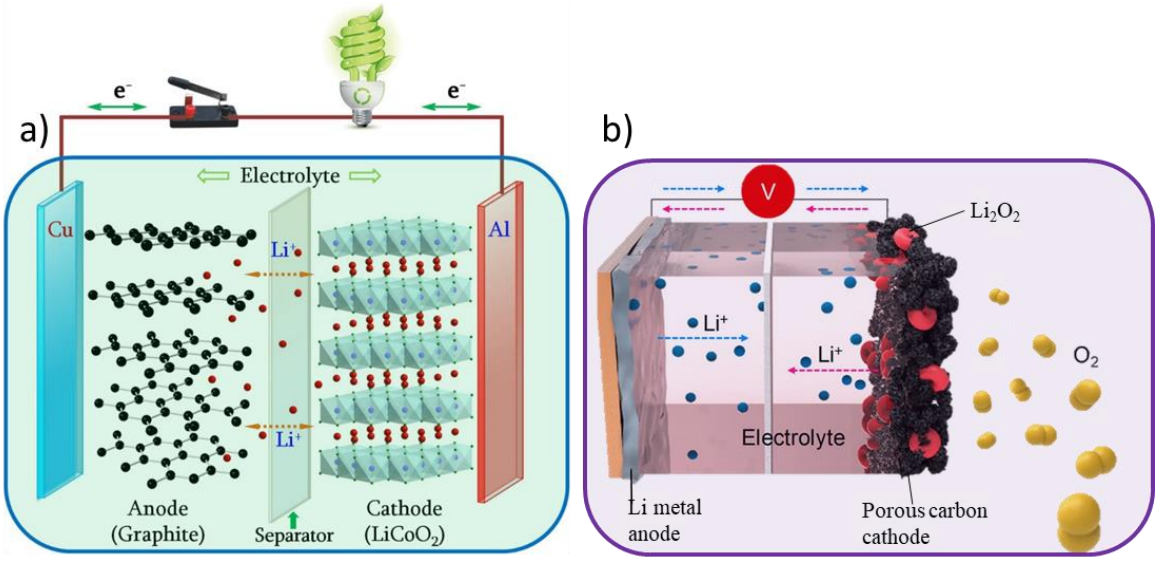

Figure 1-2 *Configuration of a a) Li-ion battery with $LiCoO_2$ as the intercalation cathode and a b) Li-O_2 battery. a) Reproduced with permission from ref 2. Copyright 2016 Elsevier. b) Reproduced with permission from ref. 3. Copyright 2016 Springer Nature.*

1.3 Aqueous Li-O_2 Batteries

Aqueous Li-O_2 batteries consist of a carbon cathode, a lithium superionic conducting film on a Li metal anode, and an aqueous electrolyte of various pH values.[7,12] Li-ion conducting membrane is used to protect the metal anode from reacting with water. In these systems the discharge product is soluble LiOH instead of solid Li_2O_2. Electrolyte solutions such as NH_4Cl/LiCl and NH_4NO_3/$LiNO_3$ can be used for primary cells. The pH of the electrolyte was shown to affect the oxygen reduction reaction and changes throughout the reaction. Polyprotic acids such as malonic acid or citric acid based electrolytes are used in secondary (rechargeable) aqueous LOBs.[8]

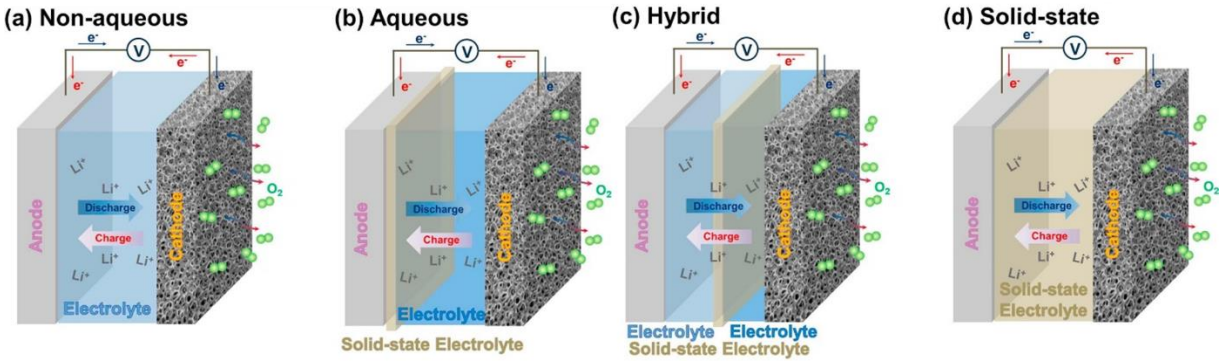

Figure 1-3 *Schematic representation of different configurations of Li-O_2 batteries. Reproduced with permission from ref 11. Copyright 2017 Elsevier.*

However, if the solution reaches saturation, LiOH starts precipitating as LiOH•H_2O.

Discharge[13]

$O_2 + 2\,H_2O + 4e^- \rightarrow 4\,OH^- \quad (4e^-\ reduction)$ eq.1

$O_2 + \ H_2O + 2e^- \rightarrow HO_2^- + OH^- \ (2e^-\ reduction)$ (whether it is a 4e$^-$ or 2e$^-$ process depends on the pH and the electrode material) eq.2

$HO_2^- + \ H_2O + 2e^- \rightarrow 3OH^-$ eq.3

$2HO_2^- \rightarrow 2OH^- + \ O_2\ (disproportionation)$ eq.4

Saturation[13]

$Li^+ + OH^- + \ H_2O \rightarrow LiOH \cdot H_2O_{(s)}$ eq.5

Charge[13]

$4OH^- \rightarrow \ O_2 + 2H_2O + 4e^-$ eq.6

$LiOH \cdot H_2O_{(s)} \rightarrow Li^+ + OH^- + \ H_2O$ eq.7

Preventing pore clogging and corrosion of Li metal anode are some of the main challenges in aqueous LOBs. H_2O was shown to improve capacity and lower the charge overpotentials when used as an additive in aprotic LOBs.[14]

1.4 Solid-State Li-O_2 Batteries

Currently, there is a big shift in research from conventional Li-ion batteries to solid-state Li batteries due to the theoretical high energy density and safety of the solid-state batteries. In the Li-O_2 batteries, although safety is an important factor, the use of a solid electrolyte mainly addresses the organic electrolyte instability issue. Solid electrolyte can protect the Li anode from reactive species. There are studies on full solid-state LOBs, quasi-solid state LOBs with liquid electrolyte and polymeric matrices, and polymeric[15] LOBs. The main challenges in solid-state LOBs are the low ionic conductivity of solid electrolytes, poor interfacial contact, reactivity of certain solid-electrolytes with the components, and accommodation of Li_2O_2 particles which most of the literature seems not to mention.

The first solid-state LOB was based on using glass-ceramic and polymer ceramic materials (LAGP between PEO membranes) as the solid electrolyte at operating temperatures between 30-105 °C.[16] Lithium ion conducting materials such as LiSICON[17], LATP[18], LLTO, LLZO and LAGP[19] were used in several studies. However, LLTO, and LATP are unstable towards Li metal[20], LLZO have lower conductivity than organic electrolytes, and all of them suffer from interfacial contact failure

problems.[21] One of the more recent studies that showed good battery parameters (500 mA g^{-1} current density and 1000 mAh g^{-1} capacity) was based on utilising lithium-ion exchanged zeolite membranes as the solid electrolyte.[22] Although zeolites are chemically inert, the cells were flexible and reached high capacities, and powered small devices. However, the authors do not quantify the Li_2O_2 yield and gas evolution and consumption which makes it hard to understand the actual electrochemistry resulting in high energy density and capacity. Additionally, even in 60 cycles, lithium acetate (a common degradation product in LOBs) formation can be seen. Polymer based LOBs reduce side reactions, but do not fully alleviate them and most of the designs still suffer from contact issues. They are usually used at elevated temperatures which allow higher capacities without electrolyte degradation.[23] However, the effect of contaminants and any CO_2 released would be more detrimental under these conditions. One of the important achievements is making these cells flexible which seems to reduce contact problems. These cells have different designs such as interwoven anodes and cathodes[24], flexible cables[25], and sheets.[23,26] Ambient air can be used in most of the cases: however, cycle life is not as long showing that there are still side reactions.[23]

1.5 Aprotic Li-O_2 Batteries

The first rechargeable aprotic LOB was developed by Abraham and Jiang in 1996 where they used a gel polymer electrolyte and reached 1400 mAh g^{-1}_{carbon} capacity.[6] They discovered this system by chance when they were studying intercalation in graphite. They showed that the discharge product was Li_2O_2 by Raman spectroscopy. However, the overpotential was very high and the cell exhibited very poor cyclability. Until 2006, there were a few studies investigating the effect of the electrolyte composition on rechargeability.[27,28] In 2006 Bruce and co-workers showed that Li_2O_2 can be oxidised by using in-situ differential electrochemical mass spectrometry to detect O_2 evolution upon charge.[29] This was a big step in showing that the aprotic LOB is rechargeable.

The components of an aprotic LOB are similar to aqueous LOBs except the electrolyte is a polar organic solvent. Ideally, on charge O_2 is reduced to form Li_2O_2 (E = 2.96 V vs. Li^+/Li) and on

charge Li_2O_2 is oxidised to Li^+ and O_2. The theoretical specific energy is 3505 Wh kg^{-1} based on the mass of Li_2O_2.[30] Recently there are some studies showing different discharge products such as Li_2O, LiOH, or stabilising LiO_2 intermediate.[31-33] However, the research mainly focuses on Li_2O_2 as the discharge product.

1.5.1 Oxygen Reduction Reaction – Discharge in Aprotic Li-O_2 Batteries

In an aprotic Li-O_2 battery, O_2 is reduced on discharge and reacts with Li^+ to form the solid discharge product Li_2O_2. The O_2 reduction reaction (ORR) has been studied in aqueous and aprotic solvents for various applications.[34,35] The reactions in the aprotic media were shown to be either reversible or irreversible depending on the media.[3] Although early studies of O_2 reduction in LOBs showed that the discharge product is Li_2O_2, the mechanism was not clear until the reaction intermediate LiO_2 was detected, the effect of donor number of the solvent and salt, and the Lewis acidity of the Li^+ was studied.[36-38]

In 1991 Aurbach et al.[39] suggested the reaction mechanism for O_2 reduction in Li^+ salt containing aprotic electrolyte as follows (note that they were not studying reversible Li-O_2 batteries at the time)

$$1)\ 2O_2^{\bullet-} \underset{e^-}{\rightleftharpoons} O_2 \underset{e^-}{+} O_2^{2-} \xrightarrow{2\,Li^+} Li_2O_2 \qquad \text{eq.8}$$

$$2)\ O_2 \xrightarrow{e^-} O_2^{\bullet-} \longrightarrow O_2^{2-} \qquad \text{eq.9}$$

$$2a)\ O_2^{\bullet-} \rightleftharpoons LiO_2 \quad \text{or} \quad 2b)\ O_2^{2-} \leftrightarrow Li_2O_2 \qquad \text{eq.10}$$

In 2009 Laoire et al.[40] found that O_2/O_2^- redox couple was reversible in bulky TBA^+ containing electrolytes whereas small Li^+ containing electrolytes did not show reversible cydic voltammetry (CV) peaks. For the discharge they suggested the following reaction pathway

$$O_2 + Li^+ + e^- \rightarrow LiO_2 \qquad \text{eq.11}$$

$$LiO_2 + Li^+ + e^- \rightarrow Li_2O_2 \qquad \text{eq.12}$$

In Li^+ containing systems Li_2O_2 is more thermodynamically stable than LiO_2 and therefore LiO_2 further reacts to form Li_2O_2. Bruce and co-workers confirmed the intermediate LiO_2 on discharge by detecting it with surface enhanced Raman spectroscopy (SERS) in 2011.[36] Solid-state LiO_2 can only be obtained at very low temperatures ~25 K.[41] Later on, it was detected on discharge

with XRD,[42] operando X-ray photoelectron spectroscopy (XPS),[43] X-ray absorption near edge structure spectroscopy (XANES),[44] Raman spectroscopy,[45,46] and magnetic measurements.[47]

It is now known that O_2 is reduced to form superoxide which then either disproportionates or undergoes a second electron transfer to form Li_2O_2. The stability of LiO_2 was studied in different solvents considering Pearson's Hard acid soft base (HSAB)[a] theory[48] and Gutmann donor number.[49] Laoire et al.[38] suggested that $TBAO_2$ is more stable than LiO_2 and Li_2O_2 is more stable than LiO_2 by using HSAB. O_2^- is a soft base, while O_2^{2-} generated by disproportionation is a harder base and Li^+ is a hard acid. Thus, Li_2O_2 is more stable than LiO_2. They also comment on the solvent basicity referring to Gutmann donor number where high donor number indicates stronger basicity. Li^+ is assumed to be solvated by four solvent molecules forming a coordination sphere around it. If Li^+ is solvated by high donor number solvents such as DMSO, its acidity decreases which makes LiO_2 more stable than in a low donor number solvent such as acetonitrile (CAN) where Li^+ is a harder acid. This was confirmed and observed by a single or two reduction peaks by Johnson et al. (**Figure 1-4**).[37]

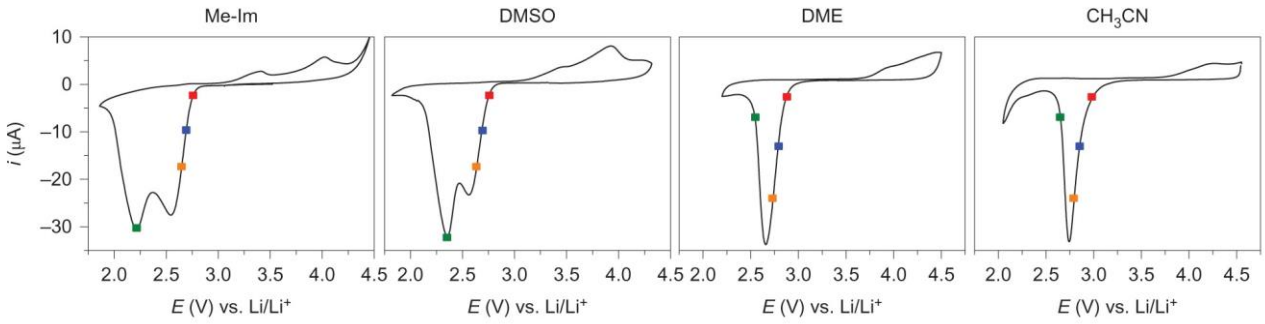

Figure 1-4 *Cyclic voltammograms for O_2 reduction with Li^+ salt in different donor number solvents Me-Im (DN = 47), DMSO (DN = 30) DME (DN = 20), and ACN (DN = 14). Two distinct peaks can be seen for high donor number solvents Me-Im and DMSO showing LiO_2 and Li_2O_2 formation whereas for low donor number solvents LiO_2 is very short lived and only Li_2O_2 peak is observed in the CV. Reproduced with permission from ref 37. Copyright 2014, Nature Publishing Group.*

In the same study, Johnson et al. reported a unified mechanism for solution-mediated and surface-mediated discharge mechanisms. In high donor number solvents such as DMSO, Li^+ is

[a] Hard acids and bases are smaller than soft acids and bases. They are weakly polarisable. Decreasing Li^+ acidity means its size without changing its charge, which decreases its charge density; hence makes it softer.

solvated and thus O_2^- is in solution. Since O_2^{2-} is more stable, Li_2O_2 forms via disproportionation. Large toroidal Li_2O_2 particles are formed from solution. In low donor number solvents such as ACN Li^+ is not solvated and LiO_2 is forms on the electrode surface. This LiO_2 either undergoes disproportionation or second electron transfer to form a passivating Li_2O_2 film on the electrode surface. This causes premature cell death. From a thermodynamic point of view, in high donor number solvents the reaction $LiO_2^* \rightarrow O_2^{\bullet-} + Li^+$ has a negative free energy ($\Delta G° = -20$ kJ mol^{-1} for DMSO) whereas for low donor number solvents it is positive ($\Delta G° = 36$ kJ mol^{-1}) (**Figure 1-5**).

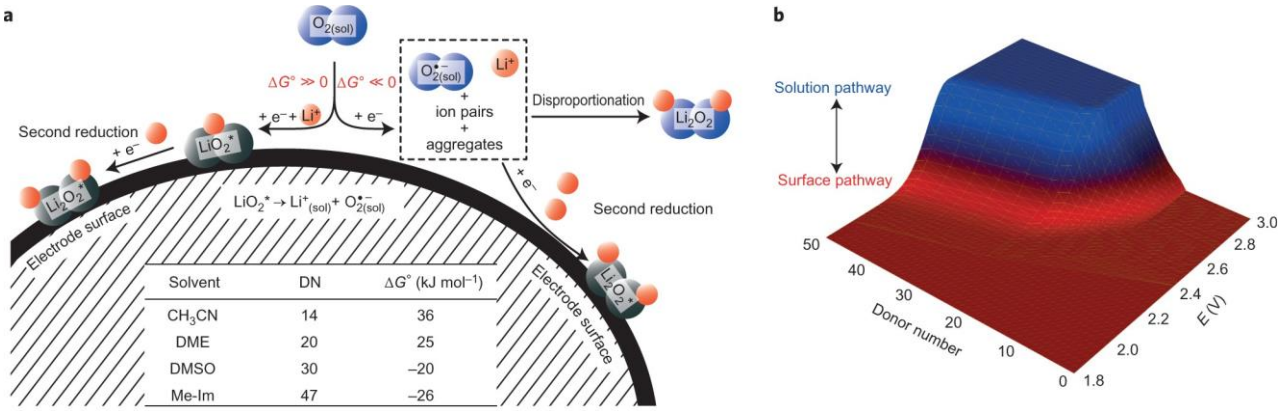

Figure 1-5 *Scheme explaining effect of solvent donor number on solution and surface mediated oxygen reduction mechanism. Reprinted with permission from ref 37. Copyright 2014, Nature Publishing Group.*

The level of dissociation of the salt and the anion of the Li salt plays a similar role on the ORR. Sharon et al.[50] studied the effect of the different anions and the dissociation level of the Li salt on discharge kinetics and morphology of the discharge product (**Figure 1-6**). They obtained a comparable ORR trend in low donor number solvents to high donor number solvents by optimising the salt. For example NO_3^- has a higher ionic association strength than $TFSI^-$ (i.e. $TFSI^-$ is strongly dissociated) and coordinates strongly with Li^+ than $TFSI^-$ does. This results in more stable O_2^- and solution-mediated growth of Li_2O_2 toroids.

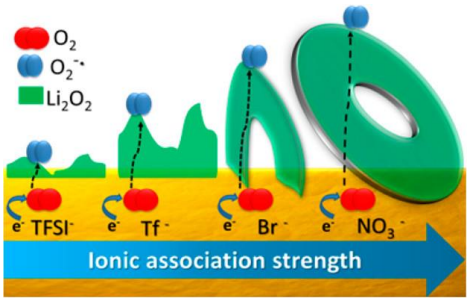

Figure 1-6 *Schematic representation of Li_2O_2 film and toroidal growth depending on the ionic association strength of the salt. Reprinted with permission from ref 50. Copyright 2016, American Chemical Society*

The effect of high acceptor number additives, aprotic additives such as H_2O, was also investigated to promote solution-mediated growth of Li_2O_2. First Gasteiger and co-workers investigated the effect of H_2O in aprotic solvents and achieved 14 times higher discharge capacity.[51] Aetukuri et al.[52] showed that the discharge capacity and the size of the Li_2O_2 particles increase as the amount of H_2O increases. However, it should be noted that if the water content is too high, LiOH will start forming. LiOH is not soluble in aprotic LOBs and is regarded as a side product. In the same study Aetukuri et al. showed that even though the discharge capacity increases, the amount of Li_2O_2 decreases when the H_2O content is more than 4000 ppm.

Other than the electrolyte composition, the cell cycling parameters such as temperature,[53] potential and current density[54,55] also affect the discharge process and the growth of Li_2O_2. Liu et al.[53] showed that at low temperatures (-20 - -10 °C) Li_2O_2 grows as ultrasmall spheres, while at temperatures between 0 - 10 °C few layers are observed and as the temperature increases (up to 40 °C) these layers stack together and form toroids (faster mass transport). Nazar and co-workers studied the effect of current densities on Li_2O_2 morphology and observed that small current densities promote growth of large toroidal particles and high current densities results in film growth of Li_2O_2.[55] They suggest that at low current densities solvation of LiO_2 is faster than direct reduction or disproportionation and Li_2O_2 is formed from solution, and high density of electron transfer at high current densities promotes second-electron reduction and film growth. Mitchell et al.[54] also studied the effect of current density on Li_2O_2 growth and reported toroid formation at low current densities. They observed few nucleation point and larger particles at low current densities

and more nucleation sites but small irregular particles at high current densities. They suggest that the overpotential is higher at high current densities and this results in more nucleation sites whereas at low current densities the potential is close to the thermodynamic Li_2O_2 formation potential and the driving force for nucleation is small. Shao-Horn and co-workers had a similar conclusion about the effect of overpotential on Li_2O_2 morphology.[56] They studied the amount of soluble LiO_2 and solid products by rotating disk electrode and electrochemical quartz microbalance, respectively.

1.5.2 Oxygen Evolution Reaction – Charge in Aprotic Li-O_2 Batteries

A unified mechanism for the charge process was not developed until recently. The main reasons are the sloping voltage profile, high overpotentials, side reactions and side products at higher voltages, difficulty in detection of LiO_2 intermediate, different charging profiles for toroids and films, whether the reaction happens at the electrode Li_2O_2 interface, different kinetics with different solvents, the need of use of redox mediators, and the insulating and reactive nature of Li_2O_2. For example, Li_2O_2 oxidation to O_2 is overall a 2 e^- process; however, whether it is two 1 e^- steps or a direct 2 e^- process was under debate until recently.[4,57-59] The thermodynamic potential for Li_2O_2 redox is 2.96 V. However, the oxidation starts above 3.1 V and the overpotential in

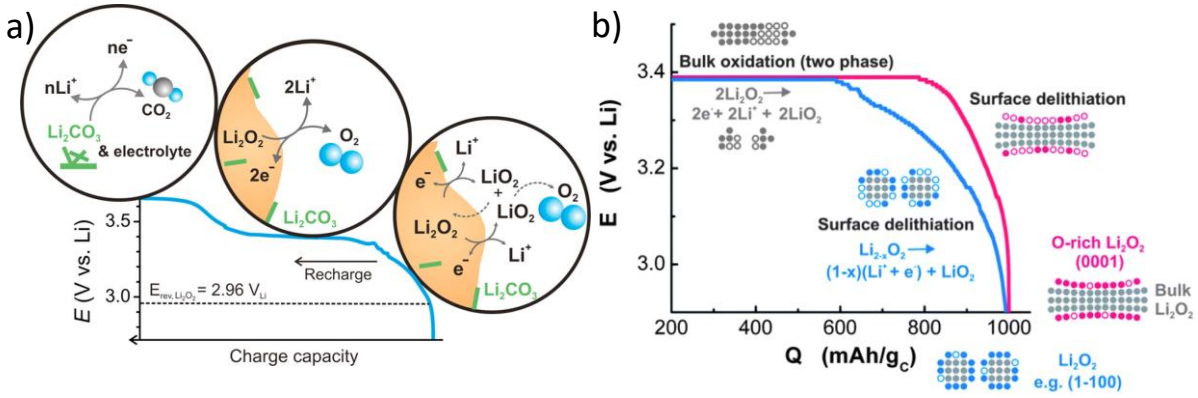

Figure 1-7 *a) Proposed Li_2O_2 oxidation mechanism that consists of three stages where the first stage is delithiation into LiO_2-like species. Reproduced with permission from ref 58. Copyright 2013, American Chemical Society b) Charging process for small particles and toroids both showing a sloping surface delithiation followed by a two-phase bulk Li_2O_2 oxidation. Particle surfaces are not as O-rich as toroid surfaces and could be lower potential than (0001) O-rich toroid surfaces. After the surfaces are oxidised, they speculate that two-phase oxidation involves both Li_2O_2 and O-rich LiO_2-like species. Reproduced with permission from ref 44. Copyright 2013, Royal Society of Chemistry.*

unmediated cells goes up to > 0.7 V. Moreover, the charge curve usually consists of multiple plateaus and does not follow the discharge curve as reverse disproportionation cannot occur.[3]

In 2011, when Bruce and co-workers detected LiO_2 intermediate on discharge by SERS, they also studied charging and could not detect LiO_2 as an intermediate by the same method.[36] They detected the oxidation peak for Li_2O_2 at 3.75 V, well above the oxidation potential of LiO_2 and SERS spectra did not show any presence of LiO_2. They also used CO_2 to track LiO_2 formation that it was previously shown that O_2^- reacts with propylene carbonate (PC) and produces CO_2.[60] They did not detect any other gases more than 1% of the evolved O_2. Hence, they concluded the oxidation is a one-step process. Around the same time, several studies attributed the sloping, stepwise charging profile to heterogeneity in electrodes, changes on the Li_2O_2 surface, and oxidation being more facile in some regions.[61-63]

Shao-Horn and co-workers showed that the charging profile has three sections in which Li deintercalation, disproportionation, and decomposition happens (**Figure 1-7A**).[58] The important point they make is that at low overpotentials (3 - 3.4 V) first lithium deintercalation occurs to form $Li_{2-x}O_2$ (25% of the whole charging). This lithium deficient phase then disproportionates to evolve O_2 and Li_2O_2. The high overpotential region is where the bulk Li_2O_2 gets oxidised. On a subsequent work Shao-Horn and co-workers showed that different Li_2O_2 morphologies display different charging profiles and commented on the formation of O-rich surfaces again.[44] They form small particles on discharge by high rate and discs/toroids by low rate discharging. Upon charge the particles yield a mainly sloping voltage profile whereas discs/toroids show a two-stage (sloping and plateau) profile (**Figure 1-7B**). They show that the sloping region is due to solid-solution like delithiation and plateau is a two-phase oxidation. Li_2O_2 particle surfaces have more bulk Li_2O_2 features and Li_2O_2 toroid surfaces have LiO_2-like electronic features. They suggest that once the surface is oxidised and bulk Li_2O_2 is exposed, two-phase oxidation occurs for both particles and discs/toroids. This two-phase mechanism involves bulk oxidation (both stoichiometric Li_2O_2 and O-rich LiO_2-like) and disproportionation of O-rich species.

Wagemaker and co-workers studied charging of electrochemically generated Li_2O_2 (E-Li_2O_2, amorphous and crystalline) and commercial bulk Li_2O_2 (C-Li_2O_2, crystalline) by operando XRD, and showed that amorphous and crystalline Li_2O_2 have different oxidation processes.[64] They show that amorphous Li_2O_2 and side products such as formate are oxidised at low overpotentials (small change in the Li_2O_2 intensity and lattice parameters) and crystalline toroidal aggregates start oxidising at higher overpotentials (Li_2O_2 intensity decreases). Thus, E-Li_2O_2 shows a two-stage oxidation process and C-Li_2O_2 displays a one-stage process where Li-deficient phase is formed and then crystalline Li_2O_2 is gradually oxidised. This is in-line with computational studies where it is shown that off-stoichiometric delithiation forms $Li_{2-x}O_x$.[65] Similar to easier charging of amorphous Li_2O_2, computational studies also showed that some facets of Li_2O_2 are easier to oxidise and require lower overpotentials.[65,66] Wilkening and co-workers showed that increased Li mobility and increased superoxide concentration lowers the charge overpotential.[67] The increased overpotential is not only due to different Li_2O_2 surfaces but due to formation of side products such as carbonates and carboxylates.

Donor number of the solvent was shown to affect the OER process as well. Lu et al.[68] showed that on charge first Li deficient $Li_{2-x}O_2$ forms and then depending on the DN of the solvent, it either disproportionates or undergoes a second electron transfer (**Figure 1-8**). In high DN solvents, $Li_{2-x}O_2$ dissolves into LiO_2 and disproportionates to form O_2, and in low DN solvents, $Li_{2-x}O_2$

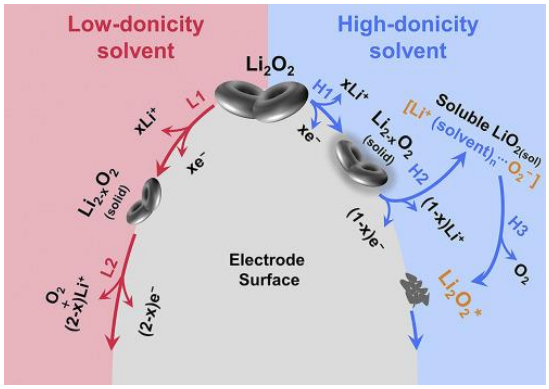

Figure 1-8 *Schematic representation of the effect of the donor number of the solvent on the charge process. Reprinted with permission from ref 68. Copyright 2018, Elsevier.*

undergoes a second oxidation, $Li_{2-x}O_2 \rightarrow O_2 + (2-x)Li^+ + (2-x)e^-$. It is low probability for solid superoxide intermediates to disproportionate, but it cannot be excluded.

Li_2O_2 can cause pore clogging and block the O_2 transport or films can passivate the cathode surface, if Li_2O_2 is not fully oxidised and side products are generated. Hence, it is important to understand whether the reaction occurs at the electrode-Li_2O_2 interface or on Li_2O_2-electrolyte interface. Zhong et al.[69] showed that unmediated Li_2O_2 oxidation starts at the carbon-Li_2O_2 interface by in-situ TEM and suggested that electron transport in Li_2O_2 is slower than ion transport (**Figure 1-9**). Peng et al.[70] studied OER and ORR on graphene surface with a DMSO-based electrolyte and tracked DMSO signal by surface-selective vibrational spectroscopy. The method is highly surface sensitive and can be used to monitor absorbed DMSO on the electrode surface. On oxygen reduction, DMSO signal decreases as the surface is covered with Li_2O_2, and on oxygen evolution before Li_2O_2 is oxidised the DMSO signal starts increasing. This increase is interpreted as the reaction happening at the carbon-Li_2O_2 interface, Li_2O_2 dislodging and DMSO adsorbing on the surface again. While soluble catalysts enable formation and decomposition of Li_2O_2 in/from solution, it is still important to understand the reaction interface for unmediated and heterogeneous catalysts-containing LOB systems. Contrary to the above mentioned studies, Lu et al.[71] showed that the reaction happens at the electrolye-Li_2O_2 interface by forming layers of $Li_2{}^{16}O_2$ and $Li_2{}^{18}O_2$ and monitoring the $^{18}O_2$ and $^{16}O_2$ signals on charge with and without catalysts. They observed the electrolyte interface Li_2O_2 generates oxygen first in both cases. They did not observe any $^{16}O^{18}O$ signal. The exact mechanisms for heterogeneous catalysts are not very clear. However,

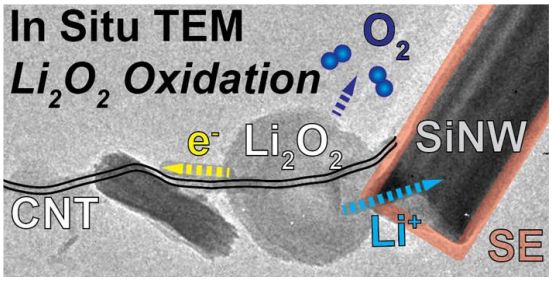

Figure 1-9 *TEM image of schematic of oxidation of Li_2O_2 particles formed by predischarging on carbon nanotubes with a delithiated $LiAlSiO_x$ solid electrolyte coated silicon nanowire anode. Reprinted with permission from ref 69. Copyright 2013, American Chemical Society*

it is more likely that unmediated oxidation starts at the electrode-Li_2O_2 interface. Moreover, unlike Lu et al., Bruce and co-workers detected O-O bond cleavage and $^{16}O^{18}O$ signal during disproportionation.[72]

1.6 Cell Components

1.6.1 Electrolyte

Electrolyte instability is one of the main problems in LOBs. A plethora of groups of solvents were tested for their stability in LOBs. However, most of the common LIB battery solvents and polar aprotic solvents that can dissolve Li salts were shown to react with reduced oxygen species, Li_2O_2 and its intermediates and a bit ambiguously with $^1O_2$. An ideal electrolyte (solvent + Li salt) should have good ionic conductivity (and negligible electronic conductivity) and thermal stability, wide electrochemical stability window, optimum viscosity (not too volatile or not too viscous to hinder the kinetics of chemical rate of reaction or mass transport) and stability towards reactive and reduced oxygen species.[73]

1.6.1.1 Solvent

The first class of solvents used in LOBs were organic carbonates since they are widely used in LIBs and have reasonably wide electrochemical window, and compatibility with Li metal anode. PC owing to its high dielectric constant, stability and low volatility was one of the first organic carbonate solvent used in LOBs. Initial reports attributed the achieved capacities to Li_2O_2 formation and decomposition.[74-76] However, the cyclability was very poor and overpotential was as high as 1.4 V. Subsequently several research groups reported carbonates and alkyl carbonates as parasitic reaction products.[62,77-79] Freunberger et al.[60] showed that these products accumulated upon cycling and the cell was not reversible. They suggested that superoxide was the cause of the decomposition and proposed the reaction scheme in **Figure 1-10**. McCloskey et al.[62] showed that CO_2 was the main gas evolved instead of O_2 in carbonate based electrolytes (**Figure 1-10**). They mixed PC with an

ether, dimethoxyethane (DME), and showed that even in the mixture PC was degrading while the system with only DME evolved considerable amount of O_2.

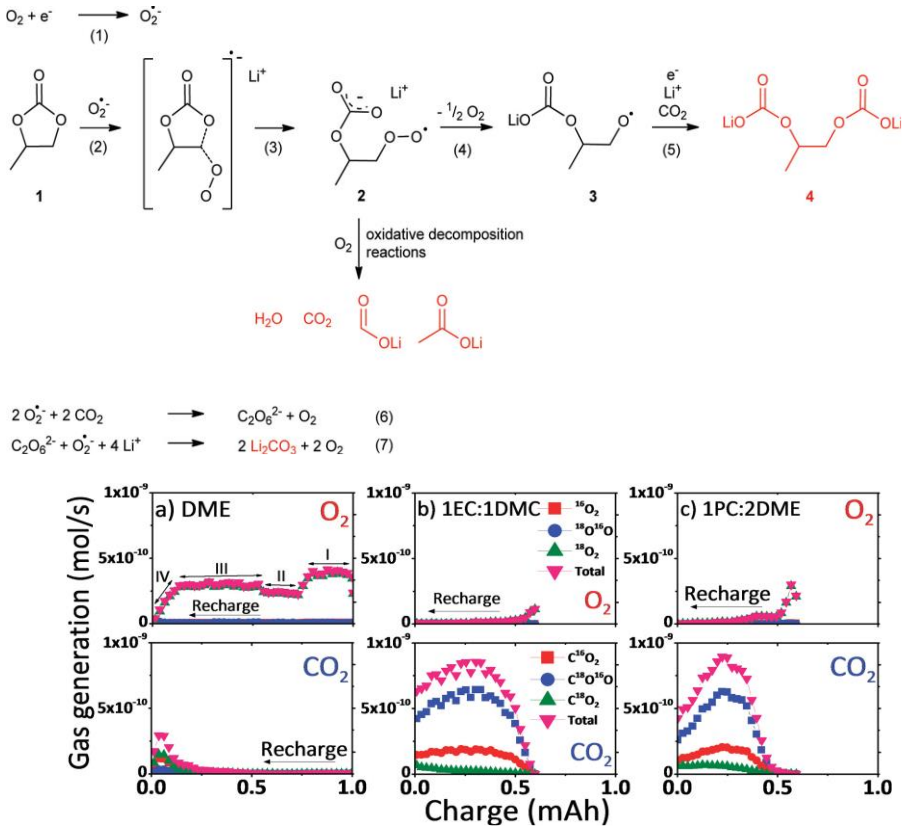

Figure 1-10 *Top: Reaction scheme proposed by Freunberger et al. for the discharge in carbonate-based electrolytes showing the decomposition due to superoxide. Reproduced with permission from ref 60. Copyright 2011, American Chemical Society. Bottom: Gas evolution data by McCloskey et al. showing O2 evolution on charge with a DME-based electrolyte and showing mainly CO_2 evolution with carbonate-based electrolytes indicating electrolyte decomposition. Reproduced with permission from ref 62. Copyright 2011, American Chemical Society.*

Dimethyl sulfoxide (DMSO) was investigated due to its high donor number.[80-82] It promotes solution-mediated growth of Li_2O_2. Its reactivity in LOBs is less than that of carbonate-based electrolytes; however, it is not a stable enough candidate for LOBs. Peng et al.[80] showed good capacity retention with DMSO-based electrolytes. Later, it was realised that this was due to the low pore volume of the Au cathode. Studies on the porous carbon electrodes showed significant amount of degradation in the DMSO system.[83] Direct reactivity of KO_2 with DMSO generates $DMSO_2$[84] and reaction between Li_2O_2 and DMSO generates LiOH.[85] However, recently, a K-O_2 battery showed very good cyclability with a DMSO-based electrolyte.[86]

Nitriles were another group of solvents used in LOBs.[38,40,87] They were previously used in O_2 reduction studies.[88,89] Nitriles were shown to be stable (high activation barriers) towards nucleophilic reactions with O_2^-.[90] McCloskey and co-workers showed 88% capacity retention with acetonitrile. However, acetonitrile is too volatile to be used in a practical battery and has low DN which would promote film-like Li_2O_2 growth. Additionally, it reacts with Li metal anode.[91] Several other aliphatic nitriles were studied by Bryantsev et al.[92] to show that they undergo base-mediated self-condensation or hydrolysis if there is trace amount of water.

Amide based solutions such as linear N,N-dimethylacetamide (DMA)[93] and N,N-dimethylformamide,[61] and cyclic N-methyl-2-pyrrolidone (NMP)[94] were also investigated as LOB electrolyte solvents due to their stability against O_2^-.[95] As C in O=C-N is less positive than O=C-O, it is more stable towards nucleophilic attack compared to esters and DMSO.[90] On the other hand, they are unstable with the Li metal anode. Uddin et al.[96] and Walker et al.[93] protected Li metal anode with $LiNO_3$, and Walker et al.[93] showed good cyclability with DMA. However, further studies by Chen et al.[61] and Sharon et al.[97] concluded that they undergo oxidative cleavage.

Ether-based electrolytes are usually considered as the most stable group of electrolytes for LOBs. They are stable up to relatively high voltages (~4 V), compatible with Li metal anodes, and have a low cost. Some ethers have lower viscosity than that of carbonates but with similar oxygen solubilities which improves the capacity of the cell.[28] Two ethers, 1,3-dioxolane (DOL) and dimethoxyethane (DME) were used as electrolyte solvents in LOBs by Read et al.[27] They achieved better rate capability and stability compared to carbonate-based electrolytes due to their low viscosity. The discharge performance and the discharge product were then investigated by Luntz et al.[62] and Xiao et al.[77] in a detailed way. They both showed that the main discharge product is Li_2O_2. Sharon et al.[98] and Freunberger et al.[99] both showed that DME is not completely stable and undergoes oxidative degradation. Sharon et al.[100] screened a variety of ethers. As DME is highly volatile, research focused on higher molecular weight glycol ethers.[100] It was shown that diethylene glycol dimethyl ether has the best cycling performance. Ethers perform better than other solvents

due to their greater cathodic stability and better resistance nucleophilic attack. However, it is important to note that they are not completely stable in LOBs. There is no unified decomposition mechanism. Freunberger et al.[99] suggested that superoxide radicals attack $–CH_2$ groups near O atoms and cause hydrogen abstraction in glycol ethers (**Figure 1-11A**). However, Sharon et al.[98] proposed that superoxide is a poor base and Li_2O_2 should be causing the nucleophilic attack. They suggested that solid Li_2O_2 is not reactive in ethers but before solid precipitation they are highly active and attack α-H or β-H near O atoms (**Figure 1-11B**).

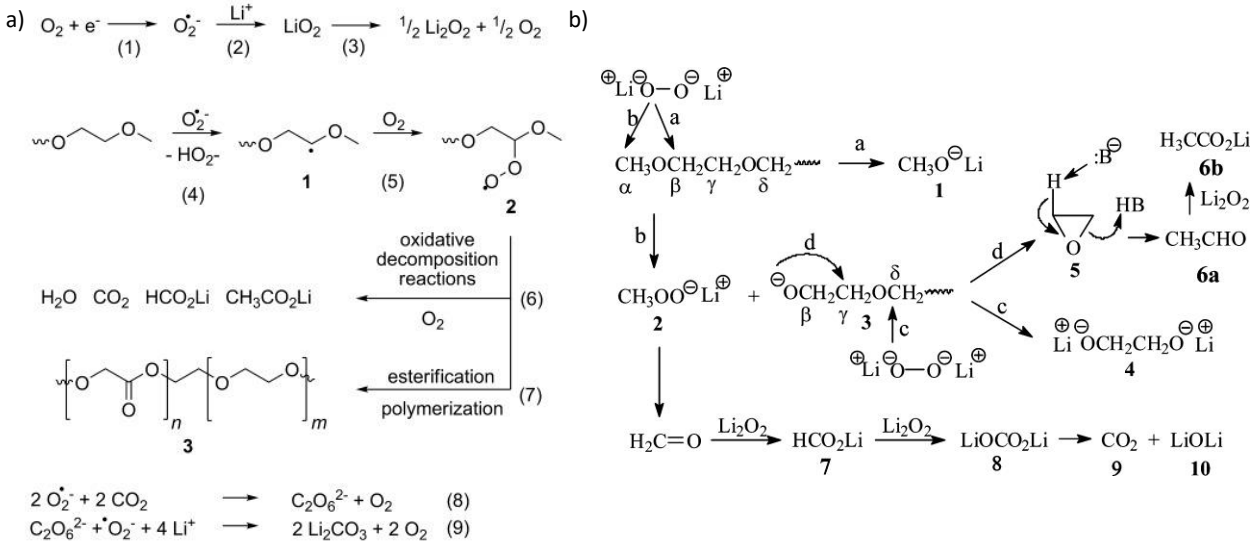

Figure 1-11 *a) Degradation mechanism on discharge proposed by Freunberger et al. Reproduced with permission from ref 99. Copyright 2011 Wiley-VCH. b) Proposed decomposition mechanism by Sharon et al. showing Li_2O_2 is reactive before solid precipitation and cause nucleophilic attack. Reproduced with permission from ref 98. Copyright 2013, American Chemical Society.*

McCloskey et al.[101] showed that the degradation mechanism with ethers is likely to be even more complex. They measured the e^-/O_2 ratio on discharge and quantified Li_2O_2 yield by iodometric titration. Although the e^-/O_2 ratio was close to 2, the Li_2O_2 yield was lower than expected and the discharge rate affected the yield. This indirectly shows that Li_2O_2 also reacts with cell components. Both Nazar and co-workers and Aurbach and co-workers suggested replacing the H atoms near O atoms by bulky groups or stable atoms.[98,102] Nazar and co-workers synthesised a novel solvent where they replaced reactive protons with methyl groups to make the molecule more resistance to O_2^- attack. This solvent exhibited better cycling performance and less decomposition.

Room temperature ionic liquids are either used as electrolyte solutions or mixed with aprotic organic solvents to make up a mixed electrolyte solvent to improve stability and conductivity.[103-105] The stability of the ionic liquids can be tailored by selecting the correct anions and cations. For example imidazolum cations were demonstrated to be prone to O_2^- attack[106] and while N-methyl-N-propyl-pyrrolidinium and N-methyl-N-butyl-pyrrolidinium were shown to be the most stable in a comparative study by Das et al.[107] One of the main problems with only using ionic liquids is their high viscosity. A recent kinetics study using scanning electron microscopy by Krueger et al.[108] showed that the apparent rate constant for the redox mediated charging was an order of magnitude smaller in ionic liquid electrolyte than tetraglyme and DME. Another issue is the impurities in ionic liquids which are difficult to purify and the impurities can contribute to parasitic reactions.[107]

Research should target novel electrolytes that are stable towards reduced oxygen species and enable fast kinetics. The main degradation reactions are H atom abstraction, acid/base reactions, nucleophilic attack (e.g. by O_2^-) and reductive degradation at the Li metal (**Figure 1-12**).[73] Some of the strategies are to replace α-hydrogen atoms with F atoms, using high concentration salts with fluorinated diluents, and to avoid double bond structures. Fluorinated additives were also shown to increase oxygen solubility.[109-111]

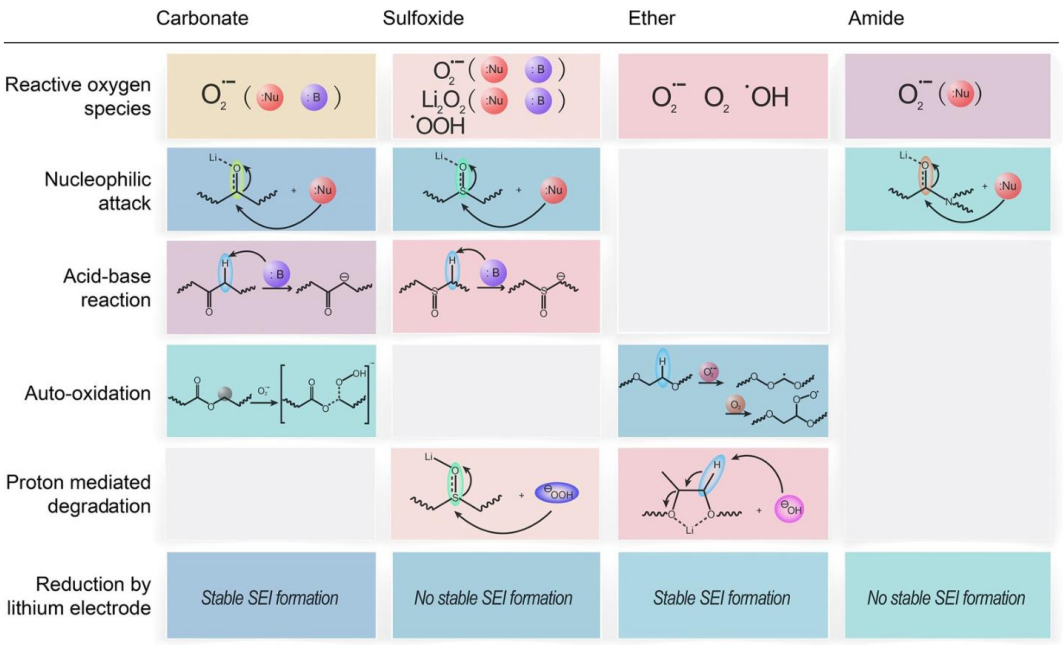

Figure 1-12 *Proposed decomposition pathways for different groups of electrolyte solvents. Reprinted with permission from ref 73. Copyright 2019 Wiley-VCH*

1.6.1.2 Salt

Li salt is a crucial part of the electrolyte. It facilitates ion transport, plays an important role in solid-electrolyte interphase formation, and affects the oxygen solubility, conductivity, and stability. Moreover, the dissociation degree of the salt affects the morphology of the discharge product as discussed in **Section 1.5.1**.[112] The salt should be highly soluble in the electrolyte solvent, have high conductivity and stability towards reduced oxygen species.[3,7]

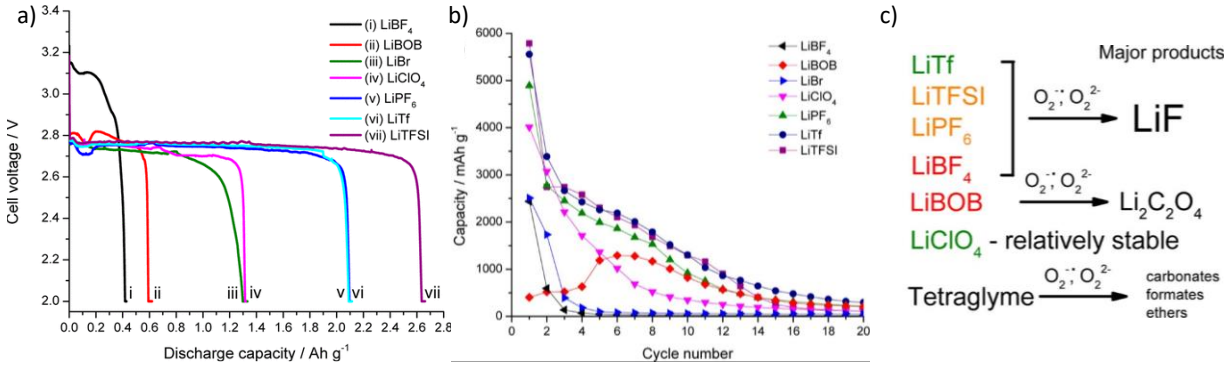

Figure 1-13 *a) Discharge profile of LOBs containing different Li salts. b) Cycling stability of LOBs with various salts and c) Summary of the main decomposition products of selected salts. LiClO4 and LiBr were now shown as they were found to be stable in this study. Reproduced from ref 123. Copyright 2013, American Chemical Society.*

Initial LOB studies used LIB salts such as $LiPF_6$, $LiBF_4$, and LiBOB. $LiPF_6$, even though it forms HF with trace amount of water and has low thermal stability, is still the most popular LIB salt. Oswald et al.[113] reported that $LiPF_6$ reacts with Li_2O_2 to form LiF. They suggested that the water content was too low for hydrolysis of the anion to form HF and the LiF formation is due to the reactivity with Li_2O_2. The instability of $LiPF_6$ in LOBs was further confirmed by other studies.[114-116] $LiBF_4$ and LiBOB completely decompose into LiF, Li_2CO_3 and boron-oxygen containing compounds such as lithium triborate. According to Nazar and co-workers superoxide radicals cause a nucleophilic substitution reaction at the boron centre.[117]

$LiNO_3$ was shown to eliminate CO_2 evolution[118], act as a OER catalyst and passivate the carbon electrode towards side reactions on charge.[119] It is also widely studied for Li metal anode protection.[93,120] Similar to $LiNO_3$, LiBr and LiI are bifunctional and can both act as the electrolyte salt and redox mediator. However, they were shown to react with cell components.[121,122]

LiTFSI and $LiClO_4$ are two of the most commonly used salts in LOBs. LiTFSI shows high discharge capacities compared to a range of salts including $LiClO_4$ and LiTf (**Figure 1-13**).[123] Also, in a DFT study, Lindberg et al.[124] show that $TFSI^-$ promotes greater O_2 solubility than ClO_4^- and Tf^-. However, in some studies it shows minor decomposition products such as LiF and $–CF_3$.[101,123,125] It should be noted that small amount of degradation from the salt is unlikely to be the main source of cathode and electrolyte degradation. $LiClO_4$ were found to be stable in few studies.[123,126] However, Younesi et al.[127], Veith et al.[116] and Shao et al.[128] reported formation of LiCl and ClO_4^- type species on the discharge products. Nasbyulin et al.[123] attributes this to the degradation of the salt with X-ray beam or Ar^+ beam.

High concentrations of salt seem to increase the stability of the solvent. One of the approaches in increasing the stability of electrolytes without finding a new solvent is using additives and high salt concentration to coordinate solvent molecules with other ions to protect them from reactive species. However, high salt concentration affects ionic mobility and viscosity of the electrolyte and kinetics of the cell. Kwak et al.[109] used high salt concentrations but diluted the

electrolyte with a fluorinated diluent to decrease the viscosity and increase the wettability. They describe that LiTf is dissolved by tetraglyme and form salt-solvating solvent complexes or clusters and these clusters are dispersed in the diluent (**Figure 1-14**). Hence, they have local high salt concentrations. They claim that higher activation energy of the new electrolyte mixture makes it is more difficult for parasitic reaction to occur. They show carbonate formation on the Li metal anode which was reported to have a stabilising effect on the anode. Another important aspect is the higher O_2 solubility which is likely due to the fluorinated diluent. It is important to balance the properties of the salt. New salts designed for current or new electrolytes should follow the same strategy as well. It is important to achieve stability and long cyclability, but capacity and kinetics should be improved as well. The salt is crucial to the solubility of LiO_2 and consequently to the formation of Li_2O_2.

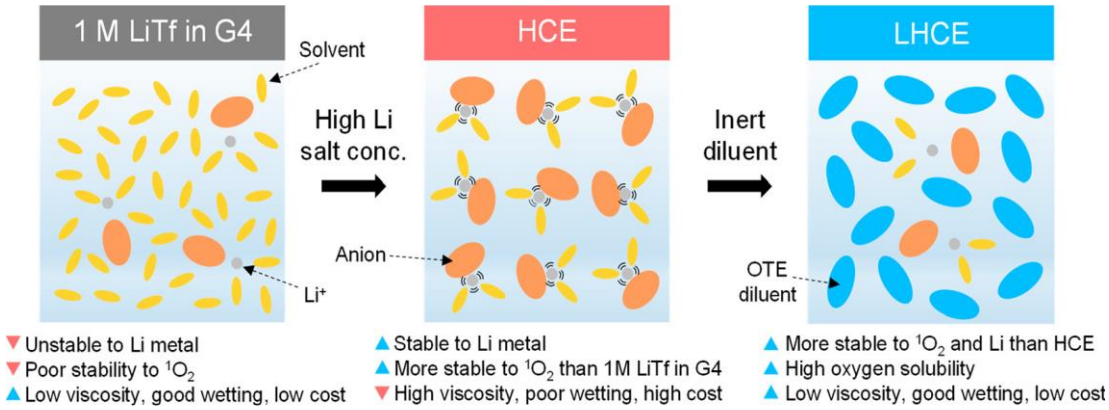

Figure 1-14 *Schematic representations of structures of commonly used 1M electrolyte, a high concentration electrolyte and a diluted high concentration electrolyte with local clusters. Reproduced with permission from ref 109. Copyright 2020, American Chemical Society.*

1.6.2 Air Cathode

In a LOB, the cathode should be conductive and able to accommodate Li_2O_2 on discharge. It should not limit the O_2 transport and dis/charge current densities for Li_2O_2 decomposition and formation. Since a porous cathode is ideal for Li_2O_2 storage, the way the cell metrics are reported is important as well. Mass (including the mass of the active material, binder and Li_2O_2), thickness and area of the cathode should be reported for fair comparisons. For example, reporting capacities

in mAh cm^{-2} for a thin gas diffusion layer without reporting its mass or mass of any catalysts loaded is not ideal.

Non-carbon materials such as nano-porous gold, TiC,[81,129] Mo_2C,[130] Ti_4O_7[131] and some other metal oxides such as RuO_x[132] were investigated as cathodes for LOBs. Porous scaffolds with electrocatalysts such as Ni foam with Co_3O_4 nanorods[133] and porous perovskite nanotubes[134] were utilised as air cathodes as well. However, these materials are more expensive and heavier than carbon. Additionally, the catalytic activities leading to electrolyte degradation and misleading high capacities are not investigated properly.

Carbons such as Super P, Ketjen Black, and Vulcan XC 72R are the most widely used cathode materials for LOBs as well as graphene and carbon nanotubes due to the good electronic conductivity, low cost and low density.[3] Although usually assumed to be inert, carbon materials are not completely stable in LOBs. McCloskey et al.[135] first suggested that carbon was reactive towards Li_2O_2. They used ^{13}C cathodes and discharged their cells with $^{18}O_2$ to distinguish between side-products evolving from cathode and electrolyte. On discharge, they found monolayers of Li_2CO_3 in the C-Li_2O_2 interface and on the electrolyte-Li_2O_2 interface, and on charge observed that this carbonate cannot be fully removed. However, Xu et al.[125] suggests that this could be due to electrolyte decomposition rather than carbon erosion by Li_2O_2. They perform similar experiments with ^{13}C cathodes, but use solid state NMR instead of XANES as Gallant et al. did. However, this contradicts the results from Leskes et al.[136] where they observe carbonate formation from the ^{13}C cathode. Their natural abundance ^{17}O solid state NMR data shows that main discharge product is Li_2O_2, but on charge Li_2CO_3 starts forming. Gallant et al.[137] showed formation of Li_2CO_3 on vertically-aligned carbon nanotube-Li_2O_2 interface in DME but noted that they did not observe this necessarily on Li_2O_2 suggesting that there is carbon degradation due to Li_2O_2 or other reduced carbon species.

Bruce and co-workers also used ^{13}C cathodes to distinguish between cathode and electrolyte degradation.[138] They recoded $^{12}CO_2$ and $^{13}CO_2$ signals during discharge and charge and

during acid and Fenton's reagents treatments of the cathode by differential electrochemical mass-spectrometry (DEMS). They decomposed all the carbonate by injecting H_3PO_4 and then all the carboxylate by injection Fenton's reagent (H_2O_2 and Fe^{2+} containing solution to form $OH^{\bullet}$) to study the amount of accumulated by-products on the cathode. They reported that the carbon cathode is stable during discharge and decomposition forming carbonate and carboxylates starts on charge above 3.5 V (**Figure 1-15**). They also conclude that the cathode does not degrade unless there is Li_2O_2 and Li_2O_2 degradation is limited as they do not detect this below 3.5 V. Additionally, they show that hydrophobic carbon is more stable than hydrophilic carbon due to the lack of reactive surface groups.

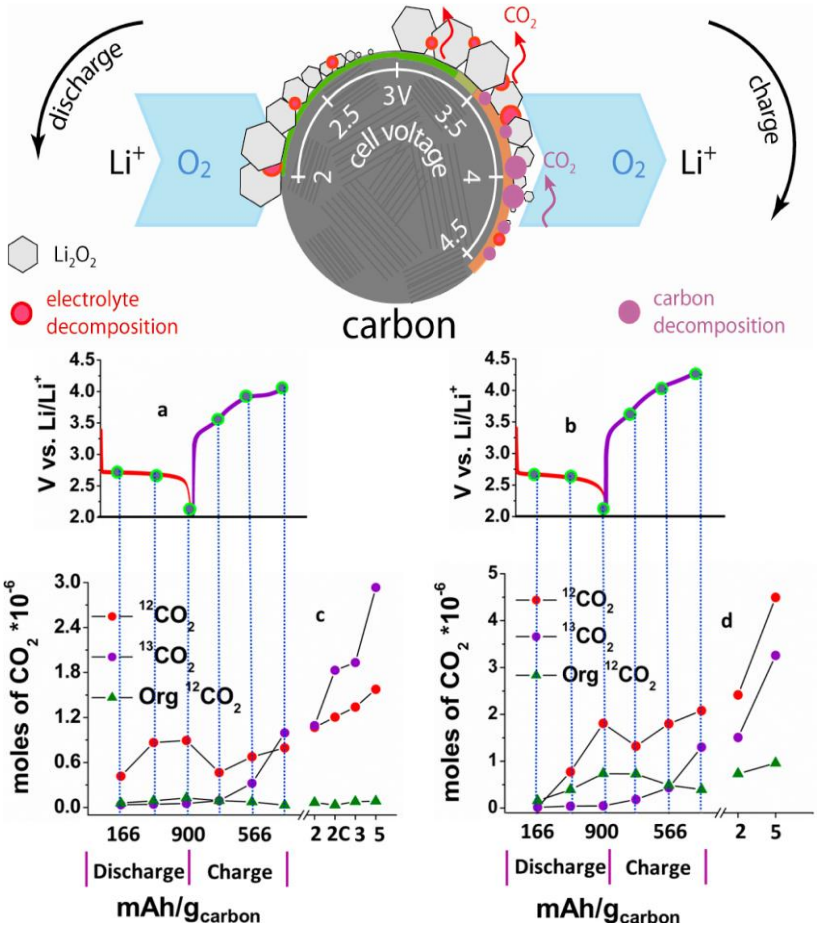

Figure 1-15 *Schematic representation of the synergistic relationship between carbon and electrolyte degradation, and discharge and charge curves and associated gas evolution (DEMS) data for a-c DMSO and b-d tetraglyme based electrolytes. Reproduced with permission from ref 138. Copyright 2012, American Chemical Society.*

Itkis and co-workers studied different carbon surfaces such as highly oriented pyrolytic graphite (HOPG), glassy carbon (GC) and edge and basal planes of graphite.[139] Similar to Bruce and co-workers, they also showed that defects on the carbon cathode surface cause more Li_2CO_3 formation. Similarly, Kang and co-workers studied cycling and degradation with pristine and heat treated (1600-2800 °C) ^{13}C cathode and showed that crystallinity boosts rechargeability and decreases degradation.[140] On the other hand, several works on different electrochemical systems show that O_2 reduction is faster at edge planes compared to basal planes.[141-143] Although Itkis and co-workers show that defects (such as on GC) cause more degradation than defectless basal planes (such as HOPG), they also show that disordered carbon electrode surfaces promote solution-mediated Li_2O_2 growth. They observed electrochemical formation of Li_2O_2 after LiO_2 formation on basal planes and not on GC. They also point out that the first electron transfer step does not depend on chemisorption and does not depend on the electrode surface morphology.

Carbon cathodes have been modified to increase oxygen mass transport, accommodate solid Li_2O_2 and prevent cathode flooding. This is either done via surface modifications or making hierarchical structures and 3D scaffolds (**Figure 1-16**). Balais et al.[144] added perflurocarbon additive (perfluoro-n-nonane) on their gas diffusion layer to increase oxygen solubility and prevent cathode flooding. They used RMs as well in this study to promote solution-mediated dis/charge. They achieved 60% increase in the discharge capacity compared to unmediated and unmodified cathode system. Liu et al.[145] develop hierarchically porous carbon nanotube films with macropores for O_2 transport and micro-nanopores for Li_2O_2 formation. Similarly, Xie et al.[146] developed an ordered mesoporous carbon. They also decorated this structure with FeO_x and Pd catalysts. Huang et al.[147] made vertically aligned gas channels by rolling CNTs with a cotton layer and gel polymer electrolyte to show the importance of O_2 mass transport. They doubled the discharge capacity by more than two times compared to planar CNT electrodes and liquid electrolyte.

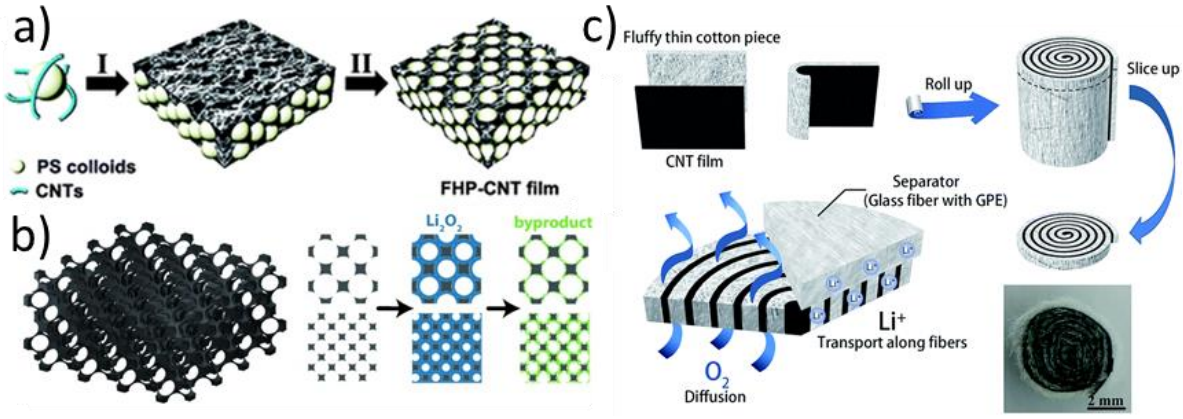

Figure 1-16 *a) Free standing carbon nanotube film with macropores after PS colloids were decomposed. Used with permission of Royal Society of Chemistry from ref 145. Permission conveyed through Copyright Clearance Center, Inc. b) Three dimensionally ordered mesoporous carbon cathode. Reproduced with permission from ref 146. Copyright 2015 John Wiley and Sons. c) Schematic representation of process of making rolled glass fibre-CNT cathodes and an image of the actual cathode. Used with permission of Royal Society of Chemistry from ref 147.*

1.6.2.1 Binder

Carbon cathodes need binder for structural integrity. Binders make up 10-20 % of the cathode mass and need to be chemically and electrochemically stable towards the other cells components and reduced oxygen species. Lately, as the importance of oxygen mass transport is understood better, fluorinated binders that promote oxygen dissolution became a popular research interest.

One of the most commonly used binders in Li-ion batteries, polyvinylidene difluoride (PVDF) was shown to be unstable in Li-O_2 cells. Black et al.[148] showed that it reacts with superoxide by chemically generating LiO_2 and mixing it with PVDF powder. This was further supported by an XPS study showing LiF formation upon cycling a cell with PVDF binder (the salt was not fluorinated).[149] Moreover McCloskey and co-workers showed that Raman shifts obtained from PVDF degradation overlap with LiO_2 peaks and this causes misleading interpretation of the results.[150] It is very important in an unstable and not fully understood system such as Li-O_2 batteries to decouple degradation related issues.

PAN, PVC, PVDF, PVDF-HPH, PVP, PEO, and CMC were found to be unstable.[151,152] PE, PMMA, Nafion, and PTFE were found to be stable.[151] However, the study by Nasybulin et al.[152] study

shows inconclusive results for PTFE and PP and their ball-milling conditions could have affected the stability of the binders.[152] The XPS spectra had additional peaks for C1s but no changes were observed for F1s. PTFE is still one of the most commonly used binders in Li-O_2 cells.

1.6.3 Anode

The high theoretical capacity of Li-O_2 batteries is based on using Li metal as the anode. Li metal has a theoretical specific capacity of ~3860 mAh g^{-1}. Due to its high Fermi level energy, Li has a high operating voltage. However, bare Li metal cannot be used due to stability and safety issues. Compared to LIBs where it is mainly the electrolyte reacting with Li metal, in LOBs, reduced oxygen species can play a detrimental role. Forming stable solid-electrolyte interphases[24,96,153-155], using gel or solid electrolytes[156], designing functional separators or using 3D lithium architectures[157] are some of the strategies towards using high capacity Li based materials as anodes.

Volume changes and dendrite formation lead to short cycle life and safety issues in all Li metal batteries. One of the main causes of dendrite formation is inhomogeneous electric field.[158,159] Defect sites and grain boundaries can also affect dendrite formation.[160] SEI ruptures and uncontrolled deposition of Li further increases the risk of dendrite formation (**Figure 1-17**). Thus, it is very important to protect the metal anode.[3]

In Li-ion batteries organic carbonate based electrolytes form a stable solid-electrolyte interface. However, these solvents are not suitable to be used in LOBs. Tetraglyme, one of the most prevalent electrolyte solvents, was shown to react with the Li metal anode when the cell was cyded

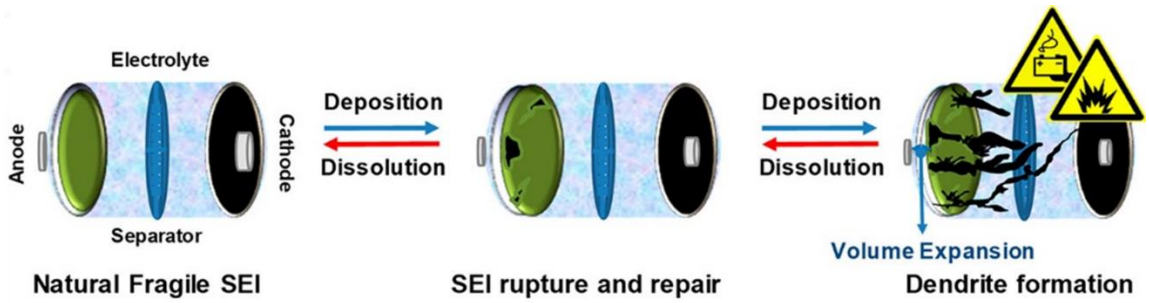

Figure 1-17 *A graphic representation of dendrite formation, SEI rupture and associated safety issues. Reproduced with permission from ref 3. Copyright 2020 American Chemical Society.*

with $LiPF_6$ salt. Abraham and co-workers showed that the Li surface was covered with brown precipitate.[161] Assary et al.[162] showed that Li metal reacts with O_2 and tetraglyme and forms LiOH and Li_2CO_3 via in-situ XRD experiments. One of the strategies to form a stable SEI was to use $LiNO_3$. Both Walker et al.[93], Giordani et al.[163], and Uddin et al.[96] show that use of $LiNO_3$ or generating $LiNO_3$ via the reaction of $LiNO_2$ with O_2 protects the anode. Giordani et al. suggests a $LiNO_3$ regenerating mechanism. Uddin et al. confirms this mechanism, however they do not comment on the accumulation of Li_2O SEI on the Li anode. Although they also suggest that $LiNO_2$-$LiNO_3$ system alleviates the negative effects of O_2. Optimising the electrolyte utilising Guttman number and ionic strength of solvents and salts to control the solubility of different intermediates and discharge is a similar strategy. It was previously shown that super concentrated electrolytes enhance cycle life.[164,165]

Lithium ion conducting membranes such as LiSICON and LiPON are used to protect the anode from the liquid electrolyte.[166,167] Similarly, to obtain a stable SEI, Kozen et al.[153] designed a stable organic/inorganic hybrid SEI by coating the metal anode with elastomer and LIPON. They achieved current densities as high as 2 mAh cm^{-2} in Li/Li symmetric cells. The solid electrolytes are sometimes used in bicompartment cells where the electrolyte on the anode side and the cathode side are different.[156] However, this reduces the volumetric energy density. Using modified separators such as modified polyurethane developed by Kim et al. [168] that block RM shuttling and O_2 crossover is more advantageous.

A practical LOB battery will operate with redox mediators. However, in a cell where Li metal is not protected, soluble RM^+ will shuttle from cathode to the anode, react with the metal and cause decrease of RM concentration and an increase in overpotential. There are only a few studies that directly investigate the effect of shuttling. This is an important aspect in evaluating the true performance of redox mediators. Chen and co-workers developed a PMMA and PVDF based gel membrane to stop redox shuttling, and avoid self-discharge and internal short circuits.[169] They used this membrane in a dual mediator cell and showed that they can both avoid redox shuttling and

superoxide intermediate diffusion to the Li metal anode. Overall, it is common practice to protect the anode with a solid electrolyte membrane in studies where RMs and Li metal are used together.[166,167] MPT^+, $FePC^+$ and $TEMPO^+$ were shown to damage the anode surface.[170-172]

3D architectures decrease the energy density, but allow volume expansion. One of the high performing examples of these architectures is achieved by prelithiating 3D cross-stacked carbon nanotubes.[157] The anode had a reversible capacity of 3656 mAh g^{-1}. Lithiated Si, Sn, and Al alloy anodes were also investigated. However, the capacity is usually low. Hassoun et al.[173] used a pre-lithiated silicon anode and achieved a capacity of 1000 mAh g^{-1}_{carbon}.

1.7 Catalysts

Heterogeneous and homogenous catalysts are used in LOBs to ease both the discharge (oxygen reduction reaction) and the charge (oxygen evolution reaction) processes. Catalysts are classified either as heterogeneous if they are in a different phase than the reactants and products or homogenous if the reactants, products and the catalyst are in the same phase. Heterogonous catalysts in LOBs are usually immobilised on the air cathode and homogenous catalysts are redox molecules that dissolve in the electrolyte. Homogenous catalyst generally operate by lowering the overpotential acting as redox shuttles with redox potentials at slightly lower or higher potentials than the thermodynamic potential of O_2/Li_2O_2 for discharge and charge, respectively. However, the exact mechanism of heterogeneous catalysis in LOBs is not well-defined as once Li_2O_2 grows on the catalyst as insoluble particles, it would foul the catalyst surface and stop its catalytic activity.

1.7.1 Heterogeneous Catalysts

Heterogeneous catalysts are utilised to decrease the discharge and mainly the charge overpotentials and increase the capacity in LOBs. These catalysts are usually supported or grown on carbon supports but can be directly on catalytic substrates as well. Although some reports in the literature show increased capacity with heterogeneous catalysts, we cannot say the same thing for cyclability. In most of the reports where heterogeneous catalysts are used, the electrolyte

degradation or Li_2O_2 yield are not studied, and such reports solely target achieving high capacities and low voltages without addressing the main causes of capacity fade such as electrolyte and carbon instability.[4] Moreover, these catalysts are passivated after lithium peroxide growth and can only oxidise Li_2O_2 if they are in direct contact. Overall, Au seems to be the only inert metal to be used as a catalyst,[3] and Ma et al.[174] and McCloskey et al.[175] showed that metal catalysts such as Pt, MnO_2, and Pd-based and Ru-based catalyst cause degradation by studying CO_2 evolution during charge.

1.7.2 Homogeneous Catalysts – Redox Mediators

Soluble redox mediators (RMs) are essential for a practical LOB. RMs are simply molecules that shuttle electrons between O_2 or Li_2O_2 and electrode surface in the electrolyte, and they lower discharge and more importantly the charge overpotentials. The charge process is more challenging in that insulating Li_2O_2 causes cathode passivation, and side-products passivate both the cathode and Li_2O_2 surfaces. Large particles of Li_2O_2 can also lose contact with the electrode surface. RMs take the reaction away from the electrode surface and facilitate formation and decomposition of Li_2O_2 in solution (

Figure 1-18).

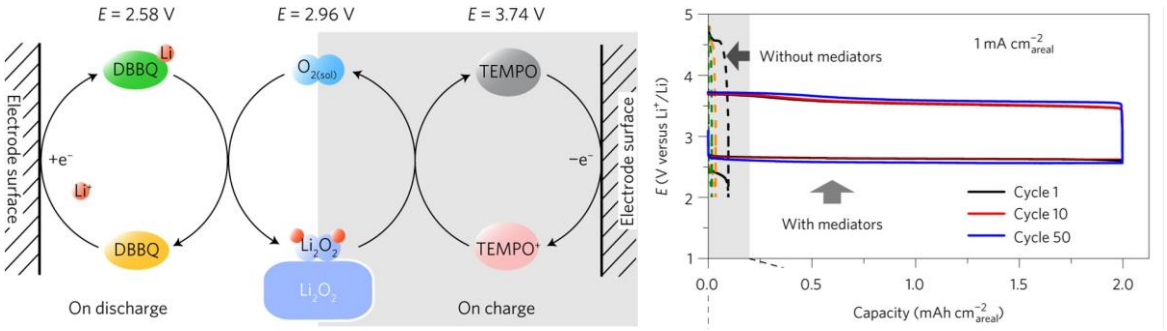

Figure 1-18 *Schematic representation of discharge and charge reactions happening on the electrode surface for a DBBQ (discharge RM) and TEMPO (charge RM) mediated cycling. Load curves for unmediated and mediated cycling. Reproduced with permission from ref 191. Copyright 2017, Nature Publishing Group.*

1.7.2.1 Discharge RMs

Growth of Li_2O_2 in solution and lowering the overpotential (~0.3 V at modest rates) are important to increase capacity and cycle life, avoid clogging of the cathode and decrease the amount of parasitic reactions. Formation of LiO_2 intermediate which has a higher free energy than that of Li_2O_2 determines the discharge overpotential. The potential of the discharge/ORR redox mediator should be lower than the thermodynamic potential for O_2/Li_2O_2, 2.96 V and it should act as a redox shuttle. The Li_2O_2 generation path should avoid the formation of LiO_2. The first discharge redox mediator

used in LOBs was ethyl viologen.[176-178] First, Lacey et al.[176] used ethyl viologen ditriflate to form O_2^- in solution which then disproportionates to form Li_2O_2. However, the operating voltage of this RM is the same as the thermodynamic O_2/Li_2O_2 potential. Hence, there is a competition between two mechanisms and electrode passivation was not completely bypassed. Ethyl viologen also decomposes at high concentrations.

Quinones[179,180] and phytalocyanines[170,181] have been surveyed as redox mediators. Some of these studies only include electrochemical measurements. However, it is important to study the Li_2O_2 yields and the e^-/O_2 ratio to understand the true efficiency of these mediators. Gao et al.[182] reported 2,5-ditert-butyl-1,4-benzoquinone (DBBQ) as am efficient ORR mediator which increased the discharge capacity 100-fold and increase the voltage of the discharge process.

The mechanism DBBQ uses is different than other discharge/ORR mediators as it works as a catalyst. DBBQ is reduced to LiDBBQ on the electrode surface and makes the $LiDBBQO_2$ complex (**Figure 1-19**). This complex is a lower energy intermediate and Li_2O_2 forms in solution rather than on the electrode surface. Overall, the discharge mediator should promote solution-based discharge ideally in lower DN solvents and form a lower activation energy intermediate. This can be done either via stabilisation of LiO_2 or forming a new low energy intermediate.

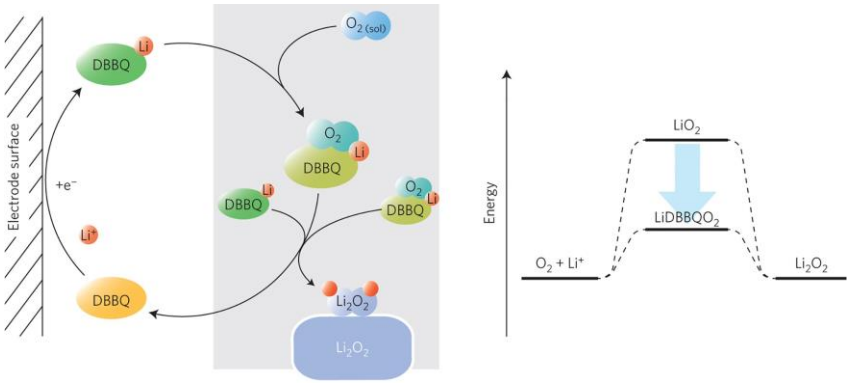

Figure 1-19 *Mediated discharge process with DBBQ. Reproduced with permission from ref 182. Copyright 2016, Springer Nature.*

1.7.2.2 Charge RMs

Charge RMs are important for oxidising Li_2O_2 without the cell reaching to potentials > 3.8 V and cause more parasitic reactions and accumulation of passivating side products. Oxidation

mediators/charge RMs are soluble in the electrolyte and ideally get oxidised slightly above the thermodynamic formation potential of Li_2O_2. Once the voltage is high enough to oxidise the RMs at the electrode surface, the oxidised RM (RM^+) diffuses and oxidises Li_2O_2. Redox potential, diffusion coefficient, kinetics and stability are important parameters to control when using and designing RMs. It is important to note that in a full Li-air cell with a Li metal anode, protective layers such as solid electrolyte membranes must be employed to stop redox shuttling.[4]

The first report on the use of charge RMs in LOBs was by Chen et al.[183] where they used tetrathiafulvalene (THF) as an RM and achieved high charge current densities (1 mA cm^{-2}). Similarly in a patent, Chase et al.[184] used LiI in LOBs for mediated charging. LiBr and LiI were previously used for overcharge protection in LIBs in the 1980s.[185,186] These were the first generation redox mediators. Recently, Shao-Horn and co-workers showed that they can tune the redox potential by mixing LiBr-LiI and generate a mixture of I^{3-}, I_2Br^-, IBr^{2-}, and Br^{3-} depending on the concentration of the starting LiBr and LiI.[187] However, they also show for the first time that the O_2/e^- ratio is considerably below 2. They suggest that it is close to 4 similar to their previous unmediated diglyme work. The 4 e^-/O_2 path does not seem feasible here and it seems that these redox mediators do not perform well.

Several other molecules were found to act as OER mediators in LOBs such as nitroxyl group containing molecules (2,2,6,6- tetramethylpiperidinyloxyl, TEMPO, 2-azaadamantane-N-oxyl, AZO)[188-192], metal phtalocyanines,[170,193] and organic materials such as N,N,N',N'-Tetramethyl-p-phenylenediamine (TMPD)[190], 5,10-dihydro-5,10-dimethylphenazine (DMPZ)[190,192,194,195] etc. The main focus of the research is to get e^-/O_2 ratio on charge close to the theoretical value of 2 and decrease the amount of side products and their accumulations; thus, to increase the capacity and cell life. However, even with the mediators, it is difficult to get $2e^-/O_2$ due to the instability of redox mediators.[194,195] Recently, the research focus shifted to the kinetics of the oxidation mechanism and driving a relation between apparent rate constants, amount of degradation and the practical

charging rates. This is the focus of Chapter 3 and the in/consistencies in the literature will be discussed in detail in that section.

Combining ORR and OER redox mediators or using bifunctional redox mediators are strategies to bypass all the direct oxygen redox chemistry at the electrode surface and increase the capacity and cycle life while decreasing the side parasitic reactions. Heme[196] and 2-phenyl-4,4,5,5-tetramethylimidazoline-1-oxyl-3-oxide (PTIO)[197] were used as bifunctional redox mediators where their reduced forms are present during discharge and oxidised forms are present during charge. Gao et al.[191] combined DBBQ and TEMPO and achieved 2 mAh cm^{-2} capacity at a rate of 1 mA cm^{-2}. The dis/charge overpotential was lowered and the dis/charge potentials were 2.7 and 3.6 V, respectively.

1.8 Singlet Oxygen and Li-O_2 Batteries

It was first predicted by Mulliken that the electronic configuration of dioxygen should lead to two singlet states and a triplet state that are close in energy.[198] Ground state dioxygen, triplet oxygen ($^3O_2$, $^3\sum_g^-$), has two unpaired electrons with parallel spins in the highest occupied molecular orbitals (HOMO) following Hund's rule and the Aufbau principle.[199] Spin inversion of one of the HOMO electrons and pairing of the HOMO electrons result in the first excited state singlet oxygen ($^1O_2$, $^1\Delta_g$) which is 94.29 kJ mol^{-1} (0.98 eV) higher in energy than that of $^3O_2$.[199,200] A second spin inversion results in the formation of second electronic excited state/high energy singlet oxygen ($^1\sum_g^+$) which is 56.4 kJ mol^{-1} (0.65 eV) energy higher than that of $^1O_2$ (**Figure 1-20**).

Even though the physical properties of $^1O_2$ are similar to that of $^3O_2$, such as similar bond lengths and closely lying electronic states, it is highly reactive and a stronger oxidising agent than $^3O_2$.[200] $^1O_2$ is electrophilic and non-radical. It can react with unsaturated carbon-carbon bonds. Both

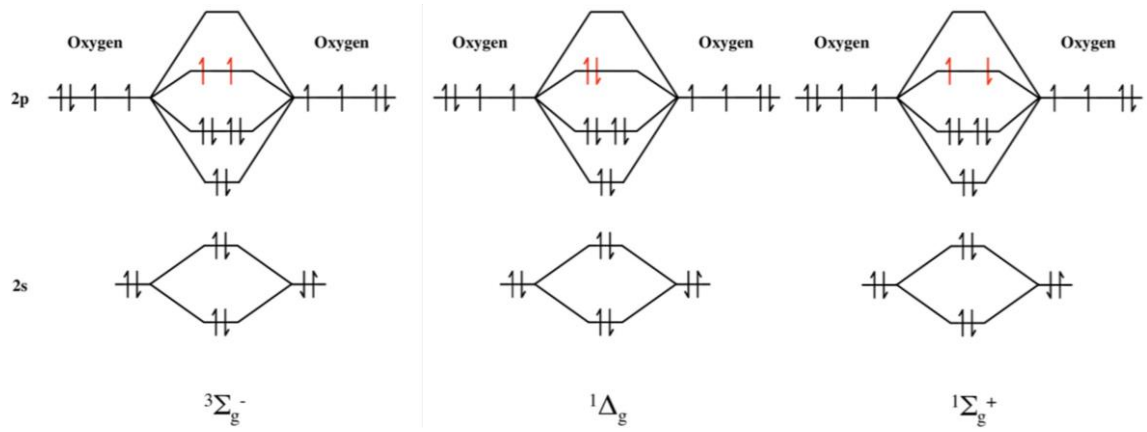

Figure 1-20 *Molecular orbital diagrams for ground state triplet oxygen ($^3O_2$), first excited state singlet oxygen ($^1O_2$) and second excited state/high-energy singlet oxygen.*

$^1O_2$ and high energy singlet oxygen have a total spin S=0, the spin restriction is removed and their reactivity/oxidising ability is increased. Both Wigner's rule and Marcus theory of electron transfer follow spin conservation.[201] However, a spin forbidden reaction with $^3O_2$ which involves a spin multiplicity change only means that it is low probability but does not necessarily mean that it is not favourable. Other factors could affect the probability of allowed and forbidden reactions such as steric interactions and energetic conditions.[202]

The lifetime of $^1O_2$ is reported to be 45-72 minutes in the gas phase.[200,203] However, it is considerably shorter in solution. The lifetime depends on the solvent, can vary several orders of magnitude and is higher in deuterated solvents. The solvent acts as a sink for electronic excitation energy of oxygen.[204] This also explains the longer life times for deuterated solvents as a pronounced H-D isotope effect is observed for electronic-to-vibrational energy transfer.[201] It was also shown that perhalogenated solvents increase the lifetime whereas lifetime decreases in protic solvents.[204]

In the last few years, singlet oxygen was shown to evolve in aprotic metal-air batteries[205-209], and was pointed out as the main source of degradation in various studies.[210] Following these reports, research focused on trapping, quenching and avoiding $^1O_2$.[59,194,211,212] $^1O_2$ is widely considered as the culprit in LOBs due to these high impact reports. However, this work and a recent review[201] questions the formation routes and the severity of the reactivity of $^1O_2$ with LOB components. The role of $^1O_2$ in LOBs is discussed throughout this Thesis. In Chapter 3, $^1O_2$ is used as a probe to understand redox mediated oxidation kinetics, in Chapter 5 reactivity of $^1O_2$ with a

carbon cathode and electrolyte is studied, and in Chapter 4 the chemical reactivity of $^1O_2$ with several common LOB solvents and salts are investigated, and alternative interpretations in its detections are discussed. A more detailed review of the literature can be found in Chapter introductions.

1.9 Thesis Outline

Owing to their high theoretical specific energy of 3500 Wh kg^{-1}, aprotic Li-O_2 batteries gained a tremendous research interest between 2006 - 2015. Achieving high capacities and long cycling stability has been a longstanding problem due to the reactive oxygen species and instability of cell components with these, and due to high overpotentials and limited capacities. A large portion of research has focused on reporting high capacities without achieving long cycling life, including additives or heterogeneous catalysts to cells without decoding the degradation mechanism. However, these strategies did not solve capacity and stability issues, and researchers are not close to making a practical LOB. Although redox mediators decreased the large overpotentials, fundamental understanding of the mediated oxidation mechanism and the overall degradation mechanism is still lacking. Recent evidence has suggested $^1O_2$ is involved in the degradation of LOBs. However, research focusing on avoiding this reactive species did not succeed in improving stability and cycle life. Hence, this research casts doubt on whether $^1O_2$ is the key to understanding the degradation in LOBs and deciphering the fundamentals of the mediated oxidation mechanism.

In Chapter 3, kinetics of redox mediated oxidation is studied. It is shown that the oxidation follows Marcus behaviour. The rate limiting step is an outer sphere 1-e^- transfer. There are two e^- transfer reactions on the overall process. To workout which step is the rate limiting, $^1O_2$ yield is investigated to understand whether the electron transfer trend and $^1O_2$ trend overlap. We show that 1st e- transfer is the rate limiting step and $^1O_2$ yield with RMs does not correlate with overall degradation. The discrepancy in the $^1O_2$ yield and the amount of degradation products suggest that $^1O_2$ may not be the main cause of degradation. Hence, in Chapter 4, chemical stability of commonly

used solvents and salts towards $^1O_2$ is investigated. There is no significant degradation observed in tetraglyme-LiTFSI electrolyte. Electrochemical stability of this system is tested in Chapter 5. Overall, it is concluded that $^1O_2$ is not the main source of degradation but fresh Li_2O_2 surfaces are. Moreover, detection of $^1O_2$ utilising DMA and HPLC is shown to be an unreliable method in Chapter 4.

2 Chapter 2 – Theory and Experimental Techniques

2.1 Cell and Material Preparation Methods

2.1.1 Cathode Preparation

In this Thesis, carbon was employed as the air-cathode (working electrode). For the majority of the degradation studies, amorphous carbon-13 powder (^{13}C, Aldrich), a stable isotope of carbon-12, was used to make the cathodes. The main purpose of using an isotopically labelled material was to differentiate between the by-products arising from cathode (^{13}C) and electrolyte (^{12}C based solvent) degradation.[135] The rest of the air-cathodes were prepared with Super P carbon black (Timcal). All the cathodes were made using polytetrafluoroethylene (PTFE) as a binder in 85:15 w/w carbon:PTFE ratio.

For ^{13}C-PTFE composite cathodes, ^{13}C powder was treated at 900 °C under Ar:H_2 (95:5, v/v) flow for 5 hours to reduce any functional groups on the carbon surface, and then transferred to an Ar-filled glovebox. The cathodes were made by mixing ^{13}C and PTFE powder in an agate mortar. 100 mg powder was mixed at least for 30 minutes. ~10 mg of the composite material was pressed into 7 mm diameter pellets using a handheld press in the glovebox. The film like pellet was then pressed onto a stainless steel mesh (100 mesh, Advent-RM) current collector. The stainless steel current collectors were prepared by spark welding the stainless steel mesh to a stainless steel wire.

Li_2O_2-preloaded cathodes were made by grinding ^{13}C and in house synthesised Li_2O_2 (80:20 w/w), and adding 15% PTFE powder to this powder mix. ^{13}C-Li_2O_2 and PTFE were mixed in an agate mortar. Similar to the ^{13}C cathodes, the ^{13}C-Li_2O_2 cathodes were pressed into ~10 mg 7mm pellets.

2.1.2 Anode/Counter Electrode Preparation

Li-O_2 cells should employ Li metal anodes to achieve the desired high energy density. However, Li metal reacts with most organic electrolytes. Moreover, if redox mediators are present, the anode would need protection due to redox mediator shuttling (catalysts diffusing to the anode) as well.[169] This Thesis does not focus on making full cells with protected Li metal anodes, but focuses on the fundamental charging and degradation mechanisms. Thus, to avoid degradation arising from

the anode-side, $LiFePO_4$ (LFP) was used as the anode, counter electrode, and the reference electrode material (CE and REF in three-electrode cells).

LFP does not react with the electrolyte used in this Thesis, and it has a flat dis/charge plateau (a well-defined potential, 3.43 V, for a wide capacity range) which makes it a good candidate to be used a reference electrode (however, it has high impedance) and counter electrode.[213] To make LFP electrodes, LFP, Super P, and PTFE were mixed in 80:10:10 w/w ratio with isopropanol. The slurry was mixed on a vortex mixer until it turns into a homogenous paste. This paste was cast on a stainless steel mesh or was compressed into a film via calendaring and cut into 1.25 cm diameter discs. To get the LFP to its stable voltage plateau at 3.425 V, LFP electrodes were chemically delithiated to ~20 % total capacity (Li_xFePO_4, x<1). This was achieved by soaking the electrodes in 1.5 ml acetic acid (Aldrich), 3.6 ml 30% H_2O_2 (Aldrich) and 250 ml MilliQ Water for 20 minutes.[214] The electrodes were washed with MilliQ water (18.2 MΩ cm) and isopropanol until all the acetic acid was removed, dried under vacuum at 85 °C overnight, and transferred into an Ar-filled glovebox.

2.1.3 Electrolyte Preparation

All the electrolyte solvents were dried over 4 Å molecular sieves (Aldrich) for at least 3 days. Before adding the molecular sieves into the solvents, they were activated at 300 °C under vacuum overnight and transferred into an Ar-filled glovebox. After the solvents were dried over the sieves, the final water content was determined by coulometric Karl Fischer titration (< 10 ppm). Solvents used in this Thesis are tetraethylene glycol ether (tetraglyme, > 99%, Aldrich), 1,2-dimethoxyethane (DME, Aldrich), dimethyl sulfoxide (DMSO, Aldrich), and acetonitrile (MeCN, Aldrich).

All electrolyte salts, including tetrabutylammonium bis(trifluoromethane)sulfonimide (TBATFSI, 99.0%, Aldrich), lithium bis(trifluoromethane)sulfonimide (LiTFSI, 99.99 %, Aldrich), and lithium perchlorate ($LiClO_4$, battery grade, Aldrich) were stored in an Ar-filled glovebox. All the salts were dried at 85 °C under vacuum overnight.

Redox mediators, 2,2,6,6-Tetramethyl-1-piperidinyloxy (TEMPO, 99%, Aldrich), 4-Methoxy-2,2,6,6-tetramethyl-1-piperidinyloxy (MeO-TEMPO, 97%, Aldrich), 1-Methyl-2-azaadamantane-N-oxyl (MAZO, 97%, Sigma-Aldrich), N–Methylphenothiazine (MPT, 98%, Aldrich), 10-Isopropylphenothiazine (PPT, Aldrich), Ferrocene (Fc, 98%, Aldrich), Tetrathiafulvalene (TTF, 97%, Aldrich), N,N,N',N'-Tetramethyl-p-phenylenediamine (TMPD, 99%, Aldrich), and 5,10-dihydro-5,10-dimethylphenazine (DMPZ, 99%, TCI) were used as purchased.

2.1.4 Synthesis of Oxidised Redox Mediators

Selected redox mediators (RMs) were chemically oxidised following the established methods.[215-218] To synthesise $RMClO_4$, the selected redox mediators were chemically oxidised by forming a slurry in aqueous $HClO_4$ (99.999%, Aldrich) and adding stoichiometric amounts of $NaClO_3$ (10%, Aldrich). The solution containing the oxidised redox mediators (RM^+) were filtered and the RM^+ were washed with ice cold distilled water and diethyl ether. The RM^+s were left to dry under vacuum at room temperature for at least overnight.

To synthesise $RMBF_4$, $NOBF_4$ and RM were dissolved in CH_3CN separately. $NOBF_4$ was added to RM solution slowly under Ar flow. The mixture was constantly stirred for 3 hours. The resulting powder was washed and filtered with cold diethyl ether in an ice bath. The final powder was dried under vacuum at 30 °C in a Buchi tube and transferred to an Ar-filled glovebox.

The oxidation state of RM^+s were confirmed using microdisc voltammetry and chronoamperometry as discussed later in this Chapter.

2.1.5 Synthesis of High Purity Li_2O_2

Li_2O_2 was synthesised by following established methods.[219] 30% H_2O_2 (99.999% trace metal basis, Aldrich) was added dropwise to LiOH (99.999%, Aldrich) solvated in distilled methanol whilst stirring rapidly. The white precipitate was filtered and washed with more distilled methanol and left to dry in vacuum at 70 °C for at least 48 hours. The purity was tested by XRD and FTIR analysis, $KMnO_4$ titration, and $TiOSO_4$ titration. $KMnO_4$ titration estimates >99% purity compared to 94% for commercially purchased Li_2O_2 (technical grade, Aldrich) as discussed below.

2.1.6 Li_2O_2 Purity Tests

2.1.6.1 $KMnO_4$ Titration

This redox titration is based on the well-known H_2O_2 determination process with $KMnO_4$. First, known amount of deionised water was added to a known amount of Li_2O_2 powder (e.g. 15 mg mL^{-1}) to generate H_2O_2. Then, 1 mL of this solution was added to 40 mL 2 % H_2SO_4. This solution was titrated with $KMnO_4$ until the end point i.e. until the solution turns just pink.

The reaction is:

$$5\ H_2O_2 + 6\ H^+ + 2\ KMnO_4 \rightleftharpoons 5\ O_2 + 2\ Mn^{2+} + 8\ H_2O + 2\ K^+ \qquad \text{eq.1}$$

2.1.6.2 $TiOSO_4$ Titration

Li_2O_2 powder was weighed in small quantities (1-3 mg) and known amount of MilliQ water was added to the powder. This reaction forms H_2O_2 and LiOH. 1 mL of this solution was added to 2 mL of 2 % titanium (IV) oxysulfate ($TiOSO_4$) in 1M H_2SO_4 solution to form the stable yellow $[TiO_2OH]^+$ complex. The solution was then analysed by UV-Vis spectroscopy as the complex has an absorption peak at λ = 409 nm. Absorbance of different solutions was plotted against concentration of Li_2O_2 to form a calibration curve, given the initial purity of Li_2O_2 from $KMnO_4$ titration. Hence, we can cross-check the purity of the synthesised Li_2O_2. Then, for samples such as cathodes, the $TiOSO_4$ titration method can be utilised by using the calibration curve and the fitted linear equation produced with the pure sample dilutions.

2.1.7 Singlet Oxygen Generation

$^1O_2$ generation methods include dye-sensitised photochemical generation, microwave-radio frequency discharge generation, laser radiation under high oxygen pressures, and chemical generation (potassium perchromate or hydrogen peroxide/hypochlorite).[220] In this Thesis, $^1O_2$ is produced using photosynthesisers (PS) such as Rose Bengal (RB) and tetraphenylporphyrin (TPP). Photosensitised oxidation with photosynthesisers occurs in two ways: S-s (sensitiser-substrate) and S-o (sensitiser-oxygen) mechanisms.[220] In the S-s mechanism, sensitiser is excited which then actives the substrate either by electron or hydrogen atom transfer. The activated substrate reacts

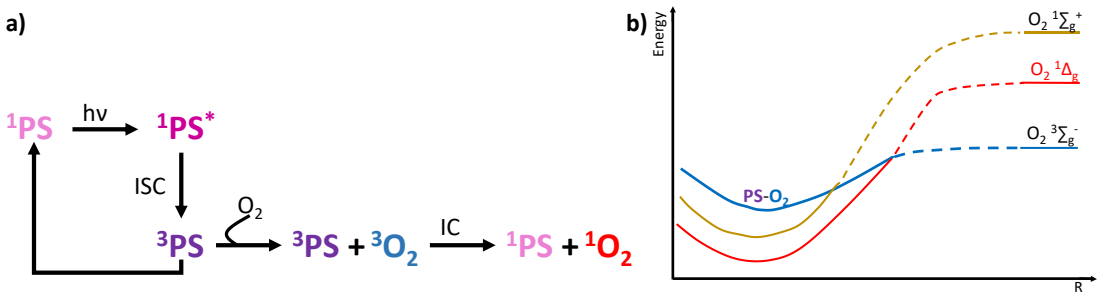

Figure 2-1 *a) Flow diagram showing steps of photosensitised $^1O_2$ generation. b) Energy levels for the reaction of O_2 with PS. ISC stands for intersystem crossing and IC stands for internal conversion.*

with the $^3O_2$ yielding the photooxidation products. In the S-o mechanism, excited state sensitiser generates $^1O_2$ which then oxidises the substrate. To avoid mixing the sensitiser with the substrate (the electrolyte), photosynthesisers were coated onto silica gel particles[220] or were synthesised with silicon based support.[221] Another method is generating Cl_2 to react with H_2O_2 which then generates HOOCl in-situ and $^1O_2$ gas.[222] However, gas phase $^1O_2$ evolution either with photosynthesiser or chemically did not work well for this study as the diffusion path for $^1O_2$ is short and the cell is moisture and air sensitive. RB and TPP does not seem to react with the electrolyte when excited with light under Ar. Hence, low concentration (<50 µM) photosynthesiser was used in electrolyte to generate $^1O_2$ photochemically (**Figure 2-1**).

For $^1O_2$ generation, RB or TPP was dissolved in the selected solvents or electrolytes. The solution was then saturated with dry $^3O_2$. Dry $^3O_2$ gas was bubbled into the solution throughout the experiments and a light source (660 nm for TPP and 530 nm for RB) was used to excite the solution i.e. the photosynthesiser (**Figure 2-2**).

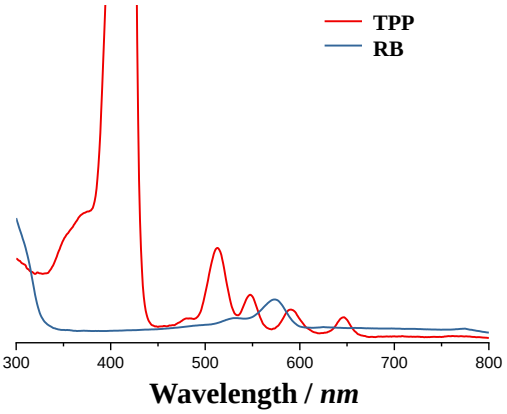

Figure 2-2 *The UV-Vis spectra of the photosynthesisers TPP and RB showing at which wavelengths they absorb light and can be excited.*

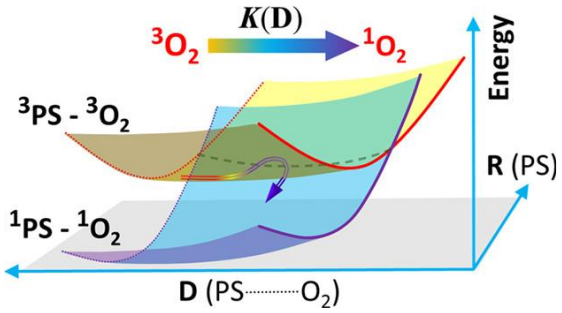

Figure 2-3 *Triplet and singlet states are parabolic and energy transfer along R follows an inverted Marcus trend and the model is extended to intramolecular coordinate D as well. D has a small effect on the state crossing. The reaction occurs on the parabolic sheets. Reprinted with permission from ref 224. Copyright 2017, American Chemical Society.*

Photosynthesiser (PS) absorbs light and gets excited to the triplet state. Excited photosynthesiser and oxygen forms a loosely bound weak couple both in triplet state. They then through internal conversion path form their respective singlet states. This process of a weakly coupled complex changing spins from triplet to singlet is termed triplet fusion, $^1[^3PS + ^3O_2] \rightarrow ^1[^1PS + ^1O_2]$ (**Figure 2-1A**).[223] PS-O_2 stabilises at the lowest energy compared to the high energy singlet sigma state and triplet state. This reaction follows a Marcus trend where ^1PS and $^1O_2$ form two coupled parabolic states.[201] We can picture these parabolas as sheets in PS internal reaction coordinate R and D (intramolecular vector for PS-O_2) (**Figure 2-3**). The internal conversion to form $^1O_2$ ($^1\Delta_g$) and $^1\sum_g^+$ will be competing, and overall these internal conversions will be competing with intersystem crossing to form back ^1PS. The rate of the singlet state oxygen generation depends on the reaction direction (where O_2 and PS reacts i.e. above-below plane, in-plane etc. and boosted towards spin density of PS). Barbatti and co-workers computationally showed that $^1\sum_g^+$ formation exceeds $^1\Delta_g$ formation; however, there is still direct $^1\Delta_g$ formation. Still, most of the $^1\Delta_g$ is formed by the activation of $^1\sum_g^+$.[224]

2.2 Characterisation Techniques

2.2.1 On-line Mass Spectrometry

On-line/real time gas analysis monitors the amount of gasses evolved and consumed in a system under constant purge gas flowing into a mass spectrometer. Mass spectrometry (MS) is a

very powerful technique to analyse trace amount of compounds by measuring the mass to charge ratio (m/z) of the ionised sample. In this Thesis, a Thermofisher Prima BT process mass spectrometer was used for gas analysis. It is equipped with an electromagnet with a laminated core produces a variable magnetic field that enables rapid and very stable analysis of multiple gases.

Sample gas is carried into the capillary and from the capillary into the ion source with the purge gas. Sample gas is ionised by electron impact and generated ions are injected into a magnetic field. In this magnetic field, ions follow a path/circular orbit of varying radius. The initial velocity, mass and charge of the ion affect the radius (as well as the strength of the magnetic field).

$R^2 = \frac{mV}{H^2 z}$ eq.2 *where R is the radius of the orbit, m is the mass of the particle, V is the voltage applied to accelerate the particle, H is the magnetic field, and z is the charge on the ion*

The detector and the voltage are fixed in the instrument. Thus, the instrument uses:

$m \propto H^2$ eq.3

Mass of the ion arriving at the detector is selected by varying the magnetic field. The signal is proportional to the concentration of the sample ion. The proportionality constant is determined by calibrating the instrument with standard gases. In this work, 1% O_2, 1000 ppm CO_2, and 500 ppm $^{13}CO_2$ in balance Ar was used as the standard calibration gas mixture.

Ionisation is done by passing a focused electron beam generated from a hot filament through the sample gas. This causes electrons to either detach or to adhere to the molecule. When electrons are removed, the sample gas becomes positively charged and only positive ions are used for the analysis. The filament can be thoriated iridium or a tungsten thoria alloy.

Ions leave the source through slits and plates which trim, focus, and steer the ions. For a given magnetic field/magnet current, only ions with a specific m/z ratio reaches the collector (**Figure 2-4**). In this work a Faraday detector is available in the collector assembly. Ions are collected in a light tight Faraday bucket coated with colloidal graphite to reduce emission of secondary electrons. Collected ions result in a current that is then amplified.

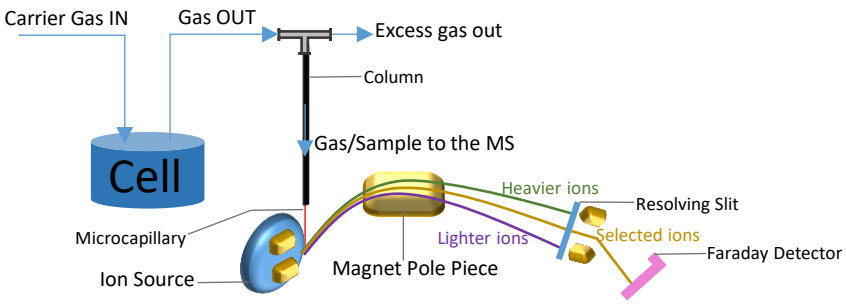

Figure 2-4 *Schematic representation of the on-line MS setup. Ions are separated through the magnetic sector.*

On-line/real time gas analysis is one of the major characterisation methods used in this Thesis. It is a popular method not only for Li-air batteries but also for Li-ion, solid-state batteries etc. For example, CO_2 evolution during charging suggests that there is electrolyte or cathode degradation, and O_2 evolution and consumption for high voltage cathode materials suggests that anionic redox is happening.[225] For Li-O_2 batteries, monitoring O_2 consumption and evolution is very important to understand the Faradaic efficiency of the cell. The ideal e-/O_2 ratio is 2 as Li_2O_2 formation or oxidation is a 2 electron process and consumes or yields one mole of oxygen.[40]

In this Thesis, on-line MS is used to study amount of $^3O_2$ evolved from chemical oxidation of Li_2O_2 with selected RM^+ in Chapter 3, to detect O_2 loss due to reactivity with singlet oxygen ($^1O_2$) in Chapter 4-5, and to study amount of organic carbonates and carboxylates formed on the cathode and Li_2O_2 in Chapter 5.

2.2.1.1 Carbonate analysis

2M H_3PO_4 is injected on the cathodes or Li_2O_2 powders to decompose all present inorganic carbonates to CO_2 i.e. Li_2CO_3 to CO_2.[138] Under very acidic conditions $CO_3^{2-} \leftrightharpoons HCO_3^- \leftrightharpoons CO_2$ equilibrium is pushed fully to the right-hand side. CO_2 is poorly soluble and is purged out into the MS. Acid does not decompose carboxylates in the system.

$$Li_2CO_3 + 2\,H_3PO_4 \rightarrow 2\,Li_3PO_4 + 3\,CO_2 + 3\,H_2O \quad \text{eq.4}$$

2.2.1.2 Carboxylate analysis

Fenton's reagent[226] was used to decompose all organic species (carboxylates, both lithium carboxylates and organic carboxylates) into CO_2. The reaction for Fenton's reagent is $Fe^{2+} + H_2O_2 \rightarrow$

Fe^{3+} + $OH^{\bullet}$ + OH^{-}. The $OH^{\bullet}$ radical attacks electron deficient sites such as –C=O in acetate and formate, and releases CO_2. 0.5M $FeSO_4$ in 2M H_3PO_3 and H_2O_2 (30%) was injected on the cathodes or Li_2O_2 powder after all CO_2 evolution from carbonate analysis ceased. $OH^{\bullet}$ causes CO_2 evolution from carboxylates and headspace/setup is purged until all the CO_2 is purged and a stable MS baseline was achieved.

2.2.1.3 On-line MS or differential electrochemical mass-spectrometry (DEMS)

DEMS refers to in-situ detection of electrochemically generated products. Initially, gasses evolving from an electrochemical reaction were collected in a vacuum system and then transferred to a mass spectrometer. This system was then improved to allow on line detection by using a Teflon membrane between the cell and the mass spectrometer and by using improved vacuum systems. The method was called differential to distinguish it from integrating approaches where there is product sampling.[227] In this Thesis, ex-situ experiments are referred to as on-line mass spectrometry experiments and electrochemistry experiments directly connected to the mass spectrometer are referred to as DEMS experiments. In DEMS experiments, gasses evolving from electrochemical reactions can be detected on-line and the evolved gasses can be matched with relevant electrochemical processes e.g., by determining the time point for start of CO_2 evolution and the charging potential to detect electrolyte degradation.

2.2.2 Nuclear Magnetic Resonance (NMR) Spectroscopy

NMR spectroscopy is a powerful tool to identify structure, determine purity, and quantify phases of chemical compounds by observing the local magnetic fields around nuclei. It can also be used to study properties such as solubility[228] and diffusion.[229] In classical terms, a superconducting magnet generates a constant magnetic field $\overrightarrow{B_0}$ and the nuclear spins (ℓ>0) in the sample align along this field (*z*-axis polarisation). An applied radio frequency pulse (a weaker oscillating magnetic field) perturbs the alignment of the spins in the sample, tipping the spins into the *x*,*y* plane. The oscillating decay away from this field and back to the main magnetic field generates an electrical current. This current is termed a free induction decay (FID) and Fourier transformation of this FID results in an

NMR spectrum. An NMR spectrometer usually consists of a superconducting magnet that generates a powerful magnetic field (1-25 Tesla, T) that samples are placed within, a probe that transmits and receives radio frequency waves, and a console which applies the pulse and processes the received signal.

Spin is a fundamental property of sub atomic particles, and both nuclei and electrons have spin. A nuclear spin is treated as a single entity and a nucleus (proton and neutrons) has an intrinsic angular momentum. Nuclear spin (*I*) for protons and neutrons is ± ½ and is associated with magnetic moment (μ). Magnetic moment is the associated torque due to the angular momentum of the nucleus in a magnetic field.

Table 1 *Possible nuclear spins numbers for nuclei*

Atomic Number (Protons)	Mass Number (Protons and Neutrons)	Nuclear Spin (*I*)	Example
Even or Odd	Odd	$^1/_2, ^3/_2, ^5/_2, \ldots$	*I* (^{1}H) = $^1/_2$
Even	Even	0	*I* (^{12}C) = 0
Odd	Even	$1, 2, 3, \ldots$	*I* (^{2}H) = 1

$\vec{\mu} = \gamma \vec{I}$ eq.5 *where γ is the gyromagnetic ratio of the isotope*

Magnetic moment has no preferred orientation unless there is an applied external field. When there is an external magnetic field $\overrightarrow{B_0}$, nuclei will orientate and nuclear spin states will have different energies and degeneracy of spin states is lost (resulting in Zeeman splitting), **Figure 2-5**. Nuclei such as ^{12}C and ^{16}O have *I* = 0 and no overall spin, nuclei such as ^{2}H and ^{6}Li have integer spins such as 1,2,…and nuclei such as ^{1}H and ^{13}C have *I* = ½- integer spins and have a spherical charge distribution making their NMR behaviour simpler to understand.

Energy is at its maximum when the magnetic moment is antiparallel to the applied magnetic field. At thermal equilibrium, these spin states also have different populations following a Boltzmann distribution. In achievable magnetic fields, the population of lower energy states is

slightly larger than the population of the higher energy states. Low temperatures and strong magnetic fields (1-25 T) increase the population of low energy state spins.

$E = -\vec{\mu}\,\overrightarrow{B_0} = -\gamma\, m_i\, \hbar\, B_0$ eq.6 *where ħ is angular momentum quantum number, m_i is the nuclear spin state, and γ is the gyromagnetic ratio*

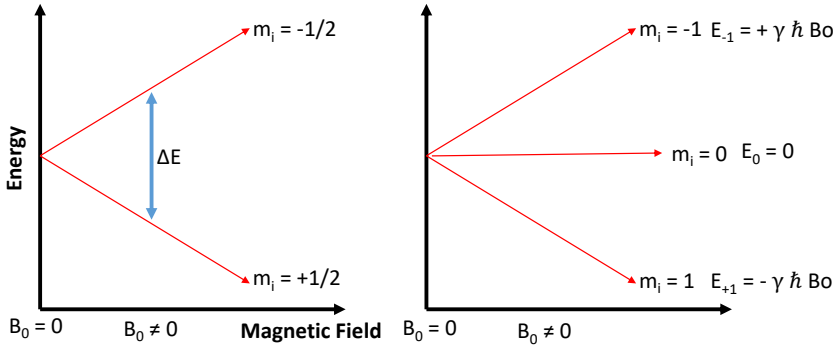

Figure 2-5 *Energy levels as a function of magnetic field showing Zeeman effect causes splitting of degenerate nuclear spin states. Different nuclei will have different values of γ. Angular momentum vectors for L=1/2 and L=1, resulting in 2L+1 vectors.*

In an NMR spectroscopy experiment, transitions between adjacent nuclear spin energy states are induced and the resulting energy difference can be expressed using the Larmor equation. The induced energy difference is proportional to frequency (ν) in MHz and this can also be expressed as angular frequency (ω) in rad sec^{-1}. The angular frequency of NMR transition is called the Larmor frequency and follows the equation (**Figure 2-6**)

$\omega_0 = \gamma\, B_0$ eq.7

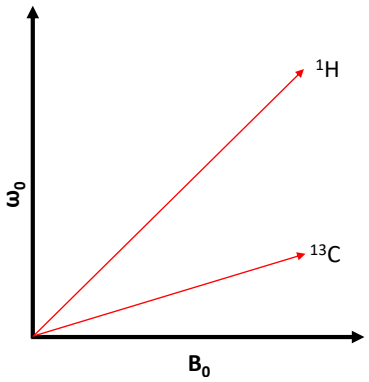

Figure 2-6 *Precession frequency depends on the gyromagnetic ratio and the magnet strength.*

When the sample is irradiated with a radio frequency pulse which is close to Larmor frequency, nuclear spins will be perturbed from the equilibrium position. The RF energy will tip the

magnetisation vector ($\vec{M}$) and Larmor precession can be observed. The RF pulse is generated via a solenoid coil of wire and lies perpendicular to the applied magnetic field $\overrightarrow{B_0}$. This generates the rotating magnetic field $\overrightarrow{B_1}$ that tips the magnetisation vector (**Figure 2-7**). The magnetisation vector does a spiral motion rotation about and away from the *z*-axis. The vector magnetization tips away from the main magnetic field (z-axis) into the transverse plane (*x,y* plane). Finally, the nuclei in the higher energy state will relax back to the thermodynamic equilibrium. This process is called spin-lattice relaxation, T_1, return of the spins back to the main magnetic field. The decay of the spin out of the transverse plane is called spin-spin relaxation, T_2. Usually T_1 is longer than T_2, and T_2* (T_2 + magnetic field inhomogeneities) determines the linewidth of the NMR resonance, and practically T_2* is the decay time of the NMR signal (FID).

A nucleus is surrounded by electrons which also produce a magnetic field, $\overrightarrow{B_{ind}}$ that reduces the energy difference. This is called shielding and chemical environments with more electron density will cause more shielding. This in turn will result in lower Larmor frequencies. Practically, chemical shift (δ/ppm) is used to define the resonant frequency change of a nucleus measure relative to a reference compound and is equal to $\left(\nu_{sample} - \nu_{reference} / \nu_{reference}\right) \times 10^6$.

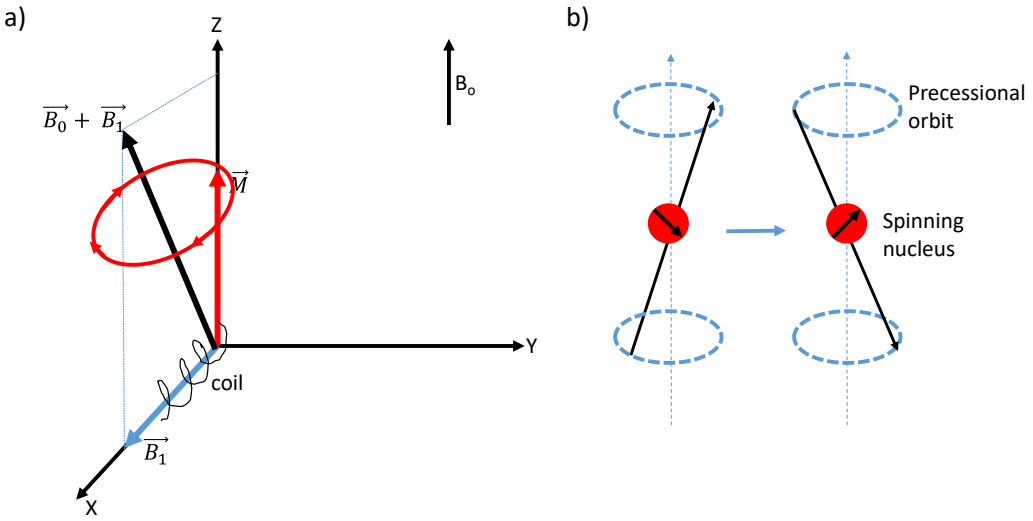

Figure 2-7 *a) Precession of the magnetisation vector if the B_1 field was stationary rather than rotating. For a rotating B_1 vector, the magnetisation vector follows a spiral motion a spherical surface. b) Applied magnetic field exerts a torque on the magnetic moment of the nucleus and the axis of rotation precesses around the magnetic field.*

In this Thesis, ^{1}H NMR analysis was employed quantify the singlet oxygen trap, DMA, and its derivatives in Chapter 3 and study the electrolyte-cathode decomposition products either by directly using the electrolyte as the sample or by washing the electrode with D_2O in Chapter5. In experiments where LiTFSI was used as the salt, ^{19}F NMR was used to study by-products as well. Additionally in Chapter 5, natural abundance ^{17}O NMR was used to study degradation products in the tetraglyme solvent. Experiments were either performed on a Bruker AVIII 400 (υ_0 (^{1}H) = 400.17 MHz with 5 mm z-gradient broadband multinuclear probe) spectrometer or on a Bruker AVIII 600 (υ_0 (^{1}H) = 600.13 MHz, with a proton-optimised TCI HCN cryoprobe) spectrometer.

2.2.2.1 Two-dimensional NMR Spectroscopy

Heteronuclear Single Quantum Coherence (HSQC)

HSQC is a 2D NMR experiment that shows proton-heteronucleus one bond correlations via ^{1}J-coupling interactions between nuclei.[230] The experiment is widely used for ^{1}H—^{13}C correlations but can also be used for ^{1}H—^{15}N and ^{1}H—^{31}P systems. Magnetisation is transferred from proton to the heteronucleus and back to the proton (**Figure 2-8**). The spectra is 2D where one axis (F2, x-axis) is for the proton and the other axis (F1, y-axis) is for the heteronucleus. The cross peaks show the shift of each proton attached to the specified heterenucleus.

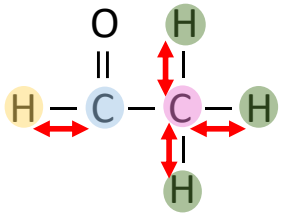

Figure 2-8 *^{1}H—^{13}C correlations for acetaldehyde. HSQC spectrum for acetaldehyde would show two peaks.*

Heteronuclear Multiple Bond Correlation (HMBC)

HMBC utilises multiple-bond couplings and gives correlations between protons and hetereonuclear atoms that are separated by two or more bonds (**Figure 2-9**). Direct one bond correlations are suppressed and usually not observed. 3-Bond correlations are expected to be stronger than 2-bond correlations.

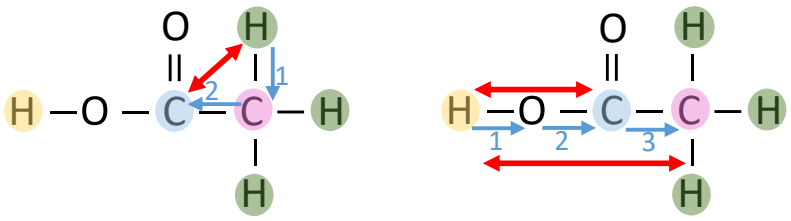

Figure 2-9 *2-bond and 3-bond correlations for $^{1}H—^{13}C$ in acetic acid which would appear in HMBC spectra.*

Total Correlation Spectroscopy (TOCSY)

TOCSY shows correlations between all bonded protons in an entire spin system. An entire chain of protons in which each is coupled to the next is displayed. Magnetisation is transferred over 5-6 bonds given successive protons are coupled, i.e. if there are heteroatoms such as oxygen, the transfer would be interrupted. In **Figure 2-10**, 3 peaks in a row marked with a yellow line shows that there are three C containing groups in a chain where protons are coupled.

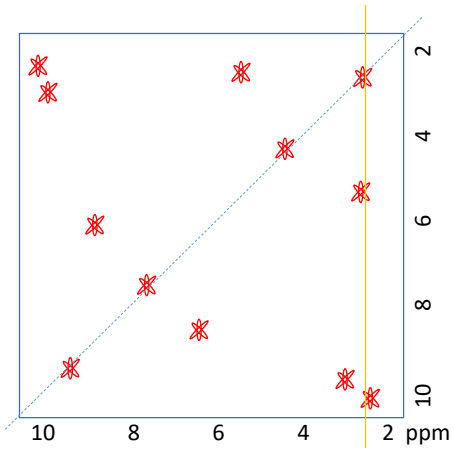

Figure 2-10 *Schematic representation of a TOCSSY spectra. The peaks outside the diagonal show proton correlations. Three peaks in a row show that there is a three-carbon chain.*

2.2.2.2 Cross-Polarisation with Magic-Angle-Spinning NMR (CP-MAS NMR)

Solid state NMR is used to study the atomic level structure in solids. Due to rapid isotropic molecular tumbling in liquid samples (due to Brownian motion) many of the spin interaction are averaged out, and NMR spectra yield sharp signals. For solids, the lack of Brownian motion means the resolution of the signals is substantially reduced.[231] Magic angle spinning (MAS) is used to reduce these interactions and increase resolution and sensitivity of the technique.[232,233] In this technique the sample is rotated at the magic angle θ_m ~54.74° with respect to the direction of the

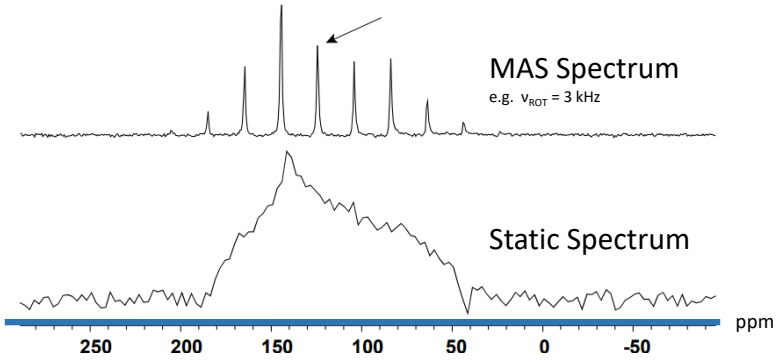

Figure 2-11 *NMR spectra for a solid sample showing broad line shapes for a static measurement and high signal to noise in MAS spectra collected by introducing artificial motions i.e. rotating the sample.*

magnetic field to mimic Brownian motion. Typically, the sample has to be spun at a high enough rate to average out all the interactions i.e. higher rate than largest component of the anisotropy (10s of kHz) (**Figure 2-11**).

Cross-polarisation is coupled to MAS to enhance the signal of a dilute nuclei such as ^{13}C or ^{15}N or to get space information[234,235]. Polarisation is transferred from an abundant nucleus such as ^{1}H to the low abundance nucleus such as ^{13}C. It requires nuclei to be dipolar coupled (through space spin-spin interactions) to one another. Abundant nuclei spins are strongly dipolar coupled and subject to large fluctuating magnetic fields. This results in rapid spin-lattice relaxations. The radio frequency field of the dilute spin is set to that of the abundant spin. Then the dilute nuclei and abundant nuclei precess at the same rate which allows for polarisation transfer.

In this work, CP-MAS is used to study decomposition products in Li_2O_2 samples in Chapter 4. The experiment was run on a HFX Bruker Avance HD 400 MHz spectrometer equipped with a 4 mm HFX MAS probe spinning between 8-12 kHz.

2.2.3 UV-Visible Spectroscopy

UV-Vis spectroscopy refers to absorption or reflectance spectroscopy of liquid or solid samples in the ultraviolet and visible range of the electromagnetic spectrum. When excited with ultraviolet and visible light, these samples (chromophores) undergo electronic transitions. The absorbed photon excites an electron in the ground state to the first excited state. Non-bonding (n) or π electrons can interact with light which has energy matching the electronic transition and can

be promoted from highest occupied molecular orbital (HOMO) to lowest unoccupied molecular orbital (LUMO) to anti-bonding molecular orbitals (**Figure 2-12**). Molar absorptivities of n→π* are lower than π → π*. The wavelength (λ) at which the absorption occurs and the degree of absorption (A) are recoded by a spectrophotometer.

Absorption usually follows the Beer-Lambert law:

$A = \varepsilon l c$ eq.8

The absorbance increases as attenuation of the beam increases. Absorbance is proportional to absorptivity (ε), light path length through the sample (l, sample holder, usually 1 cm cuvette) and concentration (c) of the absorbing species. Absorption and transmittance (*T*) are related and follow the equation:

$A = 2 - \log(\%T)$ eq.9

A UV-Vis spectrometer generally consists of a light source, optical elements, sample holder, and a detector (**Figure 2-13**). The light source is usually a deuterium or tungsten lamp. The monochromator usually consists of collimators, mirrors, slits and grating. The detector can be charge-couple devices, photomultiplier tubes, photodiodes or photodiode arrays. Charge-coupled devices and photodiode arrays can measure different wavelengths of light simultaneously.

Practically, UV-Vis is used to analyse liquid samples, because solid samples and suspensions will cause scattering and additional apparatus such as focusing optics are needed. Blank reference samples should be prepared carefully especially if the analysis is done quantitatively. If the sample is a solid dissolved in a solvent such as acetone, the UV-Vis cut-off of the solvent, i.e. below which the solvent absorbs all the light, should be considered. For example acetone has a cut-off ~329 nm

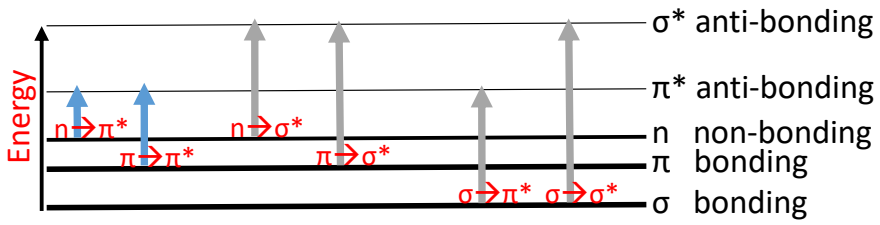

Figure 2-12 *Schematic representation of possible electronic transitions. The first two transitions shown with blue arrows are the only transitions occur in the UV-Vis region.*

and the sample peaks around this region should be investigated using a different solvent. The sample should not be too dilute or too concentrated. The electronic interactions between molecules at high concentrations removes the linearity of Beer-Lambert law.

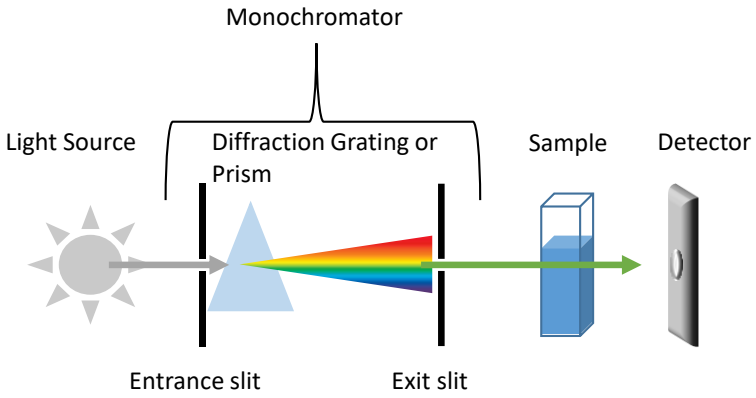

Figure 2-13 *Schematic representation of a single beam monochromatic UV-Vis spectrophotometer.*

In this Thesis, UV-Vis spectroscopy was performed on a Thermo Scientific Evolution 220 UV-Vis spectrophotometer equipped with a Xe flash lamp as the source and a silicon photodiode as the detector. It was used to study DMA to $DMAO_2$ conversion, detect the absorption peaks for the photosynthesisers, and investigate the stability of redox mediators and Li_2O_2.

2.2.4 Fourier Transform Infra-Red (FTIR) Spectroscopy

FTIR spectroscopy studies absorption of IR radiation to determine functional groups and structures and to identify organic and inorganic compounds. Functional groups in a molecule will absorb IR radiation at certain wavelengths and these groups usually have characteristic regions in the spectrum referred to as fingerprint regions (<1500 cm^{-1}) that makes identification easier. Functional groups are usually seen >1500 cm^{-1} and help the full identification of the molecule. Wavenumber is usually presented in cm^{-1}, and it is the spatial frequency equal to 1/ λ.

Energy of transitions in a molecule increase in the following order: electronic (energy of excited electronic configuration) > vibrational (oscillatory motion of atoms within a molecule) > rotational (kinetic energy associated with rotational motion of molecules). It is explained in the previous section that UV-Vis radiation causes electronic transitions. IR light has longer wavelength and lower energy than UV-Vis light. Thus, it can only cause rotational and vibrational transitions. A

quantised energy absorbed by the molecule causes it to undergo a rotational or vibrational transition. Absorption only occurs at resonant frequencies. The movement of the molecule changes and it is raised to a higher internal energy level. The absorption is recorded and interferogram is collected which is then Fourier transformed into a spectrum. For a molecule to be IR active, a change in the dipole moment should be observed. Linear molecules have 3N-5 degrees of vibrational modes and non-linear molecules have 3N-6 modes where N is number of atoms. These modes are symmetric or antisymmetric scissoring, rocking, stretching etc.

Near-IR excites overtone (excitation to the second excited state) or combination (simultaneous excitation) modes of molecular vibrations. Mid-IR shows fundamental vibrations and rotational-vibrational structure, and far-IR excites low frequency vibrations and can be used for rotational spectroscopy and to study stretching and bending of bonds between metal atoms and ligands.

Main components of an FTIR spectrometer are a source, interferometer, sample stage, detector, amplifier, and a converter (**Figure 2-14**). The Michelson interferometer with one stationary and one movable mirror is one of the core parts of an FTIR spectrometer that periodically transmits or blocks each wavelength in the beam. This means that at each mirror position, the beam coming from the interferometer has a different spectrum. It is prevalent to use an attenuated total reflection (ATR) accessory as the sample stage as it requires no sample preparation. The beam coming from the interferometer passes and reflects through the crystal and penetrates into the sample (evanescent wave) during this process. The penetration depth depends on the sample and is usually 0.5 to 2 µm. The exiting beam is then collected at the detector. Light absorption at each mirror position is recorded. The path difference resulting from the movement of the mirror is measured via a laser. Fourier transform converts the displacement in the mirror (cm) into wavenumbers (cm^{-1}).

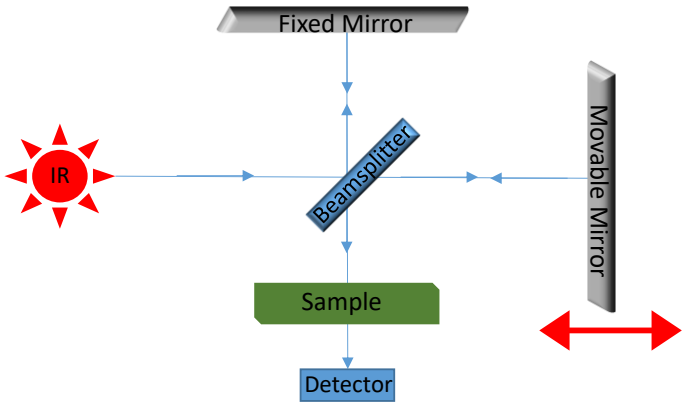

Figure 2-14 *Schematic representation of an FTIR spectrometer.*

Even though FTIR spectroscopy is considered as one of the most powerful materials characterisation methods, detection of trace components in heterogeneous samples is challenging. The sensitivity of FTIR spectroscopy can be limited by weak infrared absorption of the components overlap of major components band with the trace material bands. In such cases where trace material signal is overwhelmed by the major components, FTIR microscopy can be utilised to map the sample and enhance the spectral signal of the trace component.[236] For example, in this work changes in the tetraglyme samples cannot be detected with FTIR. When 90 mM DMA is dissolved in tetraglyme, DMA peaks are masked by tetraglyme peaks due to its higher absorption, and DMA peaks cannot be observed.

In this Thesis, FTIR spectra are recorded in a N_2-filled glovebox using a Thermo Fischer Nicolet iS50 FTIR Spectrometer equipped with a tungsten-halogen white light source, HeNe laser, CsI beamsplitter, deuterated triglycine sulfate (DTGS) detector, and a diamond ATR stage. CsI beamsplitter is used as Li_2O_2 has abruption below 600 cm^{-1}. In Chapter 4 the side products formed in DMSO upon $^1O_2$ and in Chapter 5 degradation products formed on tetraglyme aged Li_2O_2 were investigated using FTIR.

2.2.5 High-Pressure Liquid Chromatography/UV-Vis-Mass-Spectrometry

High-pressure/high-performance liquid chromatography (HPLC) is used to identify, quantify and separate components of a liquid mixture. It relies on the same principles as basic thin layer chromatography and is an adaptation of column chromatography. Chromatography methods

include a stationary phase and a mobile phase and are based on analysing different travel times of the components of the mixture with mobile phase through the stationary phase.

In HPLC, solvent is forced through a column packed with small porous particles (e.g. 5 µm diameter) under high pressure (e.g. 400 atm). The small particle size of the column material provides a high interaction surface area with the analyte, and therefore separation and resolution of the components are better. A few microliters of a sample is introduced to the mobile phase and percolates through the column. The velocity at which each component moves through the column depends on the physical interaction/adsorption of the component onto the stationary phase. The time the component elutes from the column is called the retention time and in simple systems can be used to identify components.

There are two modes of HPLC which are normal and reversed phase. In normal phase HPLC, the mobile phase is non-polar and the stationary phase is the polar silica column. Polar components in the analyte interact more strongly with the polar column compared to the non-polar components and leave the column after non-polar components elute. Reversed phase HPLC is more commonly used than normal phase HPLC and uses a hydrocarbon modified silica column. In reverse phase HPLC, the mobile phase is polar and the stationary phase is a non-polar column. Polar molecules elute through the column first. There are two elution modes which are isocratic and gradient elution. In isocratic elution, the mobile phase composition is kept constant throughout the analysis. In gradient elution, the mobile phase composition changes e.g. the procedure starts with 90% water (A) 10% acetonitrile (B) as the mobile phase and finishes with 10% water (A) and 90% acetonitrile (B) as the mobile phase. This means that mobile phase strength and elution strength change and as the composition of B, usually the strong solvent, increases late-eluting components leave the column faster (**Figure 2-15**). This prevents tailing peaks and makes peak shape easier to analyse for trace components.

The detectors measure different properties of bulk or solute such as refractive index, UV-Vis absorbance, and electric current from redox reactions etc. The most commonly used is a UV-Vis

detector. Selected wavelengths of UV light are shone on the sample exiting the column and absorbed by the sample depending on the composition. When selecting the UV light, the absorption of the mobile phase solvents should be taken into consideration to avoid false readings. The UV absorbance of different compounds will be different, hence the area under absorption peaks for different compounds cannot be directly compared.

HPLC can be coupled to mass spectrometry (LC-MS) to obtain the fragmentation pattern of the analyte at each peak position which further helps identification of unknown compounds, especially if the retention time is unknown. Components separated in the column are transferred into the MS ion source. The sample is transferred from the high pressure column to MS vacuum by methods such as electrospray ionisation (ESI), atmospheric-pressure chemical ionization and atmospheric pressure photoionisation.

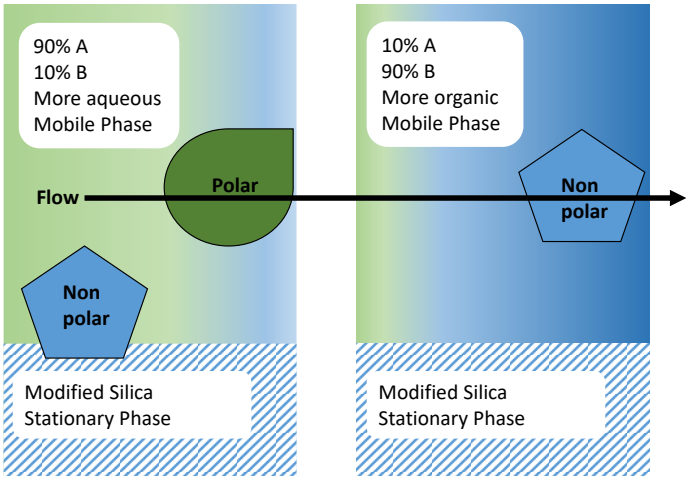

Figure 2-15 *Schematic representation of a gradient elution showing that the elution strength increases.*

In this Thesis, HPLC spectra were recorded on an Agilent 1200 Purification System and a Waters Xevo G2-XS, a bench-top QTOF mass spectrometer with ESI was used to collect the HPLC-MS spectra.

2.2.6 Scanning Electron Microscopy (SEM)

SEM is an electron microscopy technique to image surface topography and sample morphology. It uses electrons which have wavelengths shorter than the photons used in optical microscopy to scan the sample surface. Hence, compared to optical microscopy, its resolution is

not limited by the diffraction limit of light. Although SEM cannot image individual atoms, its resolution ranges between less than 1 nm to 20 nm depending on the instrument.

Electrons are produced at the top of the column at the cathode either by thermal emission (e.g. tungsten filament) or via field emission gun (FEG, brighter and more coherent electrons then thermal emission) under ultra-high vacuum. These electrons are accelerated down the column towards the positively charged anode. The beam of electrons are focused and directed down the column by electromagnetic lenses and coils. Once the electrons (primary electron/radiation) reach the sample surface some of them will be backscattered via elastic scattering interactions and some will interact with the sample at or near the surface inelastically (secondary electrons). The sample surface is scanned in a zig-zag pattern (raster) and electron count at different sites are mapped to produce a brightness contrast image. In this Thesis, the morphology of ^{13}C cathodes were investigated by SEM in Chapter 4.

2.2.7 Powder X-ray Diffraction (PXRD)

Powder X-ray diffraction is one of the main tools used in characterisation of crystalline materials. It is used as a fingerprint technique for phase identification. Quantitative phase analysis of mixtures, sample purity, lattice parameters, residual strain, particle size, and grain orientation can be determined employing this technique.

2.2.7.1 X-ray generation

X-rays (Röntgen rays) are a type of electromagnetic radiation with high energy (~100 eV - 100 keV) and short wavelength (~100 Å - 0.01 Å). Usually soft X-rays (below 5 keV energy) are used as probes for PXRD purposes as their wavelength (~ few Å - 0.1 Å) is comparable to the separation between the planes in crystallite solids.

X-rays are usually either generated by sealed or rotation anode X-ray tubes in laboratories, or by acceleration of electrons in synchrotrons. The metal anode in the X-ray tubes is usually Cu, Fe, Mo, or Cr. The target (anode) is bombarded by a focused electron beam that is generated by Joule heating of a tungsten filament and is accelerated across a high V field. When the anode is

bombarded, a continuous spectrum of X-ray (Bremsstrahlung, white radiation) is emitted and core shell electrons are ejected. The ejection of a core shell electron followed by a free electron filling the shell, generates an X-ray photon of a characteristic energy i.e. the wavelength depends on the anode material (Cu K_α = 1.5418 Å) (**Figure 2-16**). The generated X-ray beam consists of several wavelengths ($K_{\alpha1}$, $K_{\alpha2}$, K_β, and sometimes W L $_{\alpha1}$ from filament contamination)[b] and is not monochromatic. However, most of these wavelengths can be removed by optics, and $K_{\alpha1}$ and $K_{\alpha2}$ heavily overlap at low 2θ.

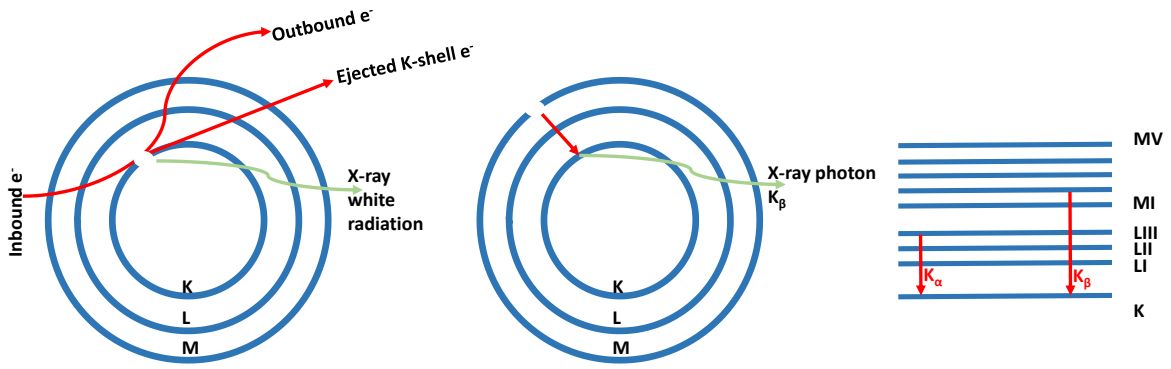

Figure 2-16 *Schematic diagram of X-ray production showing white radiation (Bremsstahlung) and characteristic X-ray (K_β) production.L to K transitions are called K_α and M to K transitions are called K_β lines.*

2.2.7.2 Diffraction pattern

When X-rays hit a powder sample with randomly oriented crystallites, they are scattered in a sphere around the sample (Ewald sphere) and each single 2θ angle creates a Debye-Scherer cone along the sphere. These concentric cones on a 2D plane forms the Debye-Scherrer rings. Bragg's law is used to calculate the angle where constructive interference occurs and a diffraction peak is observed (**Figure 2-17A**). Experimentally, it is used to find the spacing between crystallographic planes, d.

$n\lambda = 2d_{hkl}\sin\theta$ eq.10 *where n is the diffraction order, d is distance between crystallographic planes and d_{hkl} is the vector from unit cell origin to the hkl plane drawn at 90°*

[b] Siegbahn notation is used to name the spectral lines e.g. $K_{\alpha1}$. $K_{\alpha1}$ is $K\text{-}L_3$ according to IUPAC notation. It is common to denote photoelectron lines by either the final-state level or by the orbital notation, i.e. K or 1s.

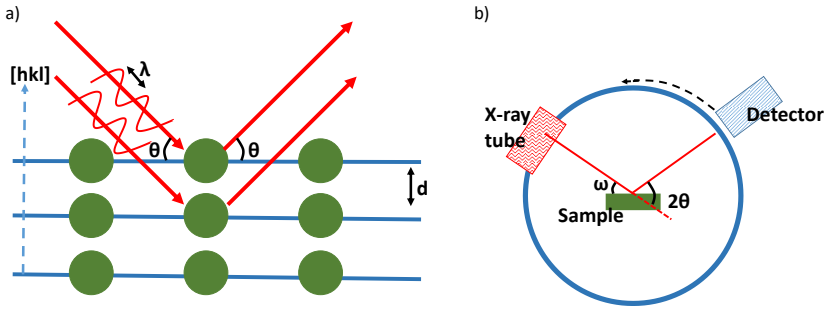

Figure 2-17 *Schematic representation of X-ray diffraction and constructive interference. b) Configuration of a modern X-ray diffractometer*

Modern X-ray powder diffractometers use Bragg-Bretano geometry where the detector moves through an arc relative to the X-ray tube and incident angle (ω) is kept constant at ½ of the detector angle (2θ) (**Figure 2-17** b). The diffraction vector is always normal to the surface of the sample.

The diffraction pattern for every crystal structure and phase is unique. Hence, PXRD is a fingerprint technique where an unknown sample's diffractogram can be compared to the reference patterns in digital libraries such as Inorganic Crystal Structure Database (ICSD) or Powder Diffraction File (PDF). The identification can be a simple comparison or could require Rietveld refinement (a method that uses least squares approach until the theoretical profile matches the experimental pattern).

Small amount of crystallites contribute to the actual observed diffraction pattern. To ease this, sample can be spun and sample preparation can be optimised to avoid preferred orientation. A small amount of the scattered X-ray is captured by the detector (a 2D detector can be used) and individual planes cannot be resolved unless it is single crystal diffraction. Practically, high electron density regions i.e. heavier elements scatter more and have higher intensities, it becomes difficult to differentiate between neighbouring elements and light elements scatter weakly.

In this Thesis, PXRD was utilised to study the purity of in house synthesised Li_2O_2 (by fingerprinting) and common side products such as lithium formate, lithium acetate, and lithium hydroxide were measured.

2.2.8 Basic Principles of Electrochemistry

2.2.8.1 Definitions, thermodynamics and potential

The secondary (rechargeable) battery is an electrochemical system where chemical energy is converted into electrical energy and vice versa. The energy change for the reaction is the change in the Gibbs free energy. The driving force for the chemical reaction depends on the thermodynamic properties of the electrodes. Electrons have a preference to be at one of the electrodes due to the voltage difference and this drives the current. The reaction usually occurs at the electrode-electrolyte interface and the rate depends on kinetic parameters. Finally, additional to reactions kinetics and electron transfer, mass transport also affects the overall process. Mass is transported through the electrolyte to bring the reactants to the electrode surface. [237]

For a reversible redox reaction the chemical equation is

$Ox + ne^- \rightleftharpoons Red$ (e.g. $Li^+ + e^- \rightleftharpoons Li$, a half-cell reaction) eq.11

The quantitative relationship between rates of the reactants and electrical charge or current is governed by the **Faraday's law**

$m = \frac{Q}{F}\frac{MW}{n}$ or $m = \frac{MW}{n}\frac{It}{F}$ eq.12 *where m is the mass of the species produced and Q is total electric charge (F is the Faraday constant, n is the number of e-, MW is the molecular weight)*

The chemical thermodynamic relationship is governed by the Nernst equation.

$\mu_i = \mu_i^\theta + RT\, ln a_i$ eq.13 *where μ is chemical potential and a is chemical activity*

$a = \gamma C$ *eq. 14 where γ is activity coefficient and C is concentration*

$Q_r = \frac{a^{red}}{a^{ox}}$ *eq.15 where Q_r is the reaction quotient (ion activity product)*

$\Delta G = -nFE$ *eq. 16 where ΔG is Gibbs free energy and E is the equilibrium/open-circuit potential*

There is no current flow at open-circuit potential (OCP). OCP depends on the intrinsic nature of the species, their concentration, and the temperature. Although there is no reaction happening, random collisions (movement of ions and thermal collisions of reactant and products causing reactions to occur) still occur that push the reaction either in the forward or backward

direction. The overall rate of the forward and backward reaction is equal at this potential. In a battery

$V_{ocv} = \frac{\mu\ anode - \mu\ cathode}{e}$ eq.17 *where e is the magnitude of the electric charge (in C)*

The reduction potential of a reaction can be calculated using the **Nernst equation**[c] and it can be derived without describing the kinetics.[238] The equation can be written as:

$$E = E^{\theta} - \frac{RT}{nF}\ln(\prod_i a_i)_{oxidation} + \frac{RT}{nf}\ln(\prod_i a_i)_{reduction} \quad \text{eq.18}$$

$$E_{cell} = E^{\theta}_{cell} - \frac{RT}{nF}\ln Q_r \quad \text{eq.19}$$

When we look at the transition state and free energy surface of $Li^{+}_{soln} + e^{-}_{metal} \rightleftharpoons Li_{metal}$ varying with reaction coordinate and solution potential, following the transition-state, we can write

$\ln k = \ln(\frac{k_B T}{h}) - \frac{\Delta G^{\ddagger}}{RT}$ eq.20 *where k is rate constant and k_B is the Boltzmann constant*

The idea behind this equation also holds for heterogeneous rate constants, and only requires a change in the frequency factor.

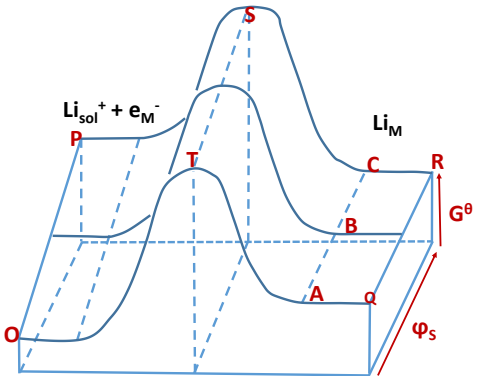

Figure 2-18 *Free energy surface showing change in free energy with ϕ_S and reaction coordinate. ϕ_S is potential of the solution when the electrode is connected to earth C>B>A.[238] OP and QR are free energies of stable states of Li^{+}. TS is important to describe the kinetics as it describes the change in free energy of the transition state with respect to potential difference. The gradient decreases as the surfaces converge i.e. the transition state is less sensitive to changes than Li^{+}.*

Reactant and product both occupy a minimum on the energy surface as they are the only arrangements with significant lifetime. The reaction path that connects these two minima pass through a maximum (transition state) and the height of this maximum is the activation energy.

[c] Another common equation is **Butler-Volmer equation** which relates the rates of electrochemical reactions to the driving force i.e. the surface overpotential. It will not be further discussed in this Thesis.

2.2.8.2 Electrodes

In an electrochemical system the electrode is the electronic conductor and ionic conductor and the electrolyte is the ionic conductor and the electronic insulator. Charge is transported by the movement of electrons and holes through the electrode.[213] In a good electrochemical system, electrodes should have low resistance. The potential difference between electrodes are measured by a potentiostat (a high impedance voltmeter). The measured potential is the potential of the working electrode, and is obtained with respect to the reference electrode. Potential is always defined with respect to a stable and well-defined value.

The working electrode is the electrode where the reaction of interest occurs. Electrochemical cells usually consist of two or three electrodes. In a three-electrode system, the working electrode is used with a counter (auxiliary electrode) and a reference electrode. The counter electrode acts as a cathode when the working electrode acts an anode and vice versa. This means that if there is reduction occurring at the working electrode, an oxidation reaction occurs at the counter electrode. The counter should ideally have high surface area and should not be limiting the rate of the reaction at the working electrode. In a two-electrode cell, the reference is usually set to counter electrode's potential (the electrode has a double function but usually causes potential stability problems). In a three-electrode cell, the counter potential is usually not measured. The reference electrode should have a stable potential with time, temperature and small perturbations in the system. There is no net reaction happening at the reference electrode and there is no passage of current. However, the distance between electrodes affects the electrical noise and it is ideal to place the reference electrode close to the working electrode. Both the reference electrode and the counter electrode can be protected with a porous frit to avoid cross contamination e.g. products forming on the working electrode diffusing to the counter or reference electrode surface. Quasi-reference electrodes such as platinum or silver wire can be used as well. However, they do not have well defined potentials and cause could potential drift throughout the experiment. However, they have low electrical resistance.

There are two types of processes that occur at electrode surfaces; faradaic and non-faradaic. Faradaic processes are governed by Faraday's law which means that electron transfer causes redox reactions and the amount of chemical reaction is proportional to electricity passed. In non-faradaic processes, the electrode-electrolyte interface changes with no charge-transfer, due to processes such as adsorption and desorption. The electrode surface area, electrolyte composition, and the potential could change with external current flow with no charge crossing the interface.

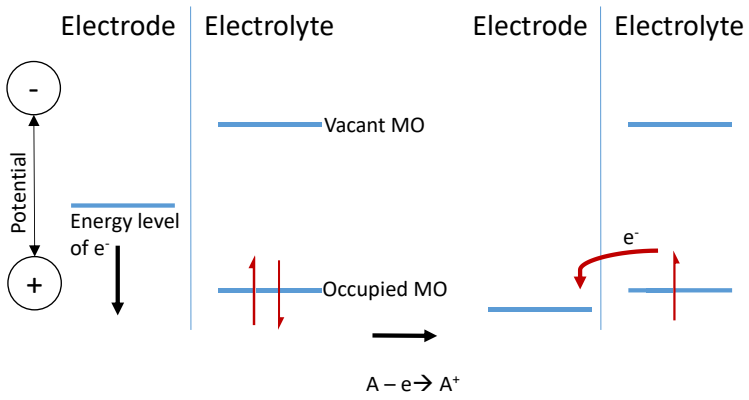

Figure 2-19 *Representation of an oxidation process of a species.*

2.2.8.3 Battery Parameters

Theoretical capacity is the amount of electrical charge that can be stored in a battery. In a battery, either the cathode or the anode will be the limiting factor for the theoretical capacity. For example, in a Li-ion battery, the theoretical capacity will be determined by the cathode material as it is the component that contains Li ions.

A typical Li-based layered transition metal oxide cathode material will undergo the following reaction:

$Li_xTMO_2 \rightleftharpoons Li_{(x-y)}TMO_2 + y\,Li^+ + y\,e^-$ eq.21

The theoretical maximum capacity (Ah g^{-1}) can be calculated using

$$Q = \frac{nF}{3600\ MW}$$ eq.22

Theoretical capacity cannot be achieved due to practical considerations. However, **specific capacity** can be calculated using:

$Q_{sp} = i\ A\frac{t}{m}$ eq.23 *where i is the current density in A cm^{-2}, A is the electrode area in cm^2, t is the time required for full charge or discharge, and m is the mass of the electrode*

Specific energy is also referred to as gravimetric energy density (Wh kg^{-1}) is the energy stored per unit mass and determines the battery weight needed to achieve a given electric range. Theoretical specific energy can be calculated using

$W_{E,theo} = \frac{\Delta G}{\sum_i n_i MW_i}$ eq.24 *where n is the number of moles of the reactant involved in the process MW is that molar mass of the reactant*

Similarly**, energy density** (Wh L^{-1}) determines the battery size needed to achieve a given electric range and can be obtained from the following equation

$W_{d,theo} = \frac{\Delta G}{\sum_i n_i V_i}$ eq.25 *where V is the molar volume of the reactant*

Energy density of a battery is proportional to the specific capacity of the electrode materials and the voltage difference between cathode and anode.

The rate at which a battery is charged or discharged to its maximum capacity is referred to as the C-rate. **C-rate** is inversely proportional to the time (h) it would take to fully charge or discharge the battery. For example. 1C for a 500 mA h capacity battery means that it will discharge at a current of 500 mA and C/2 means it will discharge at a current of 250 mA.

The dis/charge rate is dependent on both ion and electron diffusion as the electroneutrality is maintained within the cell. However, in most cases insertion-removal of ions are the rate limiting factor.

In a practical sense, for example in an electrical vehicle, high charge rate means that one would be able to charge their car in a short period of time and high discharge rates are important for high power applications such as industrial drones and unmanned aerial vehicles. It is important to make sure that battery does not deteriorate in performance at high dis/charge rates.

Cyclability

The practical capacity of a battery fades on cycling mainly because electrode and electrolyte materials degrade. How much of the initial capacity is retained and at what the capacity retention life are important for developing batteries for specific applications. Cyclability is shown by plotting dis/charge capacity (e.g. in mAh g^{-1}) versus cycle number.

Rate capability

Rate capability is similar to cyclability but also includes information about cycling rates. Usually battery is cycled galvanostaticly starting from low C rates and to high C rates and capacity is plotted versus cycle number with rates shown on the plot. Rate capability is important as it shows how fast a battery can be charged and how much power can be extracted and also gives information on cyclability and stability of the electrode and electrolyte materials.

2.2.9 Electrochemical Methods

2.2.9.1 Cyclic Voltammetry

Cyclic voltammetry (CV) is a technique to study both qualitative and quantitative information about electrochemical reactions and redox active species. Some of the main uses of CV are; determining the standard potential of redox couple, reversibility of an electrochemical reaction, heterogeneous charge transfer rate constant, and diffusion coefficients.

A potential range is swept at a fixed rate (V s^{-1}) in forward and backward directions (e.g. from OCV to a positive potential and then to a negative potential) and current response (i) is recorded to obtain a cyclic voltammogram. As a redox reaction occurs, the current increases and a reduction or oxidation peak is observed. To compare planar electrodes with different surface areas (e.g. two Au macrodisc electrodes), current density (j) is plotted instead of current. The peak current is usually studied using Randles-Sevcik equation to assess analyte's adsorption on the electrode surface (or whether it freely diffuses) and to calculate diffusion coefficients.

$i_p = 0.446nFAC(\frac{nFvD_o}{RT})^{1/2}$ eq.26 *where A is electrode surface area, v is scan rate, and D_o is diffusion coefficient*

2.2.9.2 Galvanostatic cycling

In galvanostatic cycling, constant current (e.g. 0.1 mA cm^{-1}) is passed between the working and counter electrode, and potential is recorded as a function of time. This dis/charging is usually done with a set potential cut-off (galvanostatic cycling with potential limitation). The potential can be plotted as a function of capacity to study important cell parameters such as dis/charge overpotential. Theoretically, there should not be an overpotential and discharge and charge curves should coincide. However, factors such as Ohmic losses, resistance in the electrolyte, a double layer forming on the electrode, and the work function of the solid electrolyte interface cause deviation from this ideal scenario But still, in a good practical battery, the dis/charge overpotential would be small (e.g. unmediated Li-O_2 cycling versus redox mediated Li-O_2 cycling). The capacity cut-off is usually given to prevent unwanted reactions happening at very low or high voltages. For example, in Li-O_2 cells, the discharge potential usually ~2.6 V and charge is below ~4.2 V in unmediated cells with tetraglyme electrolyte.

Another way of galvanostatic cycling is setting a capacity cut-off rather than a potential cut-off. This means that once the set discharge capacity is met, the cell will automatically start charging until it reaches the set charge capacity. One of the reason to use this method is to avoid surface passivation and achieve better cyclability.

2.2.9.3 Scanning electrochemical microscopy (SECM)

Scanning electrochemical microscopy (SECM) was developed by Bard[239] and Engstrom[240] research groups to study the current response at the electrode tip as it approaches a substrate. This response depends on the surface properties and the electrochemical activity of the substrate. SECM has been mainly used to do kinetic analysis of homogenous reactions, heterogeneous substrate kinetics, simple redox reactions or complex enzymatic reactions. It can be used in feedback, generation/collection, redox competition, direct and potentiometric modes.[241]

SECM requires the use of a bipotentiostat where both tip/probe and substrate potential are independent working electrodes (WE1 and WE2). The system also includes a counter and a reference electrode. The tip position is monitored and controlled by a piezo controller unit. Ultramicroelectrodes, usually small diameter (a = 1-25 μm) Au or Pt wires sealed in glass (insulating sheet) (radius is r_{glass}) are used as the probe. These electrodes can have disk or spherical geometries. The geometry of the electrode affects the analytical expression used to evaluate the experimentally obtained approach curves. Rg factor is defined as r_{glass}/a, and smaller Rg value means a better or more sensitive electrode. R stands for the radius of insulation sheet. Hence, Rg is the ratio of the radius of the insulating sheath to the radius of the conductive material (r or a).

When the tip is far away from the surface, the current is constant under applied potential. The steady-state tip current, $i_{T,\infty}$, is expressed as:

$i_{T,\infty} = 4nFaDC^*$ eq.27 *where D is the diffusion coefficient and C* is bulk concentration*

For small Rg electrodes the expression can be modified as:

$i_{T,\infty} = 4nFaDC^* \beta(Rg)$ eq.28 *where β (geometric factor) is expressed in various ways and all seems to give good approximations*[242]

One equation for β is[243]

$\beta = 1 + 0.639(1 - \frac{2}{\pi}\cos^{-1}\frac{1}{Rg}) - 0.186\left[1 - (\frac{2}{\pi}\cos^{-1}\frac{1}{Rg})^2\right]$ eq.29

SECM is usually used in the feedback mode for kinetics studies. In such experiments, a redox mediator is rapidly consumed at the tip of the electrode held at a sufficient voltage and as the tip approaches the substrate the mediator is regenerated.[244] The ability of the substrate to regenerate the redox mediator is measured via the tip current. As the tip moves in submicronic distances (L), different current response is observed and an approach curve is obtained.[245] The value of the current response decreases as the tip gets closer to an inert substrate and increases in the case of a conducting substrate. The current-distance feedback curve can be fitted using equations in the literature which yields the dimensionless kinetics parameter, κ.

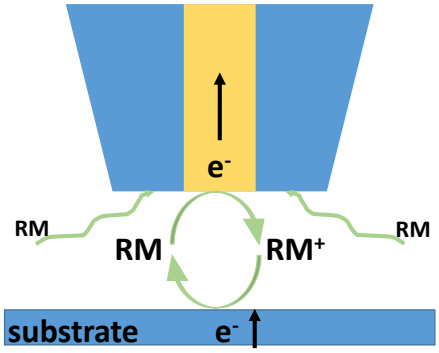

Figure 2-20 *Schematic representation of operation of SECM feedback mode.*

The uncertainty of L_0 (zero tip-substrate distance) can be neglected by good fitting unless κ is very large. Rg has a big influence on negative feedback currents. For small κ values, it is ideal to have larger Rg; however, they are difficult to use especially due to possible not perfectly perpendicular alignment.[244]

A unified expression for negative feedback is proposed by Cornut and Lefrou which has an accuracy of ± 0.01 for all experimentally feasible Rg (<200) and L values.[245] The normalised tip current (tip current / tip current at infinite distance) is expressed as:

$$Ni_T^{ins} = \left[\frac{2.08}{R_g^{0.358}}\left(\mathrm{L} - \frac{0.145}{R_g}\right) + 1.585\right] \left[\frac{2.08}{R_g^{0.358}}\left(L + 0.0023R_g\right) + 1.57 + \frac{lnR_g}{L} + \frac{2}{\pi R_g}\ln\left(1 + \frac{\pi R_g}{2L}\right)\right]^{-1} \quad \text{eq.30}$$

$$Ni_T^{cond} = \alpha(Rg) + \frac{1}{\beta(Rg)}\frac{\pi}{4\tan^{-1}L} + \frac{\left(1-\alpha(Rg)-\frac{1}{2\beta(Rg)}\right)2}{\pi}\tan^{-1}L \quad \text{eq.31}$$

where

$$\alpha(Rg) = ln2 + ln2\left(1 - \frac{2}{\pi}\cos^{-1}\frac{1}{Rg}\right) - ln2\left[1 - \left(\frac{2}{\pi}\cos^{-1}\frac{1}{Rg}\right)^2\right] \quad \text{eq.31}$$

And the general approximation for first order irreversible substrate kinetics is:

$$Ni_T(L, Rg, \kappa) = Ni_T^{cond}\left(L + \frac{1}{\kappa}, Rg\right) + \frac{Ni_T^{ins}(L,Rg) - 1}{(1+2.47\ Rg^{0.31}L\kappa)(1+L^{0.006Rg+0.0113})\kappa^{-0.0236Rg+0.91)}} \quad \text{eq. 33}$$

The fitting of this equation yields κ where

$$\kappa = \frac{\boldsymbol{k_{eff}}*\mathrm{a}}{\mathrm{D}} \quad \text{eq.34}$$

2.2.9.4 Van der Waals Volume

Intrinsic molecular volume of a molecule is usually calculated using the Bondi method.[246] In this method the volume is calculated by summing the volumes of intersecting spheres centred on single atoms. Bond distances, bond angles and intermolecular van der Waals radii are considered in the calculation. This approach is difficult to use for large and complex molecules. There are also software programs calculating intrinsic molecular volumes. However, there is a large deviation in the volume calculated by different softwares. Zhao et al.[246] developed a new method to calculate van der Waals volume based on Bondi radii. This new method is called Atomic and Bond Contributions of van der Waals volume (VABC). The general formula for calculating the van der Waals volume of a molecule is

$$V_{wdW} = \sum \text{all atom contributions} - 5.92N_B - 14.7R_A - 3.8R_{NA} \qquad \text{eq. 35}$$

where N_B is the number of bonds, R_A is the number of aromatic rings, and R_{NA} is the number of nonaromatic rings

and

$$N_B = Total\ number\ of\ atoms - 1 + R_A + R_{NA} \qquad \text{eq.36}$$

Table 2 *Van der Waals volume calculation for N,N,N',N'-tetramethyl-p-phenylenediamine (TMPD) with VABC method based on Bondi principles for N,N,N',N'-tetramethyl-p-phenylenediamine.*

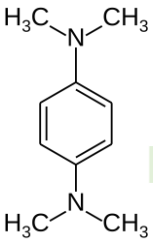

		C	H	N	O	S			
	V_{vdW}-atom (Å³):	20.58	7.24	15.60	14.71	24.43	Ring Aromatic	Ring Non-Aromatic	Volume (Å³)
TMPD		10	16	2	0	0	1	0	172.34

The above formula is used to calculate the van der Waals volume and the formula below is used to calculate the radius of redox mediators.

$$r_{vdW} = \left[\frac{V_{vdW} * 0.75}{\pi}\right]^{1/3} \qquad \text{eq.37}$$

3 Chapter 3 – The Mechanism of Redox Mediated Li_2O_2 Oxidation and Singlet Oxygen Formation

3.1 Introduction

One of the issues in the Li-O_2 battery is the disconnection of Li_2O_2 from the electrode surface. Isolated Li_2O_2 particles in the electrolyte cannot be oxidised until they diffuse back to the electrode surface. This problem leads to cell polarisation and poor round trip efficiency. To improve the utilisation of Li_2O_2 in solution, soluble redox-active molecules known as redox mediators (RMs) can be added to the electrolyte which can oxidise Li_2O_2 particles within the porous cathode that are not in direct contact with the electrode surface. RMs are oxidised at the cathode surface at a lower potential than the thermodynamic potential of O_2/Li_2O_2 (2.96 V). The oxidised RM (denoted RM^+) diffuses to the Li_2O_2 particles, oxidises Li_2O_2 releasing O_2 and reforms the reduced RM. [131,176,183,188,195,247,248] This redox cycle repeats until all the Li_2O_2 is oxidised and charging is complete. As a result of adding RMs, the overpotential is reduced and round trip efficiency is increased. [176,249-251]

However, RMs introduce their own set of challenges. A key problem is selecting a RM with the optimum balance of redox potential and kinetics. RMs with high redox potentials up to +3.9 V (e.g., TEMPO and PPT) have been reported, and tend to lead to fast Li_2O_2 oxidation, but they exhibit poor round trip energy efficiency. [108,188,190,192] In contrast, RMs close to the thermodynamic potential of +2.96 V (e.g., TMPD and DMPZ) are too slow to support even moderate charging rates. [190,192,252] Understanding this relationship between redox potential and kinetics is critical if RMs operating close to the thermodynamic potential of 2.96 V with fast kinetics are to be developed.

Another key challenge is the role of reactive singlet oxygen ($^1O_2$) which is formed in addition to ground triplet state ($^3O_2$) when Li_2O_2 is oxidised. [205,210] $^1O_2$ is a highly reactive species and has been identified as the major cause of the electrolyte and carbon cathode degradation. While high voltage RMs have close to ideal e^-/O_2 ratio compared to low voltage RMs, it is shown that there is

more degradation at high voltages. Then, the question is whether the low voltage RMs are kinetically feasible to use and what the $^1O_2$ generation mechanism is in the mediated charging.

Despite there are numerous studies on charging RMs,[59,108,190,192,195,211,252] still the process of Li_2O_2 oxidation by RMs remains unclear. Kinetics of Li_2O_2 oxidation by SECM (direct kinetics measurement)[108,190] and gas evolution or RM concentration (assuming for order reaction and approximating a kinetic constant)[187,192,212] were investigated, but no unified mechanism was presented. A recent study by Petit et al.[59] also studied the kinetics of redox mediated Li_2O_2 oxidation, but used a UV-Vis method to track the RM concentration instead. They indicated that this reaction follows a Marcus relationship and the kinetics of low voltage RMs should offer high charging rates whereas high voltage RMs will be low rate. They also suggested that the amount of $^1O_2$ formed is minimal at low voltages and high at high voltages. These results do not seem to accord with the trends in literature between redox potential and rate performance, where lower voltage mediators, such as DMPZ and TMPD, are limited to low rate charging, and high voltage mediators such as TEMPO can sustain higher rates.[192,212] It is likely that there are some faults regarding this analysis including the way in which they interpret their UV-Vis spectroscopy and the possible effect of degradation on the rate constants extracted. There are two major parts to both studies, determination of how the kinetics of Li_2O_2 oxidation varies with the redox potential of the molecules and how the evolution of singlet oxygen also varies with redox potential.

In this Chapter, the mechanism of RM mediated Li_2O_2 oxidation and its influence on $^1O_2$ evolution is studied. Analysis of $^1O_2$ and $^3O_2$ evolution also helped establishing the rate determining step for Li_2O_2 oxidation. There are two e^- transfer steps and here it is shown that the initial 1 e^- oxidation of Li_2O_2 to form LiO_2 is the rate liming step and not the subsequent oxidation of LiO_2 to O_2. Furthermore, this Chapter concurrently with Petit's work also shows that the kinetics can be explained by Marcus theory of electron transfer. Contrary to their findings, it shows that low voltage mediators provide lower oxidation rates compared to higher voltage mediators which is in line with the charging behaviour in the literature. It is demonstrated that the mechanism is an outer

sphere single electron transfer. The dominant subsequent step is the disproportionation of LiO_2 to $^3O_2$ and not the 1 e^- oxidation of LiO_2 to triplet or singlet oxygen. This study also shows the $^1O_2$ yield changes depending on the RMs with different potentials and this does not correlate well with degradation. This is an important result casting doubt on whether $^1O_2$ is the major source of degradation during charge.

3.1.1 Marcus Theory

In introductory chemistry, it is usually stated that thermodynamics and kinetics are independent such that a non-spontaneous reaction can proceed faster than a spontaneous reaction.[253] However, this is an oversimplification and the most widely used exception showing thermodynamics and kinetics are not independent is Marcus theory. Marcus theory was first used to explain rates of homogenous outer sphere electron transfers and was then extended to describe inner sphere reactions.[254] Later on, heterogeneous electron transfer (electron transfer at an electrode where the band structure of the metal has to be taken into account) was explained using similar approach by Marcus-Hush-Chidsey theory.[255-257]

Li_2O_2 oxidation with redox mediators is considered a homogenous electron transfer in this work. Marcus theory can be used to describe electron transfer for semiconductor-liquid interfaces. Regarding narrow bandwidth semiconductors, it is easy to picture that only few states of the electrode need to be considered (whereas at a metal electrode exergonity of the reaction can be tuned by applied potential).[201] The theory was also used to explain electron transfer for wide bandgap semiconductors such as ZnO, PtO, and electrooxidation of $LiFePO_4$ where Fe^{2+} is discrete.[258-261] Li_2O_2 is a wide bandgap material with discrete O_2^{2-} ions coordinated by Li^+. The lattice vibrations provide a narrow Gaussian distribution of electronic energies. Hence, following the literature, it is feasible to use Marcus theory in this work.

3.1.1.1 Fundamentals of Marcus Theory

A reaction in solution generally involves diffusion, rearrangement of ionic atmosphere, and solvation change for the transition state steps before atom or electron transfer.[238] Electron transfer

is fast and the time scale for it is of the order of 10^{-16} seconds range, whereas reorientation of the ion atmosphere and solvent dipoles are slower, in the 10^{-8} and 10^{-11} seconds range, respectively. Hence, as the Franck-Condon principle states, there is no time for nuclei to alter positions. In an outer sphere electron transfer the two chemical species are separate before, during and after the electron transfer and a chemical bridge that connects the two species is present for an inner sphere electron transfer. Electron transfer follows Franck-Condon principle; there is no change in nuclear momenta and nuclei appear to be frozen. This means that the transfer happens at or around the intersection of reactant and product parabolas (potential energy curves). The transfer is radiationless and the electron moves from initial state to a receiving state with the same energy.

Free energies of reactants and products depend on the reaction coordinate and form parabolas (**Figure 3-1A**). These are diabatic surfaces i.e. they cross each other unlike adiabatic surfaces. Reorganisation energy (λ) is the energy of the reactant parabola at the minimum of the product parabola.[201] It is the energy required to move the reactants along their potential curve to correspond to the most stable configuration of the products.[253] It is composed of solvational and vibrational components. Reorganisation energy (λ, eq. 1) is a component of the activation energy (ΔG^*, eq. 4):

$$\lambda = \lambda_o + \lambda_i$$ eq.1 *solvational and vibrational (inner) components of the reorganisation energy*

$$\lambda_o = \frac{n^2 e_0^2}{4\pi\epsilon_0}\left(\frac{1}{\epsilon_{op}} - \frac{1}{\epsilon_s}\right)\left(\frac{1}{2a_1} - \frac{1}{2a_2} - \frac{1}{r}\right)$$ eq.2 *where a_1 and a_2 are the radii of the spheres exchanging the e^- and r is the separation between them*

$$\lambda_i = \frac{1}{2}\sum_j (k_j (Q_j^r - Q_j^p)^2$$ eq.3 *where k is the reduced force constant and Q is the normal mode coordinate for the jth mode*

And

$$\Delta G^* = \frac{1}{4\lambda}(\Delta G^\circ + \lambda)^2$$ eq.4

Then the Arrhenius rate constant becomes

$$k_{ET} = A\exp\left(-\frac{(\Delta G^\circ + \lambda)^2}{4\lambda kT}\right)$$ eq.5

The crossing of the parabolas corresponds to the transition state, and as the activation energy decreases the position of the transition state shifts more towards the reactants. The

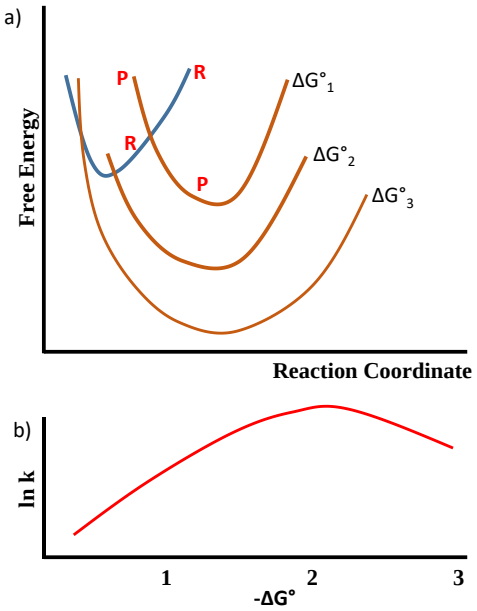

Figure 3-1 *Potential energy curves for an exothermic electron transfer reaction. Marcus theory shows that as the exergonity increases the reaction rate increases up to a certain point and then the reaction slows down again. Hence, the Marcus inverted region is observed. The figure is recreated from Marcus' 1992 Nobel lecture.*

transition state becoming more reactant-like is known as Hammond's postulate.[201] In an atom transfer, the system would normally climb up the barrier between R and P. However, electrons which are ~2000 times lighter than protons will be tunnelling. The system will not go over the barrier and the electron can tunnel through distances up to ~ 1 nm.[238] The reactions are spin allowed (adiabatic).

Marcus theory predicts an inverted regime for ΔG as seen from the above equation. When a reaction is showing increasing exothermic character, it will reach a minimum activation energy; however, as the exothermic character keeps increasing the activation energy will start increasing again. The activation energy virtually vanishes at $\Delta G^\circ = -\lambda$ and increases as ΔG° gets more negative. Marcus termed $-\Delta G^\circ < \lambda$ as the normal region and $-\Delta G^\circ > \lambda$ as the inverted region (**Figure 3-1B**).

Donor and acceptor are weakly coupled and maintain their individuality. The solvation sheath around these molecules is rearranged (**Figure 3-2A**). Dogonadse and Levich showed that the free energy is parabolic upon displacement along the solvent coordinate. One can think that the

solvent undergoes harmonic oscillatons.[238] Hence, the donor, acceptor, and the solvent environment around them can be visualised as shown in **Figure 3-2B**. The reaction coordinate include the solvation/coordination shells and represents the nuclear coordinates of the overall system undergoing the reaction unlike a nuclear coordinate which shows bond distances and angles between reactants.

Marcus theory explains non-adiabatic electron transfer and the possibility of an electron jump. Hence, passage through the intersection of the potential curves play an important role. In **Figure 3-3**, the surfaces on the left show an adiabatic case where the coupling is considerable. There is mixing of the states at the transition state position which causes the splitting of the curves. The gap 2H (H, electronic coupling energy) is large and the system prefers to stay on the lower curve. Nuclear motion is coupled to electron motion. The surfaces on the right show the weak interaction case where 2H is small, there is a certain probability of an electron jump, and the system can go from the initial to the final potential curve. This probability helps to define the pre-exponential A in the rate equation (in Arrhenius rate equation, considering the tunnelling through the barrier and overlap of donor and acceptor wavefunctions).

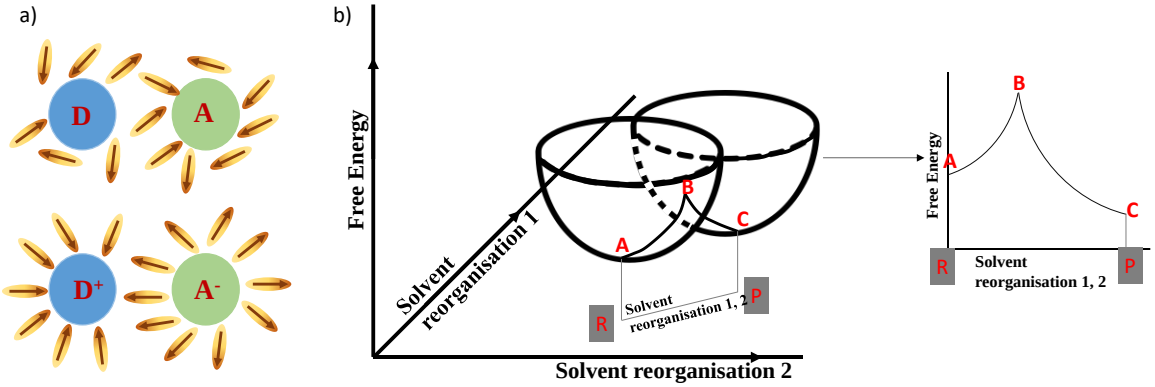

Figure 3-2 *a) Reorganisation of the dipoles/solvent molecules around the donor and acceptor. b) Changes in the solvation energy for electron transfer reactions showing that the barrier is concerned with solvent changes. The electron transfer can only happen at the lowest point where the bowls insect i.e. isoenergetic point.*

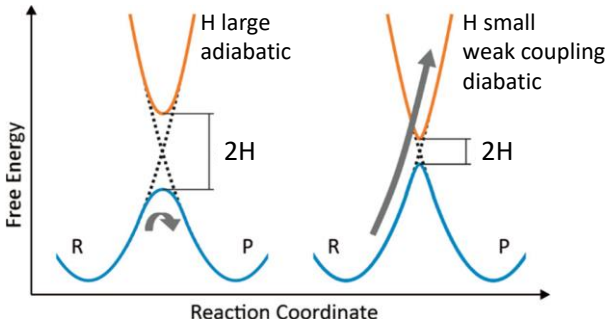

Figure 3-3 *Free energy diagrams for electron transfer showing the splitting of the energy surfaces and the importance of electronic coupling on the electron jump i.e. adiabatic and non-adiabatic cases. H is the electronic coupling energy. Reproduced with permission from ref 201. Copyright 2021, American Chemical Society.*

3.2 Experimental Methods

3.2.1 Materials Preparation

Li_2O_2 (**Figure S1**) and oxidised redox mediators (RM^+) were synthesised following the methods detailed in Section **2.1.5** and **2.1.4**, respectively. Preparation of the electrolyte and delithiated $LiFePO_4$ (LFP) was described in Section **2.1.3** and **2.1.2**, respectively.

3.2.2 Electrochemistry

Electrochemical measurements and electrolyte preparation were conducted in Ar and N_2 gloveboxes. A scanning electrochemical microscopy (SECM) set-up (CH Instruments 920D, CH Instruments) was used with a 12.5 µm Au microdisc working electrode and glass-fritted LFP counter and reference electrodes (3 electrode setup). The Rg factor of the working electrode is estimated by comparing the ratio of steady state currents between the sharpened SECM electrode with an electrode with very large Rg (non-sharpened electrode) (**Figure S2**). Li_2O_2 powder was pressed into 6 mm diameter pellets with a die set at 1 tonne pressure. To find the first order effective rate constant (k_{eff}), the current was measured as a function of electrode-Li_2O_2 pellet distance by moving the working electrode at a rate of 1.5 µm per second. SECM measurements were done by Dr Sunyhik Ahn. The diffusion coefficients of redox mediators were calculated via microdisc steady-state chronoamperometry. Redox potential of RMs (E_{RM}) were estimated by fitting microdisc voltammetry data using DigiElch 4F simulation software.

3.2.3 Marcus Theory Analysis

For λ_{ET} calculation, λ_i is assumed to be significantly smaller than λ_o. as the inner vibrational energy is smaller than ions' reorganisation energy. The solution reorganisation energy for Li^+ is also assumed to be independent of the chosen RM. Hence, λ_{ET} is calculated using the Born solvation model shown in eq.6; e_0 is the electron charge, ϵ_0 is the permittivity of vacuum, ϵ_{op} is the optical dielectric constant of the electrolyte, ϵ_s is the static dielectric constant of the electrolyte, and a is the radius of the RM molecule. The average radius of the RM molecules was estimated by calculating the van der Waals volume following the cited procedure (**Section 2.2.9.4**) and by approximating that RMs have a spherical shape.[246] Dielectric constants of solvents were taken from literature sources (**Table S1**). The variation of λ_{ET} does not change significantly for RMs as the molecular volumes are similar.

$$\lambda_{ET} = \frac{e_0^2}{4\pi\epsilon_0}\left(\frac{1}{\epsilon_{op}} - \frac{1}{\epsilon_s}\right)\frac{1}{2a} \qquad \text{eq.6}$$

3.2.4 On-line Mass Spectrometry

In-house synthesised Li_2O_2 (> 98.5%, determined by $KMnO_4$ titration, see **Section 2.1.6.1**) and RM^+ were weighed into a stoppered vial with a stir bar and a gas inlet and outlet. Inlet/purge gas was argon flowed at a rate of 0.35 mL/min passing to an on-line mass spectrometer to detect the triplet oxygen ($^3O_2$) evolved (**Figure 3-9A**). No oxygen evolution was observed from the mixing of the solid reactants. The reaction was initiated by injection of 9,10-dimethylanthracene (DMA, 30 mM) in tetraglyme (which dissolves the RM^+). DMA reacts rapidly with $^1O_2$ to form 9,10-dimethylanthracene-endoperoxide ($DMAO_2$) in solution. The mixture was stirred throughout the reaction. The amount of $^3O_2$ released was quantified by integrating the on-line mass spectrometry data.

LiO_2 is thermodynamically unstable; therefore, to quantify $^1O_2$ formation during LiO_2 disproportionation, well-established methods starting with KO_2 precursor were followed.[36,148] 1.5 to 15 mg of KO_2 was weighed into a stoppered vial and connected to an on-line mass spectrometer.

1.5 ml of LiTFSI (1 M), crown-6-ether (0.1 M), and DMA (30 mM) in tetraglyme is injected into the vial while rapidly stirring. $^3O_2$ release is quantified with on-line mass spectrometry. Similar to the above Li_2O_2 reaction, any $^1O_2$ is captured by DMA to form $DMAO_2$. The amount of $DMAO_2$ is quantified using HPLC. $^1O_2$ yield is calculated following $^1O_2/(^1O_2+^3O_2)$. The same ratio derived from the KO_2 experiment is applied to calculate the $^1O_2$ amount from LiO_2.

3.2.5 High-Pressure Liquid Chromatography/UV-Vis Spectrometry

In their previous $^1O_2$ work, Freunberger et al.[210] developed a quantification method for $DMAO_2$ by high-performance liquid chromatography (HPLC) with a UV-Vis detector (HPLC/UV-Vis), and since then, using DMA-HPLC became standard method of detecting $^1O_2$ in LOBs. Following the same protocol, $DMAO_2$ was quantified by HPLC with a UV-Vis detector (1200 series, Agilent Technologies), calibrated using $DMAO_2$ solutions of known concentration. The procedure is based on gradient reverse phase elution and the gradient system/mobile phase is acetonitrile (B) and 0.01%formic acid in MilliQ water (A). The elution starts with isocratic 50% B of for 1 minute and then increased to 100 % B in 5 minutes at 0.7 mL min^{-1} mobile phase flow rate. The column temperature is kept at 20 °C. A UV-Vis detector set to monitor 210 nm and 245 nm wavelengths was used to analyse the components. All sample vials were covered with aluminium foil, and amber HPLC vials were used to avoid exposure to light.

Standard $DMAO_2$ solutions were made by exposing DMA solution to $^1O_2$. $^1O_2$ was generated by exciting 5,10,15,20-tetraphenyl-21H,23H-porphine photosensitizer (TPP, < 1% concentration of DMA) with a 660 nm light source whilst bubbling dry $^3O_2$ (N5.0 grade, BOC) into the solution (**Section 2.1.7**). As it is possible for $^1O_2$ to be quenched by other chemical and physical pathways rather than reaction with DMA and as the kinetics of the reaction with DMA are not known, $^1O_2$ amount quantified using this method can only be taken as the minimum amount. The values are not absolute and should be only used to evaluate the trend in $^1O_2$ formation.

3.2.6 Nuclear Magnetic Resonance (NMR) Spectroscopy

$^1O_2$ quantification with the trap DMA was also studied with nuclear magnetic resonance (NMR) spectroscopy (υ_0 = 600.13 MHz, with a proton-optimised TCI HCN cryoprobe). 60 mM DMA in tetraglyme was injected onto a stoppered vial containing an excess in-house synthesised Li_2O_2 and RM^+ (10 mM) whilst stirring. $^3O_2$ evolution was monitored by on-line mass spectrometry, and the solutions were filtered once O_2 evolution ceased to remove any solid residue. The lower detection limit using this high-field NMR experiment with a ^{1}H-optimised cryoprobe and an 18-hour quantitative (T_1 = ~3 s, D_1 = 30 s, $\pi/2$ direct observe experiment) experiment is 2 µM.

3.3 Results and Discussion

3.3.1 Marcus Theory Explains Redox Mediator Kinetics

To investigate the RM mediated charging mechanism (oxidation of Li_2O_2 by RM^+) (eq. 7a), the rate constants for this reaction with various RMs, redox potentials (E_{RM}) between 3.2 - 3.9 V vs. Li^+/Li, were obtained employing scanning electrochemical microscopy (SECM) as shown in **Figure 3-5A**.

$$2RM^+ + Li_2O_2 \leftrightarrows 2RM + O_2 + 2Li^+ \qquad \text{eq.7a}$$

SECM is a technique used to study of electron transfer kinetics for homogeneous and heterogeneous electron transfer processes.[258,262-267] This method accurately models mass transport effects, which can mask true kinetic constants if not taken into account. For example, the rate of stirring affects the reaction rate, and this is problematic for the UV-Vis spectroscopy method employed by Petit et al (**Figure S3**).[59] Moreover, some RMs react with the electrolyte and prolonged measurements affect their oxidative ability (**Figure 3-4**).

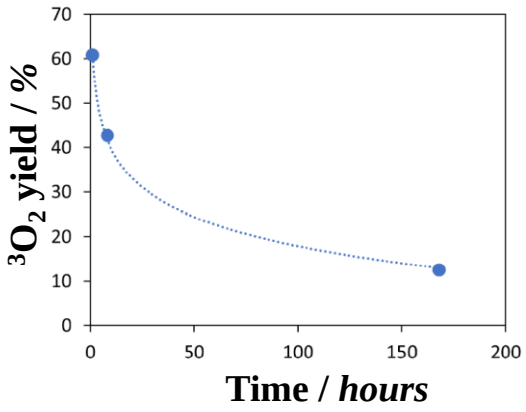

Figure 3-4 *The $^3O_2$ evolution from Li_2O_2 upon oxidation by TEMPO·BF_4 (10 mM) and LiTFSI (0.1 M) in tetraglyme. The TEMPO$^+$ solution was aged for various times before addition of Li_2O_2. This suggests that SECM measurements which take very short time are a better way of tracking kinetics than long spectroscopy methods or indirect gas evolution analysis.*

SECM is employed to quantitatively measure the effective rate constant (k_{eff}) for the reaction of RM^+ with Li_2O_2. This is achieved by bringing the ultramicrodisc electrode (UME) in close proximity to the surface of an Li_2O_2 pellet, and measuring the feedback current from the reaction of RM^+ with Li_2O_2, with subsequent fitting of the current using established methods (shown in **Figure 3-5B** and in **Section 2.2.9.3**).[190,242,268,269] The fitting of the approach curve yields.[242,245,268,269] κ, where $\kappa = \frac{\boldsymbol{k_{eff}} \text{ x a a}}{\text{D}}$, and hence, the rate of the reaction The diffusion coefficients, D, can either be taken from the literature or can be measured from chronoamperometry experiments, as done here, and *a* is the area of the electrode. Hence, the rate of the reaction, only unknown in the equation for κ , k_{eff}, can be determined.

The SECM measurements give an effective rate constant (k_{eff}) for the overall reaction which will be dominated by the rate determining step i.e. k_{eff} is proportional to the rate constant of the rate determining step in the RM mediated Li_2O_2 oxidation (eq. 7b-f). The resulting feedback approach curves for selected RMs in **Figure 3-5B** show that a higher current at low UME-Li_2O_2 distances indicates a higher k_{eff}. Plotting ln k_{eff} of RMs as a function of the thermodynamic driving force (E_{RM}, estimated from cyclic voltammograms shown in **Figure S 2**) results in the volcano shaped plot shown in **Figure 3-5C**. This follows the characteristic volcano shape trend for the rate constant, k_{et}, as predicted in Marcus theory for electron transfer, (), shown in eq. 5 and eq.8. The k_{eff} values

for TMPD and DMPZ could not be measured by SECM as the values are too low. Hence, a pressure monitoring method was used where Li_2O_2 and RM^+ are mixed together in a gas tight cell and the pressure change was measured as a function of time (**Figure S5**).

$2RM^+ + Li_2O_2 \leftrightarrows 2RM + O_2 + 2Li^+$ eq.7a

$RM^+ + Li_2O_2 \leftrightarrows RM + LiO_2 + Li^+$ eq.7b

$RM^+ + LiO_2 \leftrightarrows RM + {}^3O_2 + Li^+$ eq.7c

$RM^+ + LiO_2 \leftrightarrows RM + {}^1O_2 + Li^+$ eq.7d

$2LiO_2 \leftrightarrows Li_2O_2 + {}^3O_2$ eq.7e

$2LiO_2 \leftrightarrows Li_2O_2 + {}^1O_2$ eq.7f

The calculated effective rate constant, k_{eff}, is proportional to k_{et}. According to Marcus theory, k_{et} is determined by the reorganisation energy (λ), the redox potential of the RMs (E_{RM}) and the redox potential of Li_2O_2 or LiO_2 ($E_{Li_xO_2}$). As $E_{Li_xO_2}$ is constant and the variation of λ across different RMs is estimated to be small due to their similar volumes (**Table S 2** and **Section 2.2.9.4**), plotting ln k_{eff} versus the redox potential of RMs (E_{RM}, taken as the average E_{RM}) reveals the agreement between k_{eff} and k_{et}. This agreement implies that the rate determining step for all RMs studied here involve a single outer-sphere electron transfer process.

$$k_{et} = \frac{A}{\lambda^{1/2}} \exp\left[\frac{-[(\lambda - F(E_{RM} - E_{Li_2O_2}))]^2}{4\lambda RT}\right] \quad \text{eq.8}$$

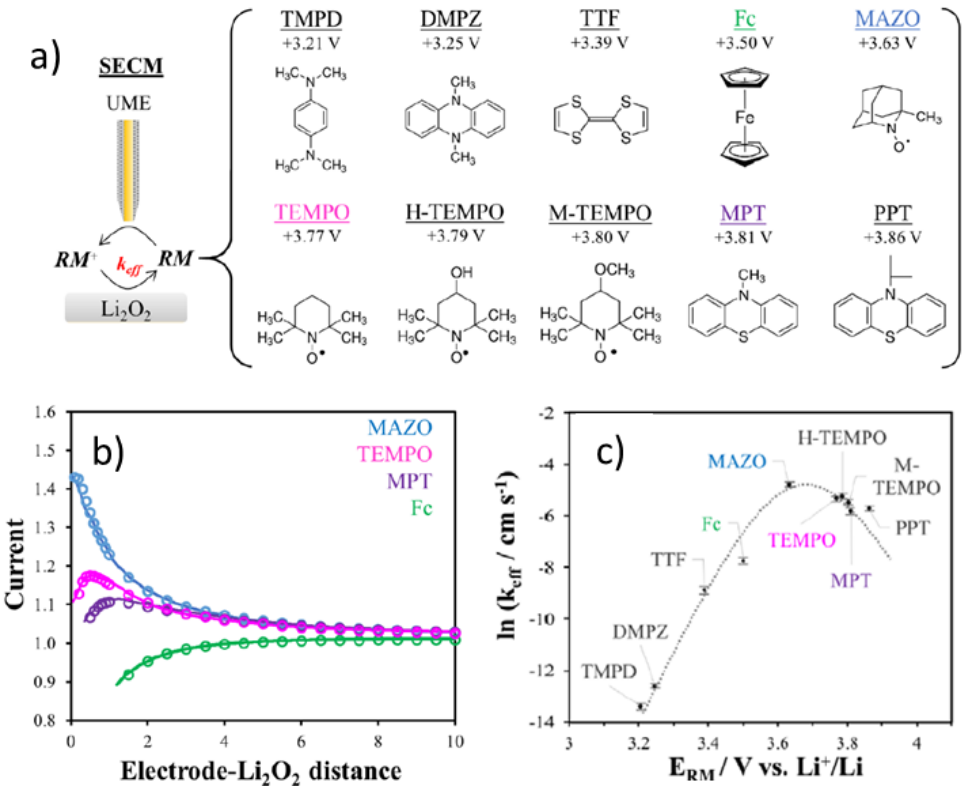

Figure 3-5 *a) A schematic of the scanning electrochemical microscopy (SECM) set-up with an ultramicrodisk electrode (UME) and redox potentials (E_{RM} vs. Li^+/Li) and molecular structures of the redox mediators (RMs). b) SECM approach curves for selected RMs. Lines are experimentally obtained data and circles are model fitting. The axes are dimensionless. The accuracy of the approach curve and the region close to zero distance depends on the radius of the UME which in turn affects κ. κ is more accurately determined in the range of 0.1-1.*[244] *c) Marcus plot of $\ln k_{eff}$ as a function of E_{RM} in 0.1 M LiTFSI in tetraglyme (the points are the experimental data and the dotted line is a guide to visualise the volcano shape).*

3.3.1.1 Modifying the reorganisation energy

To further show that RM mediated charging follows Marcus theory of electron transfer, λ was modified by varying the Li^+ concentration. Electron transfer between the RM^+ and Li_2O_2 is coupled to Li^+ transfer to maintain charge neutrality following the stoichiometry in eq. 7b to 7d. The effect of Li^+ on k_{eff} was studied by varying ratios of Li^+ to TBA^+ while keeping total electrolyte salt concentration constant at 0.4 M. **Figure 3-6A** shows that increasing $[Li^+]$ systematically reduces the k_{eff} of all RMs. This is partially dependent on the change in $E_{Li_2O_2 \rightarrow LiO_2}$. Hence, measuring the change in open circuit potential of Li_2O_2 loaded carbon electrode vs. partially delithiated $LiFePO_4$ reference electrode shows that $E_{Li_2O_2 \rightarrow LiO_2}$ becomes more positive with increasing $[Li^+]$, making Li_2O_2 oxidation thermodynamically more demanding. Plotting the Marcus plots by taking into account the change in $\Delta E (=E_{RM} - E_{Li_2O_2 \rightarrow LiO_2})$ due to electrolyte composition results in Marcus

volcano plots that broaden as a function of increasing [TBA⁺] (**Figure 3-6B**). The broadening of Marcus volcanos is linked to the reorganisation energy (λ).

A major component of λ is the solution reorganisation energy for electron transfer (λ_{ET})

$$\lambda_{ET} = \frac{e_0^2}{4\pi\epsilon_0}\left(\frac{1}{\epsilon_{op}} - \frac{1}{\epsilon_s}\right)\frac{1}{2a} \qquad \text{eq.6}$$

which according to the Born model is proportional to (ε_{op}^{-1} - ε_s^{-1}) where ε_{op} is the optical and ε_s is the static dielectric constant of the electrolyte (eq. 6). It is known from the literature that this sum is greater for glyme solvents containing TBA⁺ salts than alkali metal salts.[270] Hence, electrolytes containing greater TBA⁺ component have a larger λ which leads to the broadening of Marcus volcano plots in **Figure 3-6B**. The peak of the Marcus plots where $\Delta E = \lambda$ also shift towards the right hand side with increasing λ as predicted by predicted Marcus theory (eq.8). TBA⁺ electrolytes having higher λ explains why they enable Li_2O_2 oxidation with higher k_{eff} compared to Li^+ rich electrolyte. These results show that kinetics of Li_2O_2 oxidation are a function of both RM thermodynamics and solvent dynamics, and can be consistently explained under the framework of Marcus theory.

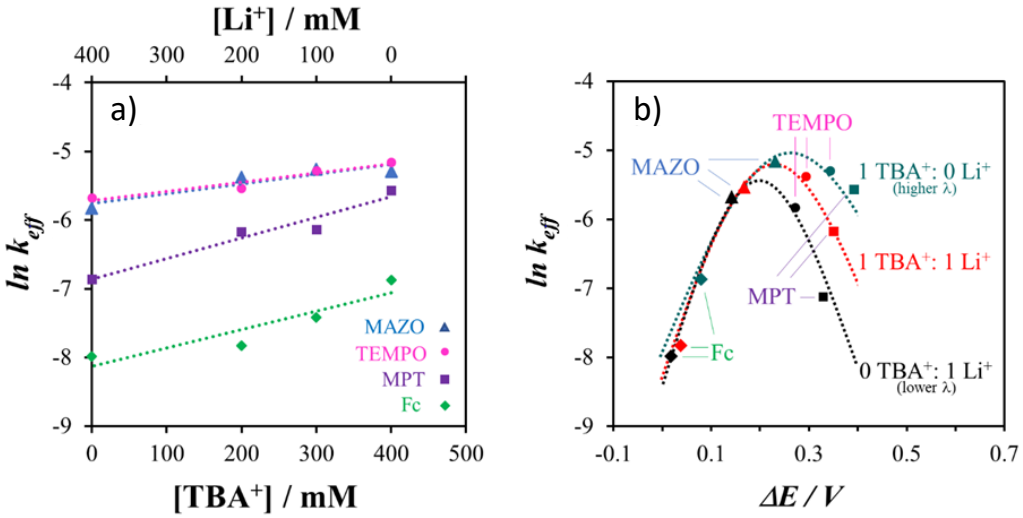

Figure 3-6 *a) Plot of k_{eff} (of RM^+ reaction with Li_2O_2) as a function of [Li^+] (with $TFSI^-$), total concentration of electrolyte is made up to 0.4 M with TBATFSI in tetraglyme. b) Same data as a) shown as Marcus plots with varying ratios of TBA^+:Li^+, $\Delta E_o = E_{RM} - E_{Li_2O_2 \rightarrow LiO_2}$, the dotted lines are a guide for the eye.*

It is suggested here that mediated charging follows Marcus theory and an outer sphere 1-e⁻ transfer is the rate limiting step. Before moving to determining which one of the e- transfer steps

(eq.7b or 7c+d) is the rate limiting one, it is important to compare the trend obtained here with literature data. The trend of rate vs. RM^+ potential in this Thesis is in accord with the known behaviour of LOBs with RMs. The data in this study agrees with kinetic studies by Ko et al., [192] and with the trend of O_2 evolution from mediated cells by Kwak et al.[212] as shown in **Figure 3-7**. They differ from the recently published results by Petit et al., [59] also shown in the same figure. In particular, there is a big contrast in DMPZ and TEMPO results obtained by the different authors. To further validate the trend here, pressure monitoring was used to measured O_2 evolution during Li_2O_2 oxidation by $TEMPOBF_4$ and $DMPZBF_4$ (similar to determining k_{eff} for TMPD and DMPZ as mentioned above) as shown in **Figure S8**. The pressure measurements show much faster O_2 release with TEMPO compared to DMPZ, in contrast to the results of Petit et al. [59]

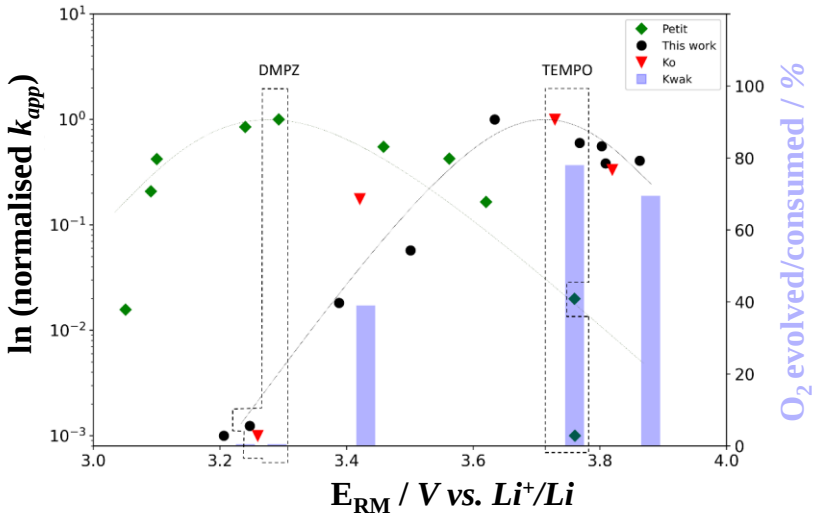

Figure 3-7 *Normalised rate constants (k_{app}) for the RM mediated Li_2O_2 determined by different studies[59,192] and the O_2 evolution during cycling of mediated cells by Kwak (purple bars).[212] The redox potentials of RMs are shown in the x-axis, with DMPZ and TEMPO highlighted for all studies by dashed boxes. The plots show that the results of this work are in accord with those published previously. This can be easily appreciated when comparing the results within the boxes.*

3.3.2 Singlet Oxygen Evolution and the Rate Determining Step for RM^+ Oxidation

Oxidation of Li_2O_2 first forms LiO_2 (eq. 7b), which then evolves O_2 as $^3O_2$ or $^1O_2$ by two pathways: second electron transfer/oxidation of LiO_2 by RM^+ (eq. 7c and 7d) and chemical LiO_2 disproportionation (eq. 7e and 7f). Theoretically, Li_2O_2 oxidation should lead to a charge to oxygen ratio (e^-/O_2) of 2. However, it has been shown for both unmediated and mediated charging that

this ratio is often greater than 2 which points the existence of parasitic side reactions.[101,154,271] Since the first detection of reactive $^1O_2$ in LOBs, such parasitic chemistries have been attributed to the reactivity of the electrolyte and/or carbon cathode towards $^1O_2$. The charging voltage also has been shown to impact the $^1O_2$ yield.[59,205,210] Following these literature findings, the amount of $^1O_2$ was used as a tool to identify the rate determining step. The $^1O_2$ yields were quantified by mixing Li_2O_2 with in-house synthesised RM^+ in tetraglyme to avoid contributions from direct electrode oxidation of Li_2O_2 and LiO_2 (**Figure 3-9A**). In addition, $^1O_2$ yield for chemical disproportionation of LiO_2 was quantified by mixing KO_2 with Li^+ and 6-crown ether containing tetraglyme solution. Upon addition of KO_2, LiO_2 forms then spontaneously disproportionates following eq. 7e and 7f.[36,148] This reaction offers the closest replacement to that occurring in LOBs and has been used widely in the field, although it is important to note that it cannot fully replicate this reaction.

The amount of $^3O_2$ was quantified using on-line mass spectrometry and $^1O_2$ by capturing it in solution using DMA[210] to form $DMAO_2$, which is then quantified using HPLC/UV-Vis (**Figure 3-8** and **Figure 3-9**). The $^1O_2$-RM potential trend obtained by HPLC/Uv-Vis was further confirmed by NMR spectroscopy experiments which will be discussed later in this Chapter. $^1O_2$ yield is expressed as a percentage of the total amount of $^3O_2$ and $^1O_2$ and plotted as a function of E_{RM} in **Figure 3-9B**. UV-Vis measurements of DMA/$DMAO_2$ mixture show that they remain stable at room temperature for at least 62 hours when stored this way (**Figure 3-8**). All DMA solutions were tested by on-line mass spectrometry, HPLC and NMR within this period.

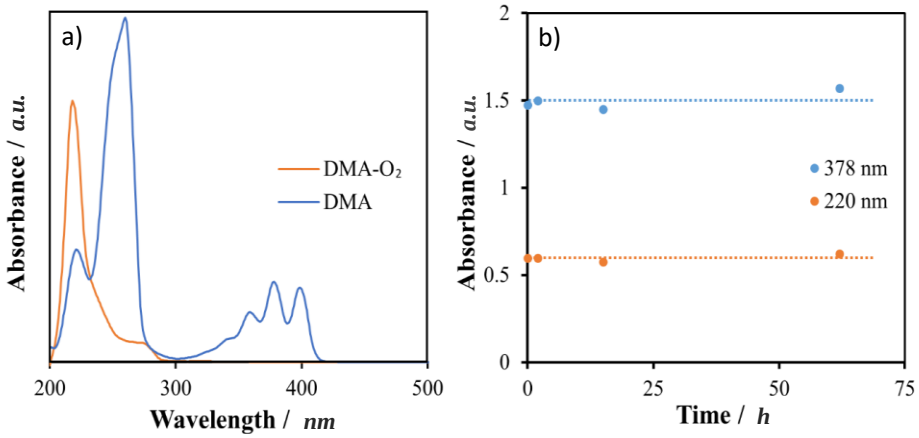

Figure 3-8 *a) The UV-Vis spectrum of DMA and DMA-O_2. b) Absorbance of DMA (at 378 nm) and DMA-O_2 (at 220 nm) mixture as a function of time show that they are stable for at least 62 hours.*

The yield of $^1O_2$ quantified using DMA is likely a lower bound estimate as it does not account for physical quenching of $^1O_2$ and the kinetics of trapping reaction. Also, it does not account for any side reactions that $^1O_2$ can be quenched in. The yield of $^1O_2$ quantified this way is independent of the rate of $^1O_2$ generation and the concentration of redox mediators present (**Figure 3-10**).

$$\frac{d[\,^1O_2\,]}{dt} = k_{p,1}[electrolyte][\,^1O_2\,] + k_{p,2}[DMA][\,^1O_2\,] + k_{p,3}[RM][\,^1O_2\,] + k_{c,1}[electrolyte][\,^1O_2\,] + k_{c,2}[DMA][\,^1O_2\,] + k_{c,3}[RM][\,^1O_2\,] \quad \text{eq.7}$$

$$= (k_{p,1} + k_{c,1})[electrolyte][\,^1O_2\,] + (k_{p,2} + k_{c,2})[DMA][\,^1O_2\,] + (k_{p,3} + k_{c,3})[RM][\,^1O_2\,]$$

$$^1O_2\ trapping\ efficiency = \frac{k_{c,2}[DMA]}{(k_{p,1}+k_{c,1})[electrolyte]+(k_{p,2}+k_{c,2})[DMA]+(k_{p,3}+k_{c,3})[RM]} \quad \text{eq.8}$$

The yield of $^1O_2$ quantified this way is independent of the rate of $^1O_2$ generation and the concentration of redox mediators present (**Figure 3-10**).

This implies that

$$(k_{p,1} + k_{c,1})[electrolyte] + (k_{p,2} + k_{c,2})[DMA] \gg (k_{p,3} + k_{c,3})[RM] \quad \text{eq.9}$$

Hence, the quenching of $^1O_2$ by redox mediators is not appreciable under the conditions used in this Chapter. Therefore, the $^1O_2$ trapping efficiency of DMA is constant for all the electrolyte compositions used here.

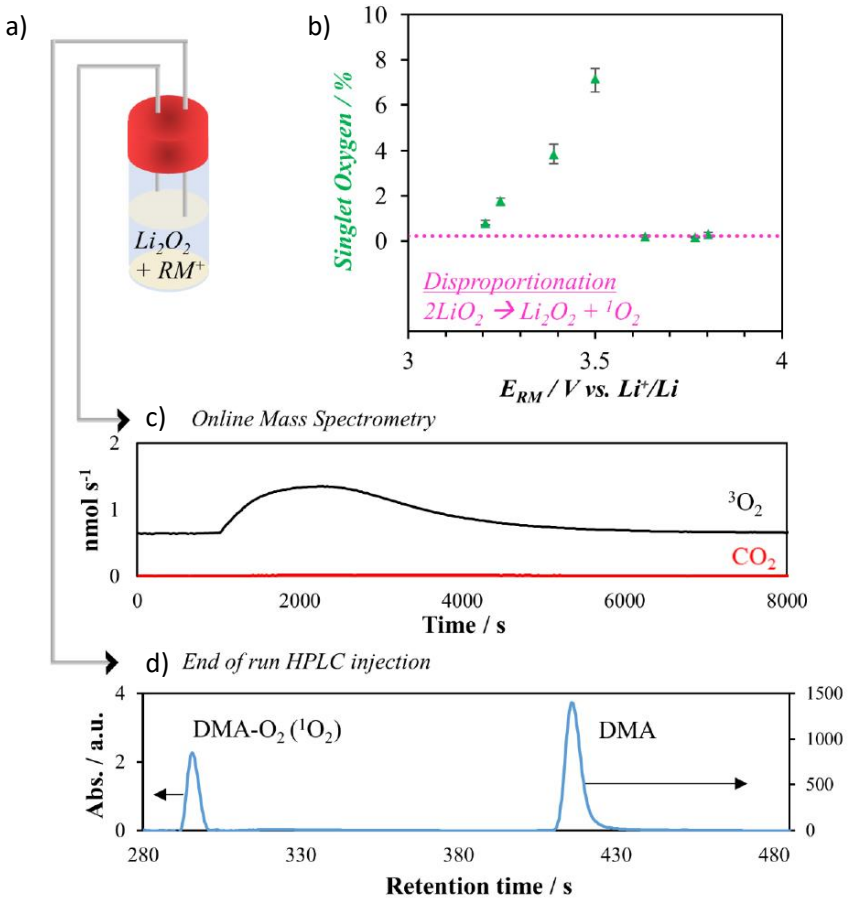

Figure 3-9 *a) A schematic representation of the setup to determine $^1O_2$ yield from oxidation of Li_2O_2 by RM^+. b) $^1O_2$ yield (% of $^1O_2$ /($^1O_2$ + $^3O_2$)) from different RMs as a function of E_{RM} and comparison with that from LiO_2 disproportionation (dotted line). See* ***Table S2*** *for tabulated values. c) Example of on-line mass spectrometry of gases released ($^3O_2$ in black and CO_2 in red) in this case from $TEMPO^+$ reaction with Li_2O_2. d) HPLC spectra for the completed reaction in C). The solution contains DMA, which reacts with $^1O_2$ to form $DMAO_2$, which is then detected by HPLC.*

Small amounts of CO_2 was also detected when RMs with redox potentials < 3.5 V were mixed with Li_2O_2 in tetraglyme. Li_2CO_3 oxidation is reported to evolve 100% $^1O_2$ following the stoichiometry in eq. 10.[209] The relative contribution of $^1O_2$ from Li_2CO_3 was estimated by conducting a separate experiment where RM^+ was mixed with dried Li_2CO_3 power in tetraglyme and quantifying the CO_2, $^3O_2$ and $^1O_2$ evolved. There was no $^3O_2$ detected, and the amount of $^1O_2$ evolved implied that 3.4% (±2) of CO_2 estimated to have come from Li_2CO_3 oxidation for all RMs tested, with remaining 96.6% coming from RM^+ reaction with the solvent. The values presented have estimate of $^1O_2$ contribution from Li_2CO_3 removed, the absolute % of singlet oxygen yield subtracted are 0.02% for MAZO, 0.01% for TEMPO, and 0.05% for M-TEMPO.

$$2Li_2CO_3 \rightarrow 4Li^+ + 4\,e^- + 2CO_2 + {}^1O_2 \qquad \text{eq. 10}$$

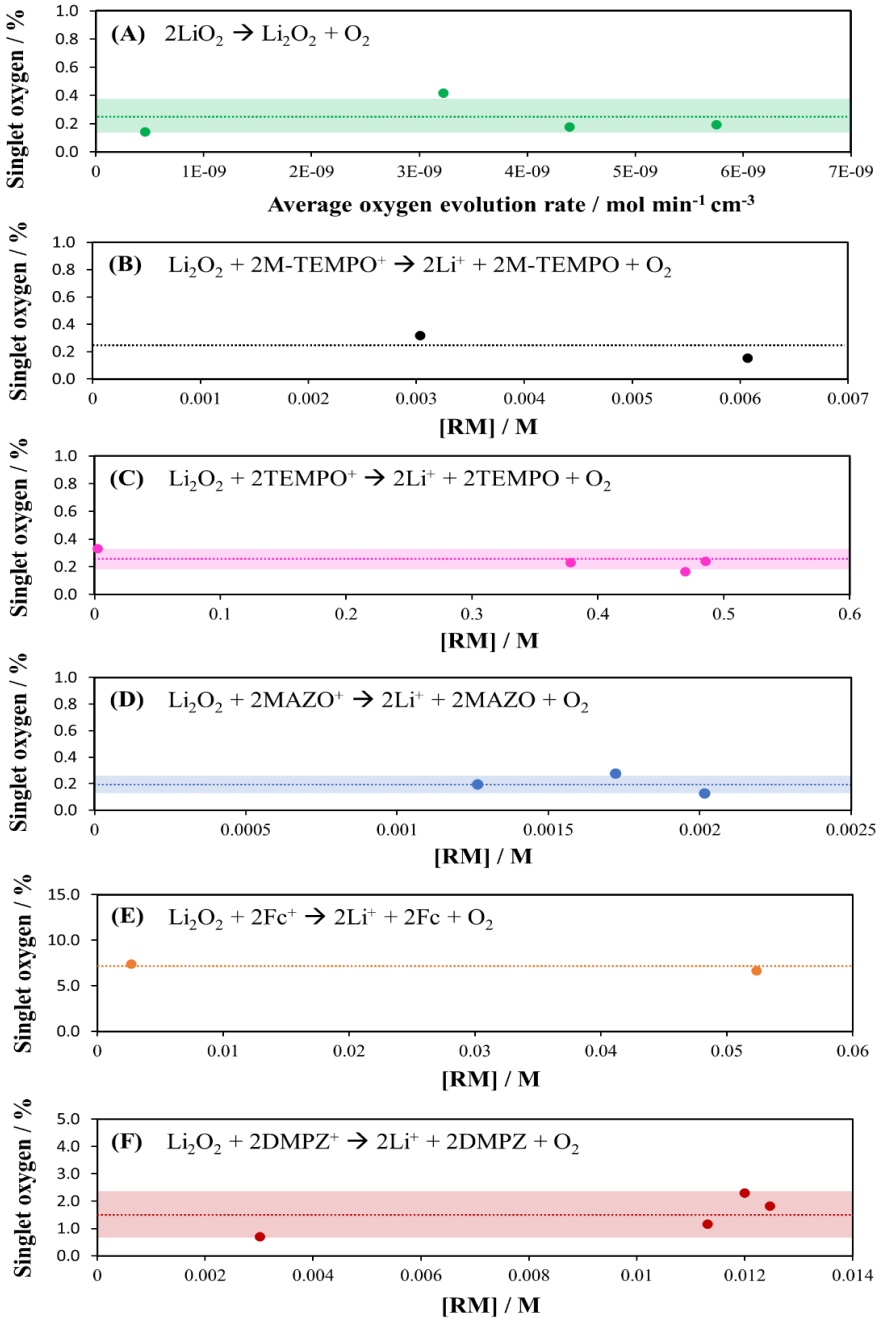

Figure 3-10 *Yields of singlet oxygen a) as a function of average oxygen evolution rate for LiO_2 disproportionation, b-f) as a function of total RM^+ concentration for M-TEMPO, TEMPO, MAZO, Fc, and DMPZ. Dots represents experimental values and dotted line is the average. The shaded areas show ±1 standard deviation.*

Higher $^1O_2$ yield is found for lower voltage RMs (3.2 - 3.5 V vs. Li^+/Li) whereas RMs with formal potentials > 3.6 V evolve a yield of $^1O_2$ that coincides with the yield from chemical disproportionation (**Figure 3-9B**). Turning to identifying the rate limiting step, this $^1O_2$ trend can be explained by considering the kinetics of individual electron transfer steps and using Marcus theory. It is shown in the previous section that the rate determining step for Li_2O_2 oxidation is either the

first or second 1-e^- oxidation, i.e., either $Li_2O_2 \rightarrow LiO_2$ or $LiO_2 \rightarrow {}^1O_2$ or ${}^3O_2$. In **Figure 3-9B**, the ${}^1O_2$ evolved in excess of that from LiO_2 disproportionation must originate from the second electron transfer i.e. LiO_2 oxidation to form ${}^1O_2$ (eq. 7f). Comparing the trend for k_{eff} in **Figure 3-5** with the trend for the ${}^1O_2$ evolution in **Figure 3-9**, it is unambiguous that the rate limiting step is not $LiO_2 \rightarrow Li^+ + {}^1O_2 + e^-$, since the potential of the maximum rate of Li_2O_2 oxidation, does not correspond to the highest proportion of ${}^1O_2$. Indeed, at the maximum k_{eff}, ${}^1O_2$ is formed by disproportionation alone.

Following a similar logic, it is easy to rule out $LiO_2 \rightarrow Li^+ + {}^3O_2 + e^-$ as the rate determining step, as again the potential of the highest k_{eff} does not correspond to any increase in the fraction of ${}^3O_2$ over that observed from disproportionation alone. Hence, the rate limiting step is the first 1-e^- oxidation of Li_2O_2 i.e. $RM^+ + Li_2O_2 \leftrightarrows RM + LiO_2 + Li^+$.

The analysis of the ${}^1O_2$ yields can also elucidate the relative rates of the four potential second step reactions i.e. steps represented by eq. 7c to 7f:

The ${}^1O_2$ yield in **Figure 3-9** shows that the dominant O_2 product is ${}^3O_2$. Hence, the dominant second step forms ${}^3O_2$ not ${}^1O_2$. Then, we can consider the two routes for ${}^3O_2$ formation, disproportionation and $LiO_2 \rightarrow Li^+ + {}^3O_2 + e^-$ (eq. 7c and e). Energetically, ${}^3O_2$ is predicted to be 0.97 eV lower than ${}^1O_2$.[208,272] **Figure 3-9** shows that $LiO_2 \rightarrow Li^+ + {}^1O_2 + e^-$ occurs between 3.2 - 3.5 V, therefore $LiO_2 \rightarrow Li^+ + {}^3O_2 + e^-$ is expected to occur < 2.96 V. This indicates that $LiO_2 \rightarrow Li^+ + {}^3O_2 + e^-$ is already driven far to the right for all potentials at which Li_2O_2 is oxidised. The fact that more ${}^3O_2$ than that from disproportionation is not observed in spite of significant thermodynamic overpotential for $LiO_2 \rightarrow Li^+ + {}^3O_2 + e^-$ suggests that the kinetics of this step is negligible. The overall mechanism is presented in **Figure 3-12**.

3.3.2.1 Further analysis on the rate determining step

Above, it is established that the Marcus plot in **Figure 3-5** is for the first electron transfer from Li_2O_2 to form LiO_2. The kinetics of the second electron transfer step can be projected by assuming that it follows Marcus theory with similar A and λ. The position of the Marcus plot for

$LiO_2 \rightarrow {}^3O_2$ (eq. 7c) relative to $Li_2O_2 \rightarrow LiO_2$ (eq. 7b) is determined by the difference in $E_{Li_2O_2 \rightarrow LiO_2}$ and $E_{LiO_2 \rightarrow O_2}$. This is estimated by taking the computed Gibbs free energy of formation of Li_2O_2 and LiO_2, which results in a gap of 1 V.[273] So the Marcus plot is translated towards the left of the Marcus plot in **Figure 3-5** by 1 V. This is shown in **Figure 3-11** where the Marcus plots are overlaid together with the experimental data for k_{eff} and $^1O_2$ yield.

Figure 3-11 shows that RMs studied in this Chapter have the correct E_{RM} for $Li_2O_2 \rightarrow LiO_2$ (eq. 7b) will exhibit very slow kinetics for $LiO_2 \rightarrow {}^3O_2$ (eq. 7c). The reason that eq. 7c does not then become the rate determining step is because LiO_2 can be consumed by an alternative pathway which is chemical disproportionation. A rapid LiO_2 disproportionation pathway can explain why high voltage RMs evolve $^1O_2$ with a yield that is independent of E_{RM} and is in close agreement with yields from pure chemical disproportionation experiments. This is strong evidence for disproportionation being the kinetically dominant path for oxygen evolution in presence of high voltage RMs. The kinetics of disproportionation must be faster than the kinetics of the RM mediated $Li_2O_2 \rightarrow LiO_2$ step such that this first electron transfer step becomes the rate determining process for the overall reaction resulting in the observation of the Marcus plot in **Figure 3-5**.

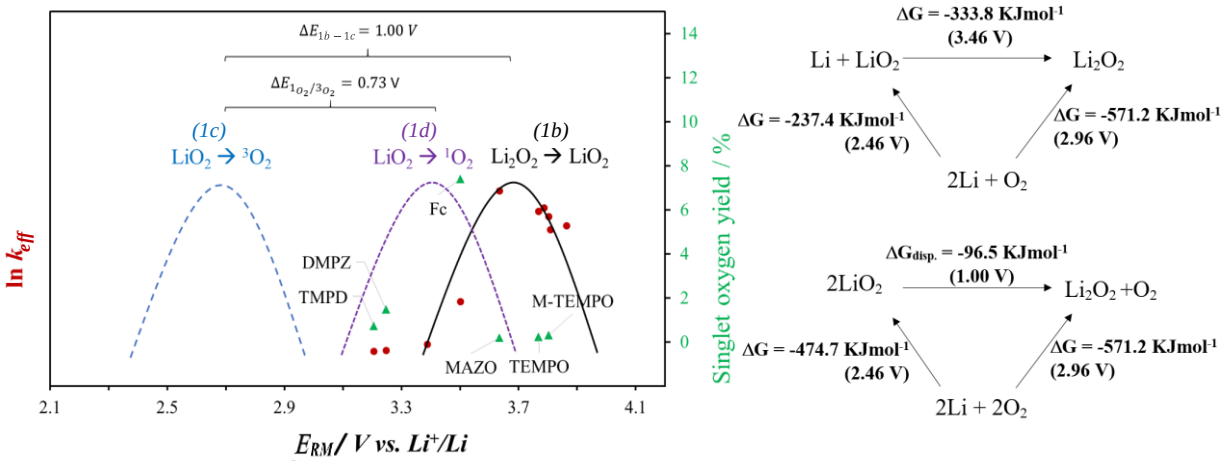

Figure 3-11 . *Experimental k_{eff} from SECM experiments (red circles, left y-axis) with overlaid singlet oxygen yield data for redox mediators (green triangles, right y-axis). The ΔG values for RMs are adjusted to represent $Li_2O_2 \rightarrow LiO_2$ process instead of the overall $Li_2O_2 \rightarrow O_2$ process. The solid inverse parabola is the fitted Marcus plot for experiments and the dotted parabolas are projections assuming the same Marcus trend but separated by the difference in energy cost (J mol^{-1}) calculated using computational thermodynamic data for LiO_2 and $^1O_2$ from literature. [208,273,274] Gibbs free energy diagrams from DFT calculations of Li_2O_2 and LiO_2.[273,275]*

There is a third electrochemical path where LiO_2 is oxidised into $^1O_2$. The energy difference between this path and the $^3O_2$ path is simply the difference between $^1O_2$ and $^3O_2$ which is estimated to be +0.73-0.78 V in 4G.[208,272] This value is a reasonable estimate, as it correctly predicts the evolution of $^1O_2$ from disproportionation. The Gibbs free energy of disproportionation is equal to the energy difference between eq. 7b and eq. 7c which is 1 V, this is sufficient energy for $^1O_2$ evolution. These thermodynamic values place the Marcus parabola for LiO_2 → $^1O_2$ (eq. 7d) in between the first (eq. 7b) and second (eq. 7c) electron transfer processes. The closeness in thermodynamics between 7b and 7d result in some overlap in the Marcus plots. This shows that low voltage RMs can have appreciable kinetics for the LiO_2 → $^1O_2$ pathway. This explains the higher $^1O_2$ yield from lower voltage RMs, with the trend in $^1O_2$ yield in qualitative agreement with the projected Marcus volcano shape of 7d. Though, from the relatively low yield of $^1O_2$ it is clear that disproportionation still remains the dominant pathway. The overall mechanism of the reaction is summarised in **Figure 3-12**. The model reveals the interplay between Marcus kinetics and $^1O_2$ selectivity, explaining the experimental trends in both kinetics and selectivity.

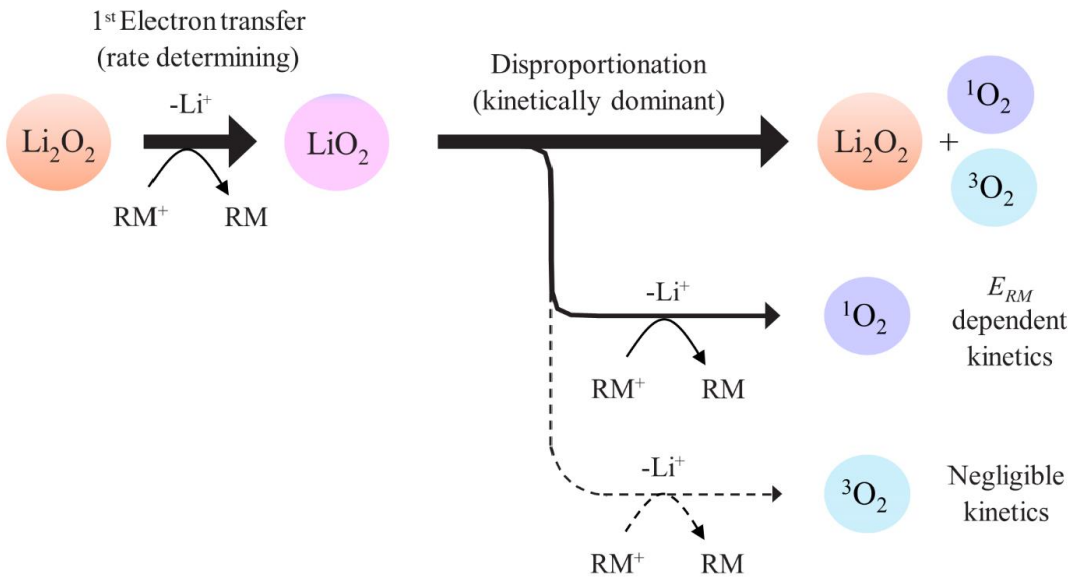

Figure 3-12 *A schematic illustration of the reaction mechanism of RM facilitated Li_2O_2 oxidation. The thicknesses of the arrows correspond to the relative rates of reaction.*

3.3.2.2 Additional NMR analysis

The detection and stability of $DMAO_2$ should be monitored carefully as the side products and environmental changes (such as viscosity, RM^+ interaction with the LC column and $DMAO_2$, pH, and temperature) in the samples could lead to false positive results. Therefore, a variety of analytical methods were coupled to confirm the presence or lack of $^1O_2$ related DMA derivatives, including ^1H NMR which can distinguish protons belonging to DMA from $DMAO_2$ It must be noted that the results of such analyses do not measure the total amount of $^1O_2$ generated as mentioned before.

When subjected to $^1O_2$, DMA forms $DMAO_2$ via dissociative electron-transfer reduction of the O–O bond, yielding a distonic radical anion, it can form $DMA(OH)_2$.[276] The reaction of $^1O_2$ with DMA can be pushed towards $DMA(OH)_2$ by the presence of protons forcing the formation of the more stable hydroxide. This can be detected in the NMR as deshielded aromatic -CH resonances at 8.5 and 7.7 ppm. Thus, here it is found that $DMA(OH)_2$ is a better indicator for $^1O_2$ formation than $DMAO_2$ during NMR studies.

The ^1H NMR spectrum of 10 mM of $TMPD^+$ and 60 mM DMA dissolved in tetraglyme exposed to Li_2O_2 is dominated by the solvent resonances from the tetraglyme (**Figure 3-12A**). However, the aromatic -CH resonances from the DMA appear in an unobstructed region of the spectrum, as shown in the expansion in **Figure 3-12B**. The ^1H NMR spectrum of DMA has been previously assigned (**Figure 3-12C**) with DMA showing two aromatic resonances at 8.0 and 7.2 ppm, representing the two -CH environments on the outer aromatic rings and a CH_3 singlet at 2.8 ppm which is partially obscured by the tetragylme resonances.[210] Ex-situ formation of $DMAO_2$ using the photosynthesiser method outlined in the methods, produced more shielded aromatic peak shifts at 7.1 and 6.9 ppm. The more deshielded resonances observed in **Figure 3-12B** are attributed to $DMA(OH)_2$ with aromatic -CH resonances at 8.5 and 7.7 ppm. The -OH groups are likely to be in exchange, however, the formation of broadened density at 6.5 ppm is consistent with -OH groups neighbouring aromatic systems and a singlet at 1.0 ppm is observed for the methyl groups. The

isolation of these aromatic resonances and lack of obstruction from the neighbouring DMA peaks and their ^{13}C satellites means they can be accurately integrated to determine the concentration of the $DMA(OH)_2$. The lower detection limit using this high-field NMR experiment with a ^1H-optimised cryoprobe and an 18-hour quantitative (T_1 = ~3 s, D_1 = 30 s, $\pi/2$ direct observe experiment) experiment is 2 µM. These experiments show only 0.10% $^1O_2$ in the $TEMPO^+$ samples. In contrast, NMR analysis of low voltage RMs suggests 3.69% and 12.5% $^1O_2$ from Li_2O_2 oxidation by $TMPD^+$ and TTF^+, respectively.

These experiments show only 3.4 µM $DMA(OH)_2$ in the $TEMPO^+$ samples. Petit et al.[59] use 10 mM $TEMPO^+$ in their experiments, as it is done in this study. If Li_2O_2 oxidation with $TEMPO^+$ generates 15 % $^1O_2$ as per Petit et al., it would mean that the authors detect 750 µM $DMAO_2$ using HPLC-UV/vis. HPLC has numerous shortcomings and discrepancies for studying this system, whilst NMR gives discrete peak shifts to form isolated resonances. Turning to low voltage RMs, NMR spectroscopy suggests 3.69 % and 12.5% $^1O_2$ evolution from Li_2O_2 oxidation with $TMPD^+$ and TTF^+, respectively. The total products from reaction of DMA with $^1O_2$ is 93 µM and 429 µM for $TMPD^+$ and TTF^+, respectively, which can be detected via this quantitative ^1H NMR method. The NMR data confirms that low voltage RMs have higher $^1O_2$ formation than that of TEMPO, and follow the trend outlined above.

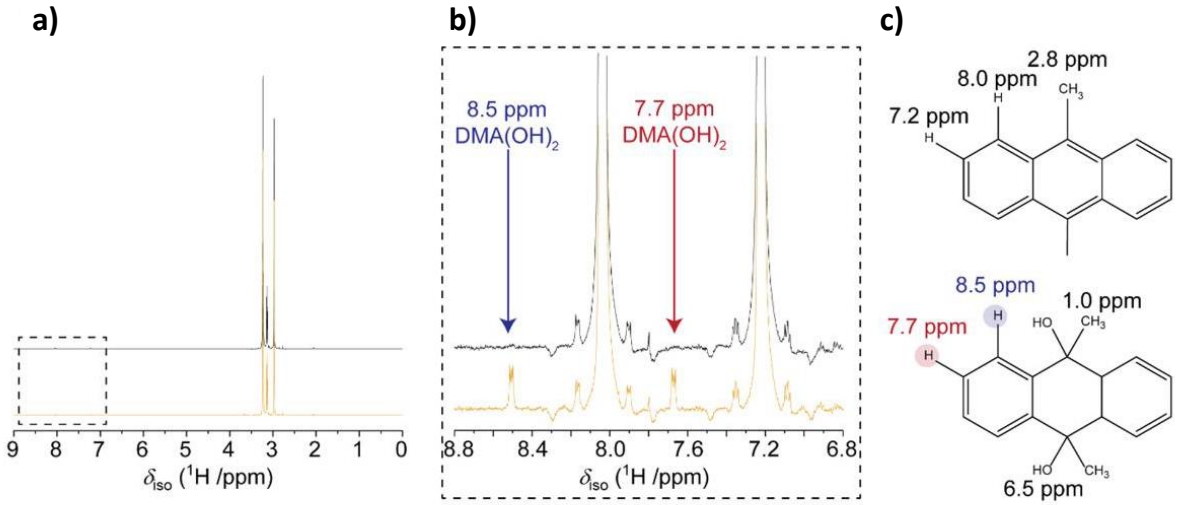

Figure 3-13 *a) ^{1}H NMR spectra of 60 mM stock solution of DMA in tetraglyme (black) and the TMPD$^+$ sample after Li_2O_2 oxdiation (orange). (b) An expansion of the aromatic 6.8 – 8.8 ppm region showing the isolated -CH groups present in the DMA and the formation of new deshielded resonances from DMA(OH)$_2$. (c) Assignment of the resonances for the DMA and DMA(OH)$_2$.*

3.4 Conclusion

Scanning electrochemical microscopy is utilised to study the kinetics of redox mediator facilitated Li_2O_2 oxidation. The findings here explain the kinetics of all reported RMs for charging under a single kinetic framework. A classic Marcus trend is observed, which combined with the dependence of kinetics on thermodynamics of delithiation, points to lithium coupled electron transfer as the kinetic rate determining step. By studying the trend of $^1O_2$ yield as a function of the formal potential of RMs, it is shown that the rate determining step is the outer sphere 1-electron oxidation of Li_2O_2 to form LiO_2. The subsequent reaction (LiO_2 to O_2) is dominated by the disproportionation to $^3O_2$, $2LiO_2 \leftrightarrows Li_2O_2 + {}^3O_2$, and not the 1-e$^-$ oxidation of LiO_2, $RM^+ + LiO_2 \leftrightarrows RM + {}^3O_2 + Li^+$.

Quantifying the $^1O_2$ evolution has not only revealed which electron transfer step is rate limiting, but has also shown how the redox mediator potential affects the amount of $^1O_2$ formed, with lower voltage redox mediators evolving more singlet oxygen than higher voltage ones. The trend in $^1O_2$ with RM potential casts doubt on whether $^1O_2$ is the main source of electrolyte degradation in Li-O_2 cells. The fundamental understanding of the Li_2O_2 oxidation mechanism presented here explains why within the current generation of mediators those that operate at a

low potential and therefore good round trip energy efficiency, <3.2 V, do not deliver high charging rates. The mechanistic understanding also shows how new mediators might be designed to give high rates at low potentials, which is essential if Li-air batteries are to be realised. Alternatively, to completely avoid $^1O_2$ for solution phase charging, a second charge mediator is needed with rapid kinetics for $LiO_2 \rightarrow {}^3O_2$ that kinetically outcompetes both pathways for singlet oxygen formation.

4 Chapter 4 – Chemical Stability towards Singlet Oxygen and Revaluation of Singlet Oxygen in Li-O_2 Literature

4.1 Introduction

One of the main causes of faradaic efficiency loss in LOBs is electrode and electrolyte degradation. After building initial understanding of the reduction and oxidation mechanisms in LOBs, most of the research focused on understanding the causes of degradation or developing more stable cell components. Until recently, Li_2O_2,[277-279] superoxide,[90,280] and reduced oxygen species (ROS) were shown as possible sources of degradation. However, the LOB field does not have one unified answer to the degradation issue. For example, some studies show that Li_2O_2 causes degradation[278] whilst others suggest that Li_2O_2 and ROS are not the main cause of degradation and possible sources could be $^1O_2$ and oxidative stability of glymes.[281,282] In 2016, Wandt et al.[205] reported that they detected singlet oxygen ($^1O_2$) upon oxidising Li_2O_2. From this $^1O_2$ was named as the culprit of degradation in LOBs,[210] meaning the research focus shifted towards detecting and eliminating $^1O_2$. Currently there is little doubt about the origin and reactivity of this singlet state high-energy molecule in LOBs. Even though researchers seemed to decrease the amount of degradation using $^1O_2$ traps, LOBs still did not achieve the desired faradaic efficiency. A recent review paper on $^1O_2$ in LOBs casts doubt on the LOB-$^1O_2$ literature by pointing out theoretical evidence on electron transfer and spin conservation and false positive results obtained in similar $^1O_2$ systems.[201] The previous Chapter shows that $^1O_2$ release is the lowest with redox mediators E_{RM} >3.6V, but it is well-known that most of the parasitic chemistry happens above 3.6 V.[101,102] This also casts doubt on whether $^1O_2$ is the main source of electrolyte degradation in LOBs.

This project aims to understand any effect from $^1O_2$ on the LOB components by generating this reactive species in excess amount in-situ generated excess amounts of this reactive species. Large amounts of degradation was anticipated due to the reports in the literature. The $^1O_2$ experiments were completed under both chemical (Chapter 4) and electrochemical (Chapter 5) conditions. Here, in Chapter 4, it is shown that tetraglyme, one of the most commonly used LOB

solvents, does not show any significant reactivity with $^1O_2$ under chemical conditions. Several common LOB electrolyte salts were dissolved in tetraglyme and the stability towards $^1O_2$ was tested under chemical conditions. Finally, the commonly used $^1O_2$ trap, 9,10 dimethlyanthracene (DMA), was shown to react with superoxide and several possible misinterpretations in the DMAO2 detection and quantification in the literature are identified. It is important to note that this research does not rule out the evolution of $^1O_2$ or does not state that it does not cause any degradation. The total degradation due to $^1O_2$ is very small compared to the degradation due to fresh and/or Li deficient Li_2O_2 surfaces as further demonstrated in Chapter 5.

4.2 Experimental Methods

4.2.1 Singlet Oxygen Generation

$^1O_2$ was generated photochemically using a photosynthesiser, Rose Bengal (RB) (**Section 2.1.7**). 10 - 100 µM RB was dissolved in solvents (tetraglyme, DMSO, EC:DMC, and DMF) or 1 M salt containing tetraglyme based electrolytes. The samples were saturated with dry 20% O_2-80% Ar gas and kept stirring under constant gas flow (**Figure 4-1**). The samples were irradiated with 530 nm light to generate $^1O_2$. The gas outlet was connected to an on-line mass spectrometer for experiments in which gas consumption and evolution was monitored.

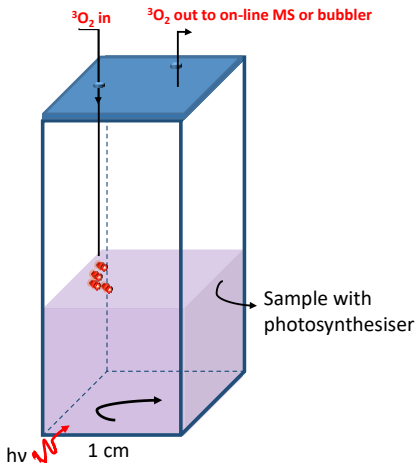

Figure 4-1 *Schematic representation of $^1O_2$ generation setup for testing the reactivity of solvents and salts towards $^1O_2$ under chemical conditions.*

4.2.2 NMR Analysis

For the electrolyte and solvent-samples, deuterated benzene (C_6D_6) or deuterated acetonitrile (CD_3CN) was used as the lock solvent with a ratio of 1:9 (lock solvent: sample). ^{1}H, ^{31}P, and ^{19}F NMR experiments were performed on a Bruker AVIII 400 (υ_0 (^{1}H) = 400.17 MHz) spectrometer equipped with 5 mm z-gradient broadband multinuclear probe. To study the stability of DMA, fresh and aged samples were prepared using CD_3CN as the lock solvent with 9:1 lock solvent:sample ratio. The 1D and 2D NMR experiments were performed on a Bruker AVIII 600 (υ_0 (^{1}H) = 600.13 MHz, with a proton-optimised TCI HCN cryoprobe) spectrometer. The T_1 was calculated using an inversion recovery sequence, and a 30 second recycle delay (>5T_1) was used throughout.

4.2.3 High-Pressure Liquid Chromatography-UV/Vis-Mass-Spectrometry

HPLC-UV/Vis analysis was carried out using the procedure described in **Section 3.2.5** and published in the literature.[210] Here, additional to HPLC-UV-Vis spectrometry, HPLC/UV-Vis-Mass-Spectrometry was used to study the peak purity in the samples. RM^+ (10 mM) and DMA (60 mM) in tetraglyme were injected onto an in-house synthesised excess amount of Li_2O_2 powder. The mixture was stirred throughout the reaction, and the $^{3}O_2$ evolution was monitored by on-line mass-spectrometry. The RM^+ samples were filtered once O_2 evolution ceased and were directly analysed by HPLC-mass spectrometry (MS, Waters Xevo G2-S bench-top QTOF mass spectrometer in positive-ion mode). Standard $DMAO_2$ samples were synthesised to confirm the isotropic chemical shift and retention time of $DMAO_2$ in the RM^+ samples. These were generated by exposing DMA solutions to $^{1}O_2$ via a meso-tetraphenylporphyrin or Rose Bengal photosynthesiser excited with a light source (660 nm and 533 nm, respectively) whilst bubbling $^{3}O_2$ into the solution.

4.3 Results and Discussion

4.3.1 Stability of Solvents and Salts towards $^1O_2$ under Chemical Conditions

The stability of non-volatile LOB solvents, such as DMSO and tetraglyme, towards $^1O_2$ were analysed by on-line MS. Any change in the $^3O_2$ concentration upon generation of $^1O_2$ indicates a reaction between the solvent and $^1O_2$. **Figure 4-2** shows that there is no change in the $^3O_2$ concentration in tetraglyme whereas a decrease in the $^3O_2$ concentration in DMSO is observed as $^1O_2$ generation starts. The $^3O_2$ concentration increases when the $^1O_2$ generation is terminated. This suggests that DMSO reacts with $^1O_2$ whereas tetraglyme is more stable towards it. These results are perspicuous that once 30 mM DMA is added to the tetraglyme, $^3O_2$ concentration decreases as expected due to DMA reacting with $^1O_2$.

Freunberger and co-workers suggest that $^1O_2$ reacts with monoglyme (DME) under chemical conditions (photosynthesised $^1O_2$ + 0.1M $LiClO_4$ in DME, 30 minute exposure).[210] However, they present gas evolution and ^1H NMR data for the $^1O_2$ treated electrolyte, and no comparison with the pristine sample is provided (**Figure S13**). In their work where they use tetraglyme in electrochemical experiments, they propose that $^1O_2$ is the major source of degradation with tetraglyme.[210] They propose that $^1O_2$ reacts with the electrolyte to produce ROOH, R•, and ROO• which then further react to form Li acetate and formate. Here, the same analysis carried out for

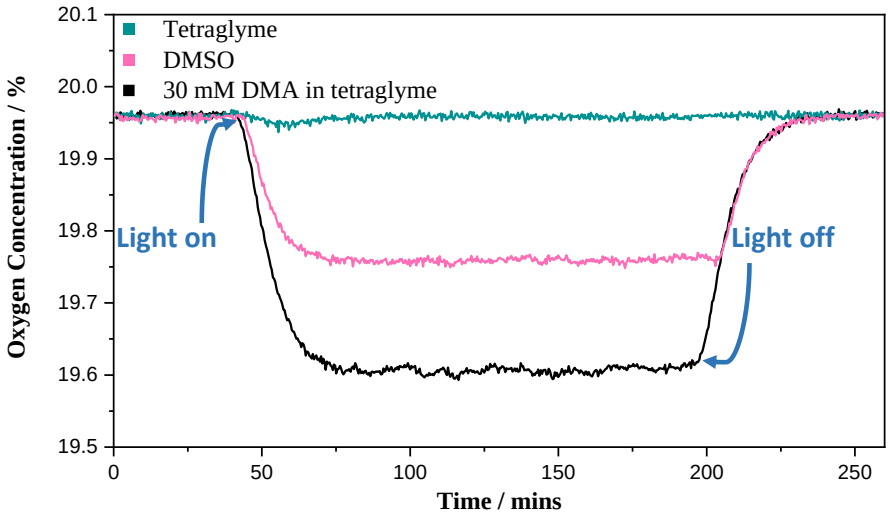

Figure 4-2 *The on-line MS data showing change in $^3O_2$ concentration upon $^1O_2$ generation and its reaction or quenching in the selected systems.*

0.1 M LiTFSI in tetraglyme electrolyte for > 12 hours. The ^{1}H NMR data in **Figure 4-3** shows that there is no significant change in amount of Li acetate and Li formate before and after $^{1}O_2$ treatment. Hence, the chemical reactivity of tetraglyme with $^{1}O_2$ is negligible. It is important to note that tetraglyme, DMSO, and DMF are not battery grade solvents and are >99% pure. The signal intensity of the impurities are smaller than the ^{13}C satellites of the main solvent peaks (<1.1%), and following the suppliers purity specifications, the total area of these peaks should be less than 1%. The main identified side products in tetraglyme are fprmate and acetate. Small changes in the spectra are disregarded if they appear both in Ar, $^{3}O_2$ and $^{1}O_2$ spectra as this work aims to elucidate the effect of $^{1}O_2$ on degradation.

Unlike the ^{1}H NMR spectra for tetraglyme before and after exposure to $^{1}O_2$, noticeable changes in the ^{1}H NMR spectra for DMSO were observed suggesting DMSO reacts with $^{1}O_2$ and forms $DMSO_2$ (**Figure 4-4A**). The newly formed peak at 3.10 ppm represents the -C**H₃** on $DMSO_2$ which is lower field compared to –C**H₃** in DMSO as it is deshielded i.e. has less electron density around the proton as the additional O atom pulls the electron density away from the proton. The formation of $DMSO_2$ is further confirmed by FTIR spectroscopy (**Figure 4-4B**). The FTIR spectra peaks are assigned as follows: the 1142 cm^{-1} peak is symmetric stretching of SO_2 $\nu_{as}(SO_2)$, the 763 cm^{-1} peak is ν_s(CSC), the 499 cm^{-1} peak is bending/wagging of δ(OSO), and the 465 cm^{-1} peak can potentially be assigned to rocking or twisting of γ or $\rho(SO_2)$ in $DMSO_2$.[283,284] The reaction of DMSO with $^{1}O_2$ to form of $DMSO_2$ has been previously elucidated by Collinet-Fressancourt et al.[285] on other systems, whilst Kwabi et al.[85] have shown that DMSO also reacts with Li_2O_2 to form $DMSO_2$ under chemical conditions and suggested that DMSO can react with superoxide like species as well.

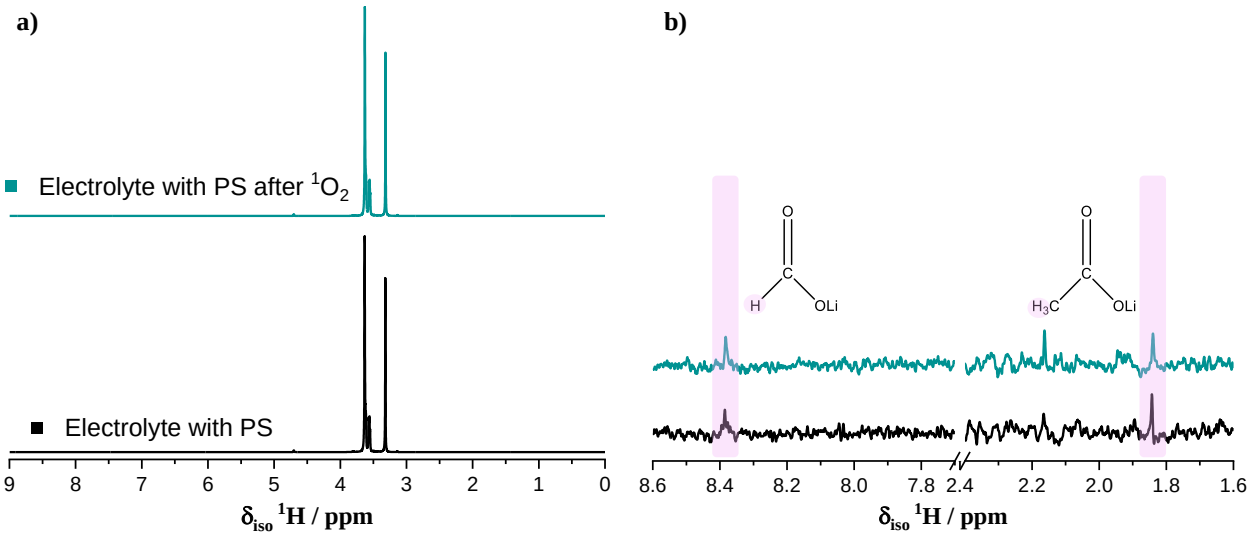

Figure 4-3 *a) The ^{1}H NMR spectra for pristine 0.1 M LiTFSI 7 µM TPP (PS) before and after exposure to $^1O_2$. 50 µL of electrolyte was added to 750 µL D_2O to dissolve any b) Li formate and acetate to form HCOOD (8.38 ppm) and CH_3COOD (1.84 ppm), respectively.*

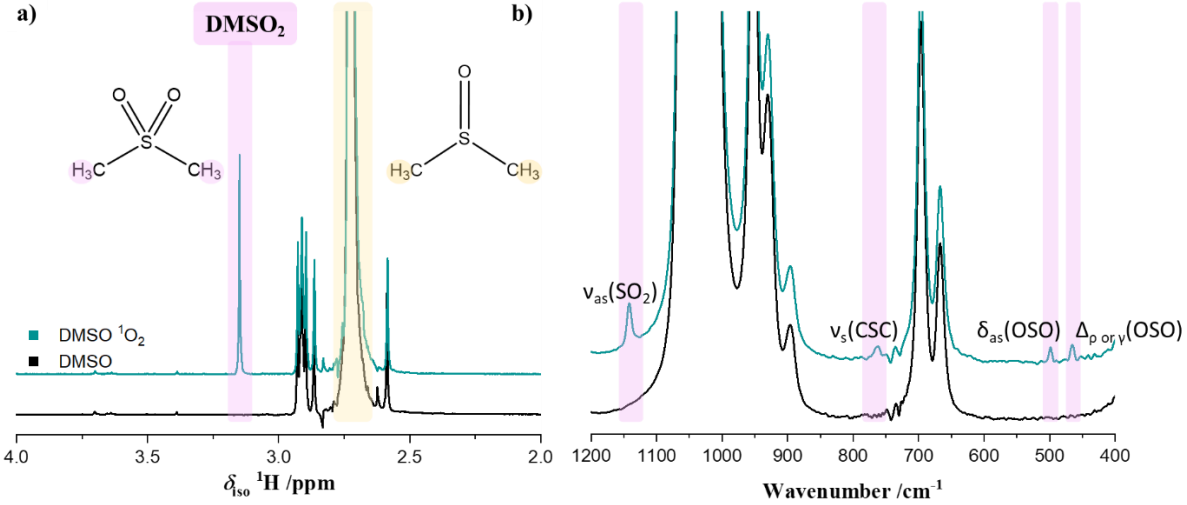

Figure 4-4 *a) The ^{1}H NMR and b) FTIR spectra for DMSO and $^1O_2$ treated DMSO showing peaks for DMSO (yellow) and $DMSO_2$ (pink).*

DMF was tested as an electrolyte solvent for LOBs due to its proposed stability towards superoxide.[3] However, it was shown to undergo oxidative cleavage and form side products such as dimethylamine and N-O containing species.[286] Here, it is shown that DMF also reacts with $^1O_2$ under chemical conditions (**Figure 4-5** and **Figure S14**). The intensity of newly arising peaks due to degradation are similar in intensity to the satellites, which are 1.1 % natural abundance, of DMF peaks suggesting that the chemical reactivity under these conditions (up to 18 hours of continuous $^1O_2$ generation with RB or TPP) is slow .

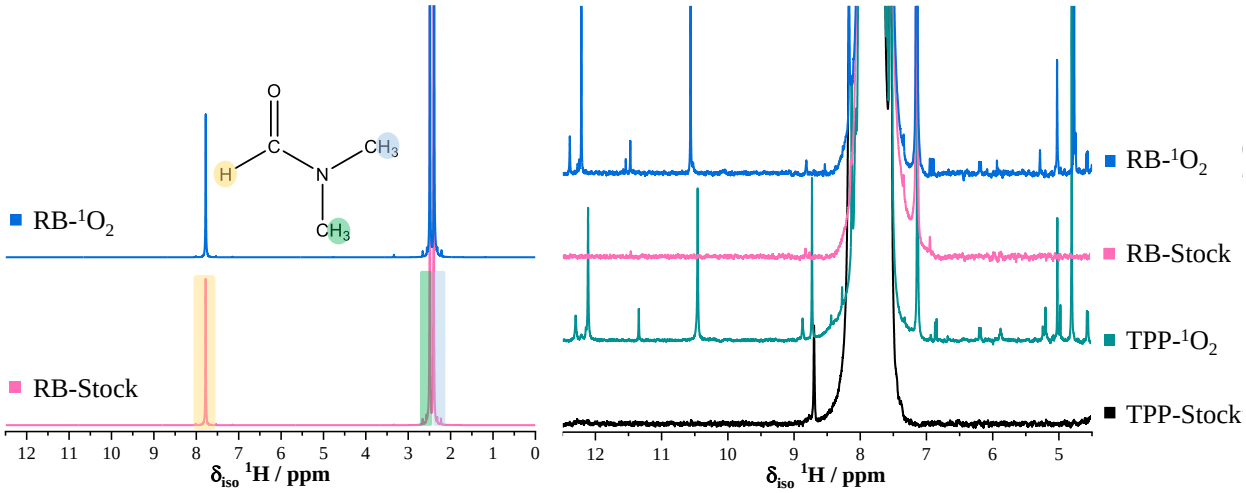

Figure 4-5 *The ^{1}H NMR spectra of DMF with photosynthesisers RB and TPP before and after $^1O_2$ exposure showing that DMF reacts with $^1O_2$. The peaks around ~8.7 ppm belongs to TPP and the peaks ~7.2 ppm belong to the NMR solvent, benzene. The NMR solvent for the TPP-stock was acetonitrile.*

The spectra in **Figure 4-6** show the evolution of degradation products over time. The short experiments were completed in 3-6 hours and the long experiments were completed in 12-18 hours. The identification of these small peaks require several days of 2D NMR measurements on a high magnetic field NMR with a cryoprobe as these products are low in concentration relative to the pure solvent and multi component analysis requires high resolution data.

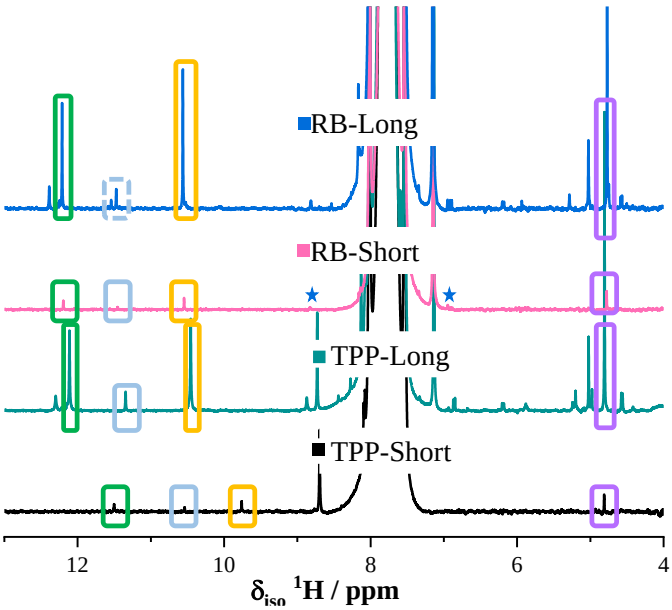

Figure 4-6 *The ^{1}H NMR spectra of DMF (with RB and TPP) after exposure to $^1O_2$ for short and long durations.*

Turning back to tetraglyme, the on-line MS and NMR spectroscopy results in **Figure 2** and **3** indicate that it is highly stable towards $^1O_2$ under chemical conditions. Hence, the next steps in

understanding the effect of $^1O_2$ in LOBs is evaluating the electrolyte stability under electrochemical conditions. $LiClO_4$, LiOTf, and LiTFSI are commonly used electrolyte salts in LOBs. Among these three, LiTFSI offers the highest discharge capacity compared to the Li salts tested in LOBs (**Section 1.6.1.2**). Its conductivity in tetraglyme is highest among these salts[d], and its oxygen solubility is higher and viscosity is lower than that of $LiClO_4$.[123] **Figure 4-7** shows that there are no changes in the electrolyte due to addition of $LiClO_4$ or LiOTf salts and only small changes in the impurities (>99% pure tetraglyme) is detected. The acetate peak at ~1.86 ppm decreases and changes around ~1.07 ppm are observed which are present in the $^3O_2$ spectra as well.

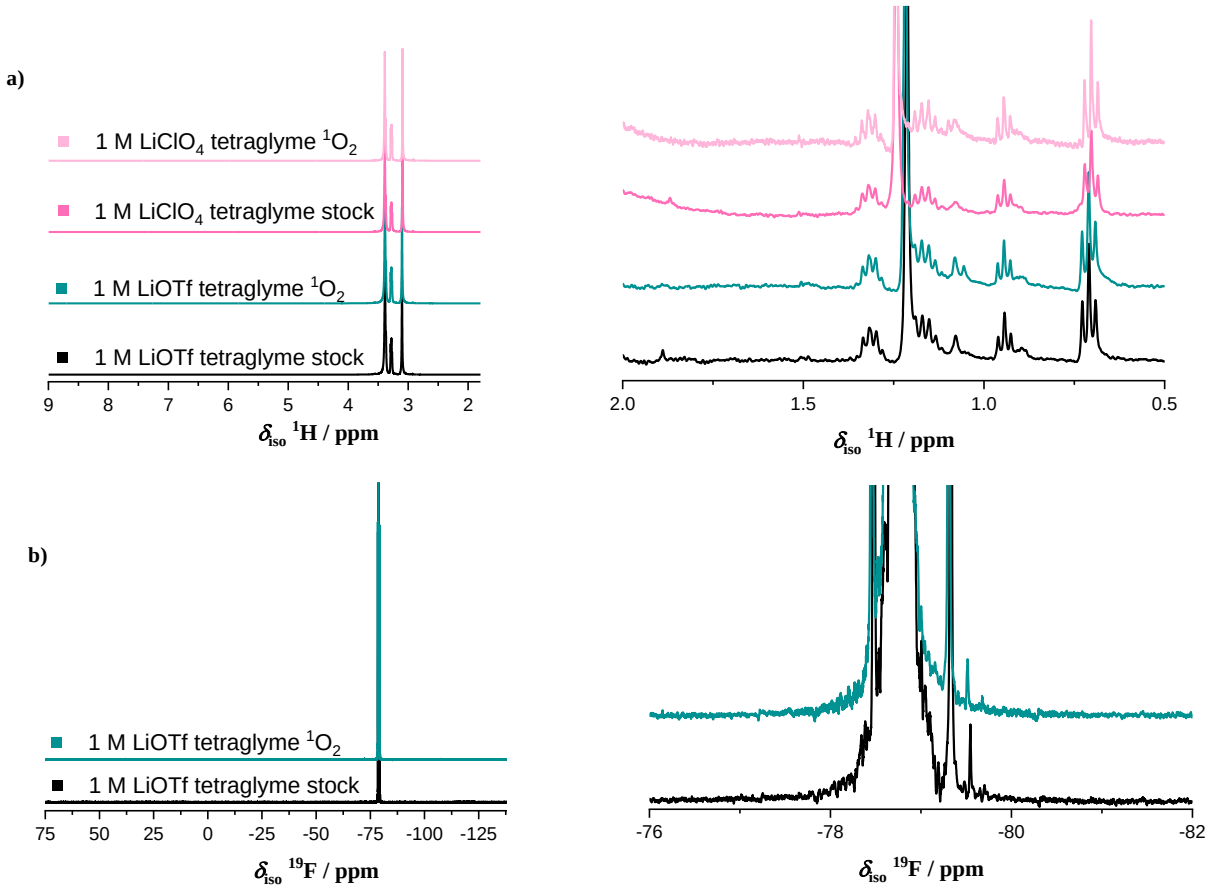

Figure 4-7 *The ^1H NMR spectra for a) 1 M $LiClO_4$ and b) 1 M LiOTf in tetraglyme before and after $^1O_2$ treatment and ^{19}F NMR for 1 M LiOTf in tetraglyme before and after $^1O_2$ treatment.*

Due to its discharge performance, LiTFSI was chosen as the salt for electrochemical experiments in Chapter 5. Its stability in tetraglyme towards $^3O_2$ and $^1O_2$ is studied. Similar to the

[d] The ionic conductivities for the following electrolytes are 2.65 mS cm^{-1} for 1 M LiTFSI in tetraglyme, 2.43 mS cm^{-1} for LiBOB, 2.11 mS cm^{-1} for $LiPF_6$, and 1.72 mS cm^{-1} for $LiClO_4$.

above findings, **Figure 4-8** shows that there are small changes at around 1.07 ppm in the impurities for tetraglyme-LiTFSI as well. These changes are happening in the impurities in the electrolyte (less than 1%) both with $^3O_2$ and $^1O_2$. The 1.86 ppm acetate peak disappears with $^1O_2$ as it does in tetraglyme-$LiClO_4$ and tetraglyme-LiOTf samples. It does not seem to change with $^3O_2$, but the 1.65 ppm peak is decreasing. Overall, as these changes are less than << 1% and affecting the impurities, tetraglyme and LiTFSI seem to be stable towards $^1O_2$ under chemical conditions and their combination can serve as a good electrolyte candidate for LOBs.

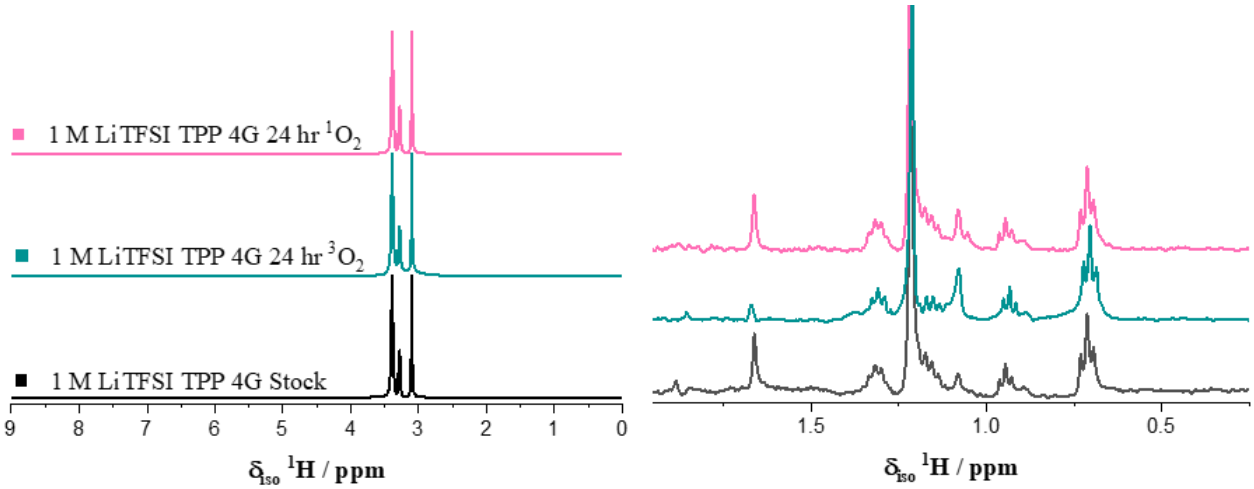

Figure 4-8 *The ^{1}H NMR spectra for 1M LiTFSI 7 µM TPP in tetraglyme under Ar (glovebox conditions), constant $^3O_2$ exposure for 24 hours and constant $^1O_2$ generation under constant $^3O_2$ bubbling for 24 hours.*

4.3.2 On the Suitability of Using DMA as a $^1O_2$ Trap in Li-O_2 Cells

Singlet oxygen detection can be done by using traps and quenchers. Traps specifically react with $^1O_2$ and form a stable compound. Quenchers can be chemical or physical. These molecules usually have π-electrons or lone pair electrons with low ionisation energy. Physical quenching can occur via spin-orbit coupling or triplet energy transfer. Quencher and $^1O_2$ form a complex and its can be categorised either as an exciplex or a charge-transfer complex depending on the ionisation energy of the quencher. Singlet complex then decays to ground-state compounds.[200] DMA is first used by Freunberger and co-workers in LOBs to detect $^1O_2$ formation as it forms the respective endoperoxide upon exposure to $^1O_2$.[210] They suggest that it is selective and does not react with superoxide.[206,210] It was then used as the main trap to detect $^1O_2$ in LOBs.[59,209,211,287,288] However, as

seen in Chapter 3, DMA forms $DMA(OH)_2$ in the presence of $^1O_2$ and protons. This suggests that $DMAO_2$ may not be the only reaction product with $^1O_2$ as proposed in the LOB literature. Hence, the photochemistry and electron transfer literature on endoperoxides show that these structures can undergo cycloreversion and peroxide bond breakage (**Figure 4-9**).[276,289-296] It was shown by Rigaudy et al. that $DMAO_2$ suffers from O-O (peroxide) bond homolysis upon heating and forms degradation products or isomers such as **1** and **2** (**Figure 4-9**).[289] Brauer and co-workers showed that photolysis of $DMAO_2$ in the 313-253 nm range either leads to formation of the parent hydrocarbon, DMA, via cycloreversion or depending on the wavelength homolytic cleave of the O-O bond to **3** and **4**.[291] Aurbry et al. suggested that peroxidic bond cleave is favoured over cycloreversion for $DMAO_2$ when it is refluxed in chlorobenzene.[290] Southern and Waters showed that the $DMAO_2$ yield decreases to 60% after heating for 2 hours in chlorobenzene and completely decomposes in 12 hours.[292] They identified some of the products as anthraquinone, **5**, and **6** $DMA(OH)_2$. They added phenol to study the effect of acidity and observed that the degradation products changed. The $DMAO_2$ yield was 52% after 2.5 hours and the product they could identify was **6**, $DMA(OH)_2$ that was confirmed by NMR spectroscopy in Chapter 3 as an additional product to $DMAO_2$. Donkers and Workentin also identified $DMA(OH)_2$ in their study of endoperoxide electron transfer (ET) mechanism.[276] They performed voltammetric analysis and electrolysis of $DMAO_2$ and concluded that reduction of $DMAO_2$ under both heterogeneous and homogenous conditions yield $DMA(OH)_2$ quantitatively. The process is a concerted dissociated ET i.e. ET and bond cleavage occur at the same time. The intermediate is the distonic radical anion (**a**) as suggested in above mentioned studies. As well as adding phenol, Southern and Waters also studied the effect of α-naphthol which is also a weak acid. The decomposition products were different from that of phenol. $DMAO_2$ decomposed completely and some of the products identified were anthraquinone, **6** ($DMA(OH)_2$), **7** (anthronol derivative R=Me), and a 9-CH_2•OH derivative. The change in the decomposition products indicates that the reactions are pH dependant. Southern

and Waters suggest that DMA can undergo intermolecular oxidation and reduction. All these findings cast doubt on the quantitative of DMA as a $^1O_2$ trap.

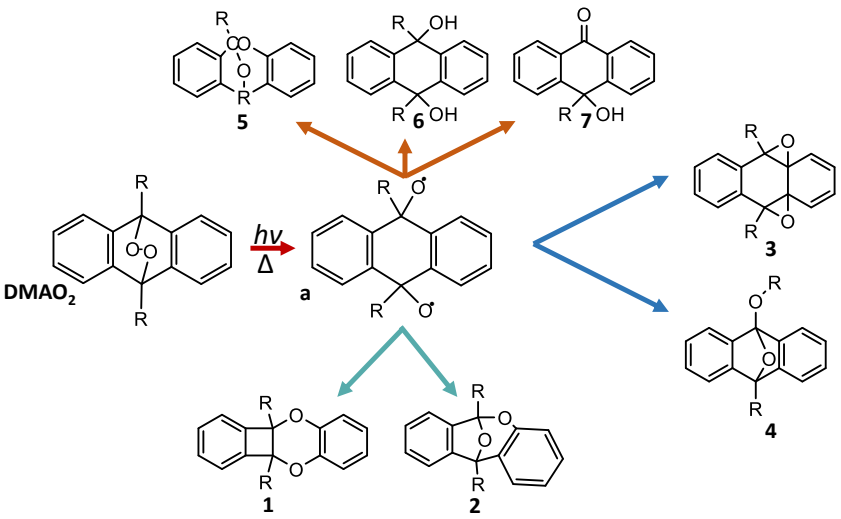

Figure 4-9 *Thermolysis and photolysis of $DMAO_2$ can lead to breaking of the peroxide bond and formation of distonic radical. This radical depending on the pH, temperature, and solvent environment is shown to form the indicated molecules (1-7). The different colour arrows (orange, blue, green) refers to different studies.*

The detection and stability of $DMAO_2$ should be monitored carefully as the side products and environmental changes (such as viscosity, pH, and temperature) could lead to false positive or misleading results. Therefore, a variety of analytical methods were coupled to confirm the presence of the $^1O_2$ related DMA derivatives. ^{1}H NMR spectroscopy can show formation of new aromatic compounds and complementary 2D NMR data can confirm the correlations between these new peaks and new side products. Solely using HPLC/UV-Vis is not reliable as only the peaks for DMA and $DMAO_2$ retention times are known and analysed. HPLC/UV-Vis can be coupled to MS to study peak purity and detect retention times of the side products with the known *m/z*. Still, interaction of RM^+ with $DMAO_2$ and the column can cause variations between different samples. Thus, it is important to note that results of such analyses should be considered to be semi-quantitative due to unclear reaction kinetics of $^1O_2$ and DMA in different RM^+ samples and due to trap and RM stability issues.

Based on the above discussion, $^1O_2$ formation after Li_2O_2 oxidation with RM^+, similar to the studies in Chapter 3, was independently investigated using HPLC-UV/vis-MS. The RM^+ samples, 60 mM DMA stock, and photosynthesised $DMAO_2$ samples were analysed using an identical column, gradient, and ionisation conditions. The retention times for $DMAO_2$ and DMA were identified via HPLC-UV/vis-MS as 2.7 and 4.5 minutes (**Figure 3-9** and **Figure 4-10A**), respectively, similar to those previously reported[210]. However, the results below (**Figure 4-10**) show that using these retention times to pinpoint the $DMAO_2$ peak and calculate the amount of $^1O_2$ in the RM^+ samples using the peak area could be problematic. Tetraglyme is highly viscous and is dragged along the column, likewise different RMs change the pH and the solution environment. These affect the retention times and peak purity. The $DMAO_2$ (*m/z* 239.107) chromatogram extracted from the HPLC-UV/vis-MS data shows that $DMAO_2$ peak retention time changes depending on the sample/environment (**Figure 4-10B**). Hence, multiple peaks for one component are observed instead of one pure peak. Another point to take into consideration is that in most of the RM^+ samples, *m/z* 239.107 peak appears at more than one retention time suggesting that the samples could contain $DMAO_2$ isomers (**Figure 4-10D**). It is unlikely for another molecule to have the same *m/z* ratio (**Figure 4-10C**). Normally, an ion will have only one retention time. If multiple *m/z* 239.107 peaks do not belong to isomers of $DMAO_2$ but belong to the same ion, then it could be due to carry-over contamination from tetraglyme.[297] This again shows that the detection method in the literature is technically challenging to be used in the tetraglyme-based electrolytes in the LOB systems. Overall, the peaks are not pure and consist of multiple components and either there is contamination due to viscous tetraglyme carry-over or there are isomers of $DMAO_2$.

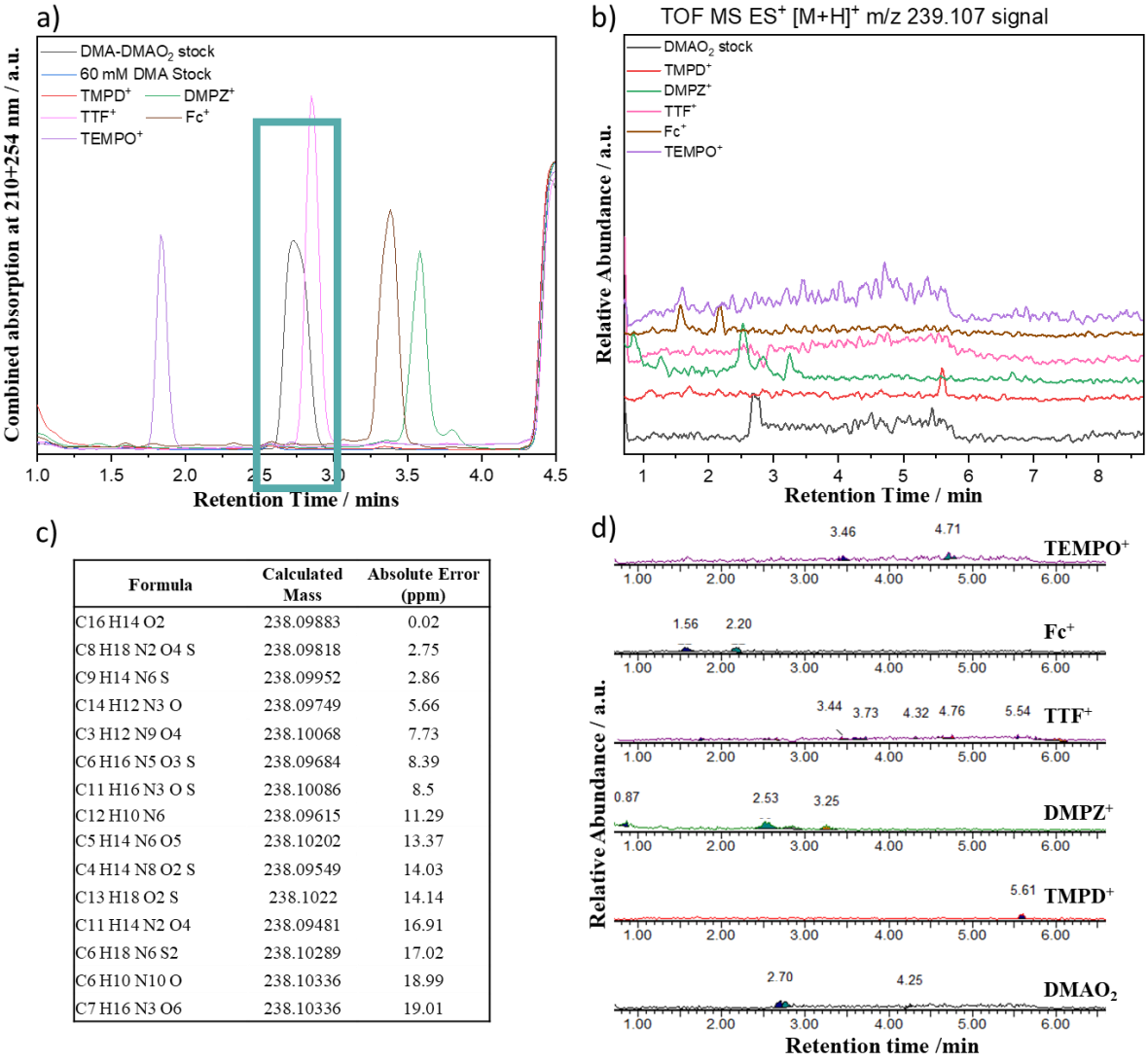

Formula	Calculated Mass	Absolute Error (ppm)
C16 H14 O2	238.09883	0.02
C8 H18 N2 O4 S	238.09818	2.75
C9 H14 N6 S	238.09952	2.86
C14 H12 N3 O	238.09749	5.66
C3 H12 N9 O4	238.10068	7.73
C6 H16 N5 O3 S	238.09684	8.39
C11 H16 N3 O S	238.10086	8.5
C12 H10 N6	238.09615	11.29
C5 H14 N6 O5	238.10202	13.37
C4 H14 N8 O2 S	238.09549	14.03
C13 H18 O2 S	238.1022	14.14
C11 H14 N2 O4	238.09481	16.91
C6 H18 N6 S2	238.10289	17.02
C6 H10 N10 O	238.10336	18.99
C7 H16 N3 O6	238.10336	19.01

Figure 4-10 *a) The HPLC data for DMA/$DMAO_2$ standards and RM^+ samples. $DMAO_2$ standards show that the retention time for $DMAO_2$ in these solutions are 2.7 minutes. b) Extracted ion chromatograms at m/z 239.10666 for RM^+ samples and DMA-$DMAO_2$ stock showing the retention times for $DMAO_2$ and/or its isomers. In the photosynthesised $DMAO_2$ samples the retention time is 2.7 minutes; however, in the RM^+ samples this varies. c-d) Extracted ion chromatograms at m/z 239.10666 for RM^+ and photosynthesised $DMAO_2$ samples showing relevant peaks detected using MassLynx software. The table shows calculated elemental compositions for compounds with the same m/z as $DMAO_2$ within a 20 ppm error. This shows that it is high unlikely for the signal to arise from another chemical composition other than $DMAO_2$.*

The peak at ~2.7-3 minutes in the disproportionation data pertains to $DMAO_2$, however, it also consists of a range of other *m/z* ions (**Figure 4-11**). This suggests that the quantitative analysis using this method are invalid. The peak purity can be low due to carryover due to high viscosity of tetraglyme, dimer-trimer formation, and more effective ionisation of the impurities than the target molecule. The difficulty in ionising $DMAO_2$, competitive ionisation, and possibility of forming

various ionisation products upon formation of the biradical can affect the peak purity and the quantitative analysis results.[298,299]

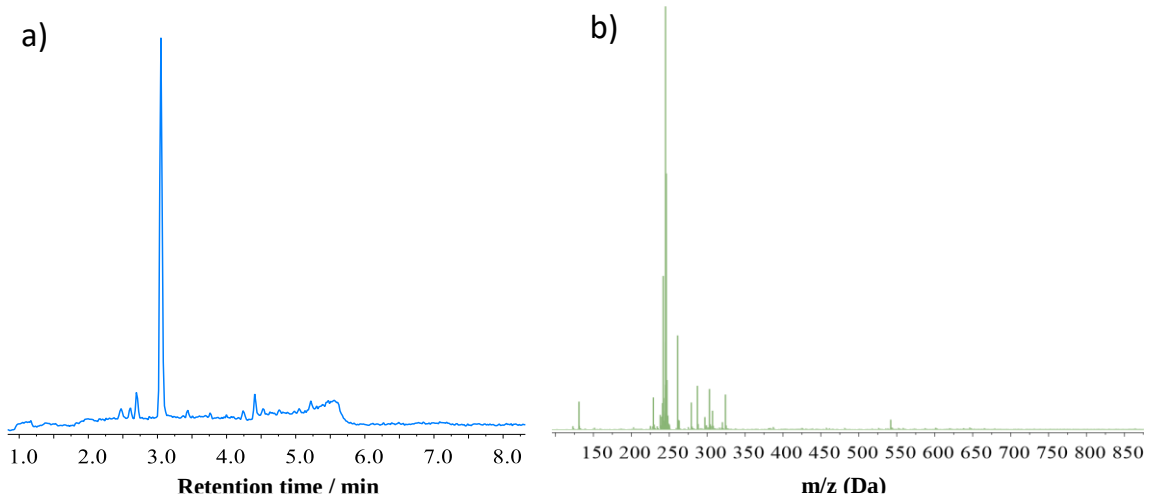

Figure 4-11 *a) The extracted ion chromatograms at m/z 239.10666 ($DMAO_2$) for a disproportionation sample (LiO_2 → Li_2O_2 + $^xO_2$). b) MS data showing the peak purity for the peak at 3 minutes in the m/z 239.10666 chromatogram.*

From the peroxide bond breakage and side product formation in $DMAO_2$ containing systems (**Figure 4-9**), the samples were screened for some of these side products. **Figure 4-12** shows that RM^+ samples contain either anthracene, $DMA(OH)_2$, anthraquinone, or a combination of these degradation products. This result suggest that only accounting for $DMAO_2$ as the reaction product of DMA with $^1O_2$ will underestimate the generated amount.

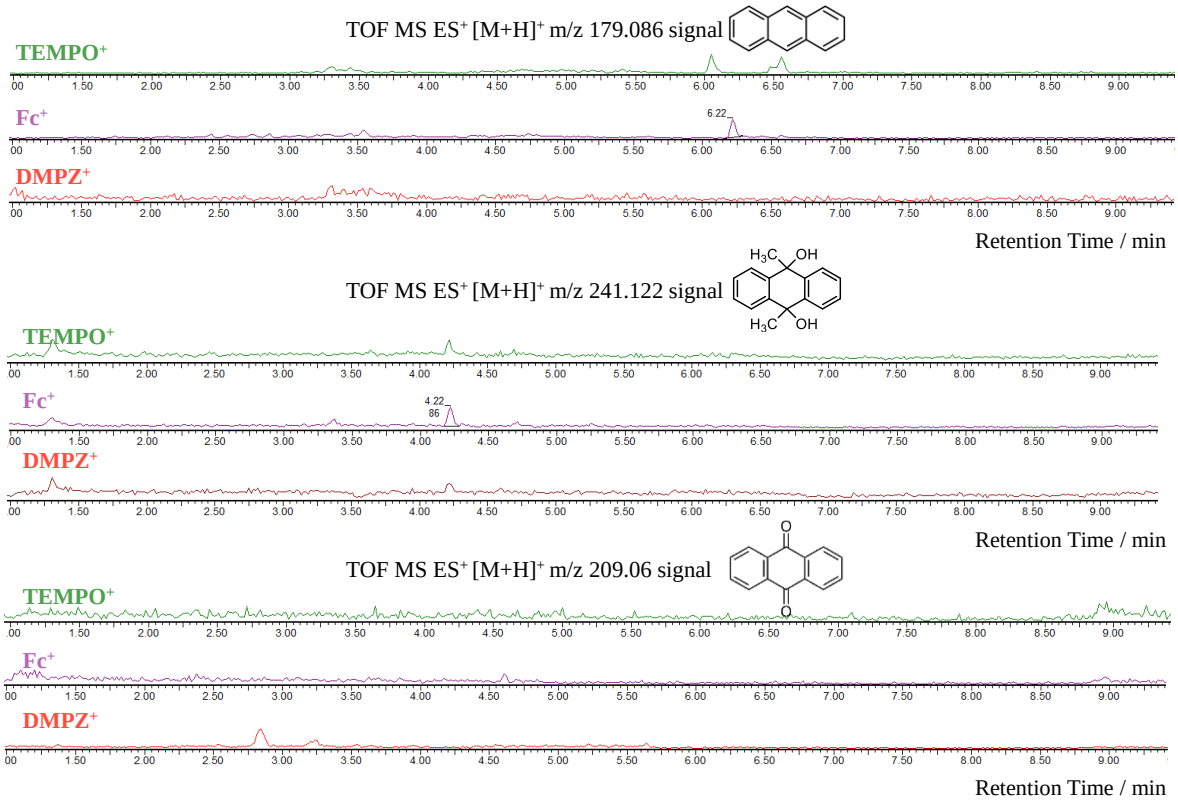

Figure 4-12 *Extracted ion chromatograms at m/z 179.086 (anthracene), m/z 241.122 (DMA(OH$_2$)), ad m/z 209.06 (anthraquinone) showing that the RM$^+$ samples can contain these side products arising from DMAO$_2$ peroxide bond breakage.*

It is shown above that DMA is not selective towards $^1O_2$ and DMAO$_2$ is not stable under different pH conditions. Now, the reactivity of DMA with superoxide is studied. Freunberger and co-workers previously showed that DMA does not react with KO_2 in 0.1 M $LiClO_4$ in DME electrolyte.[210] Here, it is studied again in different electrolytes, and demonstrated that DMA can react with KO_2 depending on the solvent and salt.

DMA (75 mM) was dissolved in tetraglyme with and without 0.1M LiTFSI. The solutions were added to an excess of KO_2 powder and aged. Visible colour changes were observed in the salt containing mixture after 2 hours and in the tetraglyme sample after 4 hours. The salt containing sample turned from yellow (KO_2 is yellow) to dark brown in 8 hours (**Figure 4-13**). The changes in the samples were also tracked by ^{1}H NMR. **Figure 4-14** shows that tetraglyme sample has significant changes in the aromatic region after 24 hours and the salt containing sample has significant changes after 4 hours. The LiTFSI containing sample completely degrades after 24 hours, and there

is no DMA remaining. $DMAO_2$ formation upon exposure to KO_2 can be seen in the blue marked regions in the spectra, and after 6 hours $DMAO_2$ also degrades.

Figure 4-13 *DMA (75 mM), LiTFSI (0.1 M) in tetraglyme with excess KO_2 after 1 hr mixing (yellow) and 8 hr mixing (brown) suggesting that superoxide reacts with DMA.*

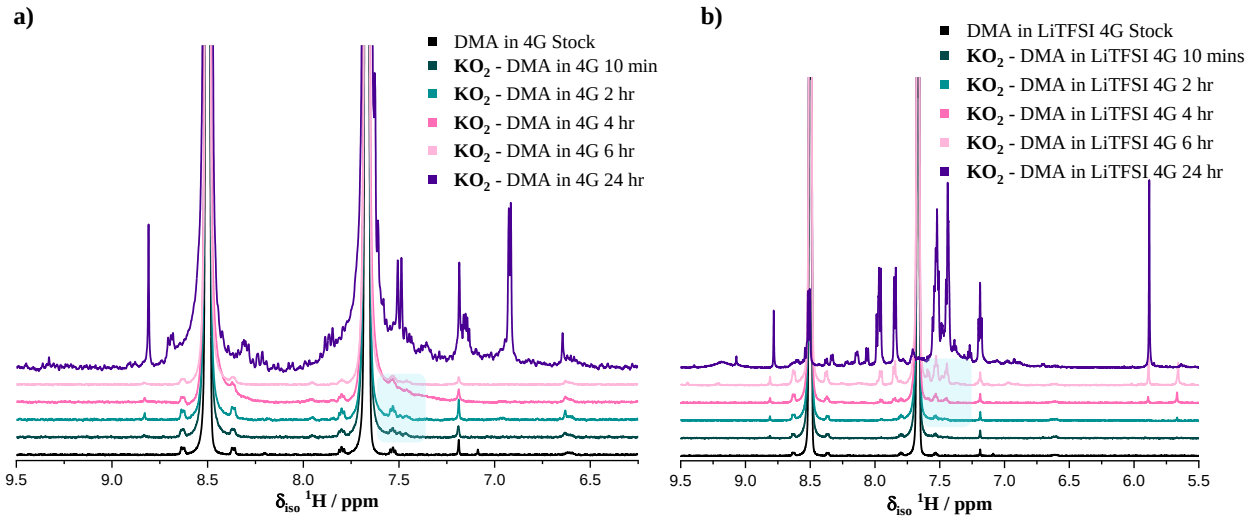

Figure 4-14 *The ^1H NMR spectra taken at several time points showing that DMA (75 mM) reacts with KO_2 in tetraglyme with(b)/without(a) 0.1M LiTFSI.*

DMA is also revealed to degrade in tetraglyme -$LiClO_4$ and DME-LiTFSI solvent and salt combinations upon exposure to KO_2. Similar to the findings of Freunberger and co-workers, the ^1H NMR spectra for DMA in 0.1M $LiClO_4$ in DME aged in KO_2 shows that DMA is stable under these conditions (**Figure 4-15**). DMA reacts with KO_2 in tetraglyme with/out salt and in DME with LiTFSI. This affects any analysis of $^1O_2$-LOB relationship where DMA is used to show $^1O_2$ evolution or related degradation in LiTFSI-tetgraglyme, LiTFSI-DME, and $LiClO_4$-tetgraglyme electrolytes. As discussed previously, DMA is 75 mM, the by-products are considerably less concentrated than that, and the tetraglyme peaks dominate both the DMA peak and the pertaining impurities. Hence, a multi

component identification with 2D NMR becomes very difficult. Additionally, knowing what the side-products are does not make any impact on the conclusion that DMA is not a stable and selective trap in LOBs.

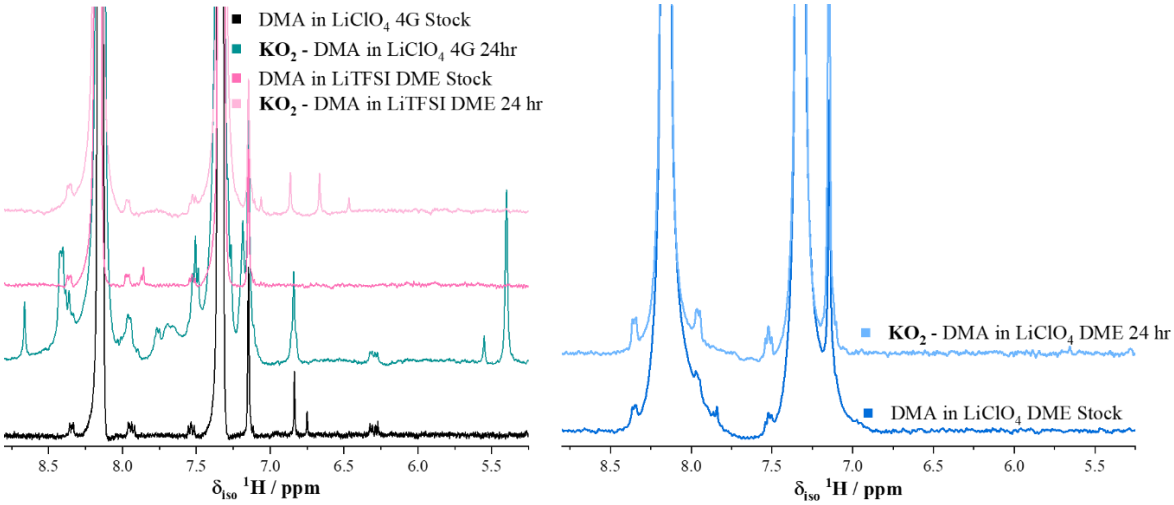

Figure 4-15 *The ^1H NMR spectra taken after 24 hours of aging DMA (40 mM) containing solution in KO_2. The data shows that DMA reacts with KO_2 in tetgraglyme-0.1 M LiTFSI and DME- 0.1 M LiTFSI, and is stable in DME- 0.1 M $LiClO_4$.*

4.4 Conclusion

It is important to elucidate the origins of $^1O_2$ formation and the methods used to detect and quantify it. Here, $^1O_2$ formation in LOBs is not ruled out. However, the data casts doubt on its reactivity, detection mechanisms and quantification. Wandt et al.[205] and in their first $^1O_2$ -LOB study Mahne et al. [210] suggested that Li_2O_2 oxidation causes $^1O_2$ formation. Zhang et al. [300] showed that the trap, 4-Meo-TEMP, used by Wandt et al. reacts with Li_2O_2 in the presence of CO_2 and form 4-oxo-TEMPO similar to its reaction with $^1O_2$. Mahne et al. used DMA as a trap which here is shown to also react with superoxide and form various side products including $DMA(OH)_2$ in the presence of protons and $^1O_2$ as shown in Chapter 3.

Schroder and co-workers pointed out that according to Marcus-Hush-Chidsey theory, the direct oxidation of Li_2O_2 on the electrode cannot generate an excited species such as $^1O_2$ as the exergonity of the reaction can be tuned by the electrode potential and there are quasi -continuous states available below or above Fermi level for a metal or metal-like electrode for the reaction to

proceed without a barrier. The inverted Marcus region is not observed, but the products are still at the lowest energetic state and spin conversion is valid. However, $^1O_2$ formation from a chemical step, from LiO_2 disproportionation is still plausible. If we assume that $^1O_2$ evolves from a chemical step in LOBs, here it is shown that the exact amount is not known and its reactivity with the cell parts is misunderstood. Here, it is shown that tetraglyme is chemically stable towards $^1O_2$ unlike DMSO and DMF. Commonly used salts such as $LiClO_4$, LiOTf, and LiTFSI do not show any significant reactivity with $^1O_2$ under chemical conditions either. Hence, one of the most widely used electrolytes, 1 M LiTFSI in tetraglyme does not seem to react with $^1O_2$ under chemical conditions. Its reactivity will be further investigated under electrochemical conditions in the next Chapter.

Finally, the detection methods and stability of DMA was studied. HPLC/UV-Vis is shown to fall short in the quantitative detection of DMA and $DMAO_2$. Once it is coupled to MS, it is seen that the retention time shifts between different RM^+ samples and the main $DMAO_2$ peak consists of different mass fragments for samples which shows that there is no peak purity. Moreover, the common degradation products identified in DMA-$DMAO_2$ systems in the literature such as anthracene, 9,10-dihydroxyanthracene, and anthraquinone were detected via MS as well. NMR spectroscopy data in Chapter 3 also confirms the formation of 9,10-dihydroxyanthracene. Lastly, it is demonstrated that DMA reacts with superoxide (KO_2) and forms $DMAO_2$ and other aromatic compounds in most of the common LOB electrolytes. This suggests that the detected formation of $DMAO_2$ could be due to LiO_2. The formed $DMAO_2$ and intermediate degradation products further degrade into other aromatic compounds over the course of 24 hours.

5 Chapter 5 – The Causes of Degradation on Charge: Unravelling the Role of Singlet Oxygen

5.1 Introduction

Singlet oxygen ($^1O_2$) has been suggested to be the major source of degradation in LOBs, and as a result of this, most of the LOB literature started attributing the majority of degradation to $^1O_2$ and focused on strategies such as using traps and quenchers to neutralise it. However, theoretical considerations cast doubt on claimed formation routes in LOBs.[201] The indirect results in **Chapter 3** show that $^1O_2$ yield from mediated charging and the amount of degradation does not correlate, and the data in **Chapter 4** demonstrates that one of the most widely used LOB electrolytes (1 M LiTFSI in tetraglyme) is stable towards $^1O_2$ under chemical conditions. It is important to understand the true cause of degradation to work towards practical LOBs. If $^1O_2$ is the main source of degradation, it should be decoupled from other degradation routes.

Formation of $^1O_2$ in LOBs was attributed to direct electrochemical oxidation of Li_2O_2, Li_2CO_3, and the disproportionation of Li_2O_2.[205,208-210] As discussed in **Chapter 4**, according to Marcus-Hush-Chidsey theory, excited states cannot be reached via electron transfer reactions on metal electrodes. A chemical step resulting in $^1O_2$ generation is possible. However, there is no evidence of direct generation of $^1O_2$ from superoxide disproportionation. On the other hand, Li_2O_2 was shown to evolve $^1O_2$[301,302] prior to work on LOBs. These are frequently cited in papers that state $^1O_2$ is the main source of degradation. However, it is important to note that these studies either used HCl or wetted Cl_2 gas and chemically formed $^1O_2$ from Li_2O_2. As discussed, it is not possible to produce excited state products from $1e^-$ or $2e^-$ transfer reactions at metal and metal-like electrodes.[303-305] However, Wandt et al.[205] charged Li_2O_2 preloaded electrodes and trapped $^1O_2$ using 4-Oxo-TEMP. They used EPR to detect 4-Oxo-TEMPO forming upon the trapping of $^1O_2$. When testing the stability of 4-Oxo-TEMP in their systems, they do not test its reactivity with superoxide-like species and the possibility of its chemical oxidation. It was shown that chemically oxidised TEMP forms $TEMP^{+\bullet}$ which then is deprotonated and reacts with $^3O_2$ to form 4-Oxo-TEMPO.[306]

More importantly, Zhang et al.[300] showed that CO_2 and peroxide-derived antioxidants can also lead to the formation of 4-Oxo-TEMPO. They used the same electrolyte and a Li_2O_2 preloaded electrode similar to Wandt et al.; however, instead of applying a potential they exposed the system to CO_2. Hence, the discrepancy between theory and the conclusion of Wandt et al. can be explained by 4-Oxo-TEMP trap not being selective enough.

If there is $^1O_2$ formation from a direct chemical step or from reactions of side products, the reactivity of the generated $^1O_2$ with cell components should be tested under electrochemical conditions. The chemical stability results in **Chapter 4** show that the widely used electrolyte tetraglyme-LiTFSI is chemically stable towards $^1O_2$. However, the literature states that this electrolyte degrades due to $^1O_2$ in LOBs. Hence, here, the electrochemical stability of this electrolyte and the carbon cathode is studied. It is concluded that $^1O_2$ does not cause any increased degradation when compared to $^3O_2$ under electrochemical conditions (12 hour 3.55 V and 3.8 V potential holds in an Ar, $^3O_2$, or $^1O_2$ atmosphere), and substantially more degradation is detected upon preloading the carbon cathode with Li_2O_2 or discharging the cell to generate Li_2O_2. This suggests that the main source of degradation is not $^1O_2$ but the peroxide. As the stability of the bulk Li_2O_2 was confirmed by aging it in tetraglyme, the fresh Li_2O_2 surfaces are shown to be the possible main cause of degradation in LOBs.

5.2 Experimental Methods

5.2.1 Electrochemistry Setup

A three-electrode cell shown in **Figure 5-1** was used to carry out the electrochemical experiments. A ^{13}C (10 mg, 7 mm dia.) working electrode (WE), a delithiated LFP counter electrode (CE), and a fritted LFP reference (REF) electrode in a LiTFSI-tetraglyme supporting electrolyte were used. The electrodes were attached to a septum and the septum was fitted onto a UV-Vis cuvette. Gas inlet and outlet were connected by inserting needles through the septum. 750 µL Tetraphenylporphyrin (TPP, 7 µM) and 0.1 M LiTFSI containing, tetraglyme was used as the

electrolyte for the potential hold experiments. For dis/charge experiments the same electrolyte without TPP was used, as it is not stable over the discharge voltage window. The electrolyte was rapidly stirred throughout the experiment.

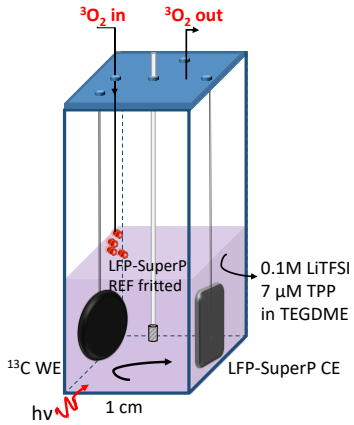

Figure 5-1 *A schematic representation of the three-electrode cell used for $^1O_2$ experiments under electrochemical conditions.*

5.2.2 Singlet Oxygen Generation

The life time of triplet photosynthesiser (^{3}PS), its quantum yield, and photo stability of PS are important factors in selecting a photosynthesiser.[204] ^{3}PS energy should be greater than 97 kJ mol^{-1} and ideally it should have a high absorption coefficient at the selected excitation wavelength.[204] However, in this study, the chemical stability of a ^{3}PS with the electrolyte and especially its electrochemical stability at the selected voltage range (3.55 - 3.8 V) play the most important role in the selection. Tetraphenylporphyrin (TPP) was used as the ^{3}PS in this Chapter as it is stable over a voltage window of 3.55 V to 3.8 V vs. Li$^+$/Li (**Figure 5-2**). Rose Bengal was also used in to generate $^1O_2$ in this Thesis. However, it is not stable in the desired voltage window, and only used in chemical experiments. A low TPP concentration of 7 µM was used to minimise any possible side reactions and degradation due to the presence of ^{3}PS. No electrolyte degradation was observed upon the addition of TPP, according to ^{1}H NMR. A 660 nm light source excited the TPP due to its absorption peak as previously shown in **Figure 2-2**.

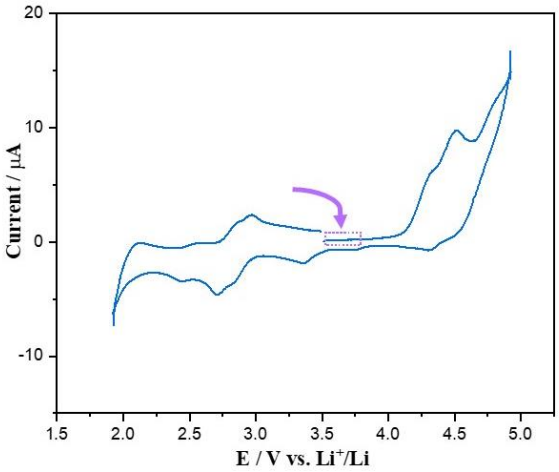

Figure 5-2 *The cyclic voltrammogram of 7 µM TPP in 0.1 M LiTFSI and tetraglyme electrolyte. The framed region indicated the voltage window used in the electrochemical experiments. The CV was recorded with a planar Au working and counter electrodes and a fritted LFP reference electrode at a scan rate of 100 mV* s^{-1}.

During the experiments, dry oxygen gas ($^3O_2$) was bubbled into the cell; oxygen (N5.0 grade) was used for experiments run in an Ar-filled glovebox and 20% O_2:80% Ar gas mixture for experiments coupled to the mass spectrometer. The $^1O_2$ generation was confirmed both by online-MS and NMR spectroscopy experiments. For on-line MS experiments, 30 mM of 9,10 dimethlyanthracene (DMA) was dissolved in tetraglyme and 1 mL of this solution was added to a stoppered UV-Vis cuvette. The solution was purged with a 20% O_2:80% Ar gas mixture with a 0.7 mL min^{-1} flow rate. Once *m/z* 40 and *m/z* 32 signals were stabilised, a 660 nm light source was turned on. $^1O_2$ generation started and some of it got trapped by DMA resulting in formation of $DMAO_2$. Hence, a decrease in the amount of $^3O_2$ is observed in the MS signal (**Figure 5-3**). This method gives a lower estimate for the $^1O_2$ content as the $^1O_2$ lifetime is short (µs) and the kinetics for trapping the molecule is unknown.

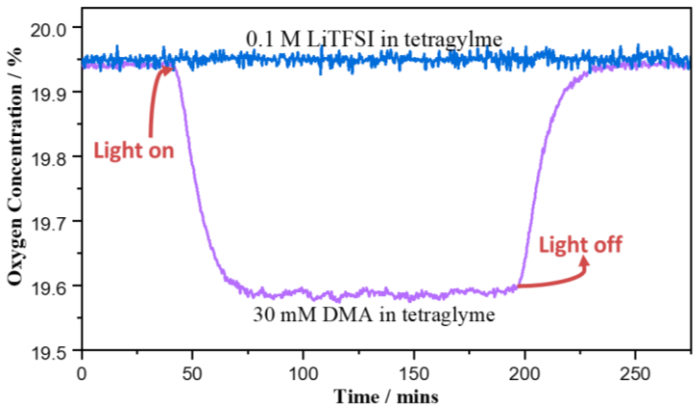

Figure 5-3 *On-line mass spectrometry data showing $^3O_2$ consumption, i.e. the $^1O_2$ generation and capture by DMA before it relaxes back to $^3O_2$.*

For ^{1}H NMR experiments, 75 mM DMA was dissolved in 0.1 M LiTFSI tetraglyme electrolyte and O_2 (N5.0 grade) was bubbled into the solution (**Figure 5-4**). The light was turned on after 2 hours to make sure that the solution was initially saturated with $^3O_2$ before $^1O_2$ generation. The duration of light exposure was recorded and samples were analysed by quantitative NMR as previously detailed in **Section 5.2.4**. The amount of $DMAO_2$ was calculated by integrating the NMR data and the $^1O_2$ generation rate was estimated as 1.56 x 10^{-5} mol min^{-1}. If we compare this rate with the literature, $^1O_2$ generation value (2% from charging) and assume 50 µA or 1 mA constant current, we get 3.11 x 10^{-10} and 6.12 x 10^{-9} mol min^{-1}, respectively. This shows that the amount of $^1O_2$ generation is several orders of magnitude higher than that of anticipated during charging a LOB (**Section 7.3.1**).

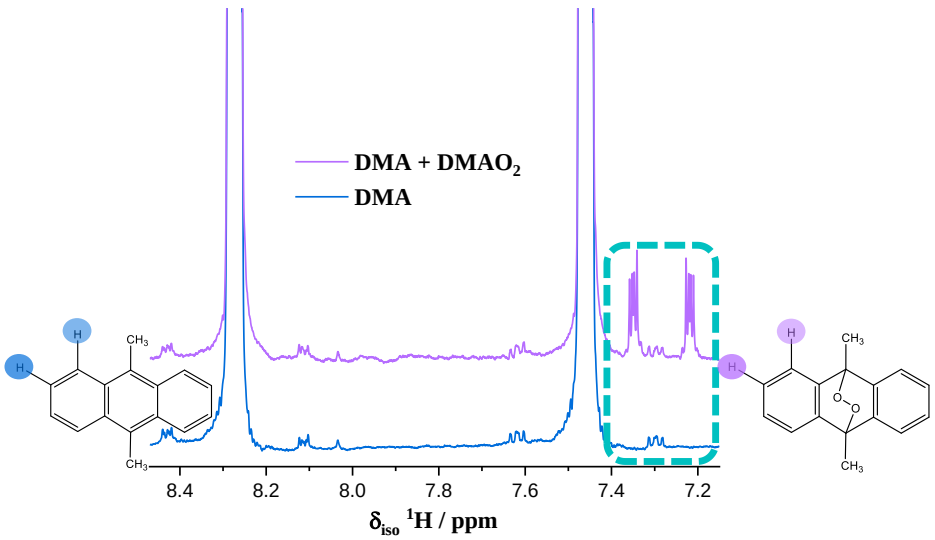

Figure 5-4 *The ^{1}H NMR spectra of the solution containing 75 mM DMA and $^1O_2$ exposed solution showing resonances for DMA and $DMAO_2$. The aromatic peaks for $DMAO_2$ are marked in the dashed box.*

The efficiency of the $^1O_2$ generation was tested under an applied potential as well. DMA (75 mM) containing electrolyte was held at 3.8 V for 3 hours and then the light was turned on to start the $^1O_2$ generation, whilst the light exposure and voltage was kept constant. The amount of $DMAO_2$ is not affected by the voltage.

5.2.3 Electrochemical Experiments

The aim of this study is to decouple the different factors that can contribute to decomposition and study the effect of $^1O_2$ separately. Hence, two different potentials (3.55 V and 3.8 V vs. Li^+/Li, all potentials herein are referenced to Li/Li^+), three different gas environments (Ar, $^3O_2$, and $^3O_2$-$^1O_2$ which will be referred to as $^1O_2$) along with pristine ^{13}C and Li_2O_2 preloaded ^{13}C WEs are used. To replicated the LOB charging conditions, pristine ^{13}C WEs were held at a constant potential (3.55 V and 3.8 V) for 12 hours in Ar, $^3O_2$, and $^1O_2$. To study the effect of Li_2O_2, Li_2O_2 preloaded (~2 mAh) ^{13}C WEs were held at 3.8 V in Ar for 12 hours. The capacity at this potential without RMs was 0.250 mAh. To compare the difference between preloaded Li_2O_2 electrodes and electrochemically generated Li_2O_2, cells with ^{13}C pristine electrodes were discharged to 2 mAh using a 0.169 mA cm^{-2} current density and after discharge some of the cells were charged to 0.250 mAh using a current density of 0.052 mA cm^{-2}.

5.2.4 NMR Analysis

^{1}H Nuclear Magnetic Resonance (NMR). For the electrolyte samples, deuterated benzene (C_6D_6) was employed as the lock solvent in a 1:9 lock solvent to sample ratio. The measurements were completed semi-quantitatively using a 30-degree tip angle (Ernst angle) i.e. measuring the side-product signals in different samples can be compared quantitatively (**Section 7.3.2**). NMR experiments were performed on a Bruker AVIII 400 (υ_0 (^{1}H) = 400.17 MHz) spectrometer equipped with 5 mm z-gradient broadband multinuclear probe. The T_1 was calculated using an inversion recovery sequence, and a 10 second recycle delay (>5T_1) was used throughout. The ^{13}C cathodes were washed with DME and dried under vacuum after the electrochemical experiments. The cathode was then soaked in 750 µL D_2O. The samples were sonicated for 1 minute and soaked for

12 hours. NMR experiments were done semi-quantitatively using the same parameters outlined above.

^{17}O solution state Nuclear Magnetic Resonance (NMR). Natural abundance ^{17}O solution state NMR spectra were completed using a Bruker Avance III spectrometer with a Larmor frequency of 67.77 MHz. A recycle delay of 0.1 seconds was used and a minimum of 4000 transients were collected. All spectra are referenced to $H_2{}^{17}O$ (aq, δ_{iso} = 0 ppm).

^{1}H-^{13}C and ^{1}H-^{6}Li Cross Polarisation (CP) Magic Angle Spinning (MAS) Solid State Nuclear Magnetic Resonance (NMR). All solid state NMR experiments were performed on a 9.45 T Bruker Avance III HD NMR spectrometer, operating at ^{1}H, ^{13}C and ^{6}Li Larmor frequencies of 400.19, 100.64 and 58.89 MHz respectively. A Bruker 4 mm double-resonance magic angle spinning (MAS) probe was used to facilitate spinning frequencies of 12 kHz. For cross polarisation experiments a 5 ms ramped (70-100 %) contact pulse was employed with 100 kHz ^{1}H SPINAL-64 heteronuclear decoupling. For direct observation experiments with decoupling, 4 µs excitation (62.5 kHz) was used. A minimum of 2048 transients were recorded for each spectrum with a recycle delay of 5 seconds. All spectra were referenced to TMS (neat, ^{1}H δ_{iso} = 0 ppm), α-^{13}C-glycine (s, δ_{iso} ^{13}COOH = 176.5 ppm) or 1M LiCl (aq, ^{6}Li δ_{iso} = 0 ppm).

5.2.5 On-line Mass-Spectrometry Analysis

On-line MS was used to monitor the reactivity of $^{1}O_2$ with the selected solvents and to quantify the carbonate and carboxylate groups on Li_2O_2 powders. For monitoring the reactivity of $^{1}O_2$, the gas outlet of the $^{3}O_2$ purged samples was connected to an on-line MS, and once a stable $^{3}O_2$ baseline was achieved, samples were irradiated to begin $^{1}O_2$ production. In the samples that react with $^{1}O_2$, $^{3}O_2$ consumption was observed as any unreacted $^{1}O_2$ returns to ground state $^{3}O_2$ within few µs.

To study the amount of carbonate and carboxylate groups generated on ^{13}C cathodes and aged Li_2O_2 powders, acid (**Section 2.2.1.1**) and Fenton's reagent (**Section 2.2.1.2**) treatments were used. For ^{13}C samples, the electrodes were rinsed with DME and dried under vacuum and for the Li_2O_2 samples, pristine or treated Li_2O_2 powder (2 mg) was added into a stoppered vial with a stir bar

(**Figure 5-5**). The sample was then connected to the on-line MS and Ar was used as the purge gas. Once *m/z* 44 (CO_2) and *m/z* 45 ($^{13}CO_2$) signals stabilised, phosphoric acid was added to decompose all the carbonate. This reaction releases CO_2.

$$CO_3^{2-} \rightleftharpoons HCO_3^- \rightleftharpoons \boldsymbol{CO_2}$$

After the $^{12\text{-}13}CO_2$ signals stabilised for the second time, Fenton's reagent was added to generate radicals such as $OH^\bullet$ and $HO_2^\bullet$ which cause one electron oxidation, hydrogen abstraction, and radical addition reactions. In the LOB literature, Fenton's reagent is used to decompose and quantify total Li acetate and Li formate.[138] These reactions release CO_2 as well. However, it is important to note that any radical formed due to Fenton's reagent can decompose any other side products with electron rich regions such as C=C as they have unpaired valence electrons. Some of the possible reactions are listed below[307-310] The products formed after Fenton's reagent will be referred to as carboxylates throughout the Chapter.

$$Fe^{2+} + H_2O_2 \rightarrow Fe^{3+} + OH^\bullet + OH^-$$
$$Fe^{3+} + H_2O_2 \rightarrow Fe^{2+} + HO_2^\bullet + H^+$$
$$OH^\bullet + H_2O_2 \rightarrow H_2O + HO_2^\bullet$$

And these radicals could cause the following reactions

$$OH^\bullet + HCOOH \rightarrow \boldsymbol{CO_2} + HO_2^\bullet/O_2^{\bullet-}$$
$$OH^\bullet + HCOOH \rightarrow HCOO^\bullet + H_2O$$
$$OH^\bullet + HCOOH \rightarrow CO_2^{\bullet-} + H_2O + H^+$$
$$HCOO^\bullet + O_2 \rightarrow \boldsymbol{CO_2} + HO_2^\bullet/O_2^{\bullet-}$$
$$CO_2^{\bullet-} + O_2 + H^+ \rightarrow \boldsymbol{CO_2} + HO_2^\bullet/O_2^{\bullet-}$$
$$HCOO^\bullet + HCOO^\bullet \rightarrow \boldsymbol{CO_2} + HCOOH$$
$$CO_2^{\bullet-} + Fe(III) \rightarrow \boldsymbol{CO_2} + Fe(II)$$
$$HCOO^\bullet + Fe(III) \rightarrow \boldsymbol{CO_2} + Fe(II) + H^+$$

$$OH^\bullet + CH_3COOH \rightarrow CH_3COO^\bullet + H_2O$$
$$CH_3COO^\bullet \rightarrow \boldsymbol{CO_2} + H_3C^\bullet$$

$$OH^\bullet + RH \rightarrow H_2O + R^\bullet$$

$$OH^\bullet + RH \rightarrow HORH^\bullet$$

$$OH^\bullet + C = C \rightarrow HOCC^\bullet$$

$$OH^\bullet + RCOOH + OH^\bullet \rightarrow RCOO^\bullet + H_2O \rightarrow \boldsymbol{CO_2} + R^\bullet$$
$$R^\bullet + Fe(III) \rightarrow Fe(II) + R^+$$

$RCO_2Fe(III) + h\nu \rightarrow RCO_2^\bullet + Fe(II) \rightarrow R^\bullet + \boldsymbol{CO_2}$ (absorption usually around near-UV and visible regions)

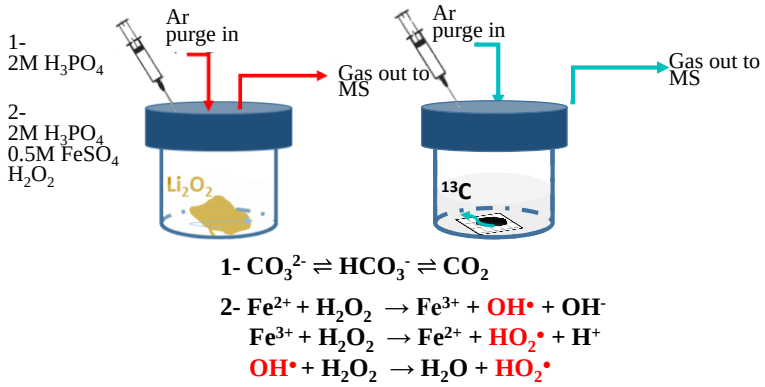

Figure 5-5 *A schematic representation of the set-up connected to the on-line MS apparatus for carbonate and carboxylate analysis.*

5.2.6 FTIR Analysis

FTIR analysis was carried out following the protocol described in **Section 2.2.4**. For electrolyte and solvent only samples, a few µL of samples was directly dropped onto a diamond ATR crystal and for powder samples the crystal was coated in the powder. The powder was flattened and fixed in place with the plunger on the measurement stage to make sure that there was a good contact between the diamond ATR crystal and the sample.

5.3 Results and Discussion

On-line MS measurements are essential for calculating the e^-/O_2 ratio on discharge and charge, allowing for evaluation of the faradaic efficiency. In the previous Chapter, tetraglyme and 1 M LiTFSI in tetraglyme were treated with $^1O_2$ and no O_2 consumption was observed during this test according to the MS data. Wandt et al.[205] suggest that the onset potential for $^1O_2$ generation is between 3.45 - 3.55 V and the amount increases with a higher potential (up to a 4 V cut-off in their experiments). To avoid electrolyte degradation, in this work, the potential hold experiments were carried out at 3.55V and 3.8V. The stability of 0.1M LiTFSI in tetraglyme is tested at 3.8 V for 12 hours under constant in-situ $^1O_2$ generation, and **Figure 5-6** shows that there is no O_2 apparent consumption. The gas evolved is swept from the cell with an O_2:Ar carrier gas at 1 mL min^{-1}. Hence, if the changes (signal) are smaller than the noise, the gas evolution or consumption will not be

detected. However, a reaction below the S/N ratio limitation of the on-line MS which can detect ppm amounts cannot be significant enough to cause the observed Faradaic efficiency loss.

The online-MS results suggest that the electrolyte and the carbon cathode are stable towards $^1O_2$ at 3.8 V. To further confirm the presence of any side products due to $^1O_2$ reacting with the electrolyte, a combination of NMR spectroscopy, acid, and Fenton's reagent treatments were carried out on both the cathode and electrolyte after 12h of exposure to $^1O_2$.

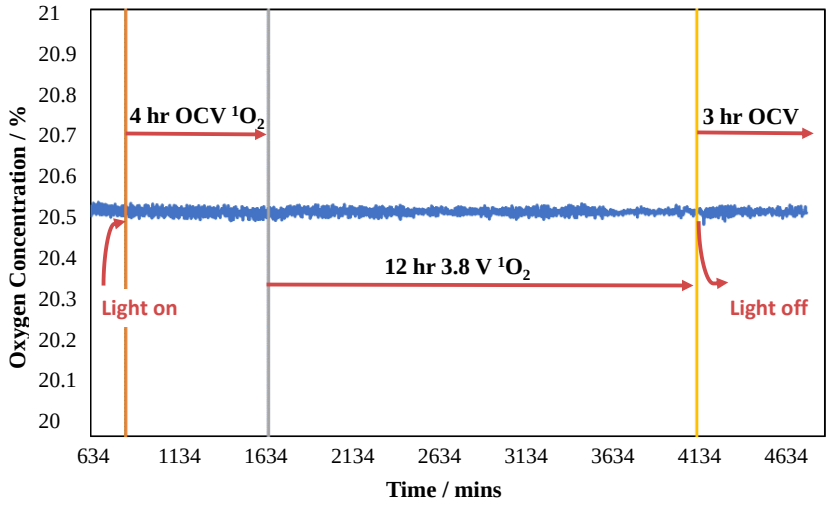

Figure 5-6 *On-line mass spectrometry data showing no significant change in the $^3O_2$ concentration, within the sensitivity limits of the instrument, due to reactions of $^1O_2$ (generated via a photosynthesiser) under chemical (OCV, ~3.15 V) and electrochemical conditions (3.8 V).*

5.3.1 NMR Results

^{1}H, proton, NMR was used to detect the electrolyte degradation due to $^1O_2$.[311,312] Li acetate and Li formate are the two main degradation products reported in LOBs.[138,313] Here, by decoupling possible causes of degradation, it is shown that $^1O_2$ is not causing any major changes in the electrolyte when compared to Ar or $^3O_2$. The overall NMR spectra for the electrolyte samples are shown in **Figure 5-7**. The tetraglyme resonances observed are a singlet at 3.21 ppm which represents the terminal –C**H$_3$**, two overlapped doublets at 3.37 ppm due to the OC**H$_2$**C**H$_2$**OCH$_3$ protons, and a doublet at 3.48 ppm for the central –OC**H$_2$**C**H$_2$**O- motif.

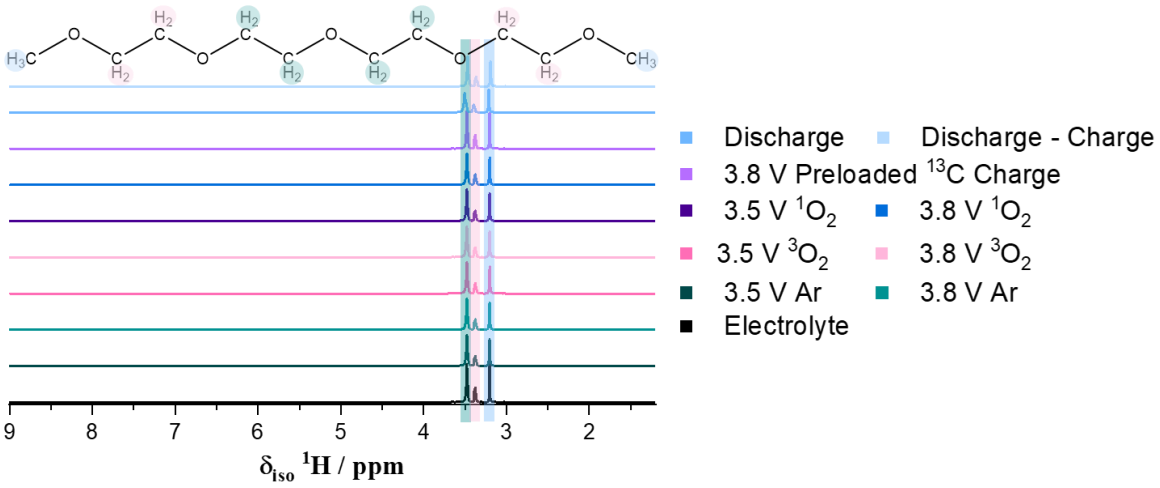

Figure 5-7 *The ^{1}H NMR spectra for electrolyte samples showing tetraglyme peaks and no other major peaks.*

Under these conditions no Li formate is detected in the constant potential hold samples, and trace amount of Li formate is identified in the discharge and discharged-charged samples (**Figure S19**). The Li acetate peak is observed at ~1.98 ppm for the majority of the samples (**Figure 5-8**). However, as mentioned above no difference is detected between the Ar, $^{3}O_2$, and $^{1}O_2$ samples. All the other small changes, such as the peaks at ~2 ppm in the Ar samples, which are less than 1% (smaller in intensity than the satellites of the tetraglyme peaks) are consistent for different gas conditions.

Kwak et al.[109] test the stability of new fluorinated solvent systems and tetraglyme towards $^{1}O_2$. Their ^{1}H NMR data shows that that tetraglyme decomposes upon exposure to $^{1}O_2$ whereas one of the selected fluorinated solvents does not show any signs of degradation. The ^{1}H NMR data is unambiguous; however, the degradation in tetraglyme is unlikely to be due to $^{1}O_2$ as the authors chemically generate $^{1}O_2$ by adding 30% H_2O_2 in water and NaOCl to the solvents which could react with the electrolyte as they are both oxidants. In this Chapter and Chapter 4, excess amount of $^{1}O_2$ was generated in-situ and no significant changes were observed in the electrolyte under chemical and the specified electrochemical conditions.

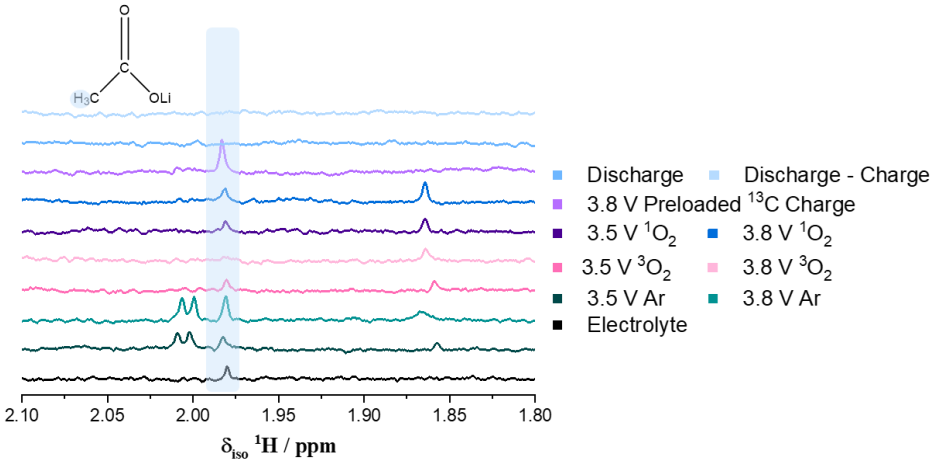

Figure 5-8 *The low frequency region of the ^{1}H spectra of the electrolyte samples showing Li acetate peak at ~1.98 ppm. No significant changes are observed for $^{1}O_2$ treated samples.*

There was not any significant degradation observed in the bulk electrolyte. Therefore, the cathode was analysed for detection of the degradation products. The cathodes were soaked in D_2O to dissolve any Li acetate and formate (**Figure 5-9**). Considerably more degradation was observed

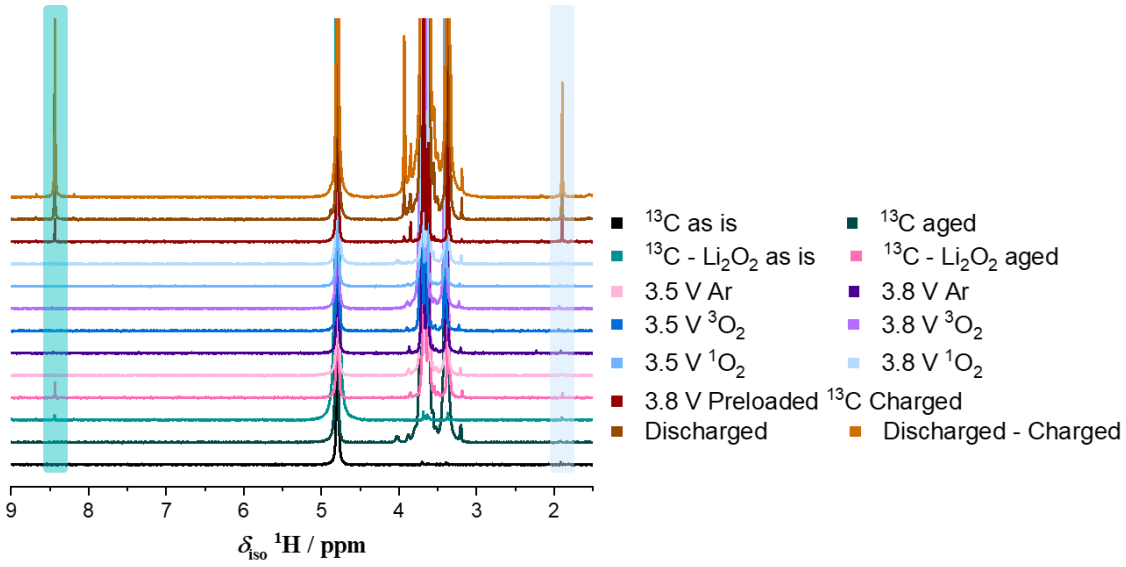

Figure 5-9 *The ^{1}H NMR spectra for D_2O washed cathodes. Any Li formate and acetate forming will be observed in the highlighted regions. The peak at 4.70 ppm is from the lock solvent D_2O and the resonances between 3 - 4 ppm are residual tetraglyme and DME peaks.*

in the samples containing Li_2O_2 i.e the samples discharged to 2 mAh and charged to 0.25 mAh, the samples discharged to 2 mAh, and the Li_2O_2 preloaded (~2 mAh) samples that were charged to 0.25 mAh capacity at 3.8 V. No significant carboxylate formation is detected on $^{1}O_2$ treated samples.

The purity of in-house synthesised Li_2O_2 is > 98.5% as determined by $KMnO_4$ titration. Li carbonate and carboxylates can be detected via acid treatment of Li_2O_2 without carbon. Through this analysis the amount of carbonate is determined to be less than 0.2% (**Section 5.3.3**). Hence, the preloaded ^{13}C cathodes show a small amount of Li formate and acetate when washed with D_2O (**Figure 5-11**). A trace amount of acetate is observed on the pristine ^{13}C cathodes as well. When Li_2O_2 preloaded cathodes were aged in the electrolyte, the amount of formate and acetate increased. This suggests that Li_2O_2 surfaces react with the electrolyte. More Li formate formed upon aging the Li_2O_2 preloaded cathodes compared to Li acetate (**Figure 5-10** and **Figure 5-11**). The total amount of side products increased as the preloaded Li_2O_2 was oxidised at 3.8 V as fresh surfaces are continuously exposed resulting in continued degradation. As seen in the **Figure 5-11**, the degree of degradation increases considerably when Li_2O_2 was electrochemically generated (discharged sample) and when the electrochemically generated Li_2O_2 was oxidised to the same capacity as the preloaded Li_2O_2 sample (discharged-charged sample). It is important to note that preloaded cathodes were oxidised at 3.8 V, but the potential increased only to 3.4 V for discharged-charged samples. Since most of the degradation in LOBs is seen above 3.6 V, this indicates that the degradation due to fresh Li_2O_2 surfaces would be higher than that of preloaded Li_2O_2. Overall, these findings strongly suggest that $^1O_2$ is not the main source of degradation and the stability of the electrolyte and cathode towards Li_2O_2 and Li deficient $Li_{2-x}O_2$ surfaces should be reconsidered.

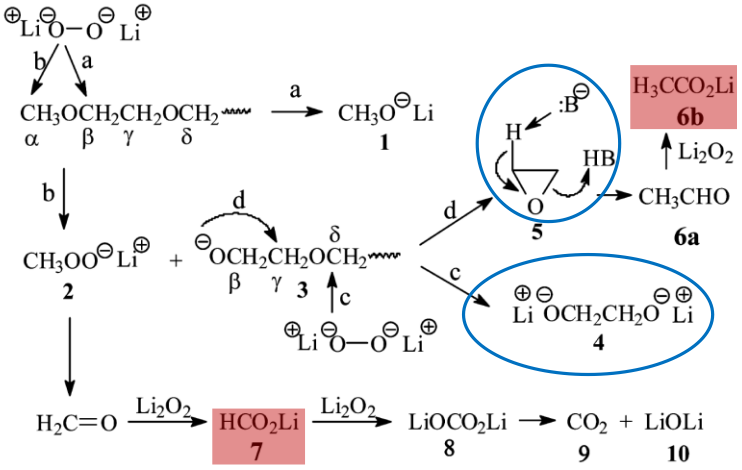

Figure 5-10 *The reaction scheme proposed by Aurbach and co-workers. It shows that Li_2O_2 can react with glymes and generate Li formate and acetate. The route leading to Li acetate involves the formation of an epoxide (5) whereas formation of dianion of ethylene (4) seems more plausible. Hence, it should be easier to form Li formate under chemical conditions as observed in the experimental data. Reprinted with the permission from ref 97. Copyright 2013, American Chemical Society.*

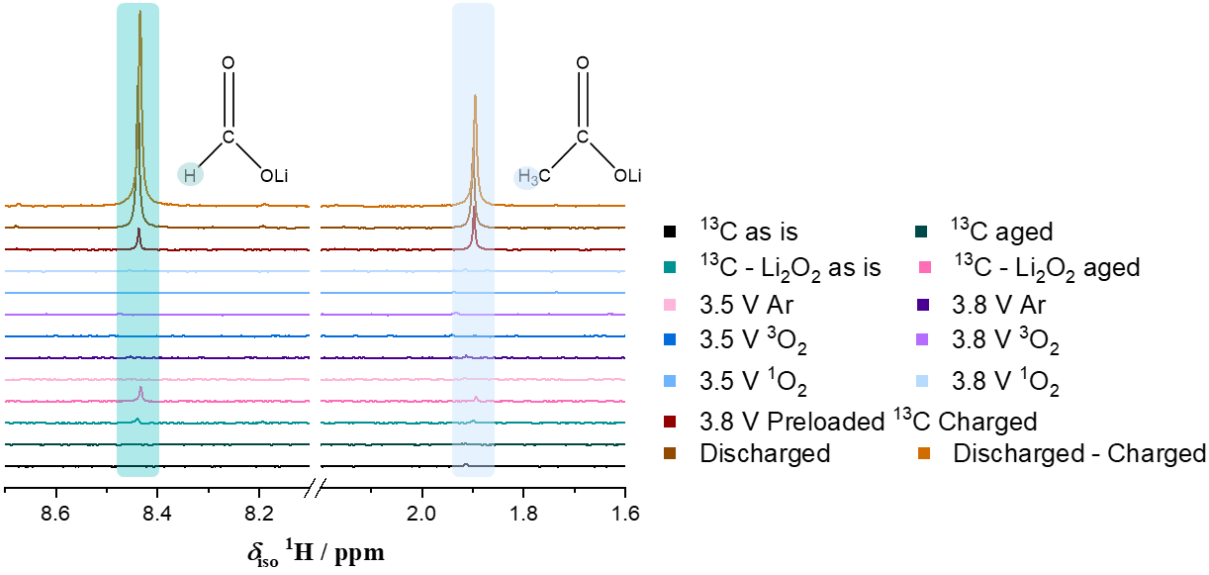

Figure 5-11 *The ^1H NMR spectra of the D_2O washed cathodes highlighting the Li formate (8.44 ppm) and Li acetate (1.90 ppm) regions.*

5.3.2 On-line Mass Spectrometry Results

Li carbonate and carboxylates on the cathode were quantified using established acid and Fenton's reagent treatments.[138] Under acidic conditions, Li carbonate decomposes to release CO_2. Any carbonate formed from cathode decomposition will release $^{13}CO_2$ whilst $^{12}CO_2$ is released due to electrolyte decomposition. After all the carbonate is decomposed and the $^{12\text{-}13}CO_2$ *m/z* 44-45 signal returns to a baseline value, Fenton's reagent is injected to decompose carboxylates. The area

under the gas evolution peaks in *m/z* 44 and *m/z* 45 data is then integrated to calculate the total amount of $^{12}CO_2$ and $^{13}CO_2$ evolved due to carbonates and other side products such Li formate (**Figure 5-12**).

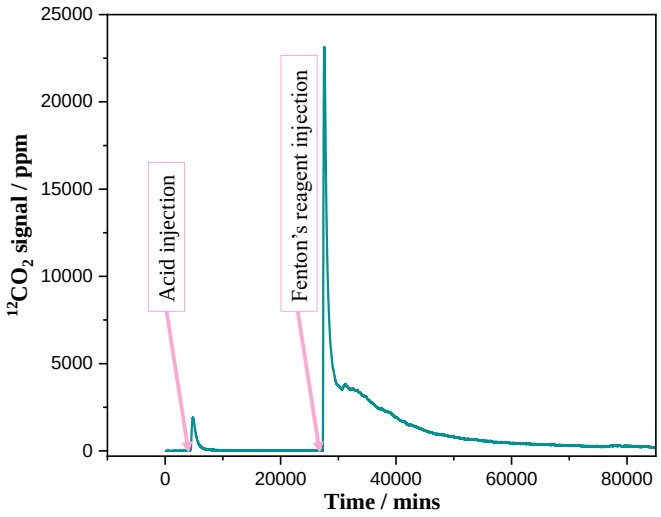

Figure 5-12 *The on-line mass spectrometry data showing $^{12}CO_2$ evolution upon injection of acid and Fenton's reagent to a ^{13}C cathode discharged to 2 mAh.*

The integrated gas evolution data shows that the main decomposition product is carboxylate from the electrolyte followed by electrolyte carbonate, cathode carboxylate, and cathode carbonate (**Figure 5-13** and **Figure S28**). The largest amount of degradation is seen in the discharged-charged samples followed by the Li_2O_2 preloaded samples. There is no significant difference in the degradation between experiments completed under an Ar, $^3O_2$, or $^1O_2$ atmosphere. This suggests that at high potentials, such as 3.8 V, and during continuous $^1O_2$ generation, the carbon cathode and electrolyte do not degrade enough to account for the faradaic efficiency loss. The increase in the degradation with the introduction of bulk Li_2O_2 and generation of fresh Li_2O_2 suggests that Li_2O_2 is the cause of parasitic reactions. The amount of preloaded Li_2O_2 corresponds to a 2 mAh capacity and the cells were discharged to the same capacity. Even at this low capacity[e], the amount of degradation is considerably higher than those under $^1O_2$ exposure. The preloaded cells give less side products compared to the discharged-charged cells even though

[e] The cells were discharged to 2 mAh at a 0.169 mA cm^{-2} current density. Currently, we can achieve 8 mAh capacity at 1 mA cm^{-2} current density using DBBQ as a discharge mediator.

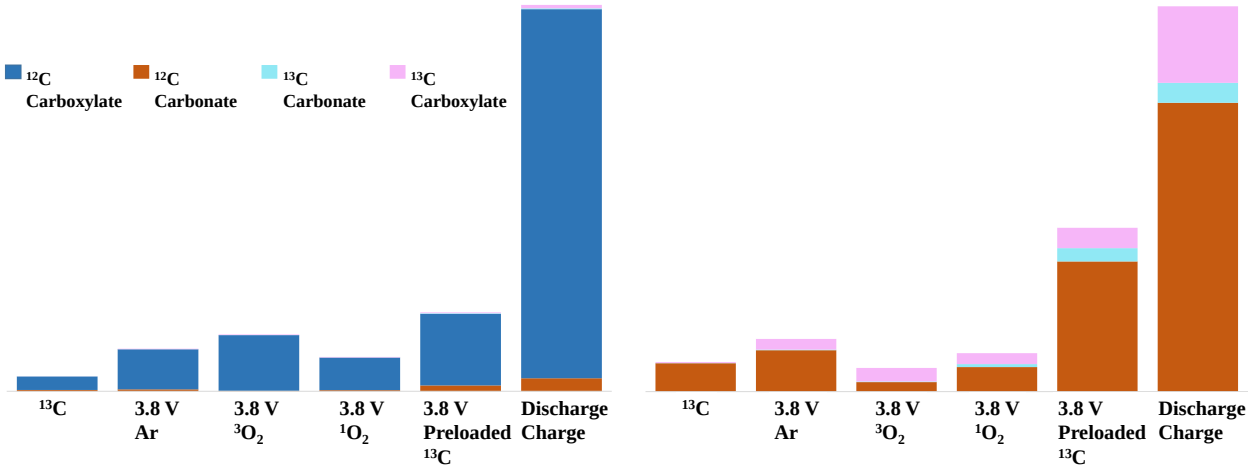

Figure 5-13 *A comparison of amount of $^{12}CO_2$ and $^{13}CO_2$ evolved from the cathodes after acid and Fenton's reagent treatments to decompose Li_2CO_3 and carboxylates, respectively. The same data including the results of 3.55 V experiments are shown in* ***Figure S28****.*

theoretically they have the same amount of Li_2O_2 and were charged to the same capacity. Moreover, all the charging of the preloaded cells were done at a constant potential of 3.8 V whereas discharged-charged cells achieved ~3.4 V at the same capacity. Hence, they have less degradation arising from high voltages or $^1O_2$ formation. This shows that fresh surfaces and potentially Li deficient $Li_{2-x}O_2$ surfaces are the true cause of faradaic efficiency loss. Li_2O_2 and any Li formate and acetate forming on the surface due to reaction with the electrolyte get oxidised at 3.8 V. Li_2O_2 oxidation is limited at this potential without a charge mediator, and Li carbonate does not get oxidised preventing Li_2O_2 from oxidation. Hence, the amount of degradation is lower than that of the discharged-charged samples where there is more fresh Li_2O_2 exposed and degraded.

A comparison of the 3.55 V and 3.8 V data shows that the electrolyte carboxylate formed is higher and electrolyte carbonate is lower at 3.55 V than those of at 3.8 V. This is a result of carboxylates getting oxidised as the potential increases. $^1O_2$ affects the amount of carboxylate (3.55 V) and carbonate (3.8 V) formation on the cathode. Compton and co-workers showed that functional groups on the carbon electrode increases due to in-situ generated $^1O_2$ in an aqueous electrolyte.[222] They hypothesise that $^1O_2$ reacts with electron rich zones on graphite surfaces such as dangling bonds and radicals following Diels-Alder [2+2] and [4+2] type of addition reactions. Carboxylates can get oxidised at 3.8 V; however, because the degradation due to Li_2O_2 surfaces is

high, the electrolyte and cathode carboxylate amount in the preloaded samples is close to that of 3.55 V and higher than that of the 3.8 V $^1O_2$ experiments. Overall, while $^1O_2$ could increase the number of functional groups on the carbon source and is a reactive species, it does not mean that it will react with any electron rich zone e.g. double bonds. For example, $^1O_2$ reacts with anthracene, DMA, and higher members of acene series by cycloaddition and the reaction yields the respective endoperoxides, but unsubstituted electron rich aromatic carbons such as benzene and naphthalene do not readily react with $^1O_2$.[290]

Table 3 *The amount of $^{12\text{-}13}C$ carbonate and carboxylate evolved from cathodes after acid and Fenton's reagent treatments under specified conditions. The data for $^{12\text{-}13}C$ carbonate and carboxylate is normalised between 0 to 100. (Units are mole/mole)*

	^{12}C Carbonate	^{12}C Carboxylate	^{13}C Carbonate	^{13}C Carboxylate	Total
^{13}C	0.3462	3.6433	0.0014	0.0124	**4.0033**
^{13}C - Li_2O_2	0.4250	4.2216	0.1291	0.0456	**4.8213**
3.55 V Ar	0.1679	22.8582	0.0000	0.1146	**23.1406**
3.55 V $^3O_2$	0.2954	17.1577	0.0000	0.0852	**17.5382**
3.55 V $^1O_2$	0.0963	31.9177	0.0000	0.2090	**32.2231**
3.8 V Ar	0.5042	10.8717	0.0080	0.1289	**11.5128**
3.8 V $^3O_2$	0.1160	15.0915	0.0069	0.1658	**15.3803**
3.8 V $^1O_2$	0.2991	8.8204	0.0355	0.1335	**9.2885**
3.8 V ^{13}C - Li_2O_2	1.5859	19.3837	0.1615	0.2479	**21.3790**
Discharge – Charge	3.5182	100.0000	0.2278	0.9319	**104.6779**

5.3.3 The Real Cause of Degradation in Li-O_2 Cells: Fresh Li_2O_2 surfaces

It has been previously suggested that Li_2O_2 reacts with the carbon cathode and the electrolytes.[98,127,313,314] However, studies contradicting each other were published and there is currently no consensus on the reactivity of Li_2O_2.[90,125,207] As $^1O_2$ was detected in LOBs, most of the degradation was attributed to this phenomena. However, based on the data presented on the reactivity under chemical conditions in **Chapter 4** and the reactivity under electrochemical

conditions presented here, it is explicitly shown that $^1O_2$ is not the major source of degradation. Hence, the reactivity of Li_2O_2 will be considered in more detail.

In-house synthesised bulk Li_2O_2 was aged in tetraglyme, centrifuged and washed with toluene to remove any remaining tetraglyme. The solvent and the powder were both investigated for changes after aging. The XRD pattern of the pristine in-house synthesised Li_2O_2 is compared with Li_2O_2 aged in tetraglyme in **Figure 5-14**. There are no new crystalline products formed on the powders, while the broad features at low 2θ (0-33°) indicate the presence of amorphous material formed on the aged Li_2O_2 powder. The long-range order is disrupted in amorphous materials, and broad features (amorphous halo) in the XRD diffractograms are due to distribution of interatomic distances within the amorphous/disordered structures. There is a broad peak at ~10° and the baseline is higher suggesting there is a hump until ~33°. This could also be due to very small partide size LiOH, which is also observed in the FTIR spectra in **Figure 5-15**.

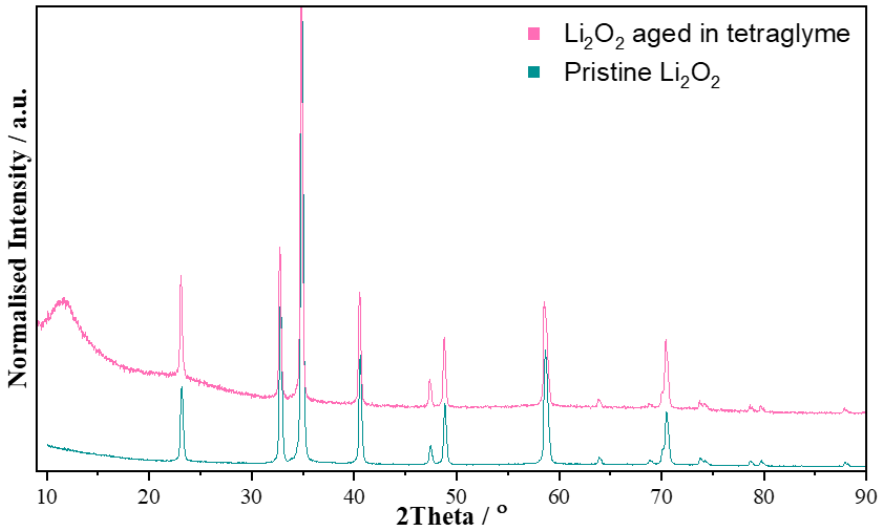

Figure 5-14 *XRD patterns for pristine Li_2O_2 and Li_2O_2 aged in tetraglyme.*

The amorphous products formed on Li_2O_2 after aging in tetraglyme were determined by FTIR spectroscopy. The FTIR spectrum is compared with that of pristine Li_2O_2 and common degradation products such as Li acetate and Li formate in **Figure 5-15**. The pristine Li_2O_2 has peaks below 500 cm^{-1}. It is > 98.5% pure according to $KMnO_4$ and $TiOSO_4$ titration. Hence, a weak peak for LiOH is observed around ~3500 cm^{-1} in the pristine material as well. The broad peaks around

1000 cm^{-1} suggest the formation of C=C and C-O bonds, as C=C bending is usually observed in the 1000 - 650 cm^{-1} region and C-O stretching is usually observed in the 1150 -1085 cm^{-1} region. The peaks around 1300 - 1400 cm^{-1} point to acyl (R-C=O) C-O and C-H bending and 1690 - 1550 cm^{-1} suggests the presence of C=O stretching in the side products.

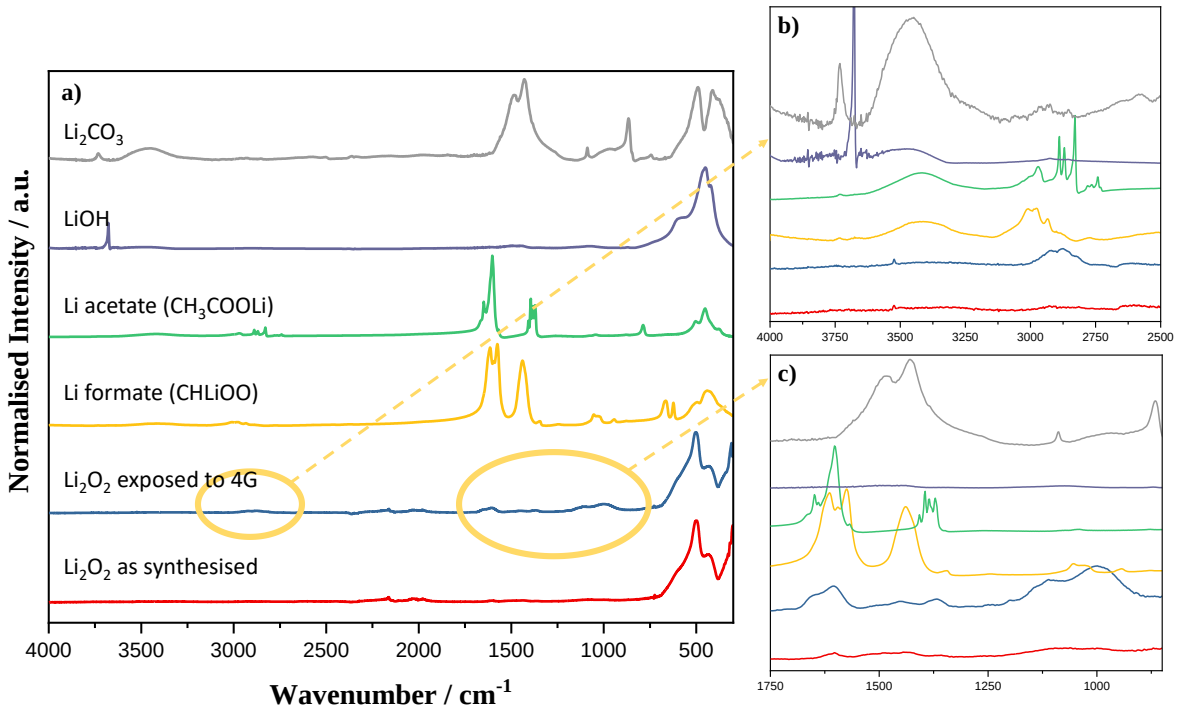

Figure 5-15 *a) The FTIR spectra of as synthesised > 99% pure Li_2O_2 before and after exposure to tetraglyme and common side products found in LOBs; Li_2CO_3, LiOH, Li acetate, and Li formate. The broadness and overlap of newly forming peaks make assignment of side products after tetraglyme exposure difficult. b-c) Expansions of the yellow marked regions showing newly formed peaks.*

The aged Li_2O_2 powder was investigated with solid state NMR spectroscopy. **Figure 5-16** shows CPMAS spectra, ^{1}H to ^{13}C and ^{1}H to ^{6}Li. The ^{6}Li spectra shows that there is some -H containing impurities on the aged Li_2O_2. This is most likely due to the presence LiOH which is also detected with FTIR. The organic side products observed in FTIR spectra could not be detected. This is due to the low concentration of newly formed species as well as the low natural abundancy of ^{13}C and inherent insensitivity of NMR. This suggests that the amount of degradation is small as the degradation will terminate once all the surface of Li_2O_2 is covered with side products meaning the bulk powder will not be reacting.

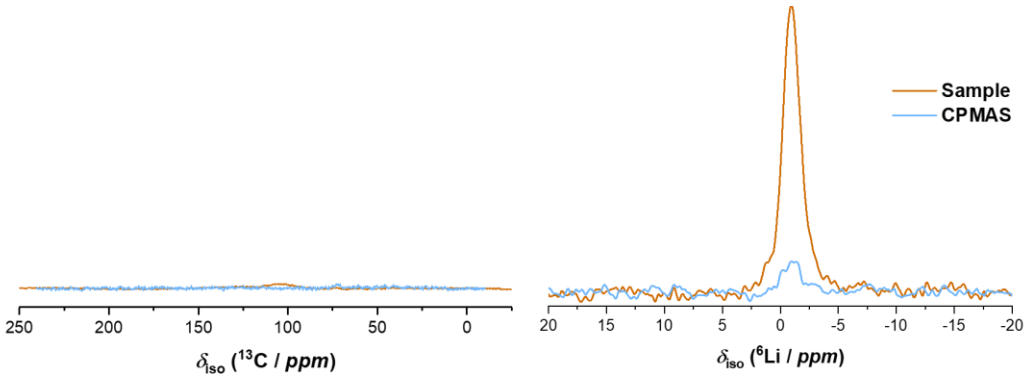

Figure 5-16 *The solid state NMR spectra for Li_2O_2 aged in tetraglyme. The MAS (Sample) and CPMAS spectra for ^{13}C does not any side product formation. The peak in the ^{6}Li CPMAS spectrum shows that there is an impurity containing Li and H. The CPMAS spectra shows the dipolar mediated through-space interactions between ^{1}H and $^{13}C/^{6}Li$ meaning the resonance observed shows $^{13}C/^{6}Li$ nuclear spins which are in close proximity to ^{1}H.*

Natural abundance ^{17}O solution state NMR spectra for tetraglyme after exposure to Li_2O_2 do not show any significant changes in the oxygen environment. Similar to solid state NMR data, this could be due to the low concentration of -O containing side products. The ^{1}H NMR spectra do not show any changes either. The concentration of the electrolyte is higher than the amount of exposed Li_2O_2 surfaces. Hence, any degradation in the electrolyte is very dilute in these conditions.

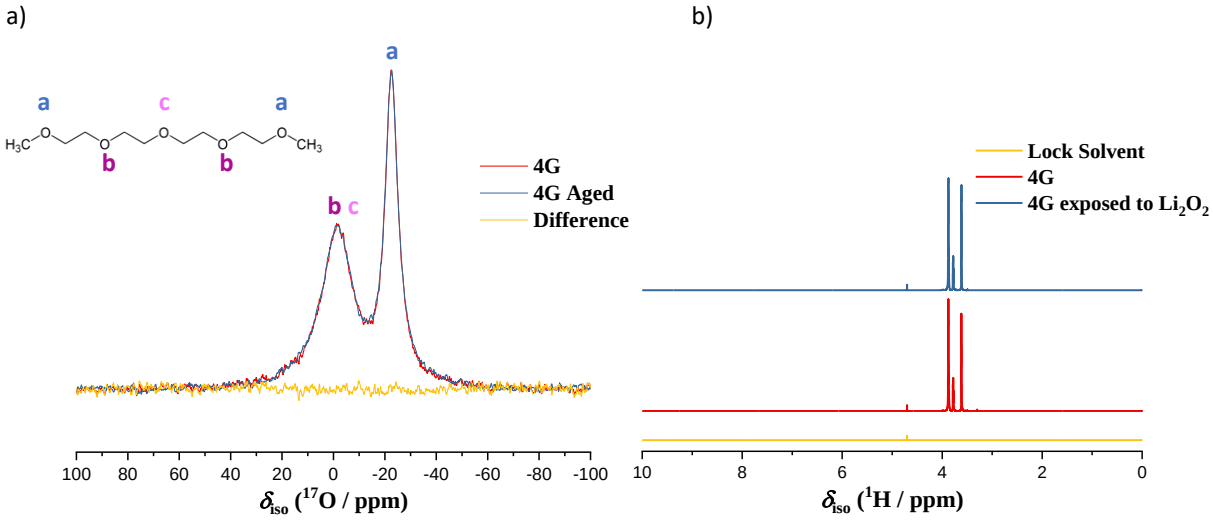

Figure 5-17 *a) Natural abundance ^{17}O NMR spectra of tetraglyme and tetraglyme exposed to Li_2O_2. b) ^{1}H NMR of pristine tetraglyme and tetraglyme after Li_2O_2 exposure.*

The degradation products on the Li_2O_2 surface was further analysed by acid and Fenton's reagent treatments to determine the amount of Li_2CO_3 and carboxylates (**Table 4**). The amount of degradation starts increasing as tetraglyme is added to the Li_2O_2 powder and terminates once all the fresh surfaces are all covered with degradation products. It is unambiguous that fresh Li_2O_2

surfaces react with tetraglyme and mainly form carboxylates under chemical conditions when the amount of degradation of Li_2O_2 after 1 hour of aging with and without constant stirring is compared. When Li_2O_2 powder is stirred, the larger Li_2O_2 particles are broken up generating fresh surfaces, which then can further react with tetraglyme.

Table 4 *Amount of Li_2CO_3 and carboxylates forming on Li_2O_2 surface after exposure to tetraglyme.*

ageing duration	mole % carbonate per mole Li_2O_2	mole % carboxylate per mole Li_2O_2
as is	0.20	3.80
5 min	0.22	4.35
1 hr	0.34	9.80
1 hr stir	0.35	54.67
2 days	0.32	6.61

The kinetics measurements for oxidation of Li_2O_2 with 10 mM $TEMPO^+$ in 100 mM LiTFSI in tetraglyme obtained by SECM show that the apparent rate constant decreases as Li_2O_2 is aged in the electrolyte (**Figure 5-18**). This is due to fouling of the Li_2O_2 surface and supports the conclusion that the main source of degradation in LOBs is the fresh Li_2O_2 surfaces.

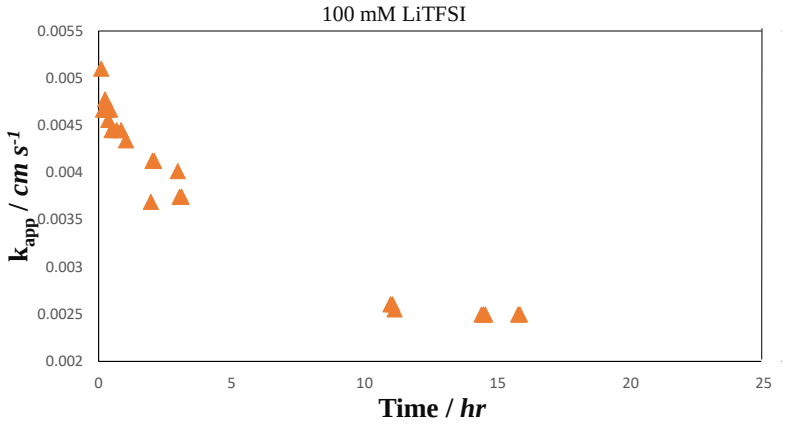

Figure 5-18 *The kinetics (k_{app}) of $TEMPO^+$ reaction with an Li_2O_2 pellet as a function of time. k_{app} decreases over time, and this is due to the Li_2O_2 surface being poisoned/reacting over time.*

5.4 Conclusion

Singlet oxygen ($^1O_2$) has been considered as the main focus of degradation studies in LOBs since Wandt et al.[205] and Mahne et al.[210] suggested that there is $^1O_2$ evolution in these systems. However, the data presented in these studies detecting $^1O_2$ using traps is ambiguous and can be attributed to reactivity of the traps with reduced oxygen species. In Chapter 4, it is shown that the

widely used $^1O_2$ trap, DMA, can react with superoxide in various solvent-salt combinations used in LOBs and can generate $DMA(OH)_2$ depending on the pH.

$^1O_2$ formation in LOBs is not ruled out, but its origins is still not clear. Schroder and co-workers pointed out that electrochemical oxidation of Li_2O_2 whether it is a 1-e^- or 2-e^- transfer cannot generate excited species according to the Marcus-Hush-Chidsey theory.[201] Freunberger and co-workers suggested that there is $^1O_2$ from LiO_2 disproportionation.[208] Even though chemical generation of $^1O_2$ i.e. from disproportionation is theoretically possible, calculations of Bodo and co-workers suggested that Li^+ catalysed O_2^-+O_2^- disproportionation only promotes $^3O_2$ release, and $^1O_2$ in LOBs is due to H^+ catalysed disproportionation which can release both $^3O_2$ and $^1O_2$.[315]

If there is $^1O_2$ formation in LOBs, its reactivity has to be studied by decoupling different possible degradation pathways. Here, by generating $^1O_2$ in-situ, decoupling the effect of Li_2O_2, and studying the effect of $^3O_2$, it is shown that $^1O_2$ is not the main source of degradation under electrochemical conditions. The fresh Li_2O_2 surfaces reacting with the electrolyte result in the faradaic efficiency loss. Hence, future LOB research may need to target finding new electrolytes stable towards peroxide-driven species.

6 Chapter 6 – Conclusions and Perspectives

Current Situation

Electrolyte and cathode instability has been the main bottleneck in developing practical LOBs as well as oxygen solubility and mass transport. Before addressing these issues, it is important to understand the fundamental reactions in the battery. The discharge (ORR) and charge (OER) reactions were studied to understand the mechanism of these multistep reactions. It was shown that LiO_2 is an intermediate both on discharge and charge to form and decompose Li_2O_2, the discharge product. The solubility of LiO_2 and formation of the insulating and insoluble Li_2O_2 were shown to depend on the donor and acceptor numbers of the electrolyte solvent and salt. A range of electrolyte solvents were screened for their stability in LOBs. Even though their donor number is not as high as DMSO, glymes were found to be the most stable solvents towards reduced oxygen species and perform better compared to other screened solvents in LOBs. Side reactions and large overpotentials still caused faradaic efficiency loss and poor cycle life. Hence, redox mediators, both on discharge and charge were utilised to decouple the ORR and OER reactions from the electrode surface, lower the overpotentials and decrease the amount of degradation. Finally, recently, it was claimed that there is singlet oxygen ($^1O_2$) evolution in LOBs and it is the main cause of degradation.

Conclusions

Most of the degradation in LOBs happens during charging, even with the RMs, and increases with the voltage. There are a range of charge RMs with different formal potentials. The low potential RMs evolve small amounts of O_2 i.e. e^-/O_2 ratio deviates from the theoretical value of 2. The high voltage RMs have e^-/O_2 ratio closer to 2, but show more degradation. Therefore, it is important to understand the mediated charging mechanism. Here, in **Chapter 3**, it is shown that mediated oxidation follows Marcus theory of electron transfer and the rate limiting step is the first electron transfer. The kinetics were studied by scanning electrochemical microscopy and the inverted Marcus region was observed. As there are two electron transfer steps, the $^1O_2$ yield was studied to determine the rate limiting process. It is revealed that disproportionation is the

kinetically dominant step, first electron transfer forming LiO_2 is the rate limiting step and the second electron transfer which is the oxidation of LiO_2 by the RM depends on the RM formal potential. The $^1O_2$ yields show that the amount of degradation and the amount of $^1O_2$ are not correlated. This casts a doubt on whether $^1O_2$ is the main source of degradation in LOBs as suggested.

Understanding the true cause of degradation is important as new electrolytes, additives and RMs and targeting the prevention of $^1O_2$ evolution have not shown significant improvements to LOB performance. Moreover, as mentioned above, the results in Chapter 3 suggest that degradation and $^1O_2$ are not correlated. Hence, it is important to study the effect of $^1O_2$ by decoupling different degradation mechanisms. In **Chapter 4** and **Chapter 5**, it is shown $^1O_2$ does not chemically or electrochemically react with tetraglyme-LiTFSI electrolyte in a significant way, respectively. It is suggested that $^1O_2$ can react with the carbon cathode to yield carboxylates at lower charging potentials and carbonate at higher charging potentials. However, the amount of carbon electrode degradation due to $^1O_2$ is negligible compared to the electrolyte degradation and electrode degradation due to Li_2O_2. In **Chapter5**, it is concluded that Li_2O_2 is the real cause of parasitic chemistry in LOBs.

It is unlikely for $^1O_2$ to result from an electrochemical step, but it could evolve from a chemical step, from LiO_2 disproportionation or from reactions of parasitic products. Although, in this Thesis, it is demonstrated that $^1O_2$ is not the culprit in LOBs, to make sure that $^1O_2$ related reactions are properly decoupled from reactions with CO_2 and reduced oxygen species, it is still important to study the stability of traps used in the literature. DMA has been widely used to detect and quantify $^1O_2$ in LOBs. However, in **Chapter 4**, it is shown that it does not only form $DMAO_2$ upon reacting with $^1O_2$ but can form $DMA(OH)_2$ as well depending on the solution environment. Following this, the reactivity of DMA and its detection using HPLC/UV-Vis was investigated. It is revealed that HPLC/UV-Vis is not a suitable method, especially with tetraglyme based electrolytes and should be coupled to MS and NMR. Detecting small amounts of products is more challenging

with NMR compared to MS, but it is easier to spot unanticipated side products with NMR. Moreover, it is shown that DMA reacts with KO_2 in various electrolyte compositions. Hence, it is not as selective as it was assumed to be.

Perspectives

A practical LOB could be feasible with a stable RMs with fast kinetics that lower the overpotentials, a stable electrolyte solvent, and a gas diffusion electrode that enables fast oxygen mass transport. Here, the optimum RM potential window for fast charging kinetics is determined. Following this, a strategy for optimum charging conditions is using one high voltage RM for fast kinetics and one low potential mediator to avoid LiO_2-$^1O_2$ path. Although $^1O_2$ does not cause significant electrolyte and carbon cathode degradation, it reacts with most of the redox mediators as they consist of multiple electron rich zones, heteroatoms and are sometimes radicals. Hence, having a discharge mediator, two charge mediators, a stable electrolyte and a good air cathode can significantly improve LOBs.

Finding a new electrolyte solvent is challenging as Li salt and oxygen solubility, viscosity, bulk ionic transport (conductivity, ion diffusion coefficients, transference numbers, and the mean molar activity coefficient), electrochemical stability in the desired voltage window, and the chemical stability against reactive species in the cell need to be considered. Here, it is shown that $^1O_2$ is not the real source of degradation and it is fresh Li_2O_2 surfaces (or Li deficient $Li_{2-x}O_2$ surfaces). Hence, a new solvent that is stable towards peroxide-driven species and reduced oxygen species is required. Hydrogen atom abstraction and nucleophilic attack are some of the main electrolyte degradation mechanisms. Substituting these reactive oxygen by fluorinating the β-carbon can prevent H-abstraction and avoiding electron deficient sites (e.g. sulfoxides) to overcome nucleophilic attack are good strategies in developing stable electrolyte solvents. Stabilising superoxide leads to solution growth of Li_2O_2 which enhance discharge capacities, but increases the chance of nucleophilic attack. Hence, formation pathway of Li_2O_2 should be also considered. Recently, using local high concentration electrolytes, fluorinated diluents and fluorinating

commonly used electrolyte solvents have been investigated. Although there is no strong candidate yet, the results seem promising.

Once an electrolyte stable towards peroxide-derived species and reduced oxygen species is combined with a true gas diffusion electrode, LOBs can achieve the desired capacities. If the growth and oxidation of Li_2O_2 is also optimised in this electrolyte, or the gas diffusion electrode can deliver facile mass transport to prevent pore clogging at the electrode/gas interface, there may not be need to use redox mediators. Gas diffusion cathodes that increase oxygen transport via utilising oxygen permeable polymers, have dual porosity for accommodation Li_2O_2 and the electrolyte and for oxygen transport, and does not get flooded with the electrolyte, together with the ideal electrolyte can achieve capacities of 40 mAh cm^{-2} at high rates such as 2 mA cm^{-2}. This would meet the market needs for practical LOBs.

7 Appendix – Supplementary Information

7.1 Additional Data - Chapter 3

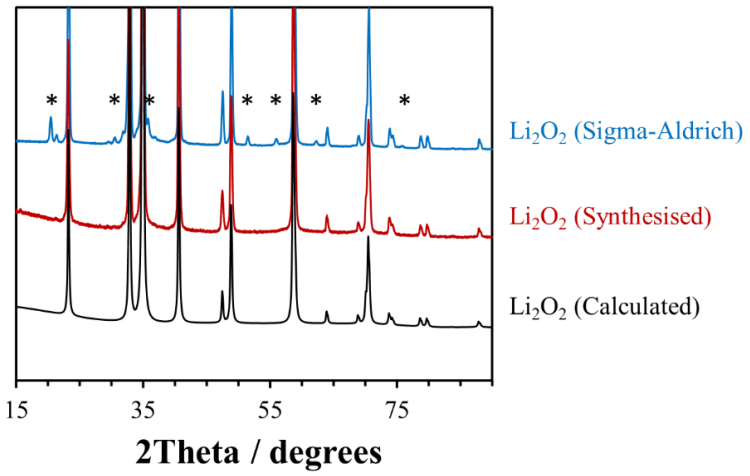

Figure S1 *Powder X-ray diffraction patterns for commercial Li_2O_2 (Sigma-Aldrich) and in-house synthesised Li_2O_2 compared with calculated pattern for the Li_2O_2 structucture.*[316] ** indicates impurities such as LiOH and Li_2CO_3 in the commercial sample.*

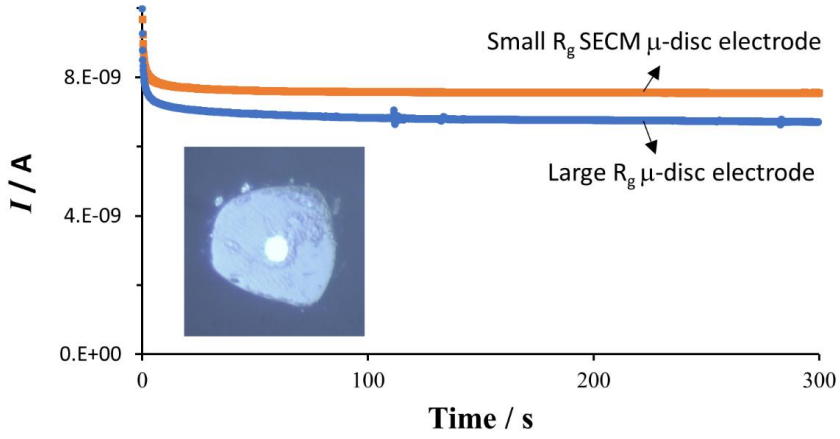

Figure S2 *The chronoamperometry data for an ultramicrodisc electrode for SECM and a 'large Rg' microdisc electrode. The experiment were run in 10 mM TEMPO in 0.1 M LiTFSI tetraglyme solution. Inset shows the optical microscope image of the tip of the SECM electrode. The R_g factor of the SECM electrode is estimated by comparing the ratio of steady state currents between the SECM and a very large R_g electrode.*

Table S1 *Dielectric constant of solvents. Optical dielectric constants are calculated by taking the square root of the refractive index (value provided by Sigma-Aldrich) of the solvent.*

	Dielectric constant	
Solvent	**Static (ε_s)**	**Optical (ε_∞)**
4G	7.78[317]	2.05
DME	7.07[317]	1.90

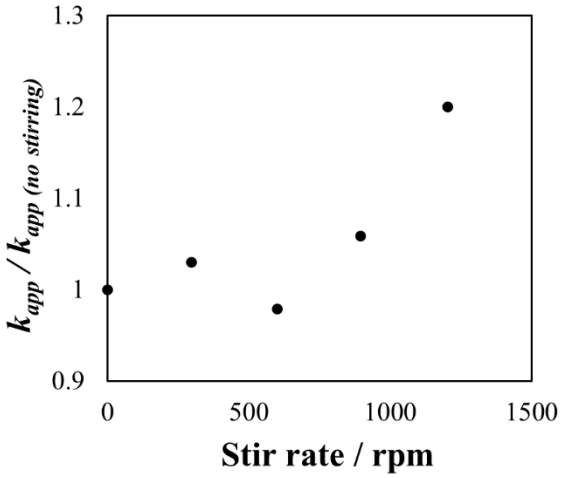

Figure S3 *The apparent rate constant (kapp) of the reaction of $DMPZ^+$ with Li_2O_2 in tetraglyme measured using the UV-Vis method from Petit's work, here shown as a function of solution stirring rate. The measurements were done by Sixie Yang.*

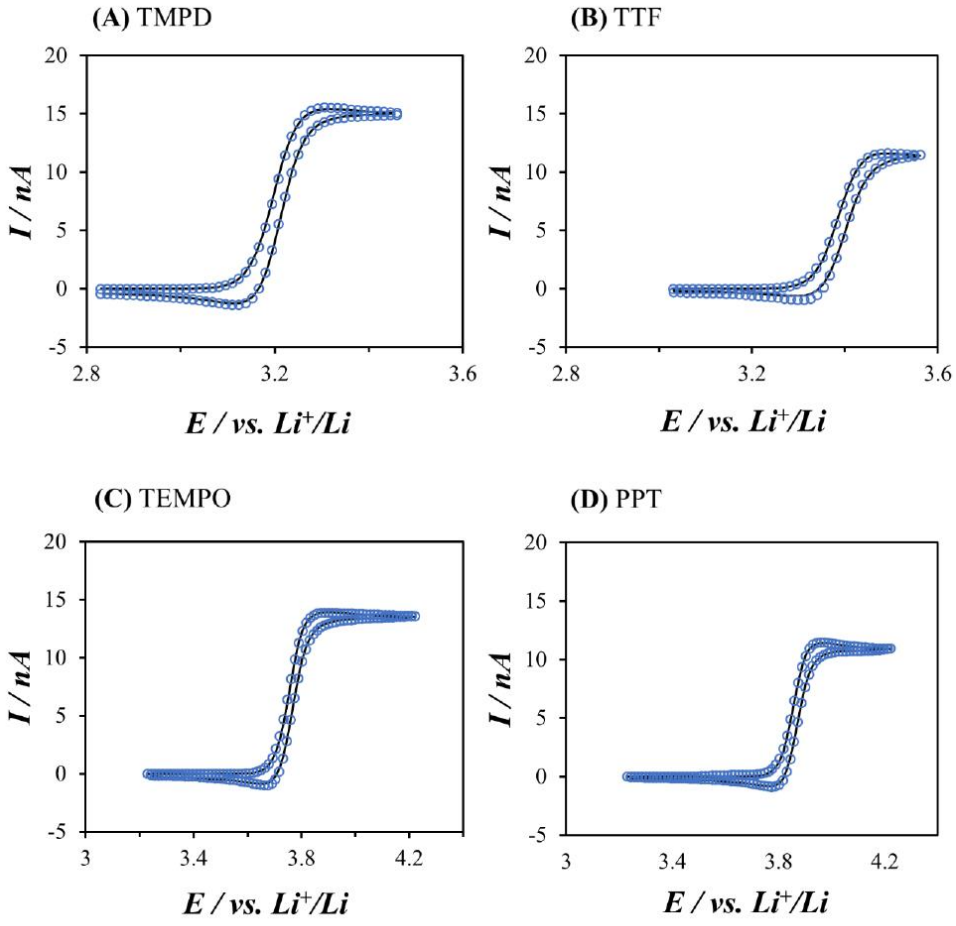

Figure S4 *Cyclic voltammograms for 10 mM a) TMPD, b) TTF, c) TEMPO, and d) PPT at 20 mV s^{-1} scan rate using a 25 µm Au disc electrode in 0.1 M LiTFSI in tetraglyme. Blue circles are experimental data and the black lines fitted using DigiElch.*

Table S2 *Experimental data for redox potential (E_{RM}) and the effective rate constant (k_{eff}) for redox mediators (RMs) in 100 mM LiTFSI in tetraglyme, their estimated molecule radius showing that the variation in molecular radius is small, and the singlet oxygen yield.*

RM	E_{RM} / *V* vs. Li^+/Li	ln k_{eff} / *cm* s^{-1}	Radius / *Å*	$^1O_2$ / *%*
TMPD	3.21	-13.4	3.45	0.82
DMPZ	3.25	-12.6	3.62	1.78
TTF	3.39	-8.88	3.32	3.85
Fc	3.50	-7.74	3.24	7.17
MAZO	3.63	-4.79	3.32	0.21
TEMPO	3.77	-5.33	3.44	0.18
H-TEMPO	3.79	-5.23	3.50	
M-TEMPO	3.80	-5.47	3.61	0.32
MPT	3.81	-5.81	3.56	
PPT	3.86	-5.72	3.76	

Oxygen Evolution Measurements

An in-house made stainless-steel pressure cell (**Figure S5A**) was used to measure the oxygen evolution rate upon mixing solid Li_2O_2 with solutions of oxidised redox mediators. This method was used to measure the kinetics for TMPD and DMPZ as their kinetics were too slow to be measured by SECM. A compartment containing a saturated RM^+ in tetraglyme solution with excess RM^+ powder was positioned above the reaction chamber and was separated with a valve. The reaction chamber contained excess Li_2O_2 to maintain a relatively constant reaction surface area during the reaction. The cell was kept in an incubator set to 25 °C. The pressure was measured with a PX409 Omega Engineering pressure transducer and the allowed to reach equilibrium before the reaction. Once a stable baseline pressure was obtained, the valve was opened to mix the RM^+ solution with Li_2O_2. The mixture was stirred rapidly using a stirrer bar throughout the measurement.

The rate of the reaction is proportional to the pressure-time gradient (**Figure S5C-D**). This gradient is then normalised by the concentration of RM^+ in solution and mass of Li_2O_2 (**Figure S5B)**. To compare the reaction rates of TMPD and DMPZ with the fast kinetics RMs, the normalised pressure-time gradient is converted to k_{eff} using TEMPO as the calibration. The k_{eff} values for TEMPO and TTF from pressure measurements and SECM are in agreement (**Figure S5E**).

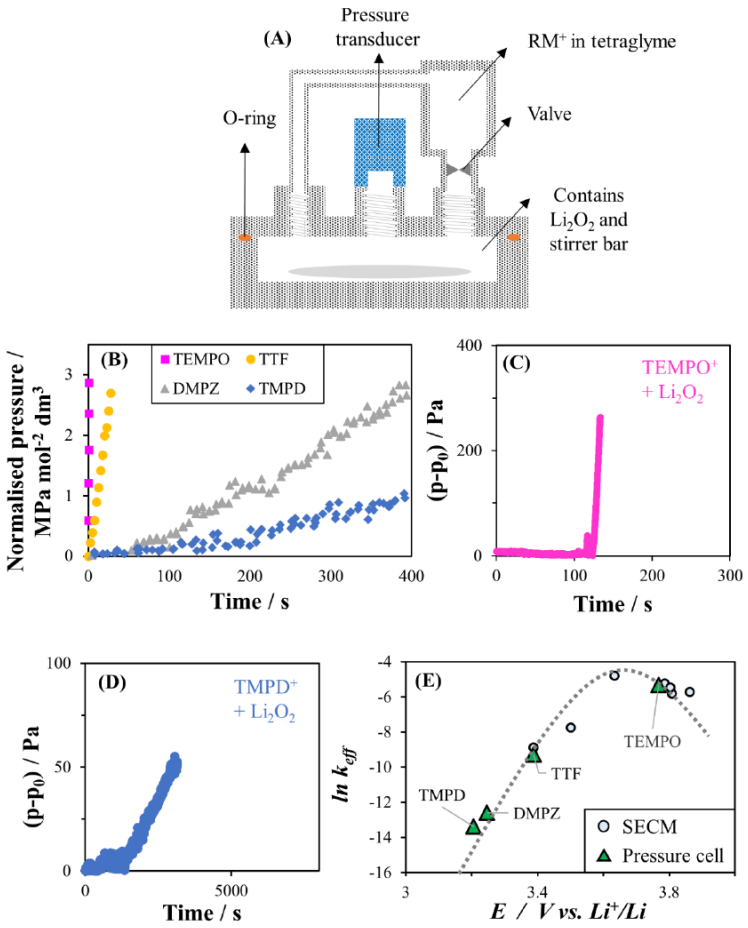

Figure S5 *a) Schematic illustration of the custom-made stainless steel pressure cell. b) Normalised pressure as a function of time for selected RMs. c-d) Change in relative pressure as a function of time for TEMPO⁺ and TMPD⁺, respectively. E) k_{eff} from SECM experiments (circles) compared to that obtained from pressure cell measurements (triangles).*

7.1.1 Additional Oxygen Evolution and Stability Data

The $^1O_2$-$^3O_2$ yields and trends in this Thesis and in the work of Petit et al.[59] are different as well. It seems that there is some misinterpretation in the approach used by Freunberger and co-workers (Petit et al.) and overall usage of DMA in the LOB literature. DMA is used to trap $^1O_2$ and quantify it; however, it does not collect all of the evolved $^1O_2$. Furthermore, additional NMR studies show that a fraction of the $DMAO_2$ converts to $DMA(OH)_2$ in the presence of protons.

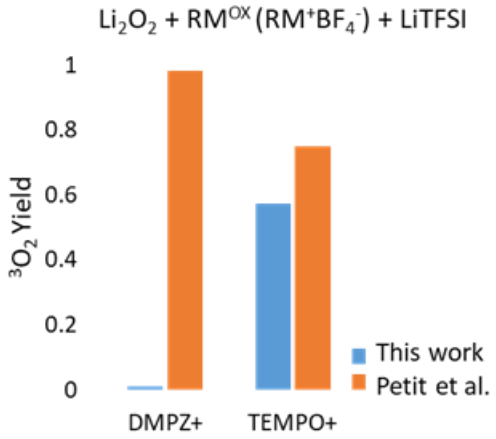

Figure S6 *$^3O_2$ yields for Li_2O_2 oxidation with $TEMPO^+$ and $DMPZ^+$. This figure compares the $^3O_2$ yield for $TEMPOBF_4$ and $DMPZBF_4$ in this work with the work of Petit et al. Both studies use excess Li_2O_2 and 10 mM $RMBF_4$ 0.1 M LiTFSI in tetraglyme. Here, 5 times excess in-house synthesised Li_2O_2 is used.*

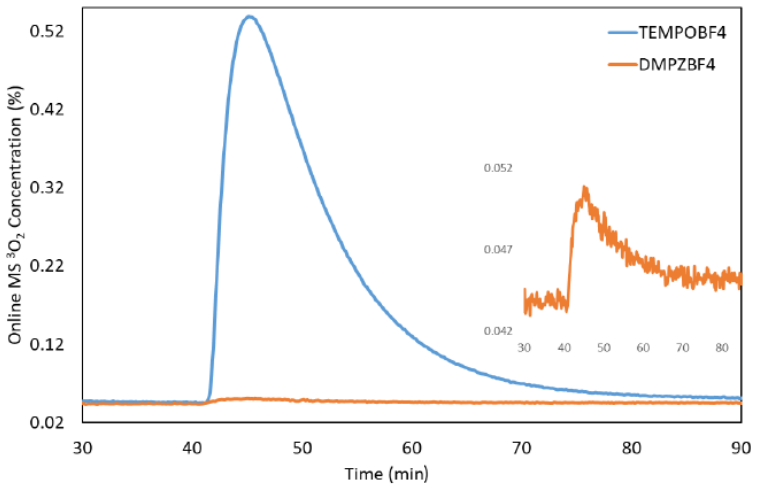

Figure S7 *On-line MS data showing $^3O_2$ evolution upon oxidising Li_2O_2 powder with 10 mM $RM^+BF_4^-$ in 0.1 M LiTFSI in tetraglyme. 5 times excess in-house synthesised Li_2O_2 is used and the injection volume is 1 mL. The mixture is stirred until O_2 signal baselines. This data does not necessarily show the rate of the reaction, but shows the $^3O_2$ evolution trend for $TEMPO^+$ and $DMPZ^+$ under the same conditions.*

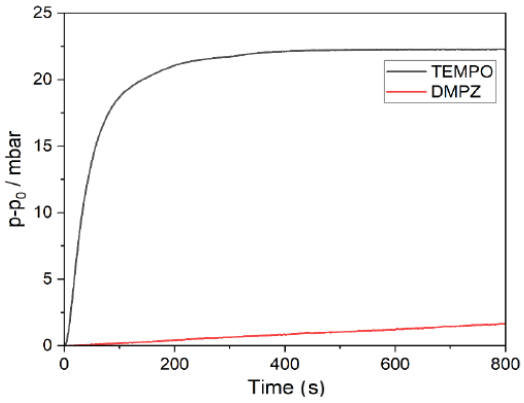

Figure S8 *Pressure monitoring of O_2 evolution upon mixing 15 mM $TEMPOBF_4$ (red) and $DMPZBF_4$ (black) 0.1 M LiTFSI in tetraglyme with 60 times excess Li_2O_2. The pressure measurements show that the kinetics of RM mediated Li_2O_2 oxidation are much faster with $TEMPO^+$ than $DMPZ^+$. The data was collected by Daniel Dewar.*

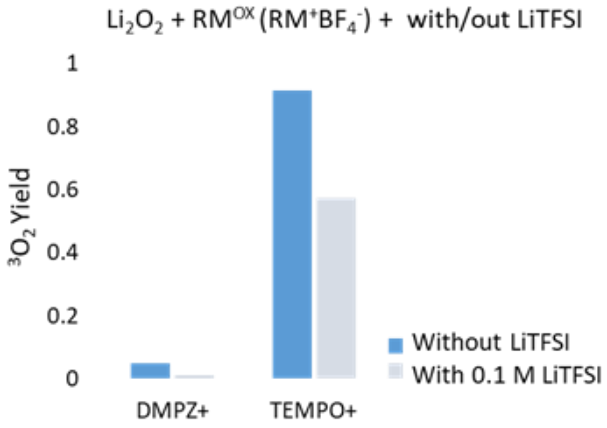

	$^3O_2$ Yield (%) WITH 0.1 M LiTFSI	$^3O_2$ Yield (%) WITHOUT salt
$DMPZ^+$	**0.97**	**4.9**
$TEMPO^+$	**57**	**91**

Figure S9 *$^3O_2$ yield for Li_2O_2 oxidation with $TEMPO^+$ and $DMPZ^+$. 1 mL of 10 mM RM^+ in tetraglyme is injected on 5 times excess in-house synthesised Li_2O_2 powder. The solution either had 0.1 M LiTFSI or no salt. The data shows that $^3O_2$ decreases significantly when there is LiTFSI. Additionally RM^+ are not very soluble in tetraglyme without salt.*

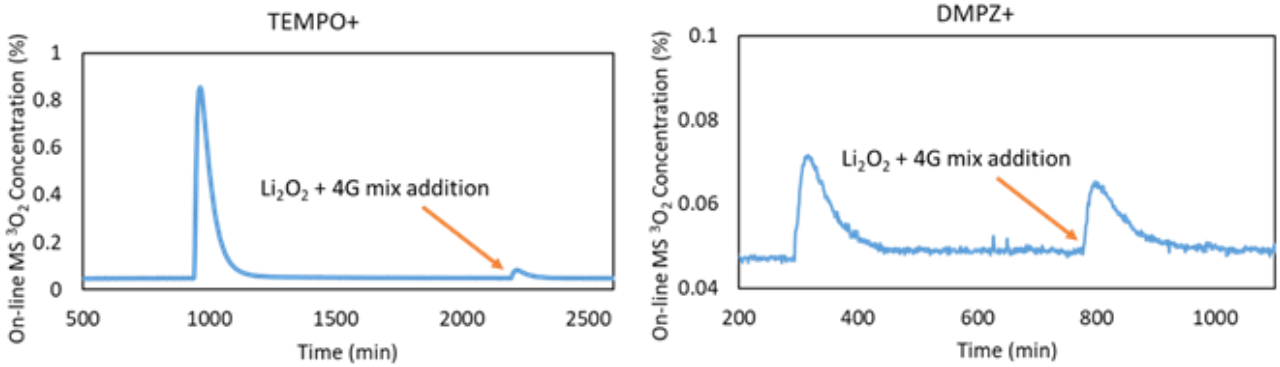

Figure S10 *On-line MS data showing $^3O_2$ evolution upon injecting 10 mM RM^+ 0.1 M LiTFSI in tetraglyme on in-house synthesised 5 times excess Li_2O_2. A suspension 3.5 times excess Li_2O_2 in 4G is added after O_2 signal baselined, and a second $^3O_2$ evolution peak is observed.*

Table S3 *$^3O_2$ yield for 1st (RM^+) and 2nd (RM^+ + Li_2O_2 top-up) injections*

		$^3O_2$ Yield (%)
$DMPZ^+$		0.66
	Add more Li_2O_2	0.75
$TEMPO^+$		71.56
	Add more Li_2O_2	0.85

This data suggest that Li_2O_2 surface in tetraglyme is being covered by an inorganic carbonate/organic carboxylate layer as 10 mM RM^+ in tetraglyme is added. The amount of inorganic carbonate/organic carboxylate is small (see **Section 5.3.3**). However, even the Li_2O_2 surface gets covered with a thin layer, it prevents $DMPZ^+$ from reaching the fresh Li_2O_2 surfaces. There are two factors here i) $DMPZ^+$ cannot easily oxidise these degradation products compared to $TEMPO^+$ and ii) the kinetics of forming these degradation products could be faster than Li_2O_2 oxidation by $DMPZ^+$ and slower than Li_2O_2 oxidation by $TEMPO^+$.

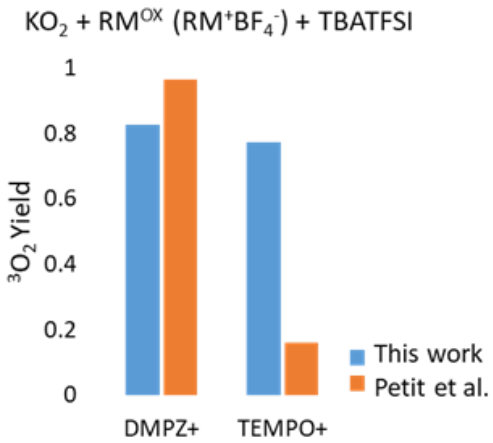

Figure S11 *$^3O_2$ yield measured by on-line MS upon oxidation of KO_2 with RM^+. 10 mM RM^+BF4^- 0.1 M TBATFSI in tetraglyme was injected onto excess KO_2 powder. The $^3O_2$ yield for $DMPZ^+$ is slightly higher than that of $TEMPO^+$; however, the yields for $DMPZ^+$ and $TEMPO^+$ are still not that different from each other. According to Petit et al. the $^3O_2$ yield from KO_2 oxidation with $TEMPO^+$ is very low.*

7.2 Additional Data - Chapter 4

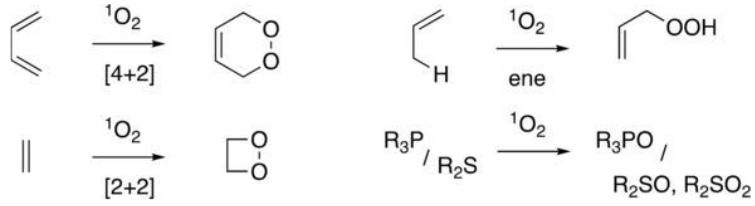

Figure S12 *Common reactions mechanisms with $^1O_2$: [4+2] cycloaddition, [2+2] cycloadditon, "ene" reaction, and oxidation of heteroatoms.[318] Reproduced with permission from ref 318. Copyright 2019, John Wiley & Sons.*

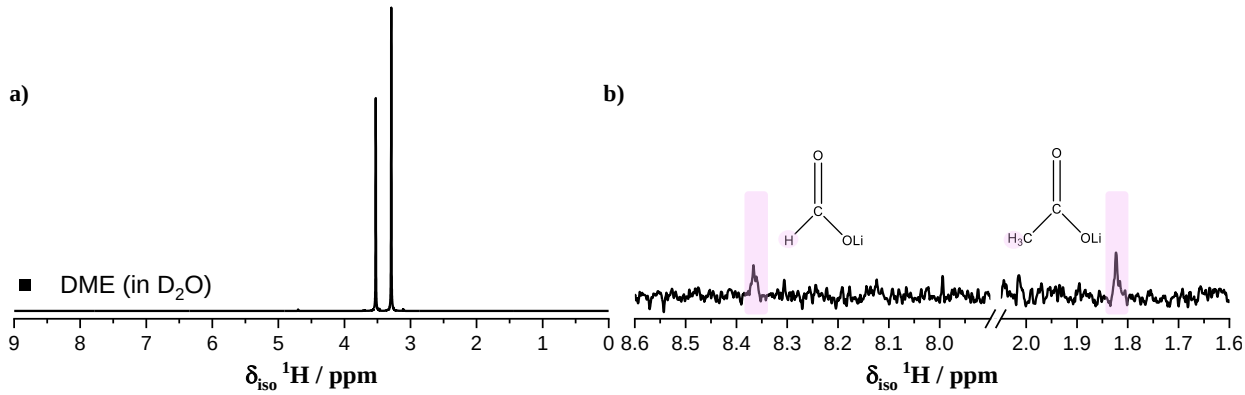

Figure S13 *a) The ^{1}H NMR spectra for pristine DME. 50 µL of solvent was added to 750 µL D_2O to dissolve any b) Li formate and acetate to form HCOOD (8.38 ppm) and CH_3COOD (1.84 ppm), respectively.*

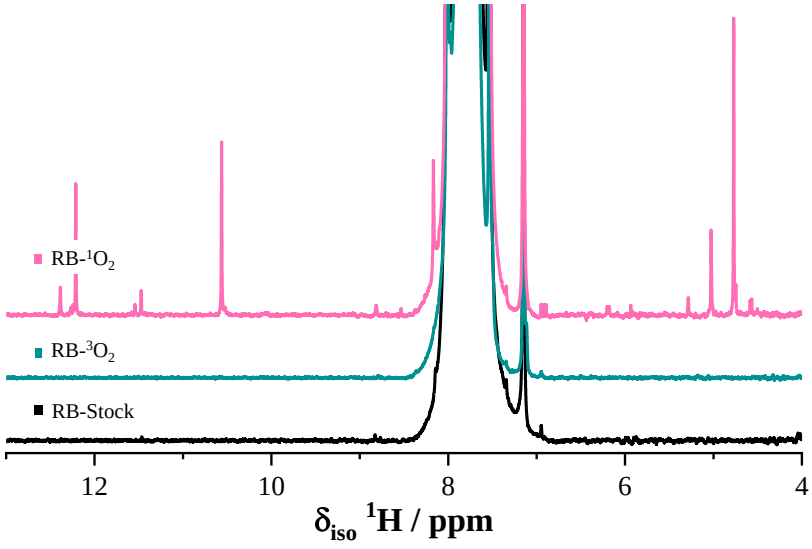

Figure S14 *The ^{1}H NMR spectra of DMF (black, with RB), DMF after $^3O_2$ exposure (green, with RB), and DMF after $^1O_2$ exposure (pink, with RB) confirming that the degradation products are due to $^1O_2$ and $^3O_2$ does not have an effect on DMF stability under these conditions.*

1 M $LiPF_6$ EC:DMC is a common electrolyte used in LIBs. Gasteiger and co-workers showed that there is $^1O_2$ formation after 80% state-of-charge with NCM cathodes in Li-ion batteries.[319] They suggest that $^1O_2$ originates from some layer transition metal oxide cathode after 80% state-of-charge and does not evolve upon oxidation of Li_2CO_3. On the other hand Freunberger and co-workers and Chen and co-workers suggest that the missing O_2 from Li_2CO_3 oxidation is due to formation of $^1O_2$.[209,320] Finally, Gasteiger and co-workers show that $^1O_2$ reacts with EC and DMC is stable towards $^1O_2$.[321] Here, it is shown that 1 M EC:DMC $LiPF_6$ is stable towards $^1O_2$ under chemical conditions at room temperature. The difference between results is either due to quenching of $^1O_2$ by DMC or because Gasteiger and co-workers run the $^1O_2$ test at 45 °C.

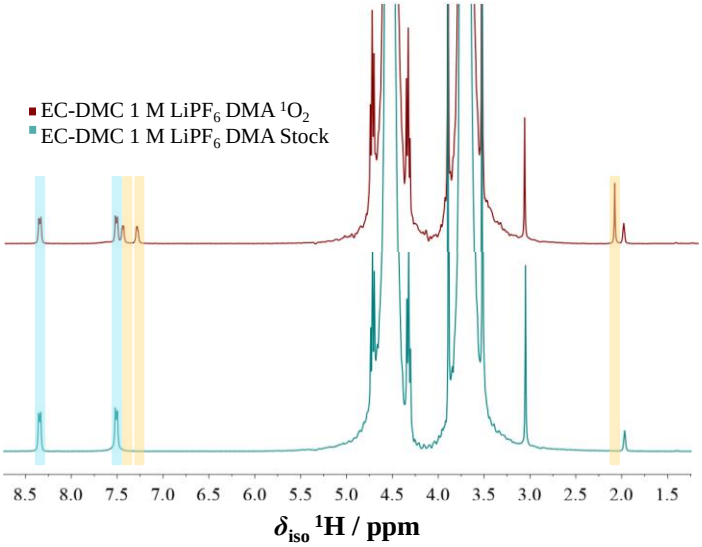

Figure S15 *The ^1H NMR spectra showing $^1O_2$ generation in 1 M $LiPF_6$ in EC:DMC using RB as the photosynthesiser. 60 mM DMA was dissolved in the electrolyte (green) and irradiated under continuous $^3O_2$ flow to generate $^1O_2$ (red). Some of the DMA (cyan) was converted into $DMAO_2$ (yellow) after reaction with $^1O_2$ (red).*

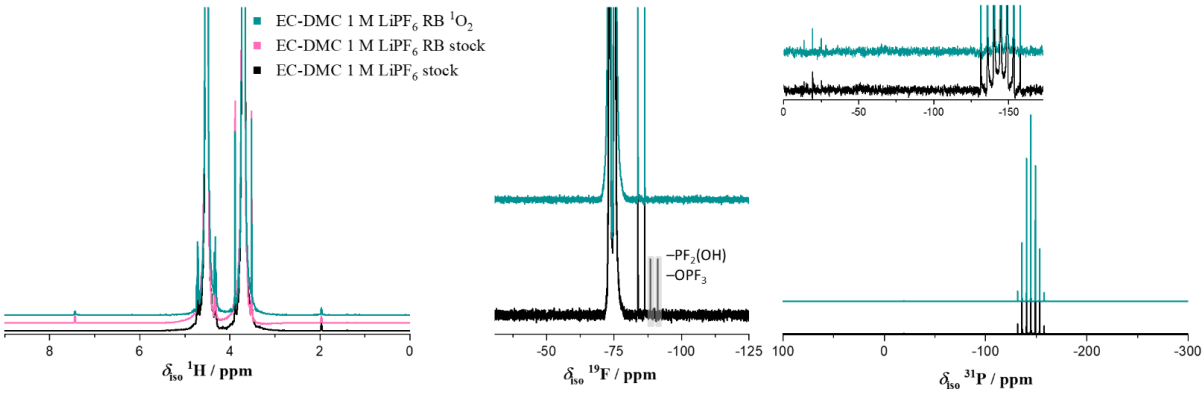

Figure S16 *The ^1H, ^{19}F, and ^{31}P NMR spectra for 1 M LiPF6 in EC:DMC and $^1O_2$ treated 1 M LiPF6 in EC:DMC. No electrolyte degradation is observed. The impurities in the $LiPF_6$ salt seem to react with $^1O_2$ as seen in the ^{19}F spectra.*

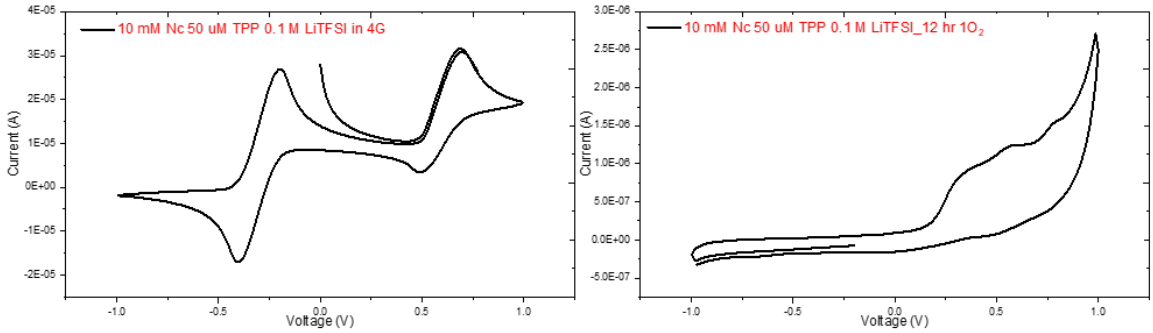

Figure S17 *The cyclic voltammogram for the redox mediator nickelocene (Nc, 10 mM) in 0.1 M LiTFSI tetraglyme before and after* $^1O_2$ *treatment showing that Nc reacts with* $^1O_2$.

7.3 Additional Data – Chapter 5

7.3.1 Amount of $^1O_2$ Generated

• Assuming 2% $^1O_2$ generation during charging due to disproportionation, as given by Mourad et al.[208]:

$^1O_2$ in a cell charging at 50 µA

$$Q = I\ x\ t = 50\ \mu A\ x\ 60\ \text{sec} = 0.003\ C$$
$$\frac{Q}{F} = mole\ electron; \frac{0.003}{96485} = 3.109x10^{-8}\ mole\ e^-$$
$$\frac{3.109x10^{-8}}{2} = 1.555x10^{-8}\ mole\ Li_2O_2\ per\ min$$
$$1.555x10^{-8}x\frac{2}{100} = \mathbf{3.109x10^{-10}\ mole\ \ ^1O_2\ per\ min}$$

$^1O_2$ in a cell charging at 1 mA

$$= \mathbf{6.1218x10^{-9}\ mole\ \ ^1O_2\ per\ min}$$

• $^1O_2$ generated in-situ photochemical experiments calculated from ^{1}H NMR data:

$$= \mathbf{1.563x10^{-5}\ mole\ \ ^1O_2\ per\ min}$$

7.3.2 Inversion-Recovery Experiments to Determine T_1

The longitudinal relaxation (spin-lattice or z direction relaxation, T_1) is obtained by performing inversion-recovery experiments. For quantitative measurements, it is necessary to have > 5T_1 duration between scans (D_1) to recover the all of the equilibrium magnetisation. T_1 is described using the equation

$$M_{z(t)} = M_{z(0)}\left(1 - 2\ e^{(-t/T_1)}\right)$$

The fitting of the data from T_1 experiments show that the relaxation time for acetate in electrolyte is 1.5 seconds and acetate and formate in D_2O are 6.3 and 2.1 seconds, respectively. For quantitative experiments with Ernst angle, the relaxation delay (D_1) is 1T_1. The D_1 value for the experiments with 30° Ernst angle is 10 seconds which is >1T_1 for deuterated water samples and >5T_1 for electrolyte samples. This methodology is used to increase the number of scans and maximise the S/N.

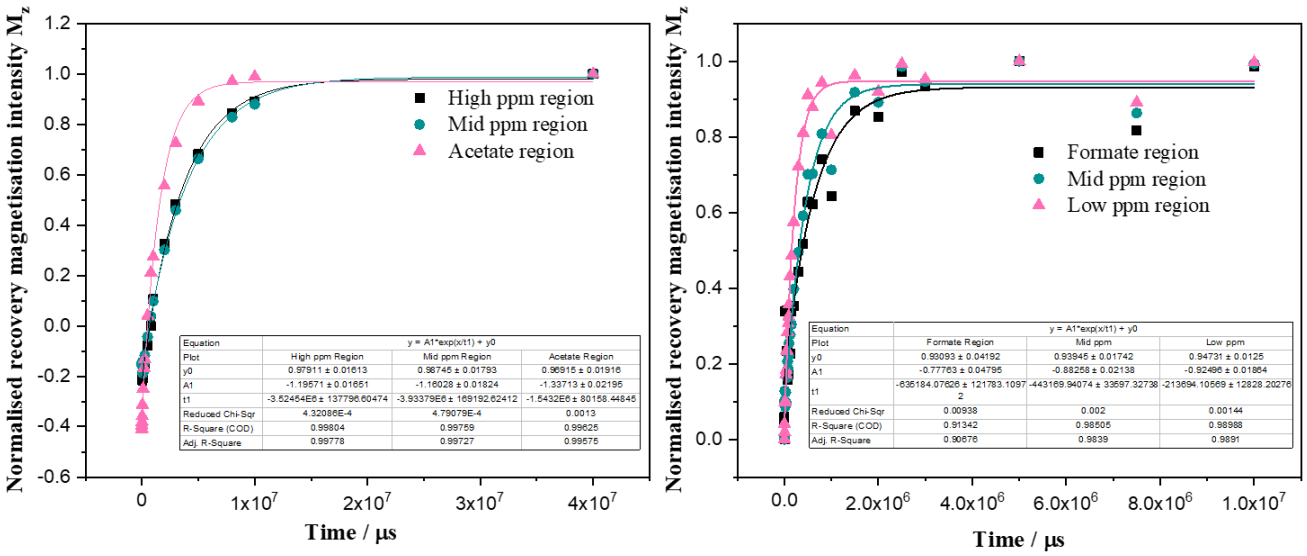

Equation	y = A1*exp(x/t1) + y0		
Plot	High ppm Region	Mid ppm Region	Acetate Region
y0	0.97911 ± 0.01613	0.98745 ± 0.01793	0.96915 ± 0.01916
A1	-1.19571 ± 0.01651	-1.16028 ± 0.01824	-1.33713 ± 0.02195
t1	-3.52454E6 ± 137796.60474	-3.93379E6 ± 169192.62412	-1.5432E6 ± 80158.44845
Reduced Chi-Sqr	4.32086E-4	4.79079E-4	0.0013
R-Square (COD)	0.99804	0.99759	0.99625
Adj. R-Square	0.99778	0.99727	0.99575

Equation	y = A1*exp(x/t1) + y0		
Plot	Formate Region	Mid ppm	Low ppm
y0	0.93093 ± 0.04192	0.93945 ± 0.01742	0.94731 ± 0.0125
A1	-0.77763 ± 0.04795	-0.88258 ± 0.02138	-0.92496 ± 0.01864
t1	-636184.07626 ± 121783.10972	-443169.94074 ± 33597.32738	-213694.10569 ± 12828.20276
Reduced Chi-Sqr	0.00938	0.002	0.00144
R-Square (COD)	0.91342	0.98505	0.98988
Adj. R-Square	0.90676	0.9839	0.9891

Figure S18 *Relative intensity of recovery magnetisation versus time for ethylacetoacetate in tetraglyme (left) and Li acetate and formate in D_2O samples (right). Data is obtained from inversion-recovery experiments where magnetisation goes from -z to z over varying time lengths.*

7.3.3 Additional NMR Data

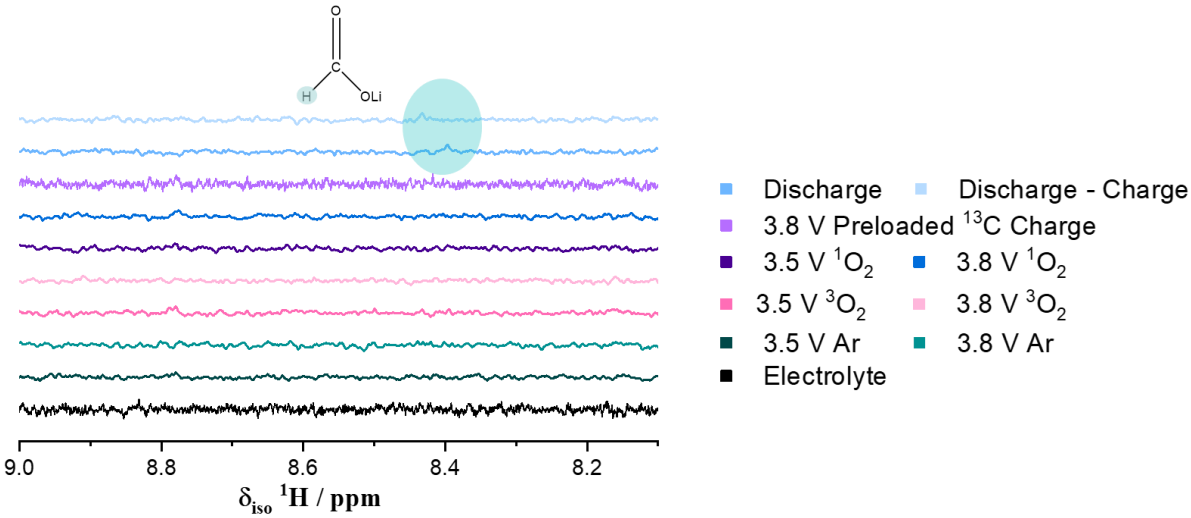

Figure S19 *The ^{1}H NMR spectra for the electrolyte samples showing the Li formate region. The solubility of Li formate in tetraglyme is very low and it is mainly detected via a D_2O wash of the cathodes or by Fenton's reagent treatment. Trace amount of formate in electrolyte is detected in the discharged-charged and discharge samples as seen in the blue marked region in the spectra which indicates that the amount of formate samples treated with $^1O_2$ is lower than that of Li_2O_2 containing samples.*

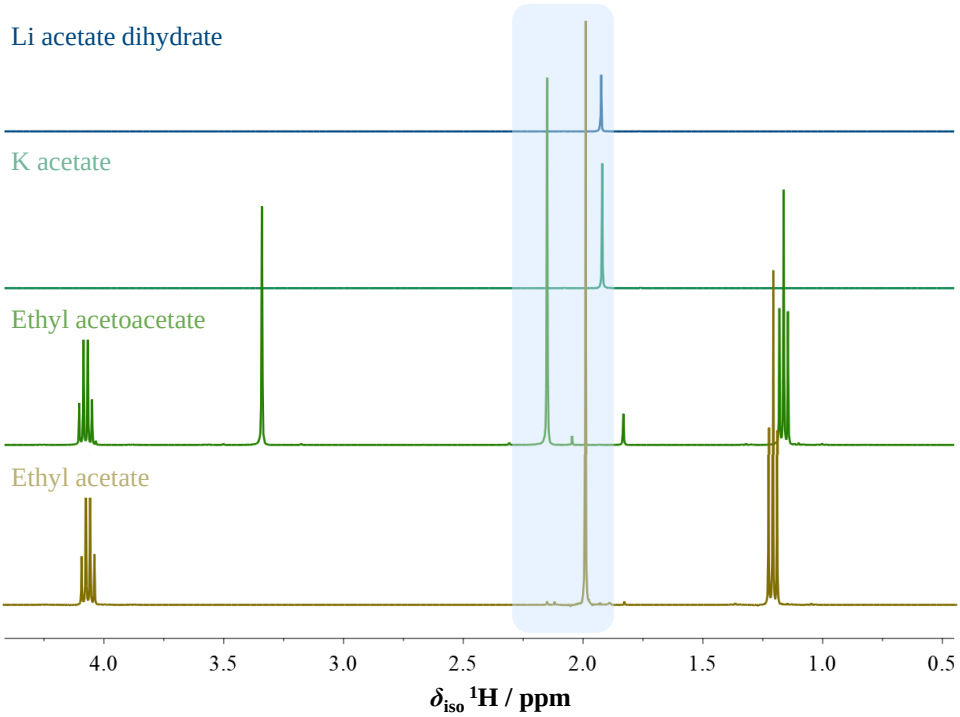

Figure S20 *The ^{1}H NMR spectra for several inorganic and organic acetate standards. The blue marked region shows the –CH_3 peak for acetate group as the organic groups increase, the acetate peak shifts to higher ppm. This is due to a decrease in the electron density around hydrogen 1s orbital and deshielding of the proton.*

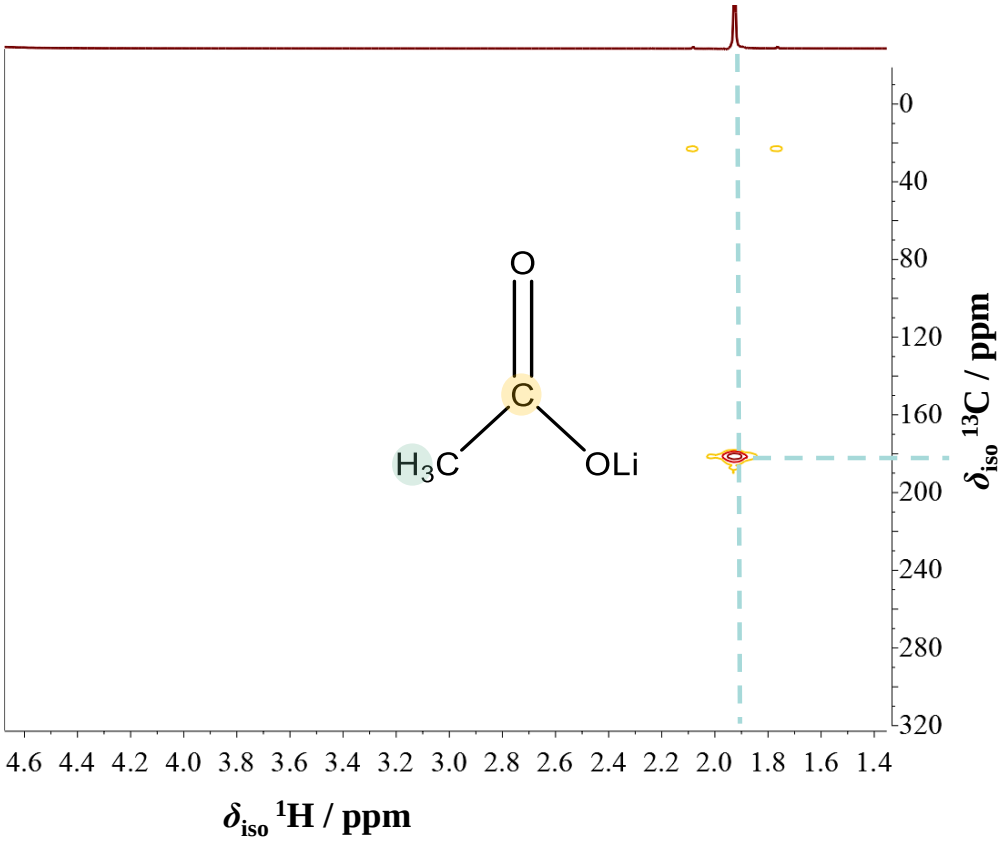

Figure S21 *The HMBC spectra for Li acetate dihydrate standard dissolved in D_2O showing correlation between 181 ppm ^{13}C and 1.92 ppm ^{1}H.*

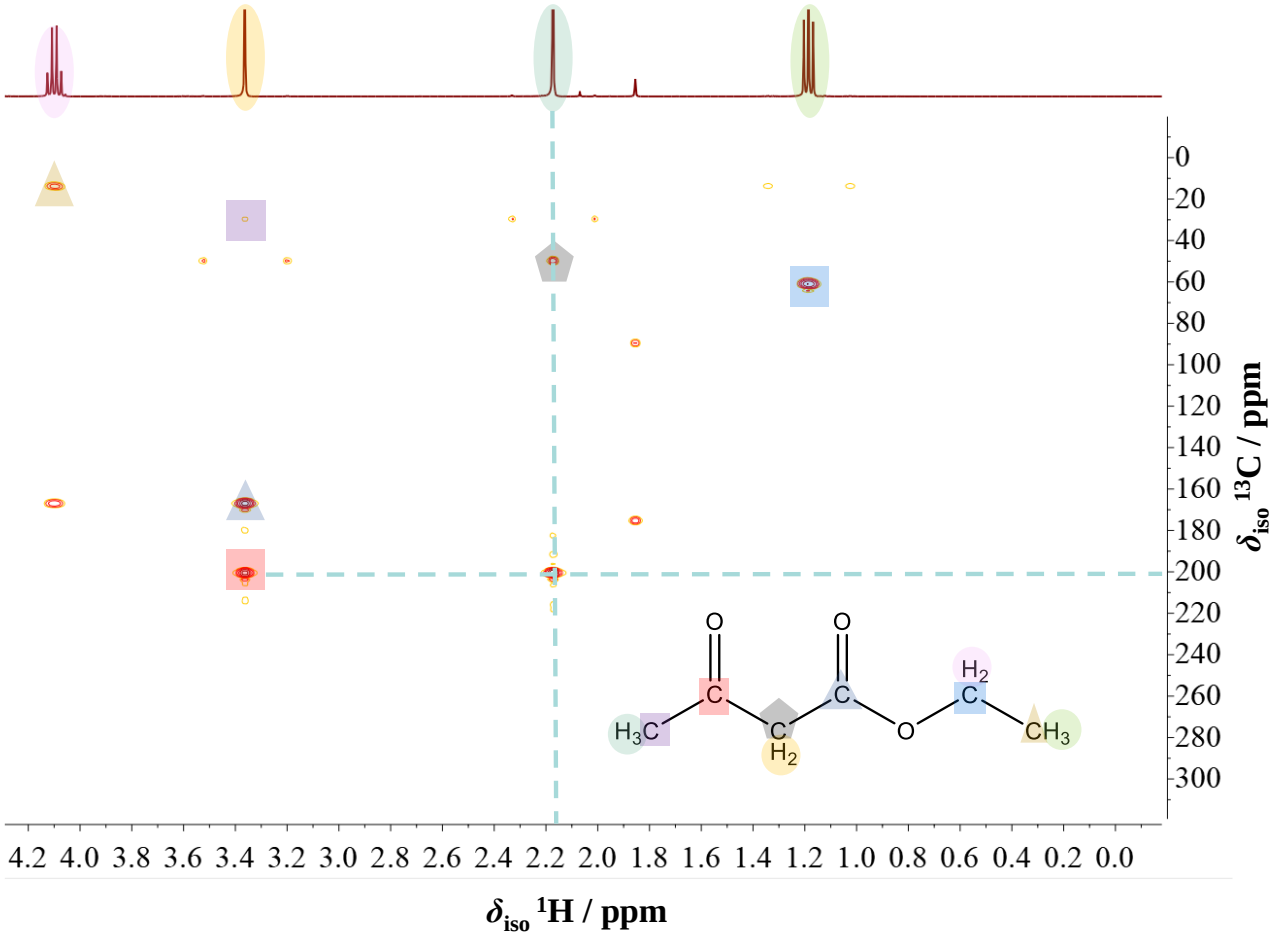

Figure S22 *The HMBC spectra for ethyl acetoacetate standard in $CDCl_3$. Unlike Li acetate where there is only one carbon-hydrogen correlation, acetate group in ethyl acetoacetate has multiple neighbouring carbons meaning it has multiple carbon-hydrogen correlation. This shows that if the acetate detected in samples was organic, more carbon peaks would be detected in HMBC spectra or organic acetates are low in concentration and the signal is too weak for detection under these conditions.*

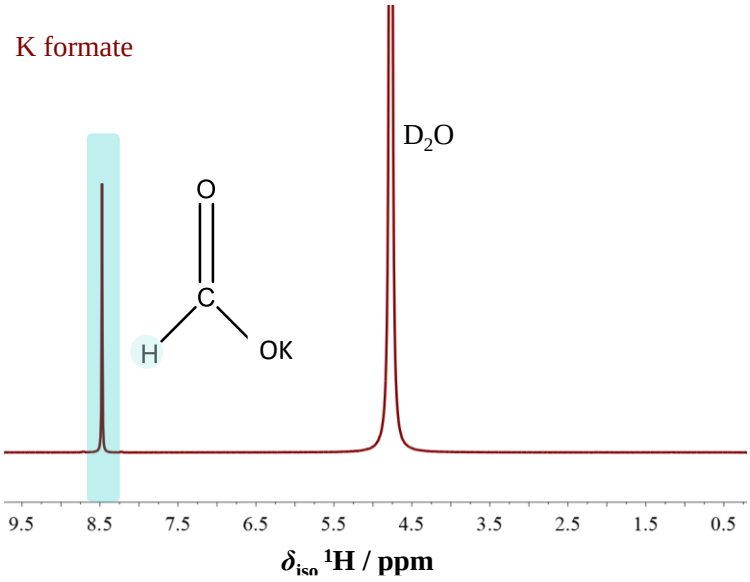

Figure S23 *The ^{1}H NMR spectra for K formate standard dissolved in D_2O showing the formate -CH peak at 8.47 ppm.*

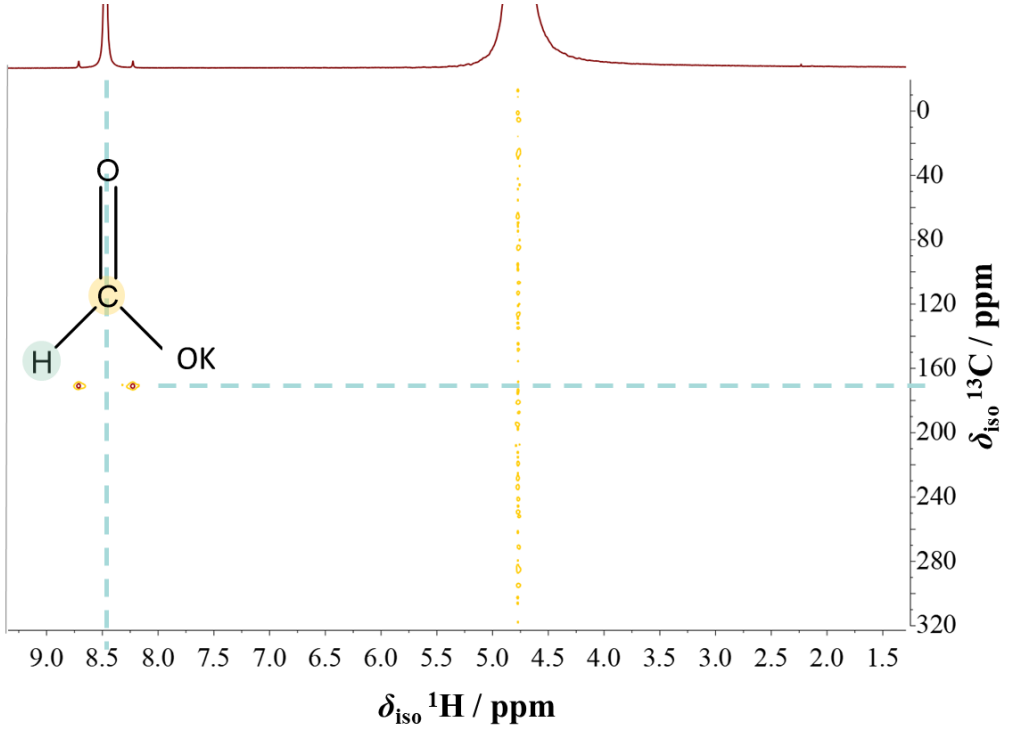

Figure S24 *HSQC spectra for K formate standard dissolved in D_2O showing correlation between 171 ppm ^{13}C and 8.47 ppm ^{1}H.*

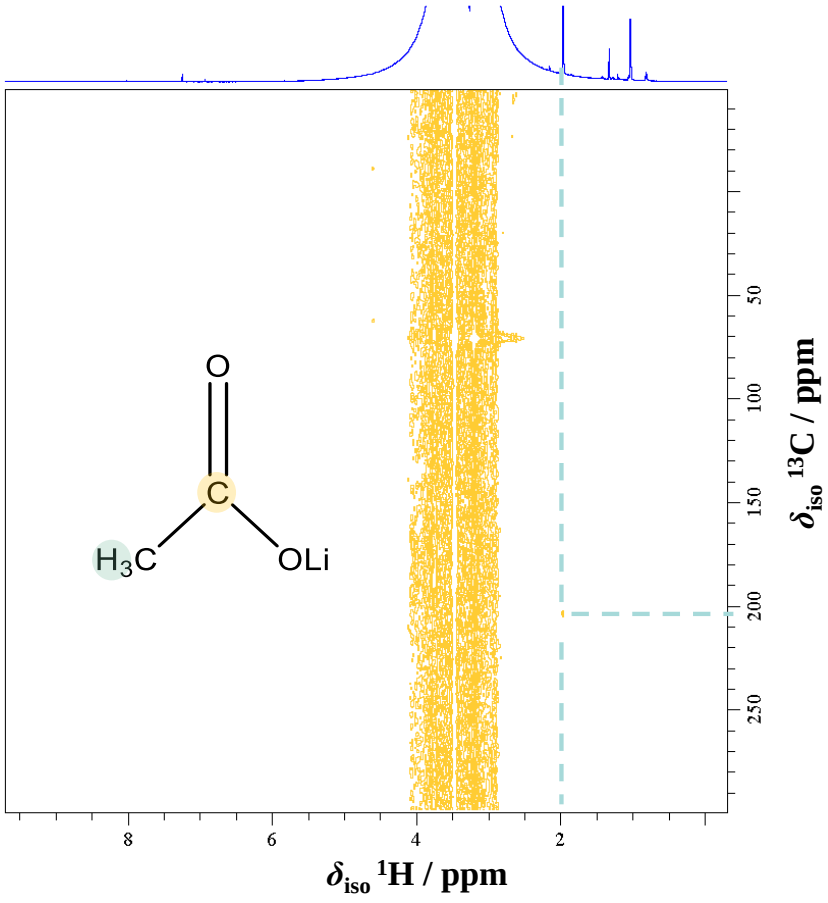

Figure S25 *The HMBC spectra of tetraglyme electrolyte after oxidising a Li_2O_2 preloaded ^{13}C cathode at 3.8 V showing Li acetate ^{13}C and ^{1}H correlations at 204 ppm and 1.95 ppm, respectively.*

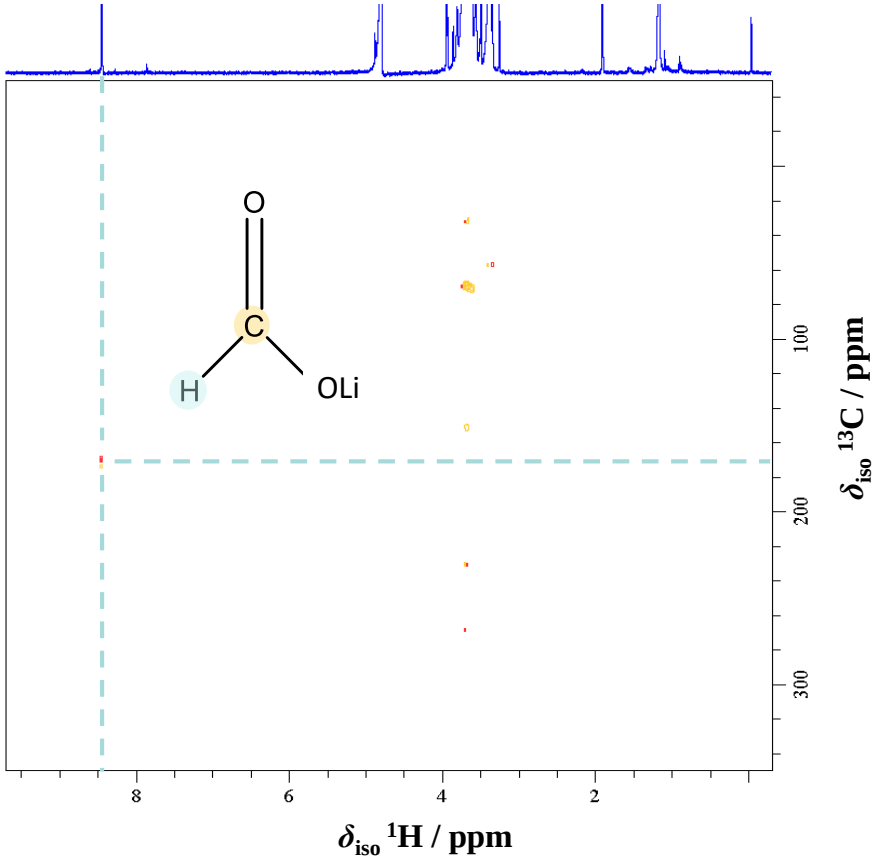

Figure S26 *HSQC spectra of the electrolyte for a discharge sample showing Li formate ^{13}C and ^{1}H peaks.*

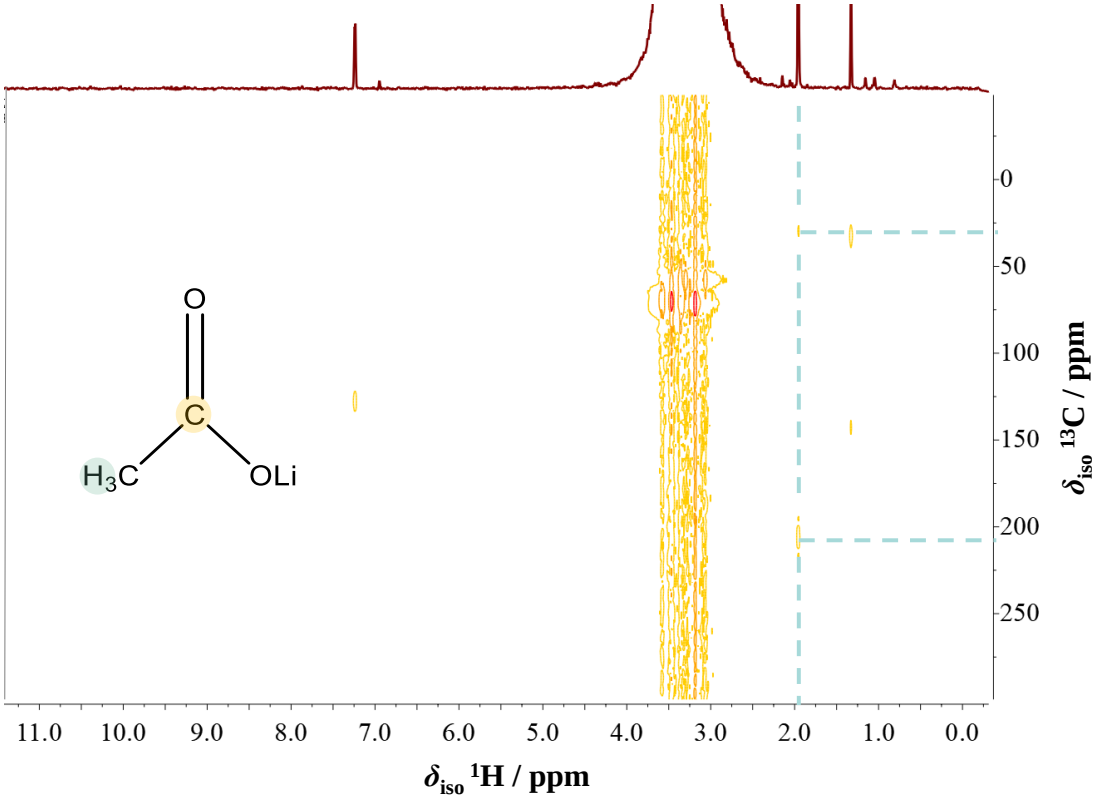

Figure S27 *The HMBC spectra of the electrolyte for a discharge sample showing Li acetate ^{13}C and ^{1}H peaks.*

7.3.4 Additional On-line MS Data

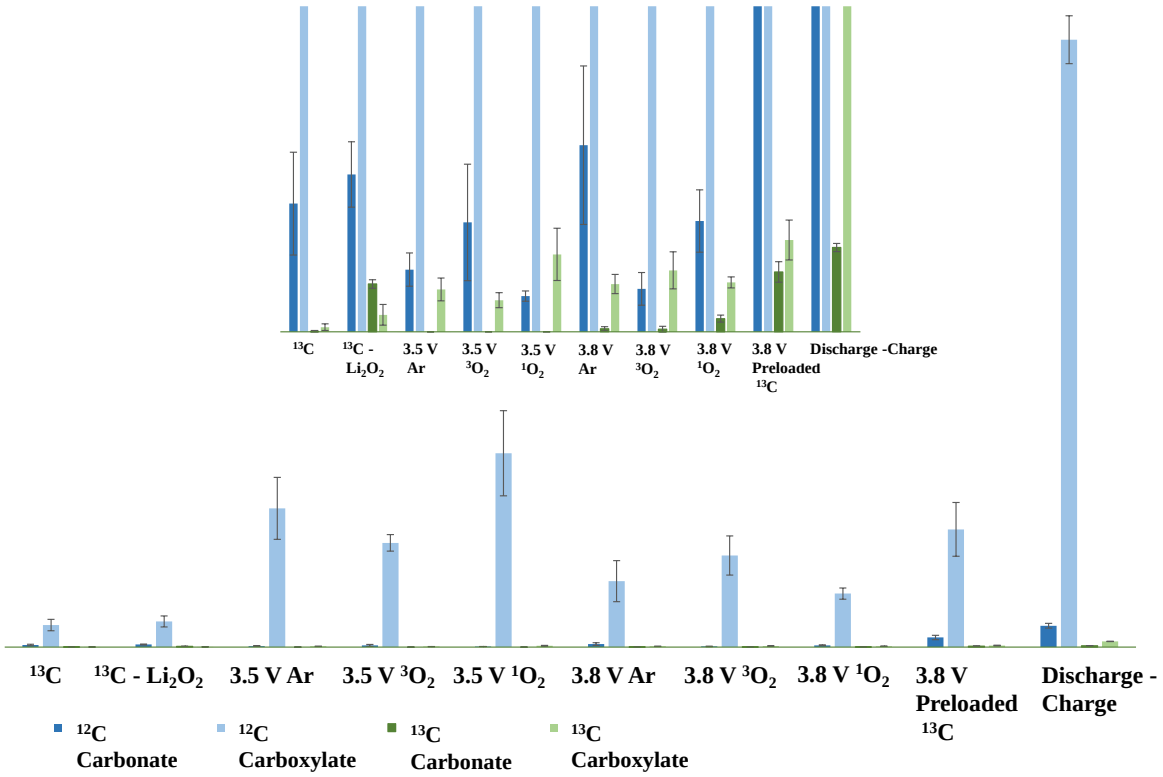

Figure S28 *A comparison of absolute amount of $^{12}CO_2$ and $^{13}CO_2$ evolved from cathodes after acid and Fenton's reagent treatments to decompose Li_2CO_3 and carboxylates, respectively. The inset is an expanded version of the same dataset to highlight the ^{13}C amounts.*

7.3.5 Morphology of ^{13}C Powder

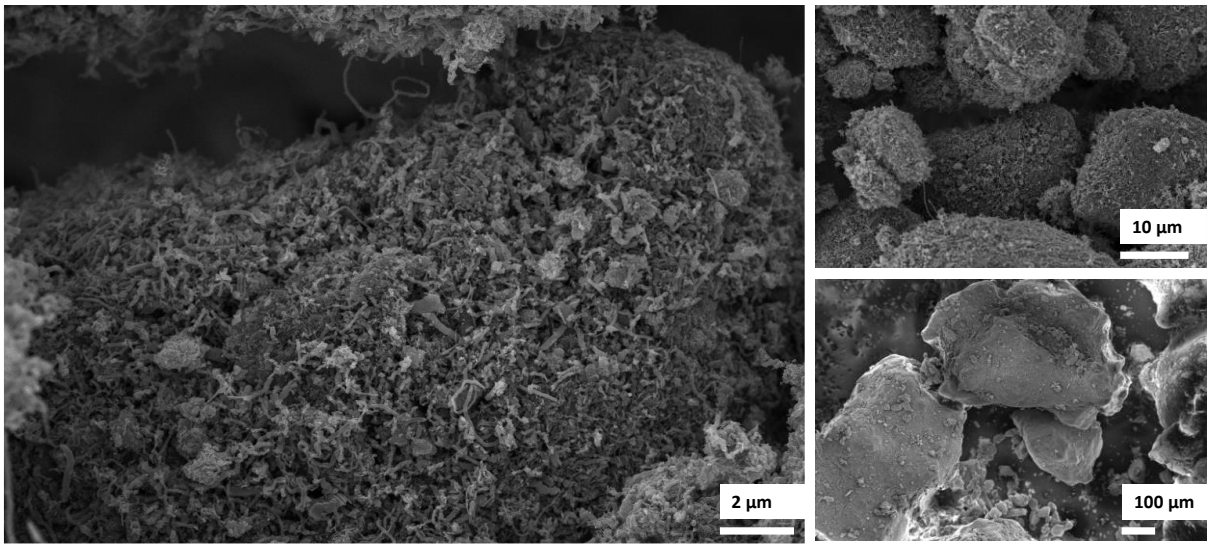

Figure S29 *An SEM micrograph of commercial ^{13}C powders imaged at 5 kV with 100 pA probe current and a secondary electron detector.*

7.3.6 Utilising GC-MS to Detect/Quantify $Li_2{}^{12}CO_3$ and $Li_2{}^{13}CO_3$

Crimp-top vials with Teflon septa were used to monitor the CO_2 evolution using GC-MS as an alternative to on-line MS. After potential hold experiments treatments, carbon cathodes were washed with DME and dried in a glovebox antechamber. The dried cathodes were then placed in an empty crimp top vial and sealed in an Ar-filled glovebox. 500 µL of degassed H_3PO_4 was injected onto the cathode and it was left react with the acid for 30 minutes. Then, the overhead gas was collected with a 10 µL gas tight Hamilton syringe and injected into a new crimp top vial sealed in the glovebox. The collected overhead gas was analysed using a ThermoFisher Scientific GC-MS in headspace mode.

This analysis can be done quantitative analysis as well by making a calibration curve using known amounts of Li_2CO_3 and $Li_2{}^{13}CO_3$. These standards were sealed in crimp top vials and decomposed with acid. Different amounts of overhead gas was collected and injected into empty sealed crimp top vials. A calibration curve was made by integrating the area under *m/z* 44 and *m/z* 45 curves.

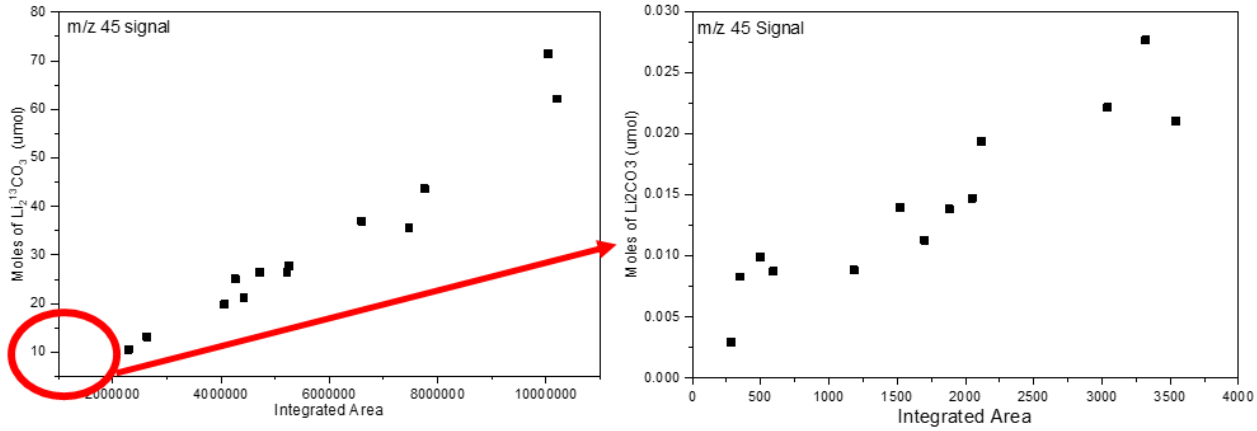

Figure S30 *The calibration curve for m/z 45 obtained by dissolving known amounts of $Li_2{}^{13}CO_3$ in 2M H_3PO_4 and collecting known volumes of evolved gas into sealed crimp top GC-MS vials.*

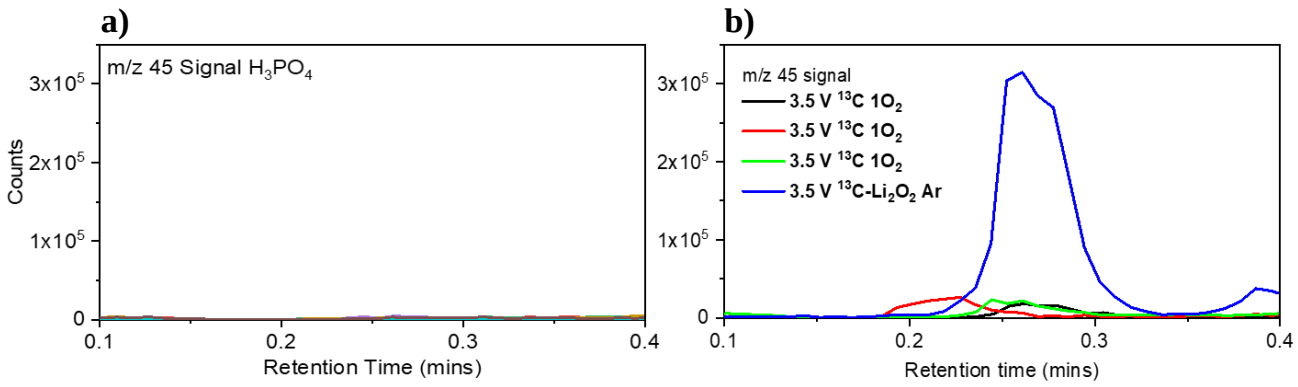

Figure S31 *The m/z 45 signal for a) 2 M H_3PO_4 (baseline measurement) and b) gas evolution for ^{13}C cathodes treated with $^1O_2$ at constant 3.5 V potential hold and a Li_2O_2 preloaded ^{13}C cathode kept at 3.5 V under Ar.*

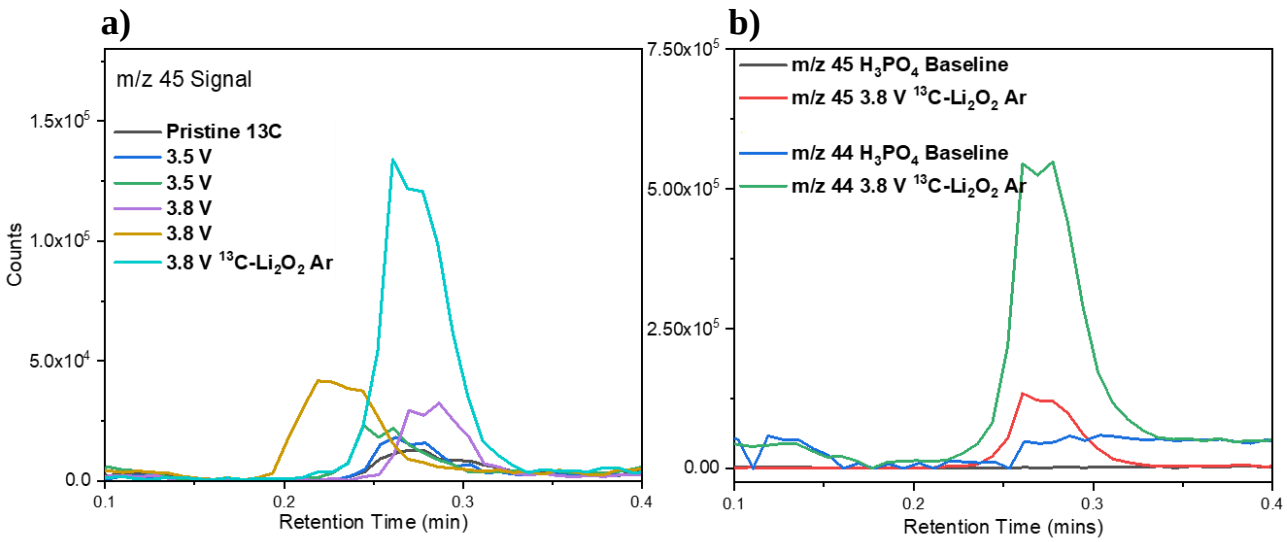

Figure S32 *The a) m/z 45 signal for ^{13}C cathodes held at different potentials and b) m/z 44-45 signal for a Li_2O_2 preloaded ^{13}C cathode held at 3.8 V.*

8 References

1 Manthiram, A. A reflection on lithium-ion battery cathode chemistry. *Nat Commun* **11**, (2020).

2 Liu, C. F., Neale, Z. G. & Cao, G. Z. Understanding electrochemical potentials of cathode materials in rechargeable batteries. *Mater Today* **19**, 109-123, (2016).

3 Kwak, W. J. *et al.* Lithium-oxygen batteries and related systems: Potential, status, and future. *Chem Rev* **120**, 6626-6683, (2020).

4 Aurbach, D., McCloskey, B. D., Nazar, L. F. & Bruce, P. G. Advances in understanding mechanisms underpinning lithium–air batteries. *Nat Energy* **1**, 16128, (2016).

5 Girishkumar, G., McCloskey, B., Luntz, A. C., Swanson, S. & Wilcke, W. Lithium–air battery: promise and challenges. *The Journal of Physical Chemistry Letters* **1**, 2193-2203, (2010).

6 Abraham, K. M. & Jiang, Z. A polymer electrolyte-based rechargeable lithium/oxygen battery. *J Electrochem Soc* **143**, 1-5, (1996).

7 Lu, J. *et al.* Aprotic and aqueous Li-O_2 batteries. *Chem Rev* **114**, 5611-5640, (2014).

8 Visco, S. J. *et al.* Aqueous and nonaqueous lithium-air batteries enabled by water-stable lithium metal electrodes. *J Solid State Electr* **18**, 1443-1456, (2014).

9 Hasegawa, S. *et al.* Study on lithium/air secondary batteries-Stability of NASICON-type lithium ion conducting glass-ceramics with water. *J Power Sources* **189**, 371-377, (2009).

10 Sunahiro, S., Matsui, M., Takeda, Y., Yamamoto, O. & Imanishi, N. Rechargeable aqueous lithium-air batteries with an auxiliary electrode for the oxygen evolution. *J Power Sources* **262**, 338-343, (2014).

11 Tan, P. *et al.* Advances and challenges in lithium-air batteries. *Appl Energ* **204**, 780-806, (2017).

12 Zhang, J. G., Wang, D. Y., Xu, W., Xiao, J. & Williford, R. E. Ambient operation of Li/Air batteries. *J Power Sources* **195**, 4332-4337, (2010).

13 *The Lithium Air Battery: Fundamentals*. Vol. 54 (Springer, 2015).

14 Schwenke, K. U., Metzger, M., Restle, T., Piana, M. & Gasteiger, H. A. The influence of water and protons on Li_2O_2 crystal growth in aprotic Li-O_2 cells. *J Electrochem Soc* **162**, A573-A584, (2015).

15 Liu, Q. C. *et al.* A flexible and wearable lithium-oxygen battery with record energy density achieved by the interlaced architecture inspired by bamboo slips. *Adv Mater* **28**, 8413-8418, (2016).

16 Kumar, B. *et al.* A Solid-State, Rechargeable, Long Cycle Life Lithium–Air Battery. *J Electrochem Soc* **157**, A50-A54, (2010).

17 Wang, Y. & Zhou, H. To draw an air electrode of a Li-air battery by pencil. *Energ Environ Sci* **4**, 1704-1707, (2011).

18 Zhu, X. B., Zhao, T. S., Tan, P., Wei, Z. H. & Wu, M. C. A high-performance solid-state lithium-oxygen battery with a ceramic-carbon nanostructured electrode. *Nano Energy* **26**, 565-576, (2016).

19 Liu, Y. J. *et al.* Intensive investigation on all-solid-state Li-air batteries with cathode catalysts of single-walled carbon nanotube/RuO_2. *J Power Sources* **395**, 439-443, (2018).

20 Inaguma, Y. *et al.* High Ionic-Conductivity in Lithium Lanthanum Titanate. *Solid State Commun* **86**, 689-693, (1993).

21 Liu, Y., He, P. & Zhou, H. Rechargeable solid-state Li-air and Li-S batteries: Materials, construction, and challenges. *Adv Energy Mater*, 1701602, (2017).

22 Chi, X. W. *et al.* A highly stable and flexible zeolite electrolyte solid-state Li-air battery. *Nature* **592**, 551-+, (2021).

23 Wu, S. C. *et al.* A super-hydrophobic quasi-solid electrolyte for Li-O_2 battery with improved safety and cycle life in humid atmosphere. *Adv Energy Mater* **7**, (2017).

24 Liu, Q. C. *et al.* A flexible and wearable lithium-oxygen battery with record energy density achieved by the interlaced architecture inspired by bamboo slips. *Adv Mater* **28**, 8413-8418, (2016).

25 Liu, T., Liu, Q. C., Xu, J. J. & Zhang, X. B. Cable-type water-survivable flexible Li-O_2 battery. *Small* **12**, 3101-3105, (2016).

26 Shu, C. Z., Long, J. P., Dou, S. X. & Wang, J. Z. Component-interaction reinforced quasi-solid electrolyte with multifunctionality for flexible Li-O_2 battery with superior safety under extreme conditions. *Small* **15**, (2019).

27 Read, J. Characterization of the lithium/oxygen organic electrolyte battery. *J Electrochem Soc* **149**, A1190-A1195, (2002).

28 Read, J. *et al.* Oxygen transport properties of organic electrolytes and performance of lithium/oxygen battery. *J Electrochem Soc* **150**, A1351-A1356, (2003).

29 Ogasawara, T., Debart, A., Holzapfel, M., Novak, P. & Bruce, P. G. Rechargeable Li_2O_2 electrode for lithium batteries. *J Am Chem Soc* **128**, 1390-1393, (2006).

30 Imanishi, N., Luntz, A. C. & Bruce, P. G. *The lithium air battery: fundamentals*. (Springer, 2014).

31 Lu, J. *et al.* A lithium-oxygen battery based on lithium superoxide. *Nature* **529**, 377-382, (2016).

32 Xia, C., Kwok, C. Y. & Nazar, L. F. A high-energy-density lithium-oxygen battery based on a reversible four-electron conversion to lithium oxide. *Science* **361**, 777-781, (2018).

33 Liu, T. *et al.* Cycling Li-O_2 batteries via LiOH formation and decomposition. *Science* **350**, 530-533, (2015).

34 Goolsby, A. D. & Sawyer, D. T. Electrochemical reduction of superoxide ion and oxidation of hydroxide ion in dimethyl sulfoxide. *Anal Chem* **40**, 83-86, (2002).

35 Merritt, M. V. & Sawyer, D. T. Electrochemical studies of the reactivity of superoxide ion with several alkyl halides in dimethyl sulfoxide. *The Journal of Organic Chemistry* **35**, 2157-2159, (2002).

36 Peng, Z. *et al.* Oxygen reactions in a non-aqueous Li^+ electrolyte. *Angewandte Chemie International Edition* **50**, 6351-6355, (2011).

37 Johnson, L. *et al.* The role of LiO_2 solubility in O_2 reduction in aprotic solvents and its consequences for Li–O_2 batteries. *Nat Chem* **6**, 1091-1099, (2014).

38 Laoire, C. O., Mukerjee, S., Abraham, K. M., Plichta, E. J. & Hendrickson, M. A. Influence of nonaqueous solvents on the electrochemistry of oxygen in the rechargeable lithium–air battery. *The Journal of Physical Chemistry C* **114**, 9178-9186, (2010).

39 Aurbach, D., Daroux, M., Faguy, P. & Yeager, E. The electrochemistry of noble metal electrodes in aprotic organic solvents containing lithium salts. *Journal of Electroanalytical Chemistry and Interfacial Electrochemistry* **297**, 225-244, (1991).

40 Laoire, C. O., Mukerjee, S., Abraham, K. M., Plichta, E. J. & Hendrickson, M. A. Elucidating the mechanism of oxygen reduction for Lithium-air battery applications. *The Journal of Physical Chemistry C* **113**, 20127-20134, (2009).

41 Qiu, S. L., Lin, C. L., Chen, J. & Strongin, M. Photoemission-studies of the interaction of li and solid molecular-oxygen. *Phys Rev B* **39**, 6194-6197, (1989).

42 Zhai, D. Y. *et al.* Interfacial effects on lithium superoxide disproportionation in Li-O_2 batteries. *Nano Lett* **15**, 1041-1046, (2015).

43 Itkis, D. M. *et al.* Reactivity of carbon in lithium-oxygen battery positive electrodes. *Nano Lett* **13**, 4697-4701, (2013).

44 Gallant, B. M. *et al.* Influence of Li_2O_2 morphology on oxygen reduction and evolution kinetics in Li–O_2 batteries. *Energ Environ Sci* **6**, 2518, (2013).

45 Yang, J. *et al.* Evidence for lithium superoxide-like species in the discharge product of a Li-O_2 battery. *Phys Chem Chem Phys* **15**, 3764-3771, (2013).

46 Zhai, D. Y. *et al.* Raman evidence for late stage disproportionation in a Li-O_2 battery. *J Phys Chem Lett* **5**, 2705-2710, (2014).

47 Yang, G., Wang, Y. & Ma, Y. A Stable, Magnetic and Metallic Li3O4 Compound as a Discharge Product in Li–Air Battery. *The Journal of Physical Chemistry Letters*, 140709203958007, (2014).

48 Pearson, R. G. Hard and soft acids and bases. *J Am Chem Soc* **85**, 3533-&, (1963).

49 Gutmann, V. Solvent effects on the reactivities of organometallic compounds. *Coordin Chem Rev* **18**, 225-255, (1976).

50 Sharon, D. *et al.* Mechanistic role of Li^+ dissociation level in aprotic Li-O_2 battery. *ACS Appl. Mater. Interfaces* **8**, 5300-5307, (2016).

51 Meini, S., Piana, M., Tsiouvaras, N., Garsuch, A. & Gasteiger, H. A. The effect of water on the discharge capacity of a non-catalyzed carbon cathode for Li-O_2 batteries. *Electrochem. Solid-State Lett.* **15**, A45-A48, (2012).

52 Aetukuri, N. B. *et al.* Solvating additives drive solution-mediated electrochemistry and enhance toroid growth in non-aqueous Li-O_2 batteries. *Nat Chem* **7**, 50-56, (2015).

53 Liu, B. *et al.* Temperature dependence of the oxygen reduction mechanism in nonaqueous Li-O_2 batteries. *Acs Energy Lett* **2**, 2525-2530, (2017).

54 Mitchell, R. R., Gallant, B. M., Shao-Horn, Y. & Thompson, C. V. Mechanisms of morphological evolution of Li_2O_2 particles during electrochemical growth. *The Journal of Physical Chemistry Letters* **4**, 1060-1064, (2013).

55 Adams, B. D. *et al.* Current density dependence of peroxide formation in the Li-O_2 battery and its effect on charge. *Energ Environ Sci* **6**, 1772-1778, (2013).

56 Kwabi, D. G. *et al.* Controlling Solution-Mediated Reaction Mechanisms of Oxygen Reduction Using Potential and Solvent for Aprotic Lithium-Oxygen Batteries. *J. Phys. Chem. Lett.* **7**, 1204-1212, (2016).

57 Ganapathy, S. *et al.* Operando nano-beam diffraction to follow the decomposition of individual Li_2O_2 grains in a non-aqueous Li-O_2 battery. *The Journal of Physical Chemistry Letters*, 3388–3394, (2016).

58 Lu, Y.-C. & Shao-Horn, Y. Probing the reaction kinetics of the charge reactions of nonaqueous Li-O_2 batteries. *The Journal of Physical Chemistry Letters* **4**, 93-99, (2012).

59 Petit, Y. K. *et al.* Mechanism of mediated alkali peroxide oxidation and triplet versus singlet oxygen formation. *Nat Chem* **13**, 465-+, (2021).

60 Freunberger, S. A. *et al.* Reactions in the rechargeable lithium-O_2 battery with alkyl carbonate electrolytes. *J Am Chem Soc* **133**, 8040-8047, (2011).

61 Chen, Y., Freunberger, S. A., Peng, Z., Barde, F. & Bruce, P. G. Li-O_2 battery with a dimethylformamide electrolyte. *J Am Chem Soc* **134**, 7952-7957, (2012).

62 McCloskey, B. D., Bethune, D. S., Shelby, R. M., Girishkumar, G. & Luntz, A. C. Solvents' critical role in nonaqueous lithium–oxygen battery electrochemistry. *The Journal of Physical Chemistry Letters* **2**, 1161-1166, (2011).

63 Zhang, Z. *et al.* Increased stability toward oxygen reduction products for lithium-air batteries with oligoether-functionalized silane electrolytes. *The Journal of Physical Chemistry C* **115**, 25535-25542, (2011).

64 Ganapathy, S. *et al.* Nature of Li_2O_2 oxidation in a Li-O_2 battery revealed by operando X-ray diffraction. *J Am Chem Soc* **136**, 16335-16344, (2014).

65 Kang, S., Mo, Y., Ong, S. P. & Ceder, G. A facile mechanism for recharging Li_2O_2 in Li–O_2 batteries. *Chem Mater* **25**, 3328-3336, (2013).

66 Mo, Y., Ong, S. P. & Ceder, G. First-principles study of the oxygen evolution reaction of lithium peroxide in the lithium-air battery. *Phys Rev B* **84**, 205446, (2011).

67 Dunst, A., Epp, V., Hanzu, I., Freunberger, S. & Wilkening, M. Short-range Li diffusion vs long-range ionic conduction in nanocrystalline lithium peroxide Li_2O_2 - the discharge product in lithium-air batteries. *Energ Environ Sci*, (2014).

68 Wang, Y. *et al.* A solvent-controlled oxidation mechanism of Li_2O_2 in lithium-oxygen batteries. *Joule* **2**, 2364-2380, (2018).

69 Zhong, L. *et al.* In situ transmission electron microscopy observations of electrochemical oxidation of Li_2O_2. *Nano Lett* **13**, 2209-2214, (2013).

70 Peng, Q. L., Chen, J. F., Ji, H. X., Morita, A. & Ye, S. Origin of the overpotential for the oxygen evolution reaction on a well-defined graphene electrode probed by in situ sum frequency generation vibrational spectroscopy. *J Am Chem Soc* **140**, 15568-15571, (2018).

71 Wang, Y. & Lu, Y. C. Isotopic labeling reveals active reaction interfaces for electrochemical oxidation of lithium peroxide. *Angew Chem Int Edit* **58**, 6962-6966, (2019).

72 Dong, S. M. *et al.* Singlet oxygen and dioxygen bond cleavage in the aprotic lithium-oxygen battery. *Joule* **6**, 185-192, (2022).

73 Lai, J. *et al.* Electrolytes for Rechargeable Lithium–Air Batteries. *Angewandte Chemie International Edition* **59**, 2974-2997, (2020).

74 Debart, A., Paterson, A. J., Bao, J. & Bruce, P. G. Alpha-MnO_2 nanowires: a catalyst for the O_2 electrode in rechargeable lithium batteries. *Angewandte Chemie International Edition* **47**, 4521-4524, (2008).

75 Thapa, A. K. & Ishihara, T. Mesoporous α-MnO_2/Pd catalyst air electrode for rechargeable lithium–air battery. *J Power Sources* **196**, 7016-7020, (2011).

76 Yang, Y., Sun, Q., Li, Y.-S., Li, H. & Fu, Z.-W. Nanostructured diamond like carbon thin film electrodes for lithium air batteries. *J Electrochem Soc* **158**, B1211-B1216, (2011).

77 Xiao, J. *et al.* Investigation of the rechargeability of Li-O_2 batteries in non-aqueous electrolyte. *J Power Sources* **196**, 5674-5678, (2011).

78 Mizuno, F., Nakanishi, S., Kotani, Y., Yokoishi, S. & Iba, H. Rechargeable li-air batteries with carbonate-based liquid electrolytes. *Electrochemistry* **78**, 403-405, (2010).

79 Bryantsev, V. S. & Blanco, M. Computational study of the mechanisms of superoxide-induced decomposition of organic carbonate-based electrolytes. *The Journal of Physical Chemistry Letters* **2**, 379-383, (2011).

80 Peng, Z., Freunberger, S. A., Chen, Y. & Bruce, P. G. A reversible and higher-rate Li-O_2 battery. *Science* **337**, 563-566, (2012).

81 Ottakam Thotiyl, M. M. *et al.* A stable cathode for the aprotic Li-O_2 battery. *Nat Mater* **12**, 1050-1056, (2013).

82 Xu, D., Wang, Z. L., Xu, J. J., Zhang, L. L. & Zhang, X. B. Novel DMSO-based electrolyte for high performance rechargeable Li-O_2 batteries. *Chem Commun* **48**, 6948-6950, (2012).

83 Sharon, D. *et al.* Oxidation of dimethyl sulfoxide solutions by electrochemical reduction of oxygen. *The Journal of Physical Chemistry Letters* **4**, 3115-3119, (2013).

84 Mozhzhukhina, N., Méndez De Leo, L. P. & Calvo, E. J. Infrared spectroscopy studies on stability of dimethyl sulfoxide for application in a Li–air battery. *The Journal of Physical Chemistry C* **117**, 18375-18380, (2013).

85 Kwabi, D. G. *et al.* Chemical instability of dimethyl sulfoxide in lithium–air batteries. *The Journal of Physical Chemistry Letters* **5**, 2850-2856, (2014).

86 Cong, G. T., Wang, W. W., Lai, N. C., Liang, Z. J. & Lu, Y. C. A high-rate and long-life organic-oxygen battery. *Nat Mater* **18**, 390-+, (2019).

87 Bryantsev, V. Calculation of solvation free energies of Li^+ and O_2^- ions and neutral lithium–oxygen compounds in acetonitrile using mixed cluster/continuum models. *Theor Chem Acc* **131**, 1-11, (2012).

88 Vasudevan, D. & Wendt, H. Electroreduction of oxygen in aprotic media. *J Electroanal Chem* **392**, 69-74, (1995).

89 Shi, C. & Anson, F. C. The effect of triphenylmethyl cations on the electroreduction of O_2 in nitrobenzene or acetonitrile. *J Electroanal Chem* **484**, 144-149, (2000).

90 Bryantsev, V. S. *et al.* Predicting solvent stability in aprotic electrolyte Li–air batteries: nucleophilic substitution by the superoxide anion radical (O_2•⁻). *The Journal of Physical Chemistry A* **115**, 12399-12409, (2011).

91 Guo, H. *et al.* Review of electrolytes in nonaqueous lithium-oxygen batteries. *Advanced Sustainable Systems* **2**, (2018).

92 Bryantsev, V. S. *et al.* Predicting the electrochemical behavior of lithium nitrite in acetonitrile with quantum chemical methods. *J Am Chem Soc* **136**, 3087-3096, (2014).

93 Walker, W. *et al.* A rechargeable Li-O_2 battery using a lithium nitrate/N,N-dimethylacetamide electrolyte. *J Am Chem Soc* **135**, 2076-2079, (2013).

94 Wang, H., Xie, K., Wang, L. & Han, Y. N-methyl-2-pyrrolidone as a solvent for the non-aqueous electrolyte of rechargeable Li-air batteries. *J Power Sources* **219**, 263-271, (2012).

95 Bryantsev, V. S. *et al.* Investigation of fluorinated amides for solid–electrolyte interphase stabilization in Li–O_2 batteries using amide-based electrolytes. *The Journal of Physical Chemistry C* **117**, 11977-11988, (2013).

96 Uddin, J. *et al.* Lithium nitrate as regenerable SEI stabilizing agent for rechargeable Li/O_2 batteries. *The Journal of Physical Chemistry Letters* **4**, 3760-3765, (2013).

97 Sharon, D. *et al.* Catalytic behavior of lithium nitrate in Li-O_2 cells. *ACS Appl. Mater. Interfaces* **7**, 16590-16600, (2015).

98 Sharon, D. *et al.* On the challenge of electrolyte solutions for Li–air batteries: monitoring oxygen reduction and related reactions in polyether solutions by spectroscopy and EQCM. *The Journal of Physical Chemistry Letters* **4**, 127-131, (2012).

99 Freunberger, S. A. *et al.* The lithium-oxygen battery with ether-based electrolytes. *Angewandte Chemie International Edition* **50**, 8609-8613, (2011).

100 Sharon, D., Hirshberg, D., Afri, M., Frimer, A. A. & Aurbach, D. The importance of solvent selection in Li-O_2 cells. *Chem Commun (Camb)* **53**, 3269-3272, (2017).

101 McCloskey, B. D. *et al.* Combining accurate O_2 and Li_2O_2 assays to separate discharge and charge stability limitations in nonaqueous Li-O_2 batteries. *The Journal of Physical Chemistry Letters* **4**, 2989-2993, (2013).

102 Adams, B. D. *et al.* Towards a stable organic electrolyte for the lithium oxygen battery. *Adv Energy Mater* **5**, 1400867, (2015).

103 Monaco, S. *et al.* An electrochemical study of oxygen reduction in pyrrolidinium-based ionic liquids for lithium/oxygen batteries. *Electrochim Acta* **83**, 94-104, (2012).

104 Kwon, H. M. *et al.* Stability of glyme solvate ionic liquid as an electrolyte for rechargeable Li-O_2 batteries. *ACS Appl. Mater. Interfaces* **9**, 6014-6021, (2017).

105 Wang, H. *et al.* A solvate ionic liquid as the anolyte for aqueous rechargeable Li-O_2 batteries. *Chemelectrochem* **2**, 1144-1151, (2015).

106 Katayama, Y., Onodera, H., Yamagata, M. & Miura, T. Electrochemical reduction of oxygen in some hydrophobic room-temperature molten salt systems. *J Electrochem Soc* **151**, A59-A63, (2004).

107 Das, S. *et al.* Instability of ionic liquid-based electrolytes in Li–O_2 batteries. *The Journal of Physical Chemistry C* **119**, 18084-18090, (2015).

108 Krueger, B., Rücker, K. K. & Wittstock, G. Redox Mediators for Faster Lithium Peroxide Oxidation in a Lithium–Oxygen Cell: A Scanning Electrochemical Microscopy Study. *ACS Applied Energy Materials* **5**, 3724-3733, (2022).

109 Kwak, W. J. *et al.* Optimized Electrolyte with High Electrochemical Stability and Oxygen Solubility for Lithium-Oxygen and Lithium-Air Batteries. *Acs Energy Lett* **5**, 2182-2190, (2020).

110 Zhang, S. S. & Read, J. Partially fluorinated solvent as a co-solvent for the non-aqueous electrolyte of Li/air battery. *J Power Sources* **196**, 2867-2870, (2011).

111 Vanhoutte, G., Hojniak, S. D., Barde, F., Binnemans, K. & Fransaer, J. Fluorine-functionalized ionic liquids with high oxygen solubility. *Rsc Adv* **8**, 4525-4530, (2018).

112 Burke, C. M., Pande, V., Khetan, A., Viswanathan, V. & McCloskey, B. D. Enhancing electrochemical intermediate solvation through electrolyte anion selection to increase nonaqueous Li-O_2 battery capacity. *Proceedings of the National Academy of Sciences of the United States of America* **112**, 9293-9298, (2015).

113 Oswald, S. *et al.* XPS investigations of electrolyte/electrode interactions for various Li-ion battery materials. *Anal Bioanal Chem* **400**, 691-696, (2011).

114 Veith, G. M., Dudney, N. J., Howe, J. & Nanda, J. Spectroscopic characterization of solid discharge products in Li–air cells with aprotic carbonate electrolytes. *The Journal of Physical Chemistry C* **115**, 14325-14333, (2011).

115 Chalasani, D. & Lucht, B. L. Reactivity of electrolytes for lthium-oxygen batteries with Li_2O_2. *Ecs Electrochem Lett* **1**, A38-A42, (2012).

116 Veith, G. M., Nanda, J., Delmau, L. H. & Dudney, N. J. Influence of lithi um salts on the discharge chemistry of Li–air cells. *The Journal of Physical Chemistry Letters* **3**, 1242-1247, (2012).

117 Hyoung Oh, S., Yim, T., Ekaterina, P. & Nazar, L. F. Decomposition reaction of lithium bis(oxalato)borate in the rechargeable lithium-oxygen cell. *Electrochem. Solid-State Lett.* **14**, A185-A188, (2011).

118 Kang, S. J., Mori, T., Narizuka, S., Wilcke, W. & Kim, H. C. Deactivation of carbon electrode for elimination of carbon dioxide evolution from rechargeable lithium-oxygen cells. *Nat Commun* **5**, 3937, (2014).

119 Rosy, Akabayov, S., Leskes, M. & Noked, M. Bifunctional role of $LiNO_3$ in Li-O_2 batteries: Deconvoluting surface and catalytic effects. *Acs Appl Mater Inter* **10**, 29622-29629, (2018).

120 Giordani, V. *et al.* Synergistic effect of oxygen and $LiNO_3$ on the interfacial stability of lithium metal in a Li/O_2 battery. *J Electrochem Soc* **160**, A1544-A1550, (2013).

121 Kwak, W.-J. *et al.* Li–O_2 cells with LiBr as an electrolyte and a redox mediator. *Energy Environ. Sci.* **9**, 2334-2345, (2016).

122 Kwak, W.-J. *et al.* Understanding the behavior of Li-oxygen cells containing LiI. *J Mater Chem A* **3**, 8855-8864, (2015).

123 Nasybulin, E. *et al.* Effects of electrolyte salts on the performance of Li-O_2 batteries. *The Journal of Physical Chemistry C* **117**, 2635-2645, (2013).

124 Lindberg, J. *et al.* Li salt anion effect on O_2 solubility in an Li-O_2 battery. *J Phys Chem C* **122**, 1913-1920, (2018).

125 Xu, W. *et al.* The stability of organic solvents and carbon electrode in nonaqueous Li-O_2 batteries. *J Power Sources* **215**, 240-247, (2012).

126 Younesi, R., Hahlin, M. & Edstrom, K. Surface characterization of the carbon cathode and the lithium anode of Li-O_2 batteries using $LiClO_4$ or LiBOB salts. *ACS Appl Mater Interfaces* **5**, 1333-1341, (2013).

127 Younesi, R., Hahlin, M., Björefors, F., Johansson, P. & Edström, K. Li-O_2 battery degradation by lithium peroxide (Li_2O_2): A model study. *Chem Mater* **25**, 77-84, (2012).

128 Shao, Y. *et al.* Making Li-air batteries rechargeable: Material challenges. *Adv Funct Mater* **23**, 987-1004, (2013).

129 Adams, B. *et al.* The importance of nanometric passivating films on cathodes for Li-Air batteries. *Acs Nano* **8**, 12483-12493, (2014).

130 Kundu, D. *et al.* Nanostructured metal carbides for aprotic Li–O_2 batteries: New insights into interfacial reactions and cathode stability. *The Journal of Physical Chemistry Letters* **6**, 2252-2258, (2015).

131 Kundu, D., Black, R., Berg, E. J. & Nazar, L. F. A highly active nanostructured metallic oxide cathode for aprotic Li–O_2 batteries. *Energy Environ. Sci.* **8**, 1292-1298, (2015).

132 Chang, Y. Q. *et al.* A carbon and binder free nanostructured cathode for high-performance nonaqueous Li-O_2 battery. *Adv Sci* **2**, (2015).

133 Cui, Y. M., Wen, Z. Y. & Liu, Y. A free-standing-type design for cathodes of rechargeable Li-O_2 batteries. *Energ Environ Sci* **4**, 4727-4734, (2011).

134 Wang, Z. *et al.* Nickel-doped $La_{0.8}Sr_{0.2}Mn_{1-x}Ni_xO_3$ nanoparticles containing abundant oxygen vacancies as an optimized bifunctional catalyst for oxygen cathode in rechargeable lithium-air batteries. *ACS Appl Mater Interfaces* **8**, 6520-6528, (2016).

135 McCloskey, B. D. *et al.* Twin problems of interfacial carbonate formation in nonaqueous Li-O_2 batteries. *The Journal of Physical Chemistry Letters* **3**, 997-1001, (2012).

136 Leskes, M. *et al.* Direct detection of discharge products in lithium-oxygen batteries by solid-state NMR spectroscopy. *Angewandte Chemie International Edition* **51**, 8560-8563, (2012).

137 Gallant, B. M. *et al.* Chemical and morphological changes of Li–O_2 battery electrodes upon cycling. *The Journal of Physical Chemistry C* **116**, 20800-20805, (2012).

138 Ottakam Thotiyl, M. M., Freunberger, S. A., Peng, Z. & Bruce, P. G. The carbon electrode in nonaqueous Li-O_2 cells. *J Am Chem Soc* **135**, 494-500, (2013).

139 Belova, A. I., Kwabi, D. G., Yashina, L. V., Shao-Horn, Y. & Itkis, D. M. Mechanism of oxygen reduction in aprotic Li–air batteries: The role of carbon electrode surface structure. *The Journal of Physical Chemistry C* **121**, 1569-1577, (2017).

140 Bae, Y. *et al.* Tuning the carbon crystallinity for highly stable Li–O_2 batteries. *Chem Mater* **28**, 8160-8169, (2016).

141 Yeager, E. Electrocatalysts for O_2 reduction. *Electrochim Acta* **29**, 1527-1537, (1984).

142 Garten, V. A. & Weiss, D. E. A new Interpretation of the acidic and basic structures in carbons. 2. The chromene-carbonium ion couple in carbon. *Aust J Chem* **10**, 309-328, (1957).

143 Paliteiro, C., Hamnett, A. & Goodenough, J. B. The electroreduction of oxygen on pyrolytic-graphite. *J Electroanal Chem* **233**, 147-159, (1987).

144 Balaish, M., Gao, X., Bruce, P.G., Ein-Eli, Y. Enhanced Li-O_2 battery performance in a binary "Liquid Teflon" and dual redox mediators. *Adv Mater Technol-Us* **4**, (2019).

145 Liu, S. *et al.* Free-standing, hierarchically porous carbon nanotube film as a binder-free electrode for high-energy Li-O_2 batteries. *J Mater Chem A* **1**, 12033, (2013).

146 Xie, J. *et al.* Three dimensionally ordered mesoporous carbon as a stable, high-performance Li-O_2 battery cathode. *Angew Chem Int Ed Engl* **54**, 4299-4303, (2015).

147 Huang, Z., Deng, Z., Shen, Y., Chen, W., Liu, W. Xie, M., Li, Y., Huang, Y. A Li-O_2 battery cathode with vertical mass/charge transfer pathways. *J Mater Chem A* **7**, (2019).

148 Black, R. *et al.* Screening for superoxide reactivity in Li-O_2 batteries: effect on Li_2O_2/LiOH crystallization. *J Am Chem Soc* **134**, 2902-2905, (2012).

149 Younesi, R. *et al.* Ether Based Electrolyte, LiB(CN)4 Salt and Binder Degradation in the Li–O2 Battery Studied by Hard X-ray Photoelectron Spectroscopy (HAXPES). *The Journal of Physical Chemistry C* **116**, 18597-18604, (2012).

150 Papp, J. K. *et al.* Poly(vinylidene fluoride) (PVDF) binder degradation in Li-O_2 batteries: a consideration for the characterization of lithium superoxide. *J. Phys. Chem. Lett.* **8**, 1169-1174, (2017).

151 Amanchukwu, C. V., Harding, J. R., Shao-Horn, Y. & Hammond, P. T. Understanding the chemical stability of polymers for lithium–air batteries. *Chem Mater* **27**, 550-561, (2015).

152 Nasybulin, E. *et al.* Stability of polymer binders in Li-O_2 batteries. *J Power Sources* **243**, 899-907, (2013).

153 Kozen, A. C. *et al.* Stabilization of Lithium Metal Anodes by Hybrid Artificial Solid Electrolyte Interphase. *Chem Mater* **29**, 6298-6307, (2017).

154 Tong, B., Huang, J., Zhou, Z. B. & Peng, Z. Q. The salt matters: Enhanced reversibility of Li-O_2 batteries with a Li[(CF_3SO_2)(n-$C_4F_9SO_2$)N]-based electrolyte. *Adv Mater* **30**, (2018).

155 Liu, Q. C. *et al.* Artificial protection film on lithium metal anode toward long-cycle-life lithium-oxygen batteries. *Adv Mater*, (2015).

156 Kwak, W.-J., Jung, H.-G., Aurbach, D. & Sun, Y.-K. Optimized bicompartment two solution cells for effective and stable operation of Li-O_2 batteries. *Adv Energy Mater*, 1701232, (2017).

157 Ye, L. *et al.* Stabilizing Lithium into Cross-Stacked Nanotube Sheets with an Ultra-High Specific Capacity for Lithium Oxygen Batteries. *Angew Chem Int Edit* **58**, 2437-2442, (2019).

158 Brissot, C., Rosso, M., Chazalviel, J. N. & Lascaud, S. In situ concentration cartography in the neighborhood of dendrites growing in lithium/polymer-electrolyte/lithium cells. *J Electrochem Soc* **146**, 4393-4400, (1999).

159 Aurbach, D. *et al.* Recent studies of the lithium liquid electrolyte interface - Electrochemical, morphological and spectral studies of a few important systems. *J Power Sources* **54**, 76-84, (1995).

160 Gireaud, L., Grugeon, S., Laruelle, S., Yrieix, B. & Tarascon, J. M. Lithium metal stripping/plating mechanisms studies: A metallurgical approach. *Electrochem Commun* **8**, 1639-1649, (2006).

161 Laoire, C., Mukerjee, S., Plichta, E. J., Hendrickson, M. A. & Abraham, K. M. Rechargeable Lithium/TEGDME-$LiPF_6$/O_2 battery. *J Electrochem Soc* **158**, A302-A308, (2011).

162 Assary, R. S. *et al.* The effect of oxygen crossover on the anode of a Li-O_2 battery using an ether-based solvent: insights from experimental and computational studies. *Chemsuschem* **6**, 51-55, (2013).

163 Giordani, V., Uddin, J., Bryantsev, V. S., Chase, G. V. & Addison, D. High concentration lithium nitrate/dimethylacetamide electrolytes for lithium/oxygen cells. *J Electrochem Soc* **163**, A2673-A2678, (2016).

164 Togasaki, N., Momma, T. & Osaka, T. Enhanced cycling performance of a Li metal anode in a dimethylsulfoxide-based electrolyte using highly concentrated lithium salt for a lithium-oxygen battery. *J Power Sources* **307**, 98-104, (2016).

165 Liu, B. *et al.* Enhanced cycling stability of rechargeable Li-O_2 batteries using high-concentration electrolytes. *Adv Funct Mater* **26**, 605-613, (2016).

166 Gao, X., Jovanov, Z. P., Chen, Y., Johnson, L. R. & Bruce, P. G. Phenol-catalyzed discharge in the aprotic lithium-oxygen battery. *Angewandte Chemie International Edition* **56**, 6539-6543, (2017).

167 Guo, Z., Li, C., Liu, J., Wang, Y. & Xia, Y. A long-life lithium-air battery in ambient air with a polymer electrolyte containing a redox mediator. *Angewandte Chemie International Edition* **56**, 7505-7509, (2017).

168 Kim, B. G. *et al.* A moisture- and oxygen-impermeable separator for aprotic Li-O_2 batteries. *Adv Funct Mater* **26**, 1747-1756, (2016).

169 Cao, D. Q., Yu, F. J., Gao, X. W. & Chen, Y. H. Improving the true cycling of redox mediators-assisted Li-O_2 batteries. *Energy Environ Mater* **4**, 201-207, (2021).

170 Sun, D. *et al.* A solution-phase bifunctional catalyst for lithium-oxygen batteries. *J Am Chem Soc* **136**, 8941-8946, (2014).

171 Lee, D. J., Lee, H., Kim, Y. J., Park, J. K. & Kim, H. T. Sustainable Redox Mediation for Lithium-Oxygen Batteries by a Composite Protective Layer on the Lithium-Metal Anode. *Adv Mater*, (2015).

172 Ha, S. *et al.* Investigation on the stability of Li metal anode in the Li–O_2 batteries with a redox mediator. *J. Mater. Chem. A* **5**, 10609-10621, (2017).

173 Hassoun, J. *et al.* A metal-free, lithium-ion oxygen battery: a step forward to safety in lithium-air batteries. *Nano Lett* **12**, 5775-5779, (2012).

174 Ma, S. *et al.* Reversibility of noble metal-catalyzed aprotic Li-O_2 batteries. *Nano Lett* **15**, 8084-8090, (2015).

175 McCloskey, B. D. *et al.* On the efficacy of electrocatalysis in nonaqueous Li-O_2 batteries. *J Am Chem Soc* **133**, 18038-18041, (2011).

176 Lacey, M. J., Frith, J. T. & Owen, J. R. A redox shuttle to facilitate oxygen reduction in the lithium air battery. *Electrochem Commun* **26**, 74-76, (2013).

177 Yang, L., Frith, J. T., Garcia-Araez, N. & Owen, J. R. A new method to prevent degradation of lithium-oxygen batteries: Reduction of superoxide by viologen. *Chem Commun* **51**, 1705-1708, (2015).

178 Lodge, A. W., Lacey, M. J., Fitt, M., Garcia-Araez, N. & Owen, J. R. Critical appraisal on the role of catalysts for the oxygen reduction reaction in lithium-oxygen batteries. *Electrochim Acta*, (2014).

179 Matsuda, S., Hashimoto, K. & Nakanishi, S. Efficient Li_2O_2 formation via aprotic oxygen reduction reaction mediated by quinone derivatives. *The Journal of Physical Chemistry C* **118**, 18397-18400, (2014).

180 Ko, Y. *et al.* Biological Redox Mediation in Electron Transport Chain of Bacteria for Oxygen Reduction Reaction Catalysts in Lithium-Oxygen Batteries. *Adv Funct Mater* **29**, (2019).

181 Trahan, M. J. *et al.* Cobalt phthalocyanine catalyzed lithium-air batteries. *J Electrochem Soc* **160**, A1577-A1586, (2013).

182 Gao, X., Chen, Y., Johnson, L. & Bruce, P. G. Promoting solution phase discharge in Li-O_2 batteries containing weakly solvating electrolyte solutions. *Nature Materials* **15**, 882–888, (2016).

183 Chen, Y., Freunberger, S. A., Peng, Z., Fontaine, O. & Bruce, P. G. Charging a Li-O_2 battery using a redox mediator. *Nature Chemistry* **5**, 489–494, (2013).

184 Chase, G. V. *et al.* Soluble oxygen evolving catalysts for rechargeable metal-air batteries. US20120028137 A1 (2012).

185 Behl, W. K. & Chin, D. T. Electrochemical Overcharge Protection of Rechargeable Lithium Batteries .1. Kinetics of Iodide Tri-Iodide Iodine Redox Reactions on Platinum in Liasf6 Tetrahydrofuran Solutions. *J Electrochem Soc* **135**, 16-21, (1988).

186 Behl, W. K. & Chin, D. T. Electrochemical Overcharge Protection of Rechargeable Lithium Batteries .2. Effect of Lithium Iodide-Iodine Additives on the Behavior of Lithium Electrode in Liasf6-Tetrahydrofuran Solutions. *J Electrochem Soc* **135**, 21-25, (1988).

187 Leverick, G. *et al.* Tunable redox mediators for Li-O_2 batteries based on interhalide complexes. *Acs Appl Mater Inter* **14**, 6689-6701, (2022).

188 Bergner, B. J., Schurmann, A., Peppler, K., Garsuch, A. & Janek, J. TEMPO: a mobile catalyst for rechargeable Li-O_2 batteries. *Journal of the American Chemical Society* **136**, 15054-15064, (2014).

189 Bergner, B. J. *et al.* Understanding the fundamentals of redox mediators in Li-O_2 batteries: a case study on nitroxides. *Phys Chem Chem Phys* **17**, 31769-31779, (2015).

190 Chen, Y., Gao, X., Johnson, L. R. & Bruce, P. G. Kinetics of lithium peroxide oxidation by redox mediators and consequences for the lithium-oxygen cell. *Nat Commun* **9**, 767, (2018).

191 Gao, X., Chen, Y., Johnson, L. R., Jovanov, Z. P. & Bruce, P. G. A rechargeable lithium–oxygen battery with dual mediators stabilizing the carbon cathode. *Nature Energy* **2**, 17118, (2017).

192 Ko, Y. *et al.* A comparative kinetic study of redox mediators for high-power lithium-oxygen batteries. *J Mater Chem A* **7**, 6491-6498, (2019).

193 Matsuda, S. *et al.* Cobalt phthalocyanine analogs as soluble catalysts that improve the charging performance of Li-O_2 batteries. *Chem Phys Lett* **620**, 78-81, (2015).

194 Kwak, W. J. *et al.* Deactivation of redox mediators in lithium-oxygen batteries by singlet oxygen. *Nat Commun* **10**, (2019).

195 Lim, H.-D. *et al.* Rational design of redox mediators for advanced Li–O_2 batteries. *Nature Energy* **1**, 16066, (2016).

196 Ryu, W. H. *et al.* Heme biomolecule as redox mediator and oxygen shuttle for efficient charging of lithium-oxygen batteries. *Nat Commun* **7**, 12925, (2016).

197 Xu, C. *et al.* Bifunctional redox mediator supported by an anionic surfactant for long-cycle Li-O_2 batteries. *Acs Energy Lett* **2**, 2659-2666, (2017).

198 Mulliken, R. S. The assignment of quantum numbers for electrons in molecules I. *Phys Rev* **32**, 0186-0222, (1928).

199 Mulliken, R. S. The interpretation of band spectra Part III. Electron quantum numbers and states of molecules and their atoms. *Rev Mod Phys* **4**, 0001-0086, (1932).

200 Schweitzer, C. & Schmidt, R. Physical mechanisms of generation and deactivation of singlet oxygen. *Chem Rev* **103**, 1685-1757, (2003).

201 Schurmann, A., Luerssen, B., Mollenhauer, D., Janek, J. & Schroder, D. Singlet Oxygen in Electrochemical Cells: A Critical Review of Literature and Theory. *Chem Rev* **121**, 12445-12464, (2021).

202 Silver, D. M. Hierarchy of symmetry conservation rules governing chemical-reaction systems. *J Am Chem Soc* **96**, 5959-5967, (1974).

203 Arnold, S. J., Kubo, M. & Ogryzlo, E. A. Relaxation and reactivity of singlet oxygen. *AdvChem Ser*, 133-&, (1968).

204 Barik, A. P., I. Mohan, H. Bajaj, P.N. Sapre, A.V., Mittal, J.P., Mukherjee, T. Singlet oxygen: Photosensitized generation, detection and reaction with organic molecules. (2006).

205 Wandt, J., Jakes, P., Granwehr, J., Gasteiger, H. A. & Eichel, R.-A. Singlet oxygen formation during the charging process of an aprotic lithium–oxygen battery. *Angewandte Chemie International Edition* **55**, 1-5, (2016).

206 Schafzahl, L. *et al.* Singlet oxygen during cycling of the aprotic sodium-O_2 battery. *Angew Chem Int Ed Engl* **56**, 15728-15732, (2017).

207 Mahne, N., Fontaine, O., Thotiyl, M. O., Wilkening, M. & Freunberger, S. A. Mechanism and performance of lithium-oxygen batteries - a perspective. *Chem Sci* **8**, 6716-6729, (2017).

208 Mourad, E. *et al.* Singlet oxygen from cation driven superoxide disproportionation and consequences for aprotic metal-O_2 batteries. *Energ Environ Sci* **12**, (2019).

209 Mahne, N., Renfrew, S. E., McCloskey, B. D. & Freunberger, S. A. Electrochemical Oxidation of Lithium Carbonate Generates Singlet Oxygen. *Angew Chem Int Ed Engl*, (2018).

210 Mahne, N. *et al.* Singlet oxygen generation as a major cause for parasitic reactions during cycling of aprotic lithium–oxygen batteries. *Nature Energy* **2**, 17036, (2017).

211 Liang, Z. J., Zou, Q. L., Xie, J. & Lu, Y. C. Suppressing singlet oxygen generation in lithium-oxygen batteries with redox mediators. *Energ Environ Sci* **13**, 2870-2877, (2020).

212 Kwak, W. J. *et al.* Oxidation Stability of Organic Redox Mediators as Mobile Catalysts in Lithium-Oxygen Batteries. *Acs Energy Lett* **5**, 2122-2129, (2020).

213 Bard, A. J. & Faulkner, L. R. *Electrochemical methods. Fundamentals and applications*. 2 edn, (Wiley, 2000).

214 Lepage, D., Michot, C., Liang, G. X., Gauthier, M. & Schougaard, S. B. A soft chemistry approach to coating of $LiFePO_4$ with a conducting polymer. *Angew Chem Int Edit* **50**, 6884-6887, (2011).

215 Ma, Z. & Bobbitt, J. M. Organic oxoammonium salts. 3. A new convenient method for the oxidation of alcohols to aldehydes and ketones. *J Org Chem* **56**, 6110-6114, (1991).

216 Giffard, H. *et al.* Oxidation of TTF derivatives using (Diacetoxyiodo)benzene: A general chemical route toward cation radicals, dications, and nonstoichiometric salts. *J Am Chem Soc* **123**, 3852-3853, (2001).

217 Reiners, M. *et al.* Teaching Ferrocenium How to Relax: A Systematic Study on Spin-Lattice Relaxation Processes in tert-Butyl-Substituted Ferrocenium Derivatives. *Eur J Inorg Chem*, 388-400, (2017).

218 Michaelis, L. & Granick, S. The polymerization of the free radicals of the Wurster dye type: The dimeric resonance bond. *J Am Chem Soc* **65**, 1747-1755, (1943).

219 Dobrynina, T. A., Akhapkina, N. A. & Chuvaev, V. F. Synthesis and properties of lithium peroxide monoperoxyhydrate $Li_2O_2 \cdot H_2O_2$. *Bulletin of the Academy of Sciences of the USSR Division of Chemical Science* **18**, 438-440, (1969).

220 Midden, W. R., Wang, S.Y. Singlet oxygen generation for solution kinetics: Clean and simple. *J Am Chem Soc* **105**, (1983).

221 Bartusik, D., Aebisher, D., Ghafari, B., Lyons, A. M. & Greer, A. Generating singlet oxygen bubbles: A new mechanism for gas-liquid oxidations in water. *Langmuir* **28**, 3053-3060, (2012).

222 Chaisiwamongkhol, K., Batchelor-McAuley, C., Palgrave, R. G. & Compton, R. G. Singlet oxygen and the origin of oxygen functionalities on the surface of carbon electrodes. *Angew Chem Int Ed Engl* **57**, 6270-6273, (2018).

223 Bai, S. M. & Barbatti, M. Mechanism of spin-exchange internal conversion: Practical proxies for diabatic and nonadiabatic couplings. *J Chem Theory Comput* **15**, 1503-1513, (2019).

224 Bai, S. & Barbatti, M. Divide-to-Conquer: A kinetic model for singlet oxygen photosensitization. *J Chem Theory Comput* **13**, 5528-5538, (2017).

225 House, R. A. *et al.* What Triggers Oxygen Loss in Oxygen Redox Cathode Materials? *Chem Mater* **31**, 3293-3300, (2019).

226 Fenton, H. J. H. LXXIII.—Oxidation of tartaric acid in presence of iron. *J. Chem. Soc. Trans.* **65**, 899-910, (1894).

227 Baltruschat, H. Differential electrochemical mass spectrometry. *J Am Soc Mass Spectr* **15**, 1693-1706, (2004).

228 Lin, M., Tesconi, M. & Tischler, M. Use of (1)H NMR to facilitate solubility measurement for drug discovery compounds. *Int J Pharm* **369**, 47-52, (2009).

229 Han, K. S. *et al.* Pulsed Field Gradient Nuclear Magnetic Resonance and Diffusion Analysis in Battery Research. *Chem Mater* **33**, 8562-8590, (2021).

230 Bodenhausen, G. & Ruben, D. J. Natural abundance nitrogen-15 NMR by enhanced heteronuclear spectroscopy. *Chem Phys Lett* **69**, 185-189, (1980).

231 Gorter, C. J. Negative result of an attempt to detect nuclear magnetic spins. *Physica* **3**, 995-998, (1936).

232 Andrew, E. R. Magic angle spinning in solid state n.m.r. spectroscopy. *Philosophical Transactions of the Royal Society of London. Series A, Mathematical and Physical Sciences* **299**, 505-520, (1981).

233 Andrew, E. R., Bradbury, A. & Eades, R. G. Removal of Dipolar Broadening of Nuclear Magnetic Resonance Spectra of Solids by Specimen Rotation. *Nature* **183**, 1802-1803, (1959).

234 Schaefer, J. & Stejskal, E. O. C-13 nuclear magnetic-resonance of polymers spinning at magic angle. *J Am Chem Soc* **98**, 1031-1032, (1976).

235 Pines, A., Waugh, J. S. & Gibby, M. G. Proton-enhanced nuclear induction spectroscopy - Method for high-resolution NMR of dilute spins in solids. *J Chem Phys* **56**, 1776-&, (1972).

236 Chan, K. L. A. & Kazarian, S. G. Detection of trace materials with fourier transform infrared spectroscopy using a multi-channel detector. *Analyst* **131**, 126-131, (2006).

237 Newman, J. S. & Thomas-Alyea, K. E. *Electrochemical systems*. 3rd edition edn, (Wiley, 2004).

238 Albery, W. J. *Electrode kinetics*. (Clarendon Press, 1975).

239 Bard, A. J., Fan, F. R. F., Kwak, J. & Lev, O. Scanning electrochemical microscopy - Introduction and principles. *Anal Chem* **61**, 132-138, (1989).

240 Engstrom, R. C. & Pharr, C. M. Scanning electrochemical microscopy. *Anal Chem* **61**, A1099-+, (1989).

241 Polcari, D., Dauphin-Ducharme, P. & Mauzeroll, J. Scanning Electrochemical Microscopy: A Comprehensive Review of Experimental Parameters from 1989 to 2015. *Chem Rev* **116**, 13234-13278, (2016).

242 Lefrou, C. & Cornut, R. Analytical expressions for quantitative scanning electrochemical microscopy (SECM). *Chemphyschem* **11**, 547-556, (2010).

243 Lefrou, C. A unified new analytical approximation for positive feedback currents with a microdisk SECM tip. *J Electroanal Chem* **592**, 103-112, (2006).

244 Cornut, R., Griveau, S. & Lefrou, C. Accuracy study on fitting procedure of kinetics SECM feedback experiments. *J Electroanal Chem* **650**, 55-61, (2010).

245 Cornut, R. & Lefrou, C. A unified new analytical approximation for negative feedback currents with a microdisk SECM tip. *J Electroanal Chem* **608**, 59-66, (2007).

246 Zhao, Y. H., Abraham, M. H. & Zissimos, A. M. Fast calculation of van der Waals volume as a sum of atomic and bond contributions and its application to drug compounds. *J Org Chem* **68**, 7368-7373, (2003).

247 Zhang, T., Liao, K., He, P. & Zhou, H. A self-defense redox mediator for efficient lithium–O2batteries. *Energy Environ. Sci.* **9**, 1024-1030, (2016).

248 Yao, K. P. C. *et al.* Utilization of cobalt bis(terpyridine) metal complex as soluble redox mediator in Li–O_2 batteries. *The Journal of Physical Chemistry C* **120**, 16290-16297, (2016).

249 Park, J. B., Lee, S. H., Jung, H. G., Aurbach, D. & Sun, Y. K. Redox mediators for Li-O_2 batteries: Status and perspectives. *Adv Mater* **30**, (2018).

250 McCloskey, B. D. & Addison, D. A viewpoint on heterogeneous electrocatalysis and redox mediation in nonaqueous Li-O_2 batteries. *Acs Catal* **7**, 772-778, (2017).

251 Liu, T. *et al.* The effect of water on quinone redox mediators in nonaqueous Li-O_2 batteries. *J Am Chem Soc* **140**, 1428-1437, (2018).

252 Bawol, P. P. *et al.* A new thin layer cell for battery related DEMS-experiments: The activity of redox mediators in the Li-O_2 cell. *Phys Chem Chem Phys* **20**, 21447-21456, (2018).

253 Silverstein, T. P. Marcus Theory: Thermodynamics CAN Control the Kinetics of Electron Transfer Reactions. *J Chem Educ* **89**, 1159-1167, (2012).

254 Marcus, R. A. Electron-Transfer Reactions in Chemistry - Theory and Experiment (Nobel Lecture). *Angewandte Chemie-International Edition in English* **32**, 1111-1121, (1993).

255 Chidsey, C. E. D. Free-energy and temperature-dependence of electron-transfer at the metal-electrolyte interface. *Science* **251**, 919-922, (1991).

256 Hush, N. S. Adiabatic rate processes at electrodes.1. Energy-charge relationships. *J Chem Phys* **28**, 962-972, (1958).

257 Hush, N. S. Electron transfer in retrospect and prospect 1: Adiabatic electrode processes. *J Electroanal Chem* **460**, 5-29, (1999).

258 Hamann, T. W., Gstrein, F., Brunschwig, B. S. & Lewis, N. S. Measurement of the free-energy dependence of interfacial charge-transfer rate constants using ZnO/H2O semiconductor/liquid contacts. *J Am Chem Soc* **127**, 7815-7824, (2005).

259 Fitch, A., Strandwitz, N. C., Brunschwig, B. S. & Lewis, N. S. A Comparison of the behavior of single crystalline and nanowire array ZnO photoanodes. *J Phys Chem C* **117**, 2008-2015, (2013).

260 Rodriguez-Lopez, J., Minguzzi, A. & Bard, A. J. Reaction of various reductants with oxide films on Pt electrodes as studied by the surface interrogation mode of scanning electrochemical microscopy (SI-SECM): Possible validity of a Marcus relationship. *J Phys Chem C* **114**, 18645-18655, (2010).

261 Wang, J. J., Chen-Wiegart, Y. C. K. & Wang, J. In operando tracking phase transformation evolution of lithium iron phosphate with hard X-ray microscopy. *Nat Commun* **5**, (2014).

262 Barker, A. L., Unwin, P. R., Amemiya, S., Zhou, J. F. & Bard, A. J. Scanning electrochemistry microscopy (SECM) in the study of electron transfer kinetics at liquid/liquid interfaces: Beyond the constant composition approximation. *J Phys Chem B* **103**, 7260-7269, (1999).

263 Rodríguez-López, J., Minguzzi, A. & Bard, A. J. Reaction of Various Reductants with Oxide Films on Pt Electrodes As Studied by the Surface Interrogation Mode of Scanning

Electrochemical Microscopy (SI-SECM): Possible Validity of a Marcus Relationship. *The Journal of Physical Chemistry C* **114**, 18645-18655, (2010).

264 Park, H. S., Leonard, K. C. & Bard, A. J. Surface interrogation scanning electrochemical microscopy (SI-SECM) of photoelectrochemistry at a W/Mo-$BiVO_4$ semiconductor electrode: Quantification of hydroxyl radicals during water oxidation. *J Phys Chem C* **117**, 12093-12102, (2013).

265 Tsionsky, M., Bard, A. J. & Mirkin, M. V. Long-range electron transfer through a lipid monolayer at the liquid/liquid interface. *J Am Chem Soc* **119**, 10785-10792, (1997).

266 Sun, P. *et al.* Observation of the marcus inverted region of electron transfer reactions at a liquid/liquid interface. *J Am Chem Soc* **125**, 9600-9601, (2003).

267 Arroyo-Curras, N. & Bard, A. J. Iridium oxidation as observed by surface interrogation scanning electrochemical microscopy. *J Phys Chem C* **119**, 8147-8154, (2015).

268 Cornut, R., Mayoral, M., Fabre, D. & Mauzeroll, J. Scanning Electrochemical Microscopy Approach Curves for Ring Microelectrodes in Pure Negative and Positive Feedback Mode. *J Electrochem Soc* **157**, F77, (2010).

269 Cornut, R. & Lefrou, C. New analytical approximation of feedback approach curves with a microdisk SECM tip and irreversible kinetic reaction at the substrate. *J Electroanal Chem* **621**, 178-184, (2008).

270 Barthel, J. & Feuerlein, F. Dielectri properties of propylene carbonate-1,2-dimethoxyethane mixtures and their electrolyte solutions of $NaClO_4$ and Bu_4NClO_4. *Z Phys Chem Neue Fol* **148**, 157-170, (1986).

271 Schwenke, K. U., Meini, S., Wu, X., Gasteiger, H. A. & Piana, M. Stability of superoxide radicals in glyme solvents for non-aqueous Li-O_2 battery electrolytes. *Phys Chem Chem Phys* **15**, 11830-11839, (2013).

272 Kwabi, D. G. *et al.* Experimental and computational analysis of the solvent-dependent O_2/Li^+-O_2^- redox couple: standard potentials, coupling strength, and implications for lithium-oxygen batteries. *Angewandte Chemie International Edition* **55**, 3129-3134, (2016).

273 Bryantsev, V. S., Blanco, M. & Faglioni, F. Stability of lithium superoxide LiO_2 in the gas phase: Computational study of dimerization and disproportionation reactions. *The Journal of Physical Chemistry A* **114**, 8165-8169, (2010).

274 Bender, C. L., Hartmann, P., Vračar, M., Adelhelm, P. & Janek, J. On the thermodynamics, the role of the carbon cathode, and the cycle life of the sodium superoxide (NaO_2) battery. *Adv Energy Mater*, n/a-n/a, (2014).

275 Bender, C. L., Schroder, D., Pinedo, R., Adelhelm, P. & Janek, J. One- or Two-Electron Transfer? The Ambiguous Nature of the Discharge Products in Sodium-Oxygen Batteries. *Angew Chem Int Ed Engl*, (2016).

276 Donkers, R. L. & Workentin, M. S. Elucidation of the electron transfer reduction mechanism of anthracene endoperoxides. *J Am Chem Soc* **126**, 1688-1698, (2004).

277 Bryantsev, V. S. & Faglioni, F. Predicting autoxidation stability of ether and amide-based electrolyte solvents for Li–air batteries. *The Journal of Physical Chemistry A* **116**, 7128-7138, (2012).

278 Kumar, N., Radin, M. D., Wood, B. C., Ogitsu, T. & Siegel, D. J. Surface-Mediated Solvent Decomposition in Li-Air Batteries: Impact of Peroxide and Superoxide Surface Terminations. *J Phys Chem C* **119**, 9050-9060, (2015).

279 Assary, R. S., Lau, K. C., Amine, K., Sun, Y.-K. & Curtiss, L. A. Interactions of dimethoxy ethane with Li_2O_2 clusters and likely decomposition mechanisms for Li–O_2 batteries. *The Journal of Physical Chemistry C* **117**, 8041-8049, (2013).

280 Zhang, X. *et al.* LiO_2: Cryosynthesis and Chemical/Electrochemical Reactivities. *J Phys Chem Lett* **8**, 2334-2338, (2017).

281 Mahne, N., Fontaine, O., Thotiyl, M. O., Wilkening, M. & Freunberger, S. A. Mechanism and performance of lithium-oxygen batteries - a perspective. *Chem Sci* **8**, 6716-6729, (2017).

282 Horwitz, G., Calvo, E. J., Méndez De Leo, L. P. & de la Llave, E. Electrochemical stability of glyme-based electrolytes for Li–O2 batteries studied by in situ infrared spectroscopy. *Phys Chem Chem Phys* **22**, 16615-16623, (2020).

283 Mkhitaryan, A., Papanyan, Z. & L., G. Quantum chemical study in the solvation of lithium chloride in demethyl and diethly sulfones. *Proceedings of the YSU B: Chemical and Biological Sciences* **52**, (2018).

284 Lin-Vien, D. *The handbook of infrared and raman characteristic frequencies of organic molecules*. (Academic Press, 1991).

285 Collinet-Fressancourt, M., Azaroual, N., Aubry, J. M. & Nardello-Rataj, V. Dimethylsulfoxide as a kinetic booster for the chemical generation of singlet oxygen in methanol. *Tetrahedron Lett* **51**, 6531-6534, (2010).

286 Sharon, D. *et al.* Reactivity of amide based solutions in lithium-oxygen cells. *The Journal of Physical Chemistry C* **118**, 15207-15213, (2014).

287 Cordoba, D., Rodriguez, D. H. B. & Calvo, E. J. Singlet oxygen formation during the oxygen reduction reaction in DMSO LiTFSI on lithium air battery carbon electrodes. *Chemistryselect* **4**, 12304-12307, (2019).

288 Samojlov, A., Schuster, D., Kahr, J. & Freunberger, S. A. Surface and catalyst driven singlet oxygen formation in Li-O_2 cells. *Electrochim Acta* **362**, (2020).

289 Rigaudy, J., Breliere, C. & Scribe, P. Photochemistry of 9,10-Diphenylanthracene Endoperoxide. *Tetrahedron Lett*, 687-690, (1978).

290 Aubry, J. M., Pierlot, C., Rigaudy, J. & Schmidt, R. Reversible binding of oxygen to aromatic compounds. *Accounts Chem Res* **36**, 668-675, (2003).

291 Schmidt, R., Schaffner, K., Trost, W. & Brauer, H. D. Wavelength-Dependent and Dual Photochemistry of the Endoperoxides of Anthracene and 9,10-Dimethylanthracene. *J Phys Chem-Us* **88**, 956-958, (1984).

292 Southern, P. F. & Waters, W. A. The Thermal Decomposition of Some Meso-Substituted Anthracene Photo-Oxides. *J Chem Soc*, 4340-4346, (1960).

293 Turro, N. J., Chow, M. F. & Rigaudy, J. Mechanism of Thermolysis of Endoperoxides of Aromatic-Compounds - Activation Parameters, Magnetic-Field, and Magnetic Isotope Effects. *J Am Chem Soc* **103**, 7218-7224, (1981).

294 Rigaudy, J., Barannelafont, J., Defoin, A. & Cuong, N. K. Thermal conversion of meso photo-oxides of acenes. 2. Case of anthracene photo-oxide. *Tetrahedron* **34**, 73-82, (1978).

295 Fudickar, W. & Linker, T. Why triple bonds protect acenes from oxidation and decomposition. *J Am Chem Soc* **134**, 15071-15082, (2012).

296 Adam, W., Kazakov, D. V. & Kazakov, V. P. Singlet-oxygen chemiluminescence in peroxide reactions. *Chem Rev* **105**, 3371-3387, (2005).

297 Yamagaki, T. & Yamazaki, T. Troubleshooting Carry-Over in the LC-MS Analysis of Biomolecules: The Case of Neuropeptide Y. *Mass Spectrom (Tokyo)* **8**, S0083, (2019).

298 Matuszewski, B. K., Constanzer, M. L. & Chavez-Eng, C. M. Strategies for the assessment of matrix effect in quantitative bioanalytical methods based on HPLC-MS/MS. *Anal Chem* **75**, 3019-3030, (2003).

299 Steckel, A. & Schlosser, G. An Organic Chemist's Guide to Electrospray Mass Spectrometric Structure Elucidation. *Molecules* **24**, (2019).

300 Zhang, S. Y. *et al.* On the incompatibility of lithium-O_2 battery technology with CO_2. *Chem Sci* **8**, 6117-6122, (2017).

301 Li, Q. *et al.* A spectroscopic study on singlet oxygen production from different reaction paths using solid inorganic peroxides as starting materials. *B Korean Chem Soc* **28**, 1656-1660, (2007).

302 Alfano, A. J. & Christe, K. O. Singlet delta oxygen production from a gas-solid reaction. *Angew Chem Int Edit* **41**, 3252-+, (2002).

303 Marcus, R. A. On Theory of Chemiluminescent Electron-Transfer Reactions. *J Chem Phys* **43**, 2654-&, (1965).

304 Santhana.Ks & Bard, A. J. Chemiluminescence of electrogenerated 9,10-Diphenylanthracene anion radical. *J Am Chem Soc* **87**, 139-&, (1965).

305 Hercules, D. M. Chemiluminescence Resulting from Electrochemically Generated Species. *Science* **145**, 808-&, (1964).

306 Nardi, G., Manet, I., Monti, S., Miranda, M. A. & Lhiaubet-Vallet, V. Scope and limitations of the TEMPO/EPR method for singlet oxygen detection: the misleading role of electron transfer. *Free Radical Bio Med* **77**, 64-70, (2014).

307 Pignatello, J. J., Oliveros, E. & MacKay, A. Advanced oxidation processes for organic contaminant destruction based on the Fenton reaction and related chemistry. *Crit Rev Env Sci Tec* **37**, 273-275, (2007).

308 Lim, Y. B., Tan, Y. & Turpin, B. J. Chemical insights, explicit chemistry, and yields of secondary organic aerosol from OH radical oxidation of methylglyoxal and glyoxal in the aqueous phase. *Atmos Chem Phys* **13**, 8651-8667, (2013).

309 Balzani, V. & Carassiti, V. *Photochemistry of coordination compounds*. (Academic Press, 1970).

310 Duesterberg, C. K., Cooper, W. J. & Waite, T. D. Fenton-mediated oxidation in the presence and absence of oxygen. *Environ Sci Technol* **39**, 5052-5058, (2005).

311 Henstock, H. 293. The solubilities of metal and ammonium salts of various organic acids in methyl alcohol and acetone. *Journal of the Chemical Society (Resumed)*, (1934).

312 Bianco, P., Haladjia.J, Lanza, E. & Asso, M. Studies on formic acid and sodium formates. 6. Solubility at 25 degrees C of acidic and neutral sodium formates in water acetone mixtures - Influence of sodium perchlorate. *B Soc Chim Fr*, 1253-&, (1971).

313 McCloskey, B. D. *et al.* Combining accurate O_2 and Li_2O_2 assays to separate discharge and charge stability limitations in nonaqueous Li–O_2 batteries. *The Journal of Physical Chemistry Letters* **4**, 2989-2993, (2013).

314 McCloskey, B. D. *et al.* Twin problems of interfacial carbonate formation in nonaqueous Li–O_2 batteries. *The Journal of Physical Chemistry Letters* **3**, 997-1001, (2012).

315 Pierini, A., Brutti, S. & Bodo, E. Superoxide anion disproportionation induced by Li^+ and H^+: Pathways to $^1O_2$ release in Li-O_2 batteries. *Chemphyschem* **21**, 2060-2067, (2020).

316 Chan, M. K. Y. *et al.* Structure of lithium peroxide. *J Phys Chem Lett* **2**, 2483-2486, (2011).

317 Riadigos, C. F., Iglesias, R., Rivas, M. A. & Iglesias, T. P. Permittivity and density of the systems (monoglyme, diglyme, triglyme, or tetraglyme plus n-heptane) at several temperatures. *J Chem Thermodyn* **43**, 275-283, (2011).

318 Elsherbini, M., Allemann, R. K. & Wirth, T. "Dark" singlet oxygen made easy. *Chemistry – A European Journal* **25**, 12486-12490, (2019).

319 Wandt, J., Freiberg, A. T. S., Ogrodnik, A. & Gasteiger, H. A. Singlet oxygen evolution from layered transition metal oxide cathode materials and its implications for lithium-ion batteries. *Mater Today* **21**, 825-833, (2018).

320 Cao, D. Q., Tan, C. & Chen, Y. H. Oxidative decomposition mechanisms of lithium carbonate on carbon substrates in lithium battery chemistries. *Nat Commun* **13**, (2022).

321 Freiberg, A. T. S., Roos, M. K., Wandt, J., de Vivie-Riedle, R. & Gasteiger, H. A. Singlet Oxygen Reactivity with Carbonate Solvents Used for Li-Ion Battery Electrolytes. *J Phys Chem A* **122**, 8828-8839, (2018).

"Journey set sail was to leave
Cause I'm only birds & bees
Lose and news and all things be
Sunlight garden low red blossoms
Moon tides of the sea"
Simon Green aka Bonobo